

SENSITIVITY IMPROVEMENT OF A NUCLEAR MAGNETIC RESONANCE METHOD  
TO MONITOR A BIOARTIFICIAL PANCREAS

By

NELLY A. VOLLAND

A DISSERTATION PRESENTED TO THE GRADUATE SCHOOL  
OF THE UNIVERSITY OF FLORIDA IN PARTIAL FULFILLMENT  
OF THE REQUIREMENTS FOR THE DEGREE OF  
DOCTOR OF PHILOSOPHY

UNIVERSITY OF FLORIDA

2009

© 2009 Nelly A. Volland

To Dr. Ioannis Constantinidis (Yanni),  
suddenly passed away  
from a massive heart attack  
the night of April 16th 2007  
at the age of 46.  
He started his project on diabetes  
over 15 years ago and  
got me involved in it in 2003.  
He has left us all orphans  
after his disappearance.  
I hope that from wherever he is,  
he is proud of our progress.

And to all the others who also left too early,  
especially Sophie (1979-1996),  
and Josephin (1980-2007),  
we biomedical engineers are  
working for this never to  
happen again.

## ACKNOWLEDGEMENTS

The author would like to thank all the people who have made this project possible. The first thanks go to the late Dr. Ioannis Constantinidis for the opportunity, finances, and resources he offered to develop this project, to Dr. Thomas Mareci for taking over the task of becoming her advisor after Dr. Constantinidis' death and offering his laboratory resources and scientific knowledge, and to Dr. Nicholas Simpson for continuing Dr. Constantinidis' work and giving her an opportunity to continue the project.

The author would also like to greatly thank the members of her committee, Dr. Brennan, Dr. Forder, and Dr. Blackband, and the Department of Biomedical Engineering faculty and staff who have always been present and helpful, especially after Dr. Constantinidis disappearance.

The author would also like to greatly thank Barbara Beck and Kelly Jenkins for the time they spent answering the numerous questions regarding electronics and hardware used in the project, discussing the meaning and accuracy of the measurements, and helping with the logistics and good functioning of the NMR equipment. Without them the project would not have gone as far it did. She is also thankful to Dr. Stabler, Dr. Carman, and Dr. Gross for sharing their knowledge on the subjects of tissue-engineered pancreatic construct, material coating, fluorine emulsion, and NMR imaging, which are valuable for the presented work. She is thankful as well to the personnel of the Tissue Laboratory, Oca and Chiab, for teaching her everything she needed to learn to successfully culture her own cells, the personnel in the NMR Laboratory, Bill, for writing piece of computer code within minutes to analyze imaging data efficiently, and all the undergraduate students who worked with her on the project and gave a tremendous help: Chris, Jessica, Matt, and Karly.

Special thanks also goes to the Advanced Magnetic Resonance Imaging and Spectroscopy Facility personnel for their knowledgeable help every time a problem came and allowing her to

keep going even late at night at the facility, as well as to the Animal Care Services employees at the McKnight Brain Institute for their kindness, understanding, and efforts to help with the animal handling, surgeries, and special requests. Special thanks also go to the other graduate students who shared lab space with her, especially Hector, Mansi, Lan, Garrett, and Chelsea for their incredible help and support over the years, their thoughtful discussions, understanding, and funny jokes.

Finally, the author would like to thank her family and closest friends, John, Alojomo, Cécile, Sid M., Sid P., Anne, Didier, Kyle J., and Kennita for all their support and guidance during this work. They have been there every minute of the way, in bad and good moments, always encouraging. Without all of those people and many more, she would have never completed this tedious and complex journey.

This work was primarily supported by funding from the National Institute of Health through grant R01 DK47858 and the support of the National High Magnetic Field Laboratory. Partial stipend support was also provided by the J. Crayton Pruitt Family Department of Biomedical Engineering at the University of Florida. This financial support to this interdisciplinary research is greatly appreciated.

# TABLE OF CONTENTS

	<u>Page</u>
ACKNOWLEDGEMENTS .....	4
LIST OF TABLES.....	10
LIST OF FIGURES .....	11
ABSTRACT .....	15
CHAPTER	
1 INTRODUCTION AND RATIONALE.....	17
1.1 Introduction .....	17
1.2 Rationale .....	20
2 BACKGROUND.....	24
2.1 Diabetes .....	24
2.1.1 General Facts.....	24
2.1.2 Diabetes Type I.....	24
2.2 Tissue-Engineered Pancreatic Substitutes .....	26
2.2.1 Types of Bioartificial Pancreas.....	26
2.2.1.1 Diffusion chamber .....	26
2.2.1.2 Microencapsulation .....	27
2.2.1.3 Macroencapsulation.....	27
2.2.2 Insulin-Producing Cells.....	28
2.2.2.1 Transformed $\beta$ -cell lines .....	29
2.2.2.2 Genetically-engineered stem cells .....	30
2.2.3 Biomaterials .....	30
2.2.3.1 Alginate .....	30
2.2.3.2 Agarose.....	31
2.3 Monitoring of Tissue-Engineered Constructs .....	32
2.3.1 Noninvasive Monitoring <i>In vivo</i> .....	33
2.3.1.1 Nuclear medicine imaging .....	33
2.3.1.2 Optical imaging.....	34
2.3.2 Nuclear Magnetic Resonance.....	35
2.3.2.1 Nuclear magnetic resonance phenomenon.....	36
2.3.2.2 Nuclei of interest.....	41
2.3.2.3 Nuclear magnetic resonance sensitivity .....	44
2.3.2.4 Radiofrequency coils .....	44
2.3.2.5 Coil coating .....	47
2.4 Summary .....	51

3	DEVELOPMENT OF AN INDUCTIVELY-COUPLED RF COIL SYSTEM FOR IMAGING AND SPECTROSCOPIC ANALYSIS OF AN IMPLANTABLE BIOARTIFICIAL CONSTRUCT AT 11.1T .....	53
3.1	Introduction .....	53
3.2	Background.....	53
3.3	Materials and Methods.....	55
3.3.1	RF Coil System Development .....	55
3.3.2	Coating Techniques .....	57
3.3.2.1	Polystyrene.....	58
3.3.2.2	Polytetrafluoroethylene .....	58
3.3.2.3	Polymethylmethacrylate.....	59
3.3.2.4	Polydimethylsiloxane .....	60
3.3.3	RF Coil Testing.....	61
3.3.4	Samples .....	64
3.3.5	Construct Development.....	65
3.3.5.1	Agarose.....	65
3.3.5.2	Alginate foam.....	65
3.3.5.3	Alginate beads.....	65
3.3.6	Animal Preparation and Handling .....	66
3.3.7	NMR Measurements.....	67
3.3.8	SNR Measurement and Statistical Analysis.....	68
3.4	Results.....	69
3.4.1	RF Coil System.....	69
3.4.2	Implantable Coil Coating .....	74
3.4.2.1	Polystyrene.....	74
3.4.2.2	Polytetrafluoroethylene .....	74
3.4.2.3	Polymethylmethacrylate and polydimethylsiloxane.....	75
3.4.3	Coil-Construct Assembly .....	79
3.4.4	Phantom Studies .....	80
3.4.5	<i>In vivo</i> Studies in Mice.....	85
3.5	Discussion.....	86
3.6	Summary.....	90
4	DEVELOPMENT OF A RECEIVE-ONLY INDUCTIVELY-COUPLED RF COIL SYSTEM TO ENHANCE <sup>1</sup> H NMR LOCALIZED SPECTROSCOPY TO MONITOR AN IMPLANTABLE BIOARTIFICIAL CONSTRUCT .....	92
4.1	Introduction .....	92
4.2	Background.....	92
4.3	Materials and Methods.....	95
4.3.1	RF Coil System Development .....	95
4.3.2	Coating Techniques .....	98
4.3.3	RF Coil Testing.....	98
4.3.4	Samples .....	99
4.3.5	Cell Culture .....	100
4.3.6	Construct Development.....	101

4.3.7	NMR Measurements.....	102
4.3.8	SNR Measurements and Statistical Analysis.....	105
4.4	Results.....	106
4.4.1	RF Coil System.....	106
4.4.2	Implantable Coil Coating.....	111
4.4.3	Phantom Studies.....	114
4.4.4	NMR Spectroscopy Studies.....	117
4.5	Discussion.....	121
4.6	Summary.....	127
5	TOWARD THE DEVELOPMENT OF A MULTIPLE-FREQUENCY INDUCTIVELY- COUPLED RF COIL SYSTEM FOR SIMULTANEOUS $^1\text{H}$ , $^{19}\text{F}$ , AND $^{31}\text{P}$ DETECTION FOR IMAGING AND SPECTROSCOPIC ANALYSIS OF AN IMPLANTABLE BIOARTIFICIAL CONSTRUCT AT 11.1T.....	129
5.1	Introduction.....	129
5.2	Background.....	129
5.3	Materials and Methods.....	131
5.3.1	RF Coil System Development.....	131
5.3.2	Coating Techniques.....	137
5.3.3	RF Coil Testing.....	137
5.3.4	Samples.....	139
5.3.4.1	Perfluorocarbons.....	140
5.3.4.2	Phosphorus samples.....	142
5.3.5	NMR Measurements.....	142
5.3.6	SNR Measurements and Statistical Analysis.....	144
5.4	Results.....	145
5.4.1	RF Coil System.....	145
5.4.2	Implantable Coil Coating.....	154
5.4.3	Sample Studies.....	155
5.4.3.1	Perfluorocarbon detection.....	156
5.4.3.2	Phosphorus detection.....	158
5.5	Discussion.....	159
5.6	Summary.....	164
6	CHARACTERIZATION OF A BIOARTIFICIAL PANCREAS AS PART OF AN IMPLANTABLE COIL-CONSTRUCT ASSEMBLY.....	166
6.1	Introduction.....	166
6.2	Background.....	166
6.3	Materials and Methods.....	168
6.3.1	Cell Culture.....	168
6.3.2	Implantable Coil-Pancreatic Construct Assembly.....	168
6.3.2.1	Implantable coil-alginate foam assembly.....	169
6.3.2.2	Implantable coil-alginate beads assembly.....	169

6.3.3	Cell Entrapment .....	170
6.3.3.1	Alginate foam.....	170
6.3.3.2	Alginate beads.....	171
6.3.4	Culture Propagation.....	172
6.3.5	Glucose Consumption .....	172
6.3.6	Histology .....	173
6.3.7	Streptozotocin Injection and Blood Glucose Monitoring .....	173
6.3.8	Animal Preparation and Handling .....	173
6.3.9	Results and Statistical Analysis .....	174
6.4	Results.....	174
6.4.1	Implantable Coil-Construct Assembly Development.....	174
6.4.1.1	Implantable Coil- Alginate foam assembly.....	174
6.4.1.2	Implantable Coil-Alginate bead assembly .....	175
6.4.2	<i>In vitro</i> Study .....	175
6.4.3	<i>In vivo</i> Study .....	180
6.5	Discussion.....	186
6.6	Summary.....	189
7	CONCLUSIONS AND FUTURE WORK.....	191
7.1	Conclusions and Contributions .....	191
7.2	Future Work.....	194
	LIST OF REFERENCES .....	199
	BIOGRAPHICAL SKETCH .....	214

LIST OF TABLES

<u>Table</u>	<u>page</u>
3-1 Implantable coil (IC), surface coil (SC), and inductively-coupled implantable coil system characteristics.....	71
3-2 Implantable coil characteristics when coated with PS.....	74
4-1 Implantable coil characteristic changes after the addition of a decoupling circuit onto the coil.....	108
4-2 Receive-only inductively-coupled implantable coil system characteristics. ....	110
4-3 Comparison of coil characteristics between transmit-receive and receive-only coils and coupled-coil systems. ....	114
5-1 Implantable coil, surface coil, and inductively-coupled implantable coil system characteristics. ....	153

## LIST OF FIGURES

<u>Figure</u>	<u>Page</u>
2-1 Molecular structure of unbranched polymer chain of alginate.....	31
2-2 Molecular structure of agarose.....	32
2-3 Example of NMR data. ....	37
2-4 A SE pulse sequence program example to acquire an image.....	38
2-5 A PRESS pulse sequence program example to acquire a localized spectrum.. ....	39
2-6 A STEAM pulse sequence program example to acquire a localized spectrum.....	40
2-7 Molecular structure of Choline.....	42
2-8 Molecule structure of ATP. ....	42
2-9 Molecule structure of the most commonly used perfluorocarbons. ....	43
2-10 Molecular structure of PMMA.....	49
2-11 Molecular structure of PS. ....	49
2-12 Molecular structure of PDMS. ....	50
2-13 Molecular structure of PTFE. ....	50
3-1 Implantable coil - bioartificial pancreas macroconstruct assembly diagram. ....	55
3-2 Circuit diagram for an inductively-coupled implantable coil system for <sup>1</sup> H detection. ....	57
3-3 Voltage standing wave ratio (VSWR) of a surface coil (SC), an implantable coil (IC), and an inductively- overcoupled system in its different modes. ....	62
3-4 Vector network analyzer outputs used for RF coils Q measurements. ....	63
3-5 Photographs of implantable coils developed as part of an inductively-coupled implantable coil system. ....	69
3-6 Photograph of the surface coil developed as part of an inductively-coupled implantable coil system. ....	70
3-7 RF coil frequency traces, simulated B <sub>1</sub> magnetic field magnitude, and their respective corresponding spin-echo images along the axis of symmetry of the coils. ....	73
3-8 Photograph of the successfully coated implantable coils. ....	75

3-9	Effects of PDMS coating thickness on the implantable coil characteristics. ....	78
3-10	Photograph of the implantable coil-construct assemblies considered in this study. ....	80
3-11	SNR comparison between different RF coils tested under unloaded conditions using a water sample. ....	81
3-12	SNR comparison between different RF coils tested under loaded conditions in a gel phantom. ....	83
3-13	SNR comparison between different RF coils tested under loaded conditions using a gel phantom or <i>in vivo</i> conditions at 11.1T. ....	84
3-14	Cross-sectional images of two bioartificial constructs implanted <i>in vivo</i> . ....	86
4-1	Circuit diagram for a receive-only inductively-coupled implantable coil system for <sup>1</sup> H detection. ....	96
4-2	Implantable coil - bioartificial pancreas macroconstruct assembly schematic and dimensions for the transmit-receive implantable coil. ....	101
4-3	Photograph of the RF coil setup to acquire NMR images. ....	103
4-4	Photographs of the different receive-only implantable coil layouts built and tested. ....	107
4-5	Photographs of the receive-only surface coils tested. ....	109
4-6	Photograph of a receive-only PDMS-coated implantable coil. ....	112
4-7	SNR comparison between transmit-receive and receive-only inductively-coupled implantable coil systems under unloaded conditions using a water sample. ....	115
4-8	SNR comparison between transmit-receive and receive-only inductively-coupled implantable coil systems under loaded conditions using a gel phantom. ....	116
4-9	Signal profiles obtained from NMR images acquired with TRX and RX inductively-coupled systems. ....	118
4-10	Volume selective imaging acquisition in preparation for <sup>1</sup> H localized spectroscopy. ....	119
4-11	<sup>1</sup> H localized spectroscopy data acquired using a transmit-receive inductively-coupled implantable coil system. ....	120
5-1	Circuit diagram for an inductively-coupled double-frequency ( <sup>1</sup> H- <sup>31</sup> P) implantable coil system. ....	134
5-2	Circuit diagram for an inductively-coupled double-frequency ( <sup>1</sup> H- <sup>19</sup> F) implantable coil system. ....	136

5-3	Photograph of PFCE emulsion. ....	141
5-4	Implantable coil - bioartificial pancreas macroconstruct assembly schematic and dimensions. ....	141
5-5	Voltage Standing Wave Ratio (VSWR) of the double frequency $^1\text{H}$ - $^{31}\text{P}$ inductively-coupled coil system at both frequencies. ....	145
5-6	Near magnetic field distribution along the axis of symmetry of the double-frequency $^1\text{H}$ - $^{31}\text{P}$ inductively-coupled coil system at 190.5 MHz and 470.75 MHz.....	146
5-7	Voltage Standing Wave Ratio (VSWR) of the double frequency $^1\text{H}$ - $^{19}\text{F}$ inductively-coupled coil system at both frequencies. ....	148
5-8	Near magnetic field distribution along the axis of symmetry of the double frequency $^1\text{H}$ - $^{19}\text{F}$ inductively-coupled coil system at 442.86 MHz and 470.75 MHz.....	149
5-9	Photograph of the double-frequency $^1\text{H}$ - $^{31}\text{P}$ implantable coil.....	149
5-10	Photograph of the double-frequency $^1\text{H}$ - $^{31}\text{P}$ surface coil. ....	150
5-11	$^{19}\text{F}$ images of a pancreatic construct surrounded by an implantable coil and containing BaA beads with 2.5% PFCE. ....	157
5-12	$^{19}\text{F}$ spectrum series from BaA beads containing 0.4% PFCE within a pancreatic construct surrounded by an implantable coil.....	158
5-13	$^{31}\text{P}$ spectrum of a saline solution containing 500 $\mu\text{M}$ of ATP and $\text{PO}_4^{-2}$ . ....	159
6-1	Photograph of an implantable coil - alginate foam construct assembly prior to being soaked in PBS.....	169
6-2	Implantable coil-bioartificial pancreatic construct assembly diagram and dimensions. .	170
6-3	Photograph of $\beta\text{TC}$ -tet cells encapsulated in alginate beads prior to insertion in a construct.....	175
6-4	Temporal changes in the glucose consumption rate (GCR) of $\beta\text{TC}$ -tet cells encapsulated in APA and BaA beads.....	177
6-5	Hematoxylin/eosin stained cross-sections from BaA beads prepared by encapsulating $\beta\text{TC}$ -tet cells in 2% (w/v) LVM alginate gelled with 55 mM $\text{BaCl}_2$ . ....	179
6-6	Hematoxylin/eosin stained cross-sections from APA beads prepared by encapsulating $\beta\text{TC}$ -tet cells in 2% (w/v) LVM alginate gelled with 100 mM $\text{CaCl}_2$ . ....	179
6-7	Hematoxylin/eosin stained cross-sections of the tissues found inside and around the construct after its retrieval from a mouse peritoneal cavity. ....	181

6-8	MR images of pancreatic substitutes implanted in the peritoneal cavity of two different mice.....	181
6-9	MR images of cell-free beads within the construct cavity over time.....	182
6-10	Photographs of a piece of PEEK mesh. ....	182
6-11	Temporal changes in diabetic mice blood glucose levels after implantation of $\beta$ TC-tet cells encapsulated in BaA beads. ....	184
6-12	Hematoxylin/eosin stained cross-section from implantable coil-construct assembly cavity tissue after 21 days of implantation in a mouse peritoneal cavity. ....	185

Abstract of Dissertation Presented to the Graduate School  
of the University of Florida in Partial Fulfillment of the  
Requirements for the Degree of Doctor of Philosophy

SENSITIVITY IMPROVEMENT OF A NUCLEAR MAGNETIC RESONANCE METHOD  
TO MONITOR A BIOARTIFICIAL PANCREAS

By

Nelly A. Volland

August 2009

Chair: Thomas H. Mareci  
Major: Biomedical Engineering

Non-invasive monitoring of implanted devices is becoming key in developing tissue-engineered structures intended to provide alternative or complementary treatment to people with organ or tissue impairment and/or loss. Bioartificial pancreases for the treatment of Type I diabetes are an example of such structures under development. Nuclear magnetic resonance (NMR) imaging and spectroscopy have already shown their potential for monitoring of these pancreatic substitutes and detecting their early marker of failure. However, the sensitivity of these NMR methods was limited. The studies presented in this dissertation investigate sensitivity improvement by developing inductively-coupled implantable RF coil systems at high magnetic field strength not only for  $^1\text{H}$  detection, but also for the detection of other informative, but less sensitive nuclei, such as  $^{19}\text{F}$  and  $^{31}\text{P}$ . An inductively-coupled implantable coil system was first developed for  $^1\text{H}$  detection to demonstrate the use on inductively-coupled implantable coil system at 11.1 T. Secondly, a development of a receive-only inductively-coupled implanted coil system was investigated to further improve  $^1\text{H}$  detection and increase localized spectroscopy performance. The feasibility of double frequency inductively-coupled implantable coil systems for simultaneous detection of  $^1\text{H}$ - $^{31}\text{P}$  and  $^1\text{H}$ - $^{19}\text{F}$  were explored next, toward the development of a multiple frequency system. The requirements of these coil systems for a complete monitoring of

a bioartificial construct were discussed. In parallel to the coil system developments, the inclusion of an RF coil within the implanted pancreatic construct was also studied to address the restrictions it imposed on the construct design. The results for  $^1\text{H}$  detection establish that large gains in signal-to-noise can be obtained with the use of inductively-coupled implanted coil systems when compared to the use of standard surface coils. This improvement provides a means to better analyze the structures of implanted bioartificial constructs and their changes over time on NMR images. It can also lower the limit of detection when spectroscopy is performed to detect choline NMR signal and allow for better quantitative analysis of bioartificial organ functions. A receive-only inductively-coupled implanted coil system was also successfully developed to further enhance localized spectroscopy since a more homogeneous NMR excitation magnetic field could be achieved with its use compared to the use of a transmit-receive system.  $^{31}\text{P}$  and  $^{19}\text{F}$  spectroscopy was also performed using single-frequency inductively-coupled implanted coil system for  $^{31}\text{P}$  detection to detect adenosinetriphosphate (ATP) and for  $^{19}\text{F}$  detection to detect perfluorocarbons (PFC). These results set the standards for the development of double-frequency inductively-coupled implantable coil systems. The feasibility of double-frequency inductively-coupled implantable coil system was assessed as well. Furthermore, data shows that a coil-construct assembly allowed insulin-producing cells to function and stay viable for extended periods of time *in vitro*. The return to normoglycemia in diabetic mice after coil-construct assembly implantation was also demonstrated while enhanced non-invasive monitoring of the implanted constructs was made possible using NMR methods.

# CHAPTER 1 INTRODUCTION AND RATIONALE

## 1.1 Introduction

Non-invasive monitoring of implanted devices is becoming key in the development of tissue-engineered structures to provide alternative or complementary treatment to people with organ or tissue impairment and/or loss. Tissue-engineered pancreatic substitutes for the treatment of Type I diabetes is one example of tissue-engineered structures that would largely benefit from such a direct *in situ* monitoring method. Bioartificial pancreatic substitutes or constructs implanted to compensate for the loss of the natural insulin-producing cells ( $\beta$ -cells) occurring in type I diabetes have shown promise toward restoring normoglycemia in diabetic animals with near normal regulation over an extended period of time (1). These constructs are made of semi-permeable membranes encapsulating insulin-producing cells. The encapsulated cells respond directly to changes in their surrounding glucose level by producing insulin. This highly-regulated system offers better blood glucose regulation than the most common and most accessible treatment consisting of regular bolus insulin injections throughout the day. Currently, therapeutic efficacy is assessed by the successful restoration of the host's glucose regulation.

Although measuring the host's blood glucose can indicate the construct status, this is an indirect technique that only evaluates the response of the host to the tissue-engineered construct functions and performances. To fully understand the function of such constructs, optimize their design and development, and predict their behavior over time, their full characterization, quality control after development, and performances and life span in a given environment are needed. Histology is a common method for such characterization, but is destructive, and invasive. However, in order to assess changes in construct function that may be predictive of construct failure well in advance of hyperglycemia, a direct and non-invasive method to monitor the

constructs *in vivo* post-implantation over time is desired. A method well suited to perform the direct and non-invasive *in vivo* monitoring of a pancreatic construct is nuclear magnetic resonance (NMR) (2-4). NMR imaging and spectroscopy can repetitively collect structural and functional information from these constructs simultaneously without altering them or their composition. Recent studies utilizing NMR to non-invasively monitor tissue-engineered pancreatic constructs were encouraging (5,6). However, the sensitivity of the monitoring system used in these studies was limited by the strength of the magnetic field and the radiofrequency (RF) antennas (or coils) used to detect the  $^1\text{H}$  NMR signal. It further prevented the detection of informative, but less sensitive, nuclei (compared to  $^1\text{H}$ ), such as  $^{19}\text{F}$  and  $^{31}\text{P}$ .

The endeavor of this thesis was to improve the sensitivity of the NMR method mentioned above to non-invasively monitor a pancreatic construct *in vitro* and *in vivo* and identify early markers of construct failure. Efforts were specifically focused on using higher magnetic field strengths and enhanced RF coils to improve the sensitivity of the NMR method used in the previous studies by at least a factor of four. Higher magnetic fields allow a higher net magnetization of the sample which increases the sensitivity of the method (7). Modifying the RF coil design by matching its size, shape, and proximity to the structure of interest can enhance the sensitivity of the MR detection as well as the selectivity of the MR signal (8).

The approach taken in this research was to develop inductively-coupled RF coil systems to increase the sensitivity of the NMR methods established previously (5,6) to non-invasively monitor a bioartificial pancreas at 11.1 T *in vitro* and *in vivo*. The coil system includes a coil surrounding the tissue-engineered construct (implantable coil) to be monitored. Implantable coil systems have been developed and successfully used over the past 25 years to increase the sensitivity of NMR detection (9,10). Inductively-coupled implantable coil systems have

appeared more recently to eliminate the external cable connection to the implantable coils, which encouraged infection and discomfort at the site of cable exit (11-13). Therefore, inductively-coupled implantable coil systems were investigated to improve the sensitivity of NMR imaging and spectroscopy toward monitoring non-invasively a tissue-engineered construct. In this study, the tissue-engineered model of choice was a bioartificial pancreas. Coil system prototypes, including an implantable coil inductively-coupled to a surface coil, were designed for  $^1\text{H}$  detection and characterized on the bench as well as *in vitro* and *in vivo*. The improvement of the detection sensitivity of the NMR imaging and spectroscopy methods was a primary concern. The effects of different coil types and different implantable coil coatings were investigated and quantified to determine the system with the best sensitivity improvement *in vivo* compared to a surface coil. Furthermore, receive-only inductively-coupled implantable coil systems were later developed and investigated to evaluate their localization improvement when used for  $^1\text{H}$  magnetic resonance spectroscopy (MRS). The feasibility of multiple-frequency inductively-coupled implantable coil systems were also explored since it would allow the simultaneous detection of different nuclei than  $^1\text{H}$ , such as  $^{19}\text{F}$  and  $^{31}\text{P}$ , which would help in the full characterization of the bioartificial pancreas *in vitro* and *in vivo*. While a  $^1\text{H}$ - $^{31}\text{P}$  and a  $^1\text{H}$ - $^{19}\text{F}$  inductively-coupled implantable coil systems were studied, their single-frequency counterparts for  $^{19}\text{F}$  and  $^{31}\text{P}$  detection were also developed to assess their efficacy and set the standards for the multiple-frequency coupled system performances. Different types of bioartificial pancreatic construct were also studied in parallel of the coil system development to define the most appropriate construct to perform its diabetes regulation duties while allowing its monitoring using NMR methods.

## 1.2 Rationale

This dissertation consists of four distinct topics presented in Chapters 3-6. Some of these chapters represent a modified version of an article published or submitted for publication. The individual chapters all include a brief introduction, a focused background, a materials-and-methods section, a presentation of results obtained, a discussion, and a brief summary. Chapter 2 presents the general background information of this research.

The use of inductively-coupled implantable coil systems to improve the sensitivity of NMR imaging and spectroscopy methods to non-invasively monitor a bioartificial pancreas required a methodical characterization of the RF coils. Therefore, the approach here was fourfold: (1) the development and characterization of an inductively-coupled single-frequency implantable coil system for  $^1\text{H}$  detection and the testing of its sensitivity *in vivo*; (2) the development and characterization of a receive-only inductively-coupled single-frequency implantable coil system to further improve the localization of the NMR signal within the construct when performing  $^1\text{H}$  localized spectroscopy; (3) the evaluation of the feasibility of multiple-frequency RF coil systems for the simultaneous detection of  $^1\text{H}$ ,  $^{31}\text{P}$ , and  $^{19}\text{F}$ ; and (4) the development and characterization of the construct in which the implantable coil of an inductively-coupled coil system was inserted. While several different implantable coil designs were explored in this research, all systems used a similar surface coil as their power source.

Initial studies were made to design and select the best inductively-coupled implantable coil system for  $^1\text{H}$  detection compared to a surface coil. Different implantable coils and configurations were considered. Different coatings for the implantable coil were also evaluated, including polymethylmethacrylate (PMMA) (14) and polydimethylsiloxane (PDMS) (15-18). Numerous studies have been published on inductively-coupled implantable coil systems (14,19-21); however, Chapter 3 discusses the development of such a system for monitoring a

bioartificial construct *in vitro* and *in vivo*, demonstrates its use at high field (11.1 T), and investigates its requirements for its use in such an environment.

While an inductively-coupled implantable coil system provides the sensitivity improvement needed to better analyze the structure and function of implanted bioartificial organs, the RF magnetic field homogeneity it creates could be further enhanced to increase the localization of  $^1\text{H}$  MR spectroscopy (MRS). Chapter 4 details the development and the characterization of a receive-only inductively-coupled implantable coil system and demonstrates its use at high field (11.1 T). Developing the inductively-coupled receive-only implantable coil system was easily made by the addition a decoupling circuit to each coil of the system. However, the receive-only implantable coil coating, the inductive coupling of a receive-only loaded system, and the magnet testing of this receive-only system required further consideration than the transmit-receive system presented in Chapter 3.

If  $^1\text{H}$  detection through imaging and localized spectroscopy is important for monitoring a tissue-engineered construct, such as a bioartificial pancreas, phosphorus ( $^{31}\text{P}$ ) and fluorine ( $^{19}\text{F}$ ) detections are essential to bring additional information about the construct well being and functioning and achieve the construct complete monitoring. Chapter 5 describes the requirements and use of single-frequency inductively-coupled implantable coil system for  $^{31}\text{P}$  and  $^{19}\text{F}$  detection as well as the feasibility of two double-frequency inductively-coupled implantable coil systems, ( $^1\text{H}$ - $^{31}\text{P}$  &  $^1\text{H}$ - $^{19}\text{F}$ ). The single frequency systems were characterized to assess the detection sensitivity and to determine, afterwards, the losses multiple-frequency systems suffer for the  $^1\text{H}$ ,  $^{31}\text{P}$ , and  $^{19}\text{F}$  simultaneous detection. The behavior of the implantable coils at different frequencies when coated and loaded was also studied to observe the changes

occurring under different conditions. This is a significant consideration for the development of double-frequency inductively-coupled implantable coil systems.

Once the use of the different inductively-coupled implantable coil systems demonstrated the sensitivity improvement obtained using NMR methods to non-invasively monitor a bioartificial pancreas, the inclusion of the implantable RF coil within the pancreatic construct was studied to characterize the restrictions it placed on the construct design and function. Chapter 6 discusses the development of two flat-disk macroconstructs including an implantable coil. It describes the steps needed to allow their design to incorporate a coil and its coating and allow the non-invasive monitoring of implantable constructs using NMR methods. The coil-construct assembly effects on the entrapped  $\beta$ TC-tet cells viability and function and its ability to reverse a streptozotocin-induced diabetic state in mice were studied. Pre-treating the assemblies was also investigated to prevent construct fibrotic overgrowth *in vivo* in a mouse peritoneal cavity. Chapter 7 summarizes the implications of the findings presented here on the use of inductively-coupled implantable coil system for  $^1\text{H}$ ,  $^{19}\text{F}$ , and  $^{31}\text{P}$  detection to perform NMR imaging and spectroscopy and monitor tissue-engineered constructs, specifically a bioartificial pancreas. The restrictions the implantable coils have on the construct development and the evolution of the inductively-coupled implantable coil systems in future research are also discussed in this last chapter.

The aim of this project is to develop highly-sensitive non-invasive NMR techniques to monitor a bioartificial pancreatic construct in the treatment of diabetes type I. This monitoring potential is critical, as it may allow for the identification of early markers of construct failure long before functional failure of the construct (i.e., hyperglycemia) easily detected by blood glucose measurements. The reason for this optimism is through analogy to the normal pancreas.

There are more insulin-secreting cells ( $\beta$ -cells) in the body than needed to maintain normoglycemia. In the initial stage of type 1 diabetes, the number of  $\beta$ -cells is dwindling. The physiological effects of this cell loss (hyperglycemia) are not experienced until 50-70% of these cells are dead. Likewise, we expect that if we also have an excess of insulin-secreting cells in a bioartificial pancreatic construct, failure of the construct may occur only after a significant fraction of the original total have died. Through careful monitoring, once the lower limit of cell number required to maintain normal function has been determined, the construct can be replaced well before that level is reached, thus preventing hyperglycemia, and effectively controlling diabetes with the implantable construct.

## CHAPTER 2 BACKGROUND

### 2.1 Diabetes

#### 2.1.1 General Facts

Diabetes mellitus, insulin and noninsulin dependent, also known as type I and type II diabetes respectively, is a yet-incurable endocrinologic disease that affected 24 million children and adults in the United States, about 7.8% of the population, in 2008. Between 5 to 10% of diabetic people are diagnosed with type I Diabetes (22). Diabetes is one of the fastest growing diseases where blood glucose levels become abnormally high and which can lead to major secondary health consequences. According to the American Diabetes Association, it currently costs an estimated \$174 billion in health care expenditures.

#### 2.1.2 Diabetes Type I

Diabetes Type I results from an autoimmune disease that destroys the  $\beta$ -cells residing within the islets of Langerhans in the pancreas thus diminishing insulin production (23). As the insulin secretion decreases, blood glucose levels cannot be sustained within the physiological range (80-120 mg/dl). The most common and most accessible treatment to compensate for the need of functional insulin is regular injection of exogenous insulin subcutaneously throughout the day via a syringe. This bolus type of delivery does not offer optimal blood glucose control making high or low blood glucose values difficult to avoid. The patient's average blood glucose level is usually higher than the physiologic average with this type of treatment. This standard management of diabetes offers patients a near normal life, but requires a close and constant monitoring of the disease. One alternative to this treatment is the use of an insulin pump via a catheter placed under the skin in the peritoneal cavity. This setup allows for continuous delivery of a low base level of insulin to the body throughout the day in addition to bolus doses similar to

the ones obtained with syringe use. If the blood glucose level is on average lower and better regulated when using the insulin pump than with the use of syringe injection alone, it still does not optimally control the blood glucose level. The large amount of glucose in the blood vessels can attach to proteins and alter their structure and function. As a consequence, blood vessels tend to become thicker and stiffer impairing blood flow and leading to more important complications, such as heart disease, nephropathy, retinopathy, and limb amputation. Even though the death rates of people with type I diabetes is much lower now than 50 years ago because their blood glucose levels are better regulated and more physiologic, 7% of them die within 25 years of diagnosis. Furthermore, their life expectancy is still reduced (24) due to the major health consequences associated with the disease and which cannot be prevented despite vigilance.

Pancreas transplantations have been increasingly performed over the past forty years in patients exhibiting advanced secondary complications and inadequate glucose control despite insulin therapy (25,26). Pancreatic islet transplantations have also been studied (26,27). Even though improved isolation, transplantation, implantation methods, and new immunosuppression regimen have been developed (28), this procedure is still greatly limited by the insufficient supply of donor tissue. Often two cadavers are needed to isolate the required number of islets for the transplantation in one patient. Therefore, this treatment is currently still reserved for people diagnosed with Diabetes type I with inadequate blood glucose level control despite insulin therapy. Furthermore, a life-long immunosuppressant treatment is required after the transplantation to prevent the rejection of the donor tissue. These limitations have been the motivating factor for the development of an effective treatment which can provide physiologic

blood glucose regulation without the use of an immunosuppressive treatment. Tissue-engineered pancreatic constructs progressively appear to fulfill these requirements.

## **2.2 Tissue-Engineered Pancreatic Substitutes**

Tissue-engineered pancreatic constructs, also called bioartificial pancreases (BAP), emerged over twenty-five years ago. They were first developed to improve islet survival after transplantation without the need for immunosuppressive therapy (1). However, with the limited availability of pancreatic islets, other sources of insulin-producing cells had to be found. The different types of BAP that have mainly been investigated thus far include diffusion chambers, microencapsulation, and macroencapsulation. These devices can be inserted into the blood supply or implanted anywhere in the body that has diffusion potential. They are comprised of individual cells or islet-like clusters of cells within a biocompatible semipermeable membrane which provides mechanical protection and partial immunoisolation. Optimally, the membrane should be permeable to low molecular weight nutrients and metabolites, but impermeable to higher molecular weight molecules, such as immunoglobulin and albumin.

### **2.2.1 Types of Bioartificial Pancreas**

#### **2.2.1.1 Diffusion chamber**

The diffusion chamber was the first BAP shown to restore normal glycemia in animals over extended periods of time (29). It can be made of one or several tubular semipermeable hollow fiber membranes. These devices are commonly referred to as intravascular devices because they are inserted as an artery-to-vein (AV) shunt in the host's body (30,31). The cells or islets are embedded on the outside surface of the fibers and the blood circulates inside the fibers. The closeness of the islets to the blood flow allows them direct access to nutrients and oxygen to maintain islet viability and functionality. High diffusion of glucose through the chamber provides immediate recognition of glucose level changes and triggers high diffusion and

immediate release of insulin. However, the surgical implantation of the device is relatively risky, and blood coagulation in the fibers has been shown to be a major issue with this intravascular device (29,32). Because of significant blood flow changes in the proximity of the device, it was quickly abandoned.

Due to these issues, the development of extravascular devices, such as micro- and macroencapsulated devices, was initiated. These latter devices present major advantages such as smaller size, flexibility in selecting implantation site, and minimal surgical risk. However, these advantages come at the cost of significant diffusion limitations.

#### **2.2.1.2 Microencapsulation**

In microencapsulated devices, the cells or islets are suspended in a polymeric material, gelled, and enclosed within a biocompatible semipermeable membrane to produce microspheres or beads with diameters from a fraction of a millimeter to a couple of millimeters (33). These capsules are small enough to be implanted almost anywhere in the body with a simple needle. The liver and the spleen were initially preferred implantation locations due to their higher diffusion capabilities and their access via the portal vein (34). Despite its limited diffusion capabilities (e.g. lower vascularization), the peritoneal cavity has subsequently become the main implantation site (33,35,36) because of simple accessibility and holding capacity.

Although microencapsulation has been widely used in the development of BAP (35,37), one drawback is the wide dispersion of the implanted capsules throughout the body. This dispersion makes *in vivo* monitoring and retrieval of this type of BAP nearly impossible.

#### **2.2.1.3 Macroencapsulation**

Macroencapsulation involves generating a construct capable of containing a large number of cells. The construct architecture encompasses a matrix, where the cells are suspended between two semipermeable membranes. These devices can take the shape of a tube or a planar

sheet and are generally implanted in either the peritoneal cavity or a subcutaneous location due to their size and geometry. The tubular or fiber macrocapsules are very similar to diffusion chambers used as vascular devices. The main difference resides in the fact that the cells, islets, or microcapsules are embedded inside the fiber instead of on the outside surface (38). Flat sheet membranes are often large circular (39,40) or rectangular (41) sealed chambers in which the cells are immobilized. These devices allow for (i) cell viability studies, (ii) membrane biocompatibility, diffusional, and immunogenic assessment studies, and (iii) insulin and glucose transport modeling.

Both micro- and macroencapsulation techniques will be considered here to generate BAP with high diffusion capability, and keep the entrapped cells all together in one location. A combination of these techniques will also be investigated to make the entire implant easy to retrieve and to monitor closely *in vivo*.

### **2.2.2 Insulin-Producing Cells**

A major component of all BAPs is the insulin-producing cells. Insulin is normally produced by the  $\beta$ -cells of the Langerhans' islets of the pancreas. Ideally, these cells would be used in transplant constructs. However, islets only constitute 1-2% of the total mass of the pancreas, thus their availability is limited. Moreover, one can only obtain islets from dead individuals, so the demand far outweighs the available supply. Furthermore, their isolation remains a tedious process in which more than one cadaveric pancreas is usually required to obtain sufficient functional islets to treat a patient. Unfortunately, their proliferation in culture has been proven to be difficult and not yet fully successful (42). These limitations strongly encouraged the development of modified insulin-producing cell lines. To this end, cell lines from either  $\beta$ - or non- $\beta$ -origin and from either human or non-human source have been generated

as possible human islet substitutes since they can easily and indefinitely be amplified *in vitro*. Many cell lines are currently available, such as porcine islets, transformed  $\beta$ -cell lines (e.g.  $\beta$ -TC3 and  $\beta$ -TC-tet line), and genetically engineered stem cells.

### **2.2.2.1 Transformed $\beta$ -cell lines**

$\beta$ TC3 cells are insulin-producing tumor cells generated from insulinomas derived from transgenic mice carrying the hybrid insulin promoter-simian virus 40 antigen gene (43,44). The major difference between these cells and normal pancreatic islet  $\beta$ -cells is that they do not exhibit a normal insulin response to glucose stimulation. They can be triggered by lower levels of glucose to produce insulin, but immediately reach a maximal insulin release rate. Additionally, they do not include all the regulatory components of the normal  $\beta$ -cells. However, their lower nutrient and oxygen requirement to maintain normal secretory function is an advantage when encapsulated in BAPs. The islet insulin production stops when the oxygen partial pressure goes below 5 mmHg (45,46), whereas the  $\beta$ TC3 cells keep an unaltered insulin production until the oxygen partial pressure becomes 7 mmHg (47). Their proliferative capacity also provides a virtually unlimited supply of these insulin-producing cells. However, this becomes a liability *in vivo* as their continuous proliferation will eventually produce enough insulin-producing cells to put animals and/or humans in danger of hypoglycemia. To alleviate this problem, cell lines with an integrated bacterial tetracycline operon regulatory system (tet) have been developed to regulate cell proliferation.  $\beta$ TC-tet cell line incorporates a 'tet-off' system that stops  $\beta$ TC cell proliferation when tetracycline (or a derivative) is present in the cell's environment (48). This latter cell line will be used in this project even though non- $\beta$  cell lines can also be genetically engineered to secrete insulin.

### **2.2.2.2 Genetically-engineered stem cells**

Genetic engineering concept has been demonstrated using hepatocytes (49), fibroblasts, and enteroendocrine cells (50,51). The main advantage of non- $\beta$  cells is that they can be derived from an autologous source, thus reducing the chances of immune response. Furthermore, stem cells, either embryonic (52) or adult/progenitor (53), have also shown the ability to form islet-like clusters of insulin-producing cells (54). However, non- $\beta$  cells and stem cells are still in their developmental phase and hence will not be considered in the presented work.

### **2.2.3 Biomaterials**

The other major component of any pancreatic construct is the material used to contain the cells and to generate the semipermeable membrane. Several materials can be selected based on their biocompatibility, structural integrity, and diffusion properties. These factors are important to consider since they impact the viability and function of the entrapped cells. Ease of manufacturing and encapsulation conditions are other criteria to take into consideration when choosing the membrane material. The most commonly used materials in studies of both micro- and macroencapsulation BAP designs are alginate (33,37,55) and agarose (39,40,56,57).

#### **2.2.3.1 Alginate**

Alginates are unbranched polymers found in a wide variety of brown seaweeds and some bacteria. They are comprised of  $\alpha$ -L-guluronic acid (G) and  $\beta$ -D-mannuronic acid (M) segments in varying proportions, order, and molecular weight (Figure 2-1). These variables dictate the physical properties of the alginate hydrogel generated in the presence of multivalent cations, such as calcium, barium, and strontium. Alginates with a high G content tend to form more rigid gels at a very specific cation concentration, whereas higher M segment ratio alginates tend to form a softer gel over a wider range of conditions (58). The divalent cation bonding to the G segments rather than the M segments is the reason for the difference in gel structure. The

different cation ionic bonding influences the physical properties of the gel (59). This flexibility in producing alginate gels or foams of various strengths offers the ability to create the cell matrices and semipermeable membranes needed in tissue-engineered constructs (60,61). Therefore, two types of alginate (gel and foam) will be considered in the presented work for both micro- and macroencapsulation. Calcium (62) and barium (59) will be also tested as cationic bonding agents.

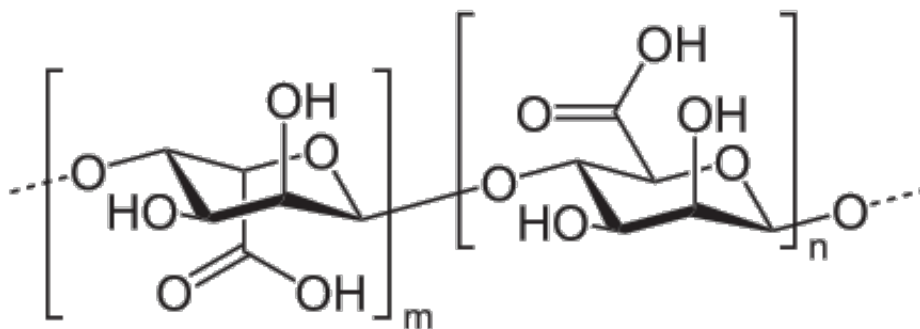


Figure 2-1. Molecular structure of unbranched polymer chain of alginate. This molecule contains both the  $\alpha$ -L-guluronic acid (G) segment (right) and  $\beta$ -D-mannuronic acid (M) segment (left) randomly ordered.

### 2.2.3.2 Agarose

Similarly, agarose is a linear polysaccharide isolated from agar found in marine red algae. It is made of basic repeating agarobiose units, comprised of alternating segments of  $\beta$ -D-galactose and 3,6-anhydro- $\alpha$ -L-galactose (Figure 2-2). It can vary widely in molecular weight. Agarose gels are formed by suspending dry agarose in aqueous buffer, then boiling the mixture until a clear solution forms (above 90°C) (63). The gel forms as the solution cools. Unlike alginate, this gel is weakly ionic with a large distribution of pore sizes depending on the agarose concentration (64).

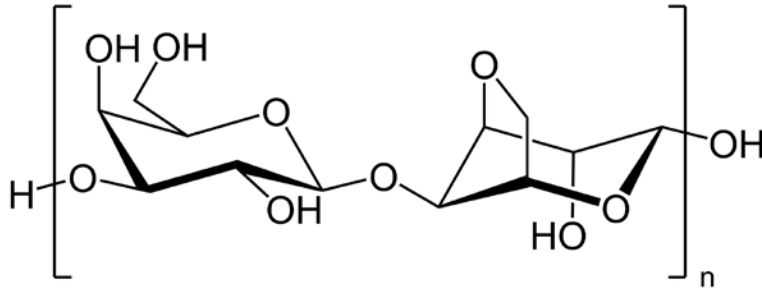


Figure 2-2. Molecular structure of agarose. This molecule is composed of agarobiose units of  $\beta$ -D-galactose and 3,6-anhydro- $\alpha$ -L-galactose.

Agarose will be explored here to generate macrocapsules. Other materials that have also been studied as cell matrices and/or semipermeable membranes are polyvinyl alcohol (PVA) (41,65) and poly(N,N-dimethyl acrylamide) or PDMAAm crosslinked by hydrophobic polyisobutylene (PIB) moieties (PDMAAm-*I*-PIB) (66), and silicate (36,67). Even though these materials have shown promising results, they are still in their early developmental stage and will not be considered in the presented work.

### 2.3 Monitoring of Tissue-Engineered Constructs

*In vitro* and *in vivo* monitoring is of primary importance for the development of tissue-engineered constructs as it can be a tool to study the construct functionality temporally and optimize its design and function. Measuring a subject's blood glucose and insulin concentrations is currently the main technique to evaluate the behavior of the cells imbedded within the semipermeable membrane of a BAP *in vivo*. These indirect techniques evaluate the response of the host to the BAP functions and performances *in vivo*. Unfortunately, they cannot provide information about the mechanical integrity of the construct nor its potential demise. Histology can assess the construct's integrity and its mechanisms of failure (if any). However, it is a destructive, non-dynamic, and non-real-time technique. Non-invasive dynamic and real-time methods for monitoring construct cell viability and metabolism can provide the time-dependant

information of experimental, developmental, environmental, and therapeutic influences on the construct in the same subject. It also allows the realization of practical and clinically relevant constructs.

### **2.3.1 Noninvasive Monitoring *In vivo***

Several methods are available to directly monitor tissue-engineered constructs non-invasively *in vivo*. Each of them differs from each other in its spatial and temporal resolution, depth penetration, image generation mode, molecular probe need and availability, specificity, and sensitivity (68). Positron emission tomography, single photon emission computed tomography (69,70), optical microscopy (71), and nuclear magnetic resonance imaging and spectroscopy (2-4), have been the most widely investigated monitoring methods as diabetes treatment modalities.

#### **2.3.1.1 Nuclear medicine imaging**

Positron emission tomography (PET) and single photon emission computed tomography (SPECT) have already been shown to be safe and feasible techniques to image transplanted pancreatic islets non-invasively (69,70). Though SPECT is less commonly used, both techniques can be used to image tissue-engineered constructs non-invasively and track cellular function and viability. PET generates images by recording high-energy  $\gamma$ -rays emitted from radionuclide probes introduced in the subject. Natural biological molecules can be labeled with an isotope, such as  $^{15}\text{O}$ ,  $^{13}\text{N}$ ,  $^{11}\text{C}$ , and  $^{18}\text{F}$  (substitute for  $^1\text{H}$ ), capable of producing a positron from its nucleus, which will eventually annihilate with a nearby electron to create two  $\gamma$ -rays needed for PET (72). DeLonlay *et al.* used  $^{18}\text{F}$ Fluoro-L-dihydroxyphenylalanine (DOPA) to evaluate the difference between diffuse and focal hyperinsulinism (70) as pancreatic  $\beta$ -cells can take this radionuclide up and convert it into dopamine. Cells can also be engineered to express a reporter

gene that will allow the uptake of a specific radionuclide. Lu *et al.* created cells expressing the herpes simplex virus-1 thymidine kinase (HSV TK) gene to allow the uptake of labeled 9-(4-fluoro-3-hydroxymethylbutyl)guanine (FHBG) (69) to monitor transplanted islets after implantation. SPECT employs the detection of  $\gamma$ -rays from  $\gamma$ -emitting isotopes, such as  $^{99m}\text{Tc}$ ,  $^{111}\text{In}$ ,  $^{123}\text{I}$ , and  $^{131}\text{I}$  to generate images. Unfortunately, the injection of these radionuclide probes or the modification of the cells of interest to express a PET or SPECT reporter gene are two major drawbacks of these techniques. Furthermore, the half-life of the radionuclide probes is relatively short. Even though these techniques have no depth penetration limitation and their sensitivity and specificity are high (only  $10^{-10}$  to  $10^{-12}$  mol/L radionuclide is needed to generate images), the best resolution they can achieve is only 1-2 mm. Simultaneous multiprobe detection is also impossible in PET, although SPECT could have some capability of using isotopes of different energy.

### **2.3.1.2 Optical imaging**

Optical imaging techniques have become of more and more interest recently with the advancement in silicon-based charged coupled devices (CCD) detectors. Bioluminescence imaging (BLI) uses the emitted light from a living structure resulting from a chemical reaction during which chemical energy is converted to light energy to generate an image. Often this requires the modification of the cells of interest to express a bioluminescence reporter gene. Fowler *et al.* created an adenovirus encoding firefly luciferase to express luciferase in pancreatic islets and monitor them after transplantation in mice and measure their mass over time (73). The detectors also need to be cooled in order to reduce thermal noise and increase the imaging sensitivity. Fluorescence imaging utilizes the emission of light triggered by the molecular absorption of a photon from an external light source with a different wavelength to generate an

image. The introduction of fluorescent probes, such as fluorophores and green fluorescent proteins (GFP), is often necessary. Quantum dots, nanoscale semiconductor crystallites with the ability to emit monochromatic light at a specific wavelength and color, are another possibility (74,75). These techniques allow real time, non-invasive, and non-destructive imaging of living tissues at a very high spatial resolution (micron and submicron level). Confocal microscopy (CM) is one popular fluorescence-mediated technique that has enabled high contrast three-dimensional imaging of tissue structures in intact, optically non-transparent samples. However, the introduction of fluorescent probes with limited lifetime in the sample (71) to enhance the imaging contrast is one major limitation of this technique. Relatively intense light power may also be required to obtain adequate image quality. These two requirements are often detrimental to cell viability. Furthermore, the limited light penetration depth (only a few hundred microns) is one more issue with this modality as constructs are implanted well beneath the skin surface (a couple of millimeters deep). The use of multiphoton microscopy instead of confocal microscopy can improve imaging depth to some degree. However, a near-infrared (NIR) optical imaging technique, like optical coherence tomography (OCT), can be used to overcome several limitations in optical imaging (76). It measures the intensity of back reflected light and relies on the variations of indices of refraction of optical scattering for image contrast. Therefore, no fluorescent probe is needed. Near-infrared light also has a greater penetration depth compared to light used to excite fluorescent probes. Nonetheless, this optical technique offers most of its advantages to *in vitro* studies because the imaging depth can never exceed two or three millimeters.

### **2.3.2 Nuclear Magnetic Resonance**

Nuclear Magnetic Resonance (NMR) has also been used to monitor non-invasively tissue-engineered constructs in real time (77). This technique can be applied to a variety of living

systems ranging from a single cell (78) to an entire human being (79), and can yield both chemical information (spectra) or structural information (images). It can be implemented to provide excellent contrast in soft tissue with high resolution ( $< 100 \mu\text{m}$ ), and can also detect a variety of important metabolites deep within a sample. NMR techniques represent the best compromise to monitor a BAP longitudinally and non-invasively *in vitro* and *in vivo* (2-4).

### **2.3.2.1 Nuclear magnetic resonance phenomenon**

The NMR phenomenon takes advantage of nuclei that have a nuclear spin. In presence of a magnetic field, referred as to the main or static magnetic ( $B_0$ ), these nuclei align with or against this magnetic field, creating a known state of equilibrium in the sample. The difference between the two nuclei (spins) populations results in a net magnetization of the sample ( $M_0$ ) along the field ( $B_0$ ). These spins have an associated resonant frequency ( $f_0$ , in the radiofrequency (RF) range) at which they can interact. Because of this property, specific RF waves or pulses can be applied to a sample to generate an excitation magnetic field ( $B_1$ ) perpendicular to  $B_0$  and put these spins in an excited state. These RF pulses are generated by RF antennas, also called transmit RF coils. An excitation or  $90^\circ$  pulse cancels the sample net magnetization ( $M = 0$ ), whereas a refocusing or  $180^\circ$  pulse inverse it ( $M = -M_0$ ). After the RF pulse, the relaxation of the spins back to equilibrium creates RF magnetic fields that can be detected by a receiver RF coil, which generates an RF signal called Free Induction Decay (FID). This return to equilibrium occurs due to various mechanisms. It can be measured as the recovery of the magnetization along  $B_0$  (defined as the Z-direction), and the loss of magnetization in the orthogonal (XY) plane after  $B_1$  ended. These components exhibit exponential decay dependence defined as longitudinal or spin-lattice ( $T_1$ ) and transversal or spin-spin ( $T_2$ ) relaxation times, respectively. Magnetic gradients can be superimposed upon the main magnetic field to localize the FID to a specific

volume of interest (VOI) in the three-dimensional object being studied. This is the basis of the formation of both NMR images and spatially localized NMR spectra (Figure 2-3).

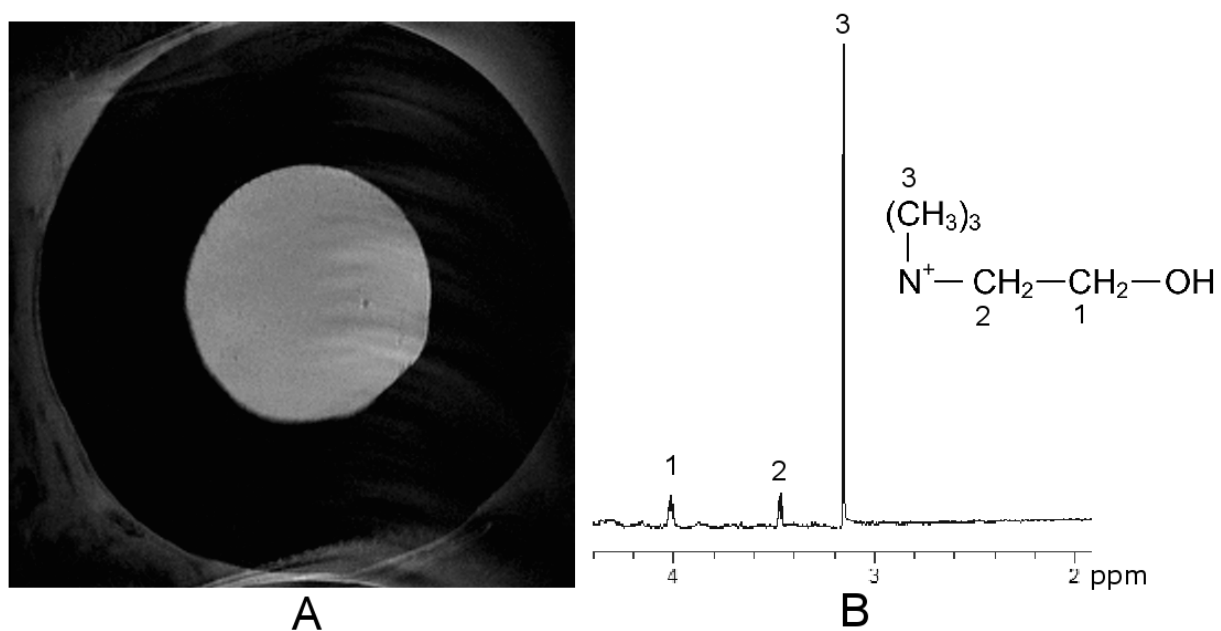


Figure 2-3. Example of NMR data. A) Image of a bioartificial pancreatic construct *in vivo*; and B) <sup>1</sup>H NMR spectrum of a 1 mM choline solution in D<sub>2</sub>O displaying the different resonances of choline.

For magnetic resonance imaging (MRI), a slice encode gradient determines the orientation of the slices acquired. Phase and frequency encode gradients, the latter often being called read out gradient, are applied perpendicular to the slice gradient to allow the signal acquisition pixel by pixel and the generation of 2D images (80) after applying Fourier transforms (FT). The combination of the gradients and RF pulses creates a pulse sequence. A commonly used imaging sequence is the spin-echo (SE) sequences where an excitation and a refocusing pulse are combined with slice, phase encode, and read out gradients (Figure 2-4). By varying times between the different pulses (repetition time (TR) and time of echo (TE)), the images (Figure 2-3A) can be T<sub>2</sub>-weighted, T<sub>1</sub>-weighted, or representing the spin density of the sample.

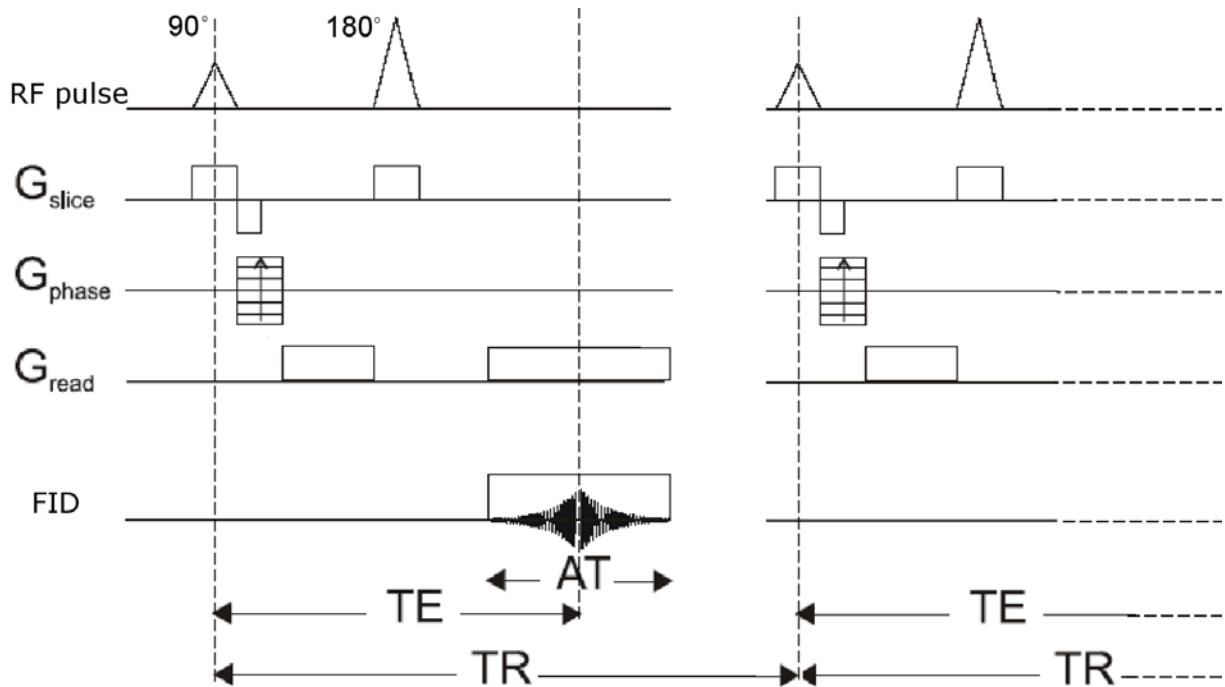


Figure 2-4. A SE pulse sequence program example to acquire an image. The RF pulses are an excitation ( $90^\circ$ ) and a refocusing ( $180^\circ$ ) pulse,  $G_{\text{slice}}$  the slice encode gradient,  $G_{\text{phase}}$  the phase encode gradient,  $G_{\text{read}}$  the frequency encode or read out gradient, FID the free induction decay, AT the acquisition time, TE the time of echo, TR the time of repetition.

For magnetic resonance spectroscopy (MRS), simple hard pulses can be applied without any gradient techniques to allow the generation of spectra. However, if the signal to be detected comes from a small specific region surrounded by regions with similar signal, localized spectroscopy will have to be applied. In this latter technique, the same gradient technique as for MRI occurs, except that it localizes a small cube region of 2-to-5  $\text{mm}^3$  (a voxel), and the signal acquisition allows the generation of a spectrum of similar nuclei within this selected voxel (Figure 2-3B) (81). Two commonly used localized spectroscopy pulse sequences are the point resolved spectroscopy (PRESS; (82)) sequence and the stimulated echo acquisition mode sequence (STEAM; (83)).

The PRESS sequence (Figure 2-5) includes three RF pulses (one  $90^\circ$  and two  $180^\circ$ ) applied in synchronization with the gradients to generate an echo at the time of acquisition in the

volume defined by the intersection of the three selective-pulse-defined planes (voxel). The sequence is  $T_2$ -weighted due to its spin echo characteristics (long TE) and may be difficult to implement to detect molecules with a short  $T_2$ . Furthermore,  $180^\circ$  pulses are harder to achieve and requires more power than  $90^\circ$  pulses.

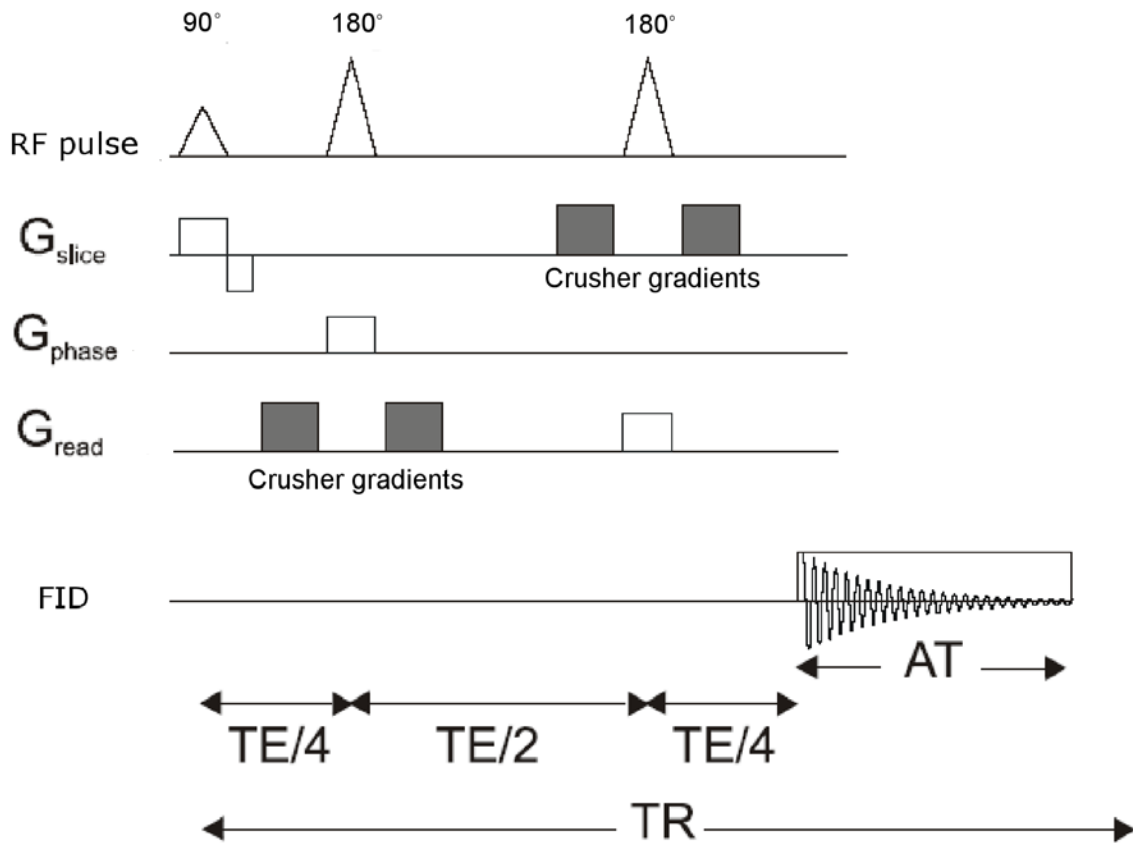


Figure 2-5. A PRESS pulse sequence program example to acquire a localized spectrum. The RF pulses are an excitation ( $90^\circ$ ) and a refocusing ( $180^\circ$ ) pulse,  $G_{\text{slice}}$  the slice encode gradient,  $G_{\text{phase}}$  the phase encode gradient,  $G_{\text{read}}$  the frequency encode or read out gradient, FID the free induction decay, AT the acquisition time, TE the time of echo, TR the time of repetition. The crusher gradients are correction gradients that manipulate the phase of the unwanted signals due to non-ideal refocusing RF pulses to eliminate them.

The STEAM sequence (Figure 2-6) includes three  $90^\circ$  pulses applied in synchronization with the gradients to generate a stimulated echo at the time of acquisition in the volume defined by the intersection of the three selective-pulse-defined planes (voxel). The sequence is not as  $T_2$ -

weighted as the PRESS as its effective TE is shorter than the PRESS sequence TE. Since only 90° pulses are used, the power requirements for this sequence are lower than the PRESS. However, the signal sensitivity is about 50% less than the PRESS sequence due to the formation of stimulated echo. Furthermore, it is more subject to diffusion weighting error because the spoiler gradients are more spaced in time than the crusher gradients are in the PRESS sequence.

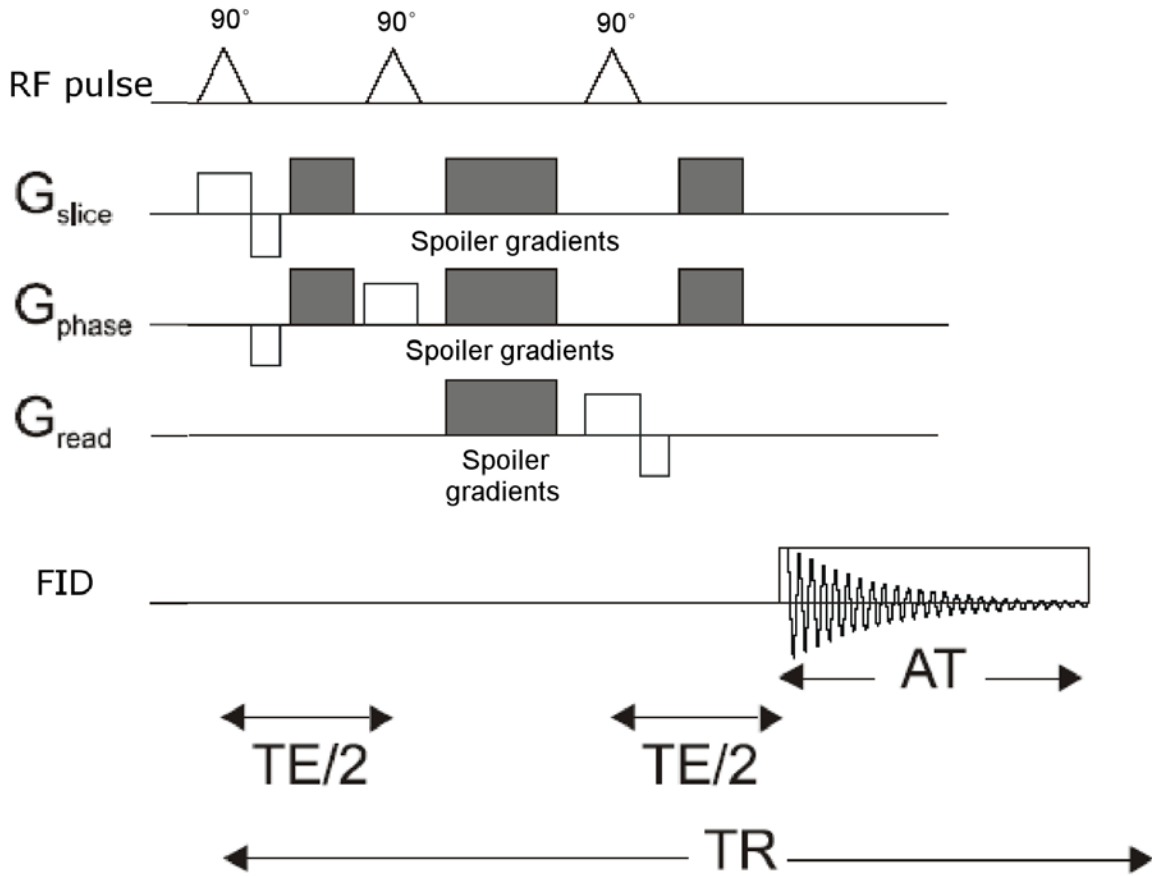


Figure 2-6. A STEAM pulse sequence program example to acquire a localized spectrum. The RF pulses are an excitation (90°) pulses,  $G_{\text{slice}}$  the slice encode gradient,  $G_{\text{phase}}$  the phase encode gradient,  $G_{\text{read}}$  the frequency encode or read out gradient, FID the free induction decay, AT the acquisition time, TE the time of echo, TR the time of repetition. The spoiler gradients are correction gradients that dephase non-selectively any residual transverse magnetization.

The PRESS sequence will initially be given the advantage when performing localized spectroscopy because of its higher sensitivity and its use in previous studies for  $^1\text{H}$  detection

(5,6). The STEAM sequence will be implemented subsequently, if the results obtained using the PRESS sequence are not judged satisfactory.

### 2.3.2.2 Nuclei of interest

There are a number of biologically relevant nuclei that are detectable with NMR. For a BAP, they include, but are not limited to, hydrogen ( $^1\text{H}$ ), phosphorus ( $^{31}\text{P}$ ), and fluorine ( $^{19}\text{F}$ ).

**Hydrogen ( $^1\text{H}$ ):** Hydrogen is the one of the most sensitive NMR nuclei and the most abundant in living tissues, primarily due to water. It is commonly detected to yield clinical images (MRI). Other important biological compounds containing  $^1\text{H}$  and in the millimolar range (such as choline and lactate) can be detected. However, to be able to observe them clearly on spectra (MRS), the large water signal has been suppressed. Water suppression methods have been developed (84) extensively for this purpose. Understanding the biochemical significance of these detectable compounds is essential to the interpretation of acquired spectra. Lactate signal relates to an increased rate of anaerobic glycolysis (anaerobic energy metabolism) indicating the presence of hypoxia (85) or a problem with the tricarboxylic acid (TCA) cycle. Choline is a vital amine molecule, which participates in cell-signaling, serves as an acetylcholine precursor, and adds structural integrity to cell membranes (Figure 2-7). The choline NMR signal, also referred to as total choline (TCho) signal, includes the signal from the following aqueous compounds: phosphocholine (PCho, a precursor of membrane phospholipids), glycerophosphocholine (GPCho, a product of the degradation of membrane phospholipids) and free choline (Cho). Variations in the signal intensity represent an increase of membrane phospholipid biosynthesis and serves as an active marker for cellular proliferation in tumors (86,87). For a BAP, TCho intensity changes have been shown to be linked to oxygen concentration (88) and proportional to the change in cell viability (5,6).

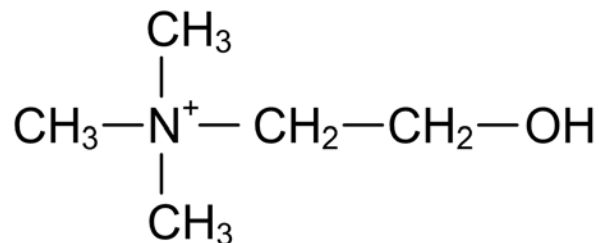


Figure 2-7. Molecular structure of Choline.

**Phosphorus ( $^{31}\text{P}$ ):** Phosphorus NMR has been used extensively to investigate the bioenergetic status of cells, phospholipid metabolism (89), and intracellular pH (90). Despite its low sensitivity (only 6.6% of  $^1\text{H}$  sensitivity), phosphocreatine (PCr), adenosine triphosphate (ATP, Figure 2-8) and inorganic phosphate ( $\text{P}_i$ ) are clearly observable on  $^{31}\text{P}$  spectra. For a BAP,  $^{31}\text{P}$  NMR (ATP detection) has been utilized *in vitro* to investigate the link between cell bioenergetics and insulin secretion following step changes in glucose or oxygen concentration in  $\beta\text{TC3}$  cells (91,92).

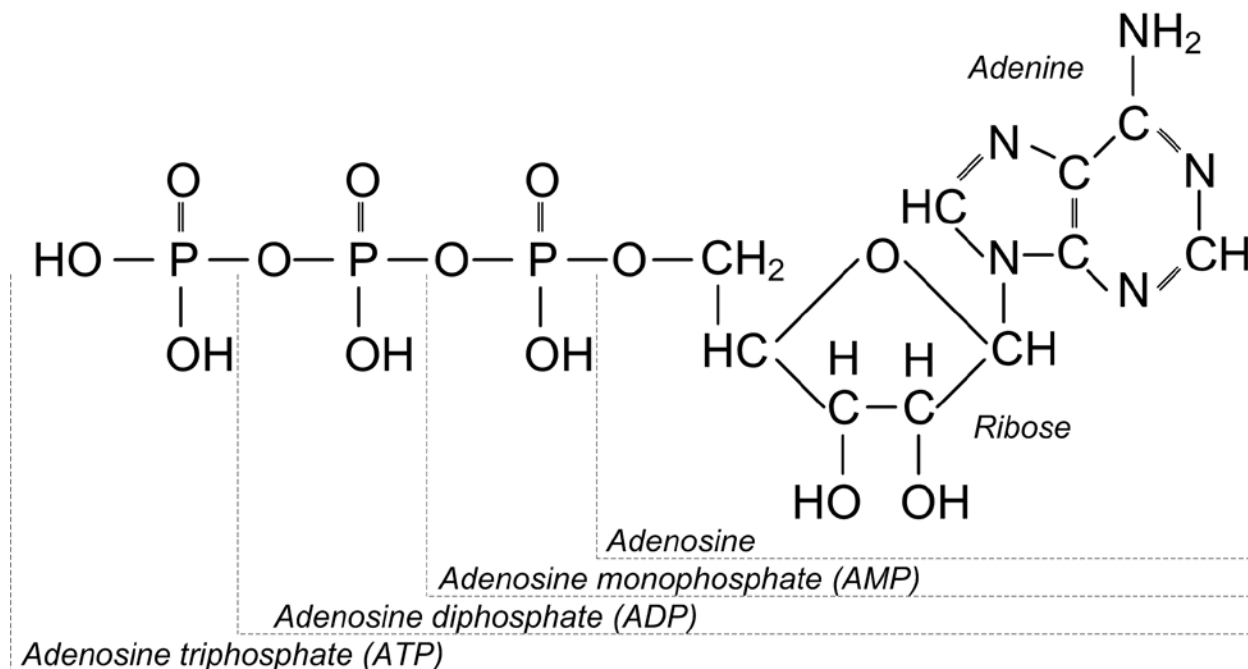


Figure 2-8. Molecule structure of ATP.

**Fluorine ( $^{19}\text{F}$ ):** Detection of  $^{19}\text{F}$  by NMR can be biologically relevant, because following excitation, the fluorine spin-lattice relaxation rate characteristic ( $1/T_1$ ) increases linearly with the concentration of oxygen in the solution. This is due to the dipolar (paramagnetic) interactions between oxygen and fluorine molecules (93). Furthermore, the high sensitivity of fluorine is advantageous (83% of that of  $^1\text{H}$ ). Even though fluorine is not commonly found in biological samples, the addition of a small amount of perfluorocarbons to a culture media can allow for determination of the oxygen concentration in a cell suspension. For a BAP,  $^{19}\text{F}$  NMR is used to monitor the oxygen tension within a construct *in vitro* (94,95) and *in vivo* (96). Different perfluorocarbons (PFC) can be used. The two most frequently encountered, which will be considered in the presented work, are perfluorotributylamine (PFTBA, Figure 2-9A) and perfluoro-15-crown-5-ether (PFCE, Figure 2-9B). Their entrapment is usually simple, and the size of their molecules prevents their clearance from within the gel material used for the BAP keeping the NMR detection sensitivity constant over time.

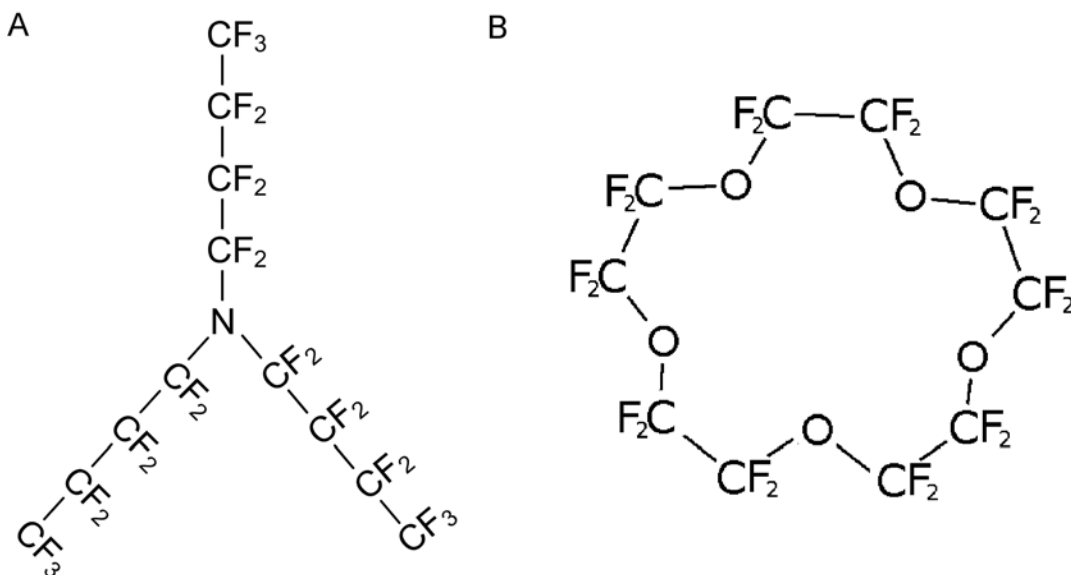


Figure 2-9. Molecule structure of the most commonly used perfluorocarbons. A) PFTBA; and B) PFCE.

### 2.3.2.3 Nuclear magnetic resonance sensitivity

The main issue of the NMR techniques is their relative insensitivity (e.g., requiring millimolar concentration ranges for detection), often characterized by their signal-to-noise ratio (SNR). For a fixed volume/number of cells, the SNR limitation can be improved upon by using higher magnetic field strengths (97). This works because the net magnetization increases with increased magnetic field strength (i.e., more nuclei align with the magnetic field, the lower energy state) (7). Another method to improve the sensitivity of the system is to enhance the RF coils. Modifying the RF coil design by matching the size, shape, and proximity to the structure of interest can enhance the sensitivity of the MR detection as well as the selectivity of the MR signal (8).

### 2.3.2.4 Radiofrequency coils

The sensitivity enhancement can be seen in the evolution from simple surface coils to quadrature surface coil combinations (98) and/or phased arrays of surface coils (99). The development of implanted coils can further increase the MR measurement sensitivity from deep specific internal structures of a relatively undisturbed system (100,101). In addition, this coil arrangement allows for better spatial localization and will be considered in the presented work.

**Implantable coils:** Implantable or implanted coils were first developed to produce high quality *in vivo* phosphorus spectra (9,10). These early systems included only one coil with wires going through the skin to connect the coil with the electronic circuit and amplifier. They were also often only implanted temporarily. Recently, implantable coil systems have been modified to eliminate the external connections (11-13). The modification consists of creating a single unit using two coils; one coil is implanted in the body (implantable coil) while the other one is positioned extracorporeally (surface coil). The surface coil excites the implantable coil and receives its response signal wirelessly. The two coils are inductively-coupled. Many types of

coils can be used in this system, such as simple wire loop, loop-gap resonators (102), solenoid (8), or bird-cage resonators (103). These inductively-coupled systems represent an advantage over a single implanted coil as no cable is going through the skin to connect the implanted coil to the power source and amplifiers (12,14,19-21). The risk of infection is largely decreased, thus increasing the time an animal may be safely monitored without additional surgery.

**Receive-only coils:** In order to get a more uniform excitation pattern within the sample, large surface coils or volume coils can be used. A smaller coil closer to the area of interest, such as the coil system described in the Implantable Coils section, can then detect the FID signal with a higher sensitivity. However, the two coil sets would interact with each other via mutual inductance, causing the acquisition of erroneous data. One way to isolate the coils from each other is to make the RF magnetic field they produce orthogonal to each other. Nonetheless, to obtain a proper decoupling between the coils requires a high degree of accuracy in the placement of one coil compared to the other and is often not pursued, nor will it be here. The second possibility is to insert a decoupling circuit into the coil circuit (104-106). This decoupling circuit added in parallel with a coil tuning capacitor will introduce a high impedance in the coil circuit, when turned on, preventing the current to flow. This decoupling can be passive or active. Unlike passive decoupling, active decoupling requires an external current source to be activated. This distinction is why the active decoupling (104,106) is used often in larger excitation coils when the amount of current supplied to activate the diodes is an issue. Passive decoupling is used in smaller receiver coils (105) as the larger excitation coils usually produce enough power to activate the diodes of the decoupling circuit. Active decoupling was quickly ruled out for the system explored here as the inductive coupling between the two coils of the system was designed to remove any external connections from the implantable coil. Consequently, passive decoupling

will be investigated to make the inductively-coupled implantable coil system receive-only when using a birdcage volume coil for excitation (14).

**Multiple-frequency coils:** Different coil systems can be developed to detect the different nuclei of interest in this project. However, since only one coil can be implanted per construct, coils that are tuned to multiple frequencies need to be considered. These types of coils will be investigated here to allow for the simultaneous assessment of different physiologically relevant parameters within a single construct and amenable direct cross-correlation studies between the different cell metabolic activities and functions.

Multiple-frequency coils have been developed for over 30 years. These coils are mainly based on tank, or “trap”, circuits (107) and transformer-coupled circuits (108). A large number of these coils can be found in solid-state NMR, essentially triple and quadruple frequency microcoils (109-111). For *in vivo* studies, these multiple-frequency coils are generally birdcage volume coils (112) or surface coils (113,114), essentially double-tuned  $^1\text{H}$  and  $^{31}\text{P}$ , due to the importance of the biological compounds observed at these frequencies (112,113,115-117).  $^1\text{H}$  detection is also often not optimized and only used for shimming purposes (114). However, every combination of two or more nuclei is theoretically possible (107,118). A few triple or more resonance coils have been developed for *in vivo* applications (119,120). Gonen *et al.* utilized a surface coil with multiple tank circuit ( $^1\text{H}$ - $^{31}\text{P}$ ) and another coil to allow  $^1\text{H}$  decoupling (119), while Eleff *et al.* used tank and capacitively-coupled tank circuit coils.

One inductively-coupled double-frequency system was developed and implanted for *in vivo* studies (121). However, only the implanted coil was double resonance. The surface coil was a system of two independent non-resonating coils. Furthermore, the implantable coil had accessible variable components and its distance to the surface coils could be changed as well.

These options are impossible to implement here as the system geometry is fixed by the anatomy of the implantable coil recipient and the implantable coil is inaccessible by experimental setting. Consequently, no fully multiple-frequency inductively-coupled coil system has yet been reported in the literature. Since the efficiency of tank and transformer-coupled circuits to generate multiple-frequency coils is relatively similar (113), both methods will be investigated.

#### **2.3.2.5 Coil coating**

Any *in vitro* and *in vivo* testing of an inductively-coupled coil system will require the development step of isolating the implanted coil from the host. The implantable coil is made of non-biocompatible material, which can potentially trigger an immune response from the host. Moreover, the strong coupling the coil can have with the body will substantially decrease the performance of the coil as biological tissues and fluids are highly conductive. Consequently, coating any coil to be implanted is necessary. First of all, this coating needs to be biocompatible not to trigger a chronic immune response from the host that would adversely affect the host's health and prevent the implanted coil from performing optimally. The coating also needs to insulate the coil from the tissues to keep the coupling between them as low as possible and the performances of coil optimal. Therefore, the coating material must have a low dielectric constant to eliminate the electric field storage and minimize the disturbance of the magnetic field generated by the coated coil and a low conductivity to minimize the electrical losses in the sample. If the dielectric constant is not low, the introduction of coupling capacitance between the coil, the coating, and the body will create a resonant frequency shift of the implantable coil. If the conductivity is not low, the loading of the coil will decrease the performances of the coil, characterized by its quality factor (Q). For the BAP, the coating will also need to be soft and flexible as it will surround the construct and will be directly in contact with body tissue when implanted *in vivo*.

A broad range of materials has been employed to coat inductively-coupled coils. Polyethylene tubing was used to coat the wires that connected the first implanted coil to its tuning and matching network outside the animal body (9,10), as well as subsequent studies done by Schmidt *et al.* (122,123). However, Plastidip, a solvated polymer resin, was likely the most extensively used material (11,124-127) because of its flexible coating and sealing properties. Other materials that have been used include polyurethane (12), silicone rubber (21,128), epoxy (polyepoxide) and fiberglass (129), PARAFilm (13,130), Gortex (122,131), and Parylene C (132). Most of these polymers are commercially available for non-medical applications. They were employed based on their flexible properties and ease of manipulation and handling rather than on their biocompatibility. Unfortunately, the methods utilized to coat coils have never been fully described nor have biocompatibility studies been reported, although some coils were tested after retrieval for fibrosis growth. No intense immune response of the animals has ever been reported, even for coils implanted for extended periods of time (133). More recently, Silver *et al.* used polymethylmethacrylate as a biocompatible polymer (Figure 2-5) to coat implantable coils for spinal cord injury studies (14).

**Polymethylmethacrylate:** Polymethylmethacrylate (PMMA) has been used extensively in intraocular lenses and orthopedic devices over 40 years for its ease of handling, biocompatibility, and stability over 10 years *in vivo* (134). It has favorable dielectric properties for the purpose of implantation, a low dielectric constant of 2.6 and a low conductivity of  $10^{-16}$ S. The preparation of the coating material and the coating itself were described as rather simple by the user (14). PMMA (Figure 2-10) forms from the mixing of a powder base and a solution of curing agent. It is easy to pour in any mold since the base-curing agent mixture stays fluid for several minutes

before drying at room temperature in a couple of hours. The use of this coating material will be explored in the presented work as well.

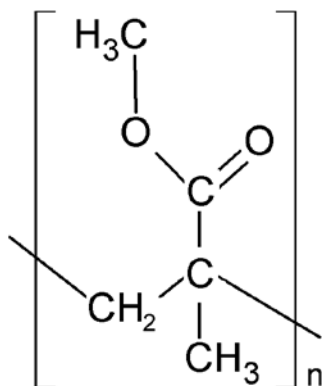


Figure 2-10. Molecular structure of PMMA.

**Polystyrene:** Polystyrene (PS, Figure 2-11) was found to have slightly better dielectric properties than PMMA: a dielectric constant of 2.6 and a conductivity of  $10^{-20}$  S. These properties have encouraged its testing as a coating material for implantable coils.

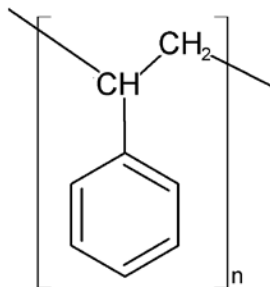


Figure 2-11. Molecular structure of PS.

It is widely used for electronic applications, such as capacitor dielectric and high-frequency circuit insulation (135). PS Petri dishes and multiwell plates are also widely used for cell culture. A dip coating procedure seems an appropriate method to use with this material for coating implantable coils (136) and will also be considered in the presented work.

**Polydimethylsiloxane:** Polydimethylsiloxane (PDMS) is a biocompatible polymer also noted for its easy handling (137). This silicon-based organic polymer has been widely used in

biomedical applications for over 50 years due to its biocompatibility and chemical stability (Figure 2-12).

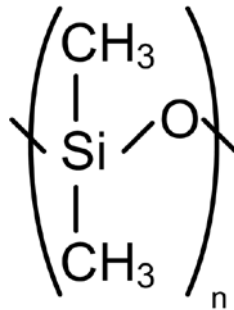


Figure 2-12. Molecular structure of PDMS.

PDMS elastomer can be found in catheters, drainage tubing, and insulation for pacemakers and membrane oxygenators, as well as ear and nose implants (137). The biomedical grade PDMS has a dielectric constant of 3 and a conductivity of  $5 \times 10^{-16}$  S. Its preparation is similar to PMMA except that both the base and curing agent are viscous solutions. Some research groups (15,17-19) have already used this material to coat their implantable coils with multiple layers and so it will be considered here.

**Polytetrafluoroethylene:** The material with the best dielectric properties possible to be used as a coating material is polytetrafluoroethylene (PTFE, Figure 2-13). It is chemically inert and has low permeability to liquids, gases, moisture, and organic vapors.



Figure 2-13. Molecular structure of PTFE.

This material has been used in vascular graft and tendon replacement for many years due to its biocompatibility, stability, and non-biodegradation (138). Its dielectric constant as low as

1.94 and its conductivity is as low as  $10^{-19}$  S and. Nonetheless, Teflon has a low bonding affinity that may complicate the coating procedure; hence a surface treatment to the coil is required before coating. Moreover, Teflon's glass transition temperature of 160°C necessitates adaptation of the materials used for coil construction since heating above this temperature is necessary to generate the coating. However, the outstanding dielectric properties of PTFE made its use as a coating material worthwhile investigating in the presented work.

## 2.4 Summary

In order to better accomplish the non-invasive *in vitro* and *in vivo* monitoring of bioartificial pancreas using NMR imaging and spectroscopy techniques, this dissertation describes the work to develop inductively-coupled implantable coil systems. Different designs of these implantable coil systems are considered (loop-gap resonator and solenoid), and their sensitivities when used with NMR are characterized. Initially, the inductively-coupled systems were single-frequency to assess their feasibility (Chapter 3). More complex systems, such as receive-only (Chapter 4) and multiple frequency systems (Chapter 5), were developed later to further improve the NMR method sensitivity and allow the acquisition of metabolic activity information from MRS data. Passive decoupling was explored to render the coupled-coil systems receive-only (Chapter 4), whereas tank circuit and capacitively overcoupling was used to render the coupled-coil systems multiple-frequency (Chapter 5). Coating materials are also an important component of the system, and the studies to determine the best material (PS, PTFE, PMMA, and PDMS<sub>e</sub>) with which to coat the implantable coil (in terms of biocompatibility and dielectric properties) and entrap the insulin-secreting cells are considered in Chapter 3. The final construct must also be able to house and maintain insulin-secreting cells. Different constructs were generated via micro- or/and macroencapsulation using agarose gel and alginate foam and

gel (Chapter 3). Their insertion in the middle of the implantable coil was tested along with their ability to hold cells and allow them to grow in Chapter 6.  $\beta$ -TC-tet cells were selected as the insulin-producing cell model as they are easily available, easy to culture, and their growth could be regulated if needed. These studies outline the many aspects required for the development of the highest sensitive NMR imaging and spectroscopy method to monitor a bioartificial pancreas and lead toward the development of a functional implantable bioartificial pancreatic construct, which can be non-invasively monitored.

CHAPTER 3  
DEVELOPMENT OF AN INDUCTIVELY-COUPLED RF COIL SYSTEM FOR IMAGING  
AND SPECTROSCOPIC ANALYSIS OF AN IMPLANTABLE BIOARTIFICIAL  
CONSTRUCT AT 11.1T<sup>1</sup>

**3.1 Introduction**

Developing a method to monitor tissue-engineered constructs non-invasively is critical for the optimization of construct design and for assessing therapeutic efficacy. NMR is a powerful technique for this purpose, as it can be used to obtain both images and spectroscopic data. But the inherent sensitivity of NMR methods limits the observation of a bioartificial construct with current RF coil technology (surface coil). In this study, this limitation was addressed through the development of an inductively-coupled, implanted coil system, demonstrate its use at high field (11.1 T), and investigate the use and requirement of this coil system for monitoring a bioartificial construct *in vitro* and *in vivo*. The results establish that large gains in signal-to-noise can be obtained with this inductively-coupled, implanted coil system over that which can be obtained with a surface coil. This coil system provides a means to analyze the structure and function of implanted bioartificial organs quantitatively.

**3.2 Background**

One approach being explored to cure diabetes is to implant insulin-secreting cells within a tissue-engineered (bioartificial) pancreatic construct (1,29,33,35). Using NMR to non-invasively monitor an implanted pancreatic construct can provide correlations between construct function and physiologic effects post-implantation (2-4). NMR also offers the possibility of assessing changes in construct function towards developing early markers of construct failure in advance of end-point diabetic effects, e.g., hyperglycemia.

---

<sup>1</sup> Modification of paper submitted for peer review, 2009.

Stabler *et al.* developed an NMR-based method to non-invasively assess the viability of a bioartificial pancreatic construct (5,6). Their method, correlating the  $^1\text{H}$  choline signal with cellular viability, was accomplished both *in vitro* and *in vivo* on macroconstructs using a 4.7 T NMR instrument and a surface coil (SC) as the RF coil for  $^1\text{H}$  NMR excitation and detection. However, a shortcoming of this measurement design is the threshold sensitivity, which at best is limited to a cellular density of seven million viable cells/ml of construct under ideal *in vitro* conditions. Because of the desire to study implanted constructs *in vivo*, and also to study lower cellular densities, improving the sensitivity of the NMR measurement is critical.

Two changes can improve the sensitivity of the NMR measurements and decrease the lower limit of detectable cells: (i) acquire the NMR data at a higher field; and (ii) improve the sensitivity of the RF coil used to measure NMR. Increasing the static magnetic field strength from 4.7T to 11.1T would improve the sensitivity of the measurements by a factor of 2.4, since the sensitivity, characterized by the signal-to-noise ratio (SNR), increases linearly with magnetic field strength in lossy samples, such as tissue (7). Furthermore, the development of an implantable coil (IC) that not only matches the size and shape of the construct, but is also inductively-coupled to an SC would also increase the sensitivity of measuring specific internal structures, yet leave the subject relatively undisturbed (11-13,100,101). Additionally, these inductively-coupled, implantable coil systems have an advantage over implanted coils since no cable passes through the skin to connect the implanted coil to the power source and amplifiers (12,14,19-21). Therefore, risk of infection is decreased, increasing the period over which an animal may be safely monitored.

This report investigates the use of inductively-coupled implantable coil systems to monitor an implanted pancreatic construct. The NMR sensitivity of these systems was then compared to

the sensitivity of an SC at a high field (11.1 T). To assess NMR sensitivity improvement of the inductively-coupled system under development compared to the SC used at 4.7T in the previous studies (5,6), an SC was also tested at two magnetic field strengths (4.7 and 11.1 T). Lastly, this report discusses important technical aspects toward generating inductively-coupled implantable coil systems, and issues to consider when applying these RF coils in conjunction with implanted tissue-engineered constructs.

### 3.3 Materials and Methods

#### 3.3.1 RF Coil System Development

Four different inductively-coupled implantable coil systems using two different implantable coils and two different configurations were constructed, optimized, and tested for NMR imaging and spectroscopy at 11.1 T, to study the NMR sensitivity dependence of RF coil design. These systems consisted of an IC inductively-coupled to an SC, functioning both transmitter and receiver for  $^1\text{H}$  NMR (470 MHz at 11.1 T). The IC surrounds a bioartificial construct, adapted from Stabler *et al.* (5,6), allowing the coil to be near the monitored cells (Figure 3-1).

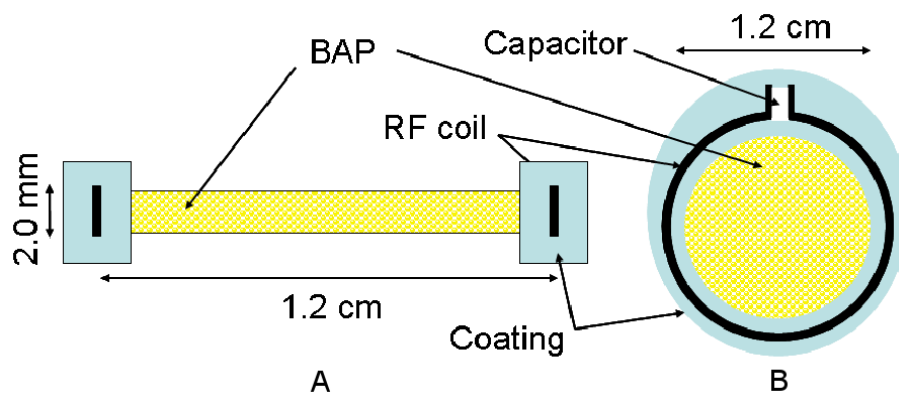


Figure 3-1. Implantable coil - bioartificial pancreas macroconstruct assembly diagram. A) Transverse view and B) coronal view.

Two types of implantable coil, a loop-gap resonator and a solenoid, with identical inductor cross-section (1.2 cm) and thickness (2 mm) were built and tested to determine the design with the highest sensitivity. These designs were considered because: (1) the solenoid design may provide a higher quality factor (139); (2) the loop-gap resonator is perhaps easier to manufacture and may perform better at higher frequency (102). A rod was used to build these implantable coils and keep their cross-section constant. A spacer was used afterwards to check their flatness and thickness.

The inductive part of the IC ( $L_i$  on Figure 3-2A) was constructed with 20-AWG heavy-armored poly-thermaleze magnet copper wire (Belden, St. Louis, MO) for the solenoid and with a 2 mm-wide 202- $\mu\text{m}$ -thick copper foil (McMaster Carr, Atlanta, GA) for the loop-gap resonator. A single fixed tuning capacitor (American Technical Ceramics, Hartford, CT,  $C_{Ti}$  on Figure 3-2A) was used to provide the desired resonance for both coil types. This capacitor was soldered between the wire ends after these ends were twisted one half-turn (approximately 2 mm total length). This construction makes the coil more stable and displaces the tuning capacitor away from the inductor. The loop-gap resonator capacitor was soldered directly between the copper foil ends.

The SC were constructed with a single 2 cm diameter circular loop of 2 mm wide, 35- $\mu\text{m}$ -thick copper tape (3M, Saint Paul, MN;  $L_s$  on Figure 3-2B) placed on a piece of 5 mm thick Plexiglas. The capacitive portion of the SC includes two variable matching capacitors (Voltronics Corporation, Denville, NJ, 1-15 pf;  $C_{Ms1V}$  and  $C_{Ms2V}$  on Figure 3-2B), one fixed tuning capacitor (American Technical Ceramics, Hartford, CT;  $C_{Ts}$  on Figure 3-2B), and one variable tuning capacitor ( $C_{TsV}$  on Figure 3-2B, 1-15 pf). The fixed capacitor was placed on the inductive loop, and three variable capacitors were soldered onto a circuit board to provide

variable tuning and matching of the system. A coaxial cable connected the coil to the source and preamplifier. A cable trap was added to the shield of the coaxial cable to block shield currents that contribute to parasitic coupling when working at high frequency (140). This SC of the inductively-coupled coil system was also used as an isolated SC since it could be tuned and matched optimally at 470.75 MHz. Furthermore, to compare these results with previous measurements performed at 4.7 T with an SC (5,6), a separate SC was built with the same geometry as the SC of the implantable system presented above, then optimized to resonate at 200 MHz ( $^1\text{H}$  frequency at 4.7 T).

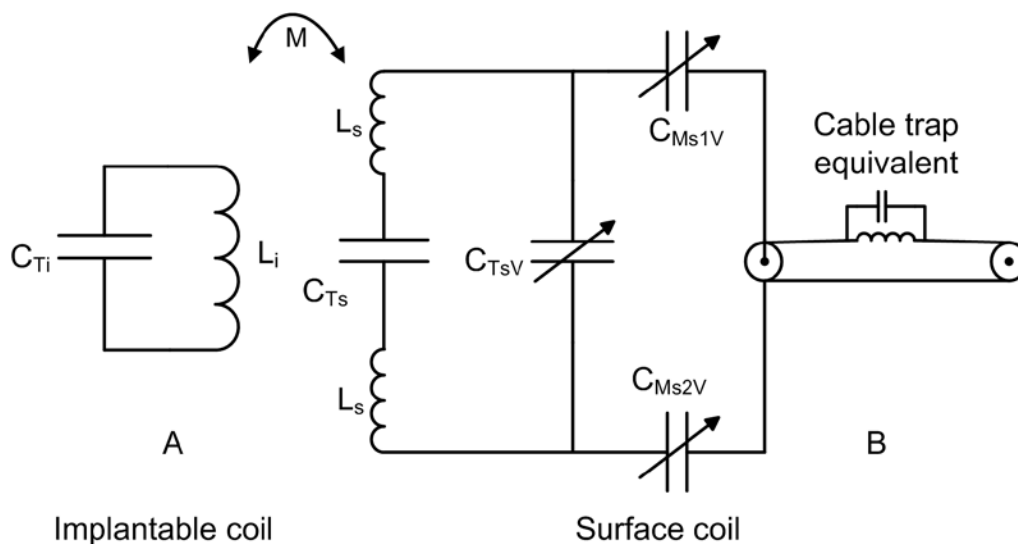


Figure 3-2. Circuit diagram for an inductively-coupled implantable coil system for  $^1\text{H}$  detection. A) Implantable coil; and B) surface coil. Inductors ( $L$ ) and capacitors ( $C$ ) are shown with subscripts denoting implantable (i) or surface (s) coil. Capacitors are also designated as tuning ( $C_T$ ) or matching ( $C_M$ ).  $M$  indicates the mutual inductance or inductive coupling between the two coils of the system and  $V$  variable. A cable trap equivalent, including an inductor and a capacitor, is also shown in the diagram.

### 3.3.2 Coating Techniques

The implantable coil required isolation from the host to allow it to function when testing the inductively-coupled coil system *in vitro* and *in vivo*. Four different materials were chosen and tested to coat the implantable coil: 1) polystyrene (PS); 2) polytetrafluoroethylene (PTFE);

3) polymethylmethacrylate (PMMA), and 4) polydimethylsiloxane elastomer (PDMSe). These materials were chosen for their biocompatibility and low dielectric properties (see Section 2.3.2.5). The coating uniformity, seal and reproducibility were the first parameters checked. The effects of the coatings and their thickness on the coils were tested afterwards by determining changes in the coil resonant frequency and quality factor (Q) both in air and in a gel phantom (139). The material having the easiest handling and the least influence on the coil performances was selected for the *in vitro* and *in vivo* studies.

### **3.3.2.1 Polystyrene**

Polystyrene (PS, Resirene, Mexico) was formed by first heating pellets at 105°C ( $T_g$  for PS) for 20 minutes in a dry oven to evaporate any water and avoid bubbles during the coil coating. PS pellets (1.56 g) were then placed in a closed container of chloroform (20 mL) and stirred at room temperature until completely dissolved. This solution was a 5% (w/v) PS solution (136). The implantable coil was dipped into the solution and hung for 30 minutes at room temperature to allow the coating to dry. The operation was repeated up to 7 times. Each time, the coil was hung at a different location around the main coil inductor to even the overall coating.

### **3.3.2.2 Polytetrafluoroethylene**

A solution of polytetrafluoroethylene (PTFE) polymer in solvent fluorinert FC-75 (Teflon AF 1600, DuPont Fluoroproducts, Wilmington, DE), 6% by weight, was used to coat the implantable coil. To increase the bonding properties of PTFE, the coil was first sanded to increase surface roughness; then wetted with an acid (solder flux in this case) and flamed to oxidize the coil surface. Traces of the wetting agent were removed by cleaning, rinsing, and blow drying the coil. The coil was then dipped in the PTFE solution for about 1 minute, as described by Regan *et al.* (141), and withdrawn from the solution very slowly to avoid bubble

formation. The coil was hung and allowed to dry in the oven at room temperature for 5 to 10 mins. The temperature was then slowly increased up to 165°C over a one-hour interval, which made the polymer chains more mobile and enhanced solvent evaporation leading to fewer defects in the dip coating. An additional 15 minutes at 165°C was attempted to improve the quality of the coating and reduce the presence of air bubbles. This process was repeated up to 3 times with the coil hung from different locations around its main inductor to produce an even coating.

Another alternative was to heat up to 20 mL of PTFE solution to 115°C (solvent evaporation temperature + 5°C) in a small beaker. With a 6% PTFE solution, a 1.5 cm height solution left a 2-3 mm film at the bottom of the beaker. The process was repeated after a coil was placed on the first film. To make sure that the temperature would not affect the coil performances, the capacitors were upgraded to high temperature capacitors able to withstand temperatures up to 310 °C instead of the regular 125°C. The solder used to connect the capacitor to the inductive loop was also upgraded from a 60%Sn / 40%Pb with a melting point of 183-190 °C to a 5%Sn / 93.5%Pb / 1.5%Ag, whose melting temperature is 296-302 °C.

### **3.3.2.3 Polymethylmethacrylate**

Polymethylmethacrylate (Cranioplastic, Plastics one, Inc., Roanoke, VA) was formed by mixing a powder base and a solution of curing agent. The powder of PMMA particles includes diethyl phthalate, a plasticizer to render the PMMA less brittle and softer. The curing agent is a thin solution of methylmethacrylate monomer which also contains an initiator (N,N-dimethyl-p-toluidine) that promoted PMMA chain formation at room temperature. The ratio by weight of base to curing agent was set at 1:10. This allowed the polymer to acquire the desired consistency to hold its shape, yet maintain its flexibility. The mixture was then poured in a mold to create a

1mm thick layer which was let to dry at room temperature overnight. The implantable coil was then added on top of the layer and another PMMA mixture was poured to cover the coil and add another 1 mm on top of the coil. The coated coil was easily removed from the mold 24 hours after the second casting.

#### **3.3.2.4 Polydimethylsiloxane**

Polydimethylsiloxane (Medical Grade Silicone Elastomer, Factor II, Lakeside, AZ) preparation was similar to the PMMA one except that both the base and curing agent were viscous solutions and the mixing proportions were a 10:1 base to curing agent ratio. Dimethylvinyl terminated dimethyl siloxane made the base solution including reinforcing filler particles of trimethylated silica, to fill the PDMS matrix, increase its tensile strength and make it mechanically more stable. A platinum catalyst was also present in the base solution to make the crosslinking possible. Dimethylvinyl terminated dimethyl siloxane and dimethyl,methylhydrogen siloxane (crosslinker) composed the curing agent. The mixing of these solutions required the degassing of the mixture for at least 20 minutes under vacuum (95-102 kPa) since both solutions were very viscous and many bubbles get trapped in during the mixing. The coils were either dip coated repeatedly up to 3 times such as done with PTFE or they were casted.

The casting was done in two steps to insure a uniform and sealed coating with the coils centered in the middle of the coat. A first PDMS elastomer layer was generated by curing a PDMS base for 24 hours at room temperature between glass plates carefully spaced to give the desired coating thickness. Once the PDMS was cured, the top glass plate was removed and several implantable coils were placed on top of this first PDMS layer carefully spaced from one another. A second PDMS layer was then poured on top of the coils. In order to obtain a uniform coating thickness around the coils, a glass plate was placed above the curing second PDMS layer

carefully spaced from the bottom glass plate. As PDMS is a crosslinked polymer, the two layers bond to each other when curing, therefore embedding the coils in a sealed coating. The curing process could be accelerated by heating the layers for about 1 hour at 50°C. The coated coils were then punched out of the PDMS slab using hollow punches. A smaller punch removed the extra PDMS in the center of the coil to allow the insertion of the bioartificial construct.

### 3.3.3 RF Coil Testing

When surface and implantable coils are in proper orientation and relative proximity, they inductively couple. When the two coils are far apart, their mutual inductance is low, they are loosely coupled. Their coupling or mutual inductance increases as the coils become closer to each other. For surface and implantable coils tuned to the same resonant frequency, critical coupling occurs when the IC resistance coupled into the SC is equal to the surface coil resistance (142). If the coupling strengthens, the coils overcouple and the resonant frequency of the coupled system splits as two current modes appear: a co-rotating (+) and a counter-rotating (-) mode (Figure 3-3; (143)). Three different configurations of the inductively-coupled coil system were then tested: 1) a loosely-coupled system where the SC was not resonant and the IC resonates at 470.75 MHz; 2) an overcoupled system where both surface and implantable coils resonate at the same frequency in the (+) mode; and 3) an overcoupled system where both surface and implantable coils resonate at the same frequency in the (-) mode. In the (+) mode, each coil was tuned and matched individually to a higher frequency (490.1 MHz), so that the lower resonant frequency of the overcoupled system occurred at the desired  $^1\text{H}$  NMR resonance of 470.75 MHz. In the (-) mode, each coil was individually tuned and matched to a lower frequency (450.75 MHz), so that the higher resonant frequency of the overcoupled system occurred at 470.75 MHz (Figure 3-3). The capacitors  $C_{M1V}$ ,  $C_{M2V}$ , and  $C_{TSV}$  (Figure 3-2) of the

surface coil were adjusted to achieve the match of the whole system to  $50 \Omega$  at 470.75 MHz.

The systems and configurations were simulated first with antenna analysis software (Graphical Numerical Electromagnetics Code, Nittany, Inc. Riverton, UT), then constructed and optimized on the bench before being tested in the magnet.

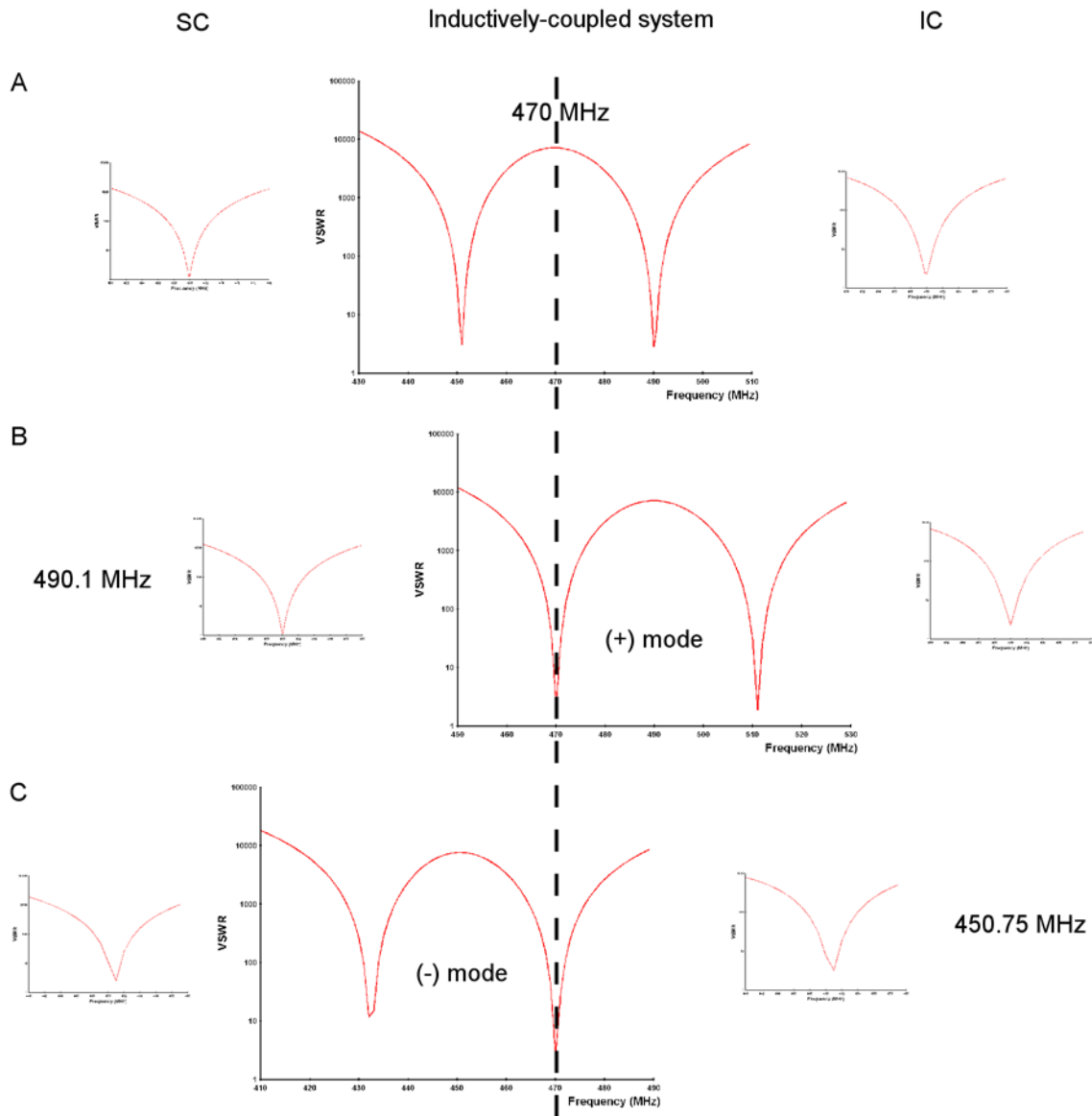


Figure 3-3. Voltage standing wave ratio (VSWR) of a surface coil (SC), an implantable coil (IC), and an inductively- overcoupled system in its different modes. A) Both the SC and IC resonate at 470 MHz initially creating two off-resonance modes; B) both the SC and IC resonate at 490.1 MHz initially allowing the (+) mode to be at 470.75 MHz; and C) both the SC and IC resonate at 450.75 MHz initially allowing the (-) mode to be at 470.75 MHz.

The characteristics of each coil taken individually and of the whole system (resonant frequency and Q) were determined after construction with a vector network analyzer (VNA Hewlett Packard 8752C, Santa Rosa, CA) with and without load and every time the system was tested in the magnet(144). The Q was measured by finding the -3 dB points (or bandwidth) from the VNA return loss plot for the SC and for the inductively-coupled coil system hooked directly to the network analyzer via its coaxial cable (Figure 3-4A), and from the VNA transmission plot for the IC (Figure 3-4B). The implantable coil, which has no direct coaxial connection, was loosely coupled with two probes connected to the reflection and transmission ports of the network analyzer. As the implantable coil placed in between the two probes absorbed energy, the absorption response was viewed on the transmission plot of the network analyzer allowing Q determination. The VNA calibration was saved for a specific center frequency and bandwidth and checked periodically using a 50 Ω load, a short, and an open for the reflection line, and a through cable for the transmission line.

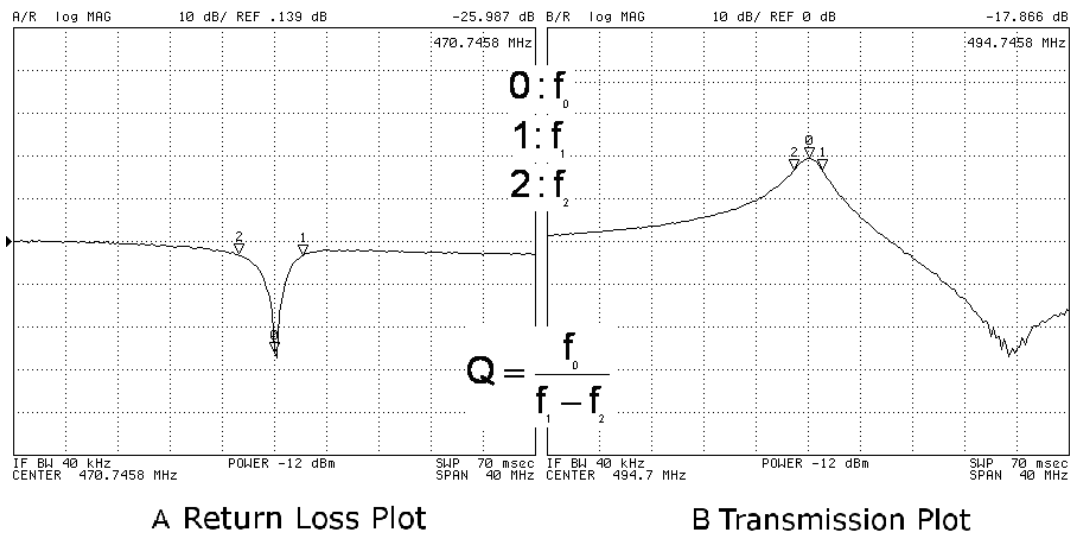


Figure 3-4. Vector network analyzer outputs used for RF coils Q measurements. A) Return loss plot; and B) transmission plot. Marker 0 was placed at the resonant frequency of the coil or system being tested and Marker 1 and 2 at the -3 dB points around the resonant frequency.

Additionally, the voltage across the implantable coil was also determined when the coil was coupled with the surface coil to insure the power deposited within the construct was appropriate and would not deteriorate the construct viability and functionality (145). This voltage was measured directly across the capacitor of implantable coil via a half wave coaxial cable connected to a high impedance port of a digital oscilloscope Tektronix DPO 4104. The surface coil was powered by the RF pulses from the spin echo (SE) sequence used to image the construct and described in Section 3.3.7. The implantable coil was placed around a water sample as described in Section 3.3.4.

### **3.3.4 Samples**

A sample of distilled water placed in a 10 mm-diameter thin-wall glass tube (Wilmad Labglass, Buena, NJ) was used to test the coupled-coil systems (with coated and uncoated IC) on the bench and in the magnet. This water phantom was considered to represent the unloaded condition because of its small size compared to the SC and the nature of the sample. To test performances under loaded conditions (similar to *in vivo* conditions), the implantable coated coil was placed in a mouse abdomen-like gel phantom (146-148) comprised of a viscous 6.7% (w/w) polysaccharide gel (TX-151; Oil Center Research, International LLC, Lafayette, LA). The permittivity of this gel phantom was determined to be at  $64.2 \pm 1.13$  ( $\pm 1.77\%$ ) and its conductivity at  $1.13 \pm 0.01$  ( $\pm 1.29\%$ ) S/m. Inductive coupling was accomplished by placing the water sample or phantom (with IC) on top of the SC. The IC were tested when placed around the water sample no more than a 1 cm away from the SC, and when placed in the gel phantom 0.5 cm and 1 cm away from the SC.

### **3.3.5 Construct Development**

Three different constructs were also developed in this study to select the most appropriate one to function as a BAP when surrounded by an implantable coil. The constructs tested were: 1) agarose gel disks (5,6); 2) alginate sponge or foam disks (149,150); and 3) alginate beads (33,37,55). The diameter of the construct could not exceed 1 cm in order to fit within the middle of the coated implantable coil (Figure 3-1) and its thickness did not exceed 500  $\mu\text{m}$  to minimize the diffusion limitations.

#### **3.3.5.1 Agarose**

A 2% agarose gel solution was prepared by suspending dry agarose powder (SeaPlaque Low Melting Agarose, Cambrex Bioproducts, East Rutherford, NJ) in Phosphate Buffer Saline (PBS, Invitrogen, Carlsbad, CA) without Calcium and Magnesium and boiling the covered mixture until a clear solution forms (about 10 minutes). Drops of this solution were then poured in the middle of the coated coil and allowed to cool down to room temperature to form a rigid agarose gel slab. The coil served as the mold.

#### **3.3.5.2 Alginate foam**

Alginate foam was purchased (Novomatrix, Trondheim, Norway). Circular, 1-cm diameter pieces were punched out from this foam and placed in the middle of the coated coil. Non-absorbable surgical sutures were used to hold the alginate foam construct in place in the middle of the coil.

#### **3.3.5.3 Alginate beads**

A 2% (w/v) sodium alginate solution was prepared by dissolving an alginate powder with 62% / 38% mannuronic/guluronic content (Novomatrix, Trondheim, Norway) into a saline solution (0.85% NaCl) overnight. Cell-free alginate beads were generated, as described by Simpson et al. (151), by running the alginate solution through a syringe at a constant flow rate

and dropping it in a cationic cross-linking solution with an electrostatic bead generator (Nisco, Zurich, Switzerland) to set the bead diameter between 400 and 600  $\mu\text{m}$ . To keep these beads together in the middle of the implantable coil, a biocompatible polyetheretherketone (PEEK) 300- $\mu\text{m}$  mesh (Small Parts, Inc., Miami Lakes, FL) was added on the top and bottom of the ring formed by the coated coil to create the construct cavity. Aliquots of freshly made beads (~0.3 ml each) were transferred into the implantable coil-construct assembly using a syringe and 16 G needle.

The three implantable coil-construct assemblies were initially placed into Hank's Buffered Saline Solution (HBSS) for up to 2 weeks to determine the most appropriate construct to be used for *in vitro* and *in vivo* studies. However, prior to the BAP insertion in the middle of the implantable coil for *in vitro* and *in vivo* studies, the coated coil had to be prepared in a two-step process. It was first acid washed and rinsed to remove proteins left on the coil during manufacturing and reduce the immune response to the chosen device when placed in a mouse abdomen. It was afterwards autoclaved to become sterile and able to receive the pancreatic construct piece (agarose slab, alginate foam, or alginate beads). For *in vivo* studies, the selected coil-construct assembly was placed into sterile HBSS until implantation. HBSS was chosen as a culture media substitute. It is the basis of complete culture media except it does not contain the amino acids and vitamins a complete media has, which would trigger an immune response *in vivo*. This solution also contained antibiotics (100 U/ml penicillin and 100 ng/ml streptomycin), anti-inflammatory and immunosuppressant (100 nM dexamethasone).

### **3.3.6 Animal Preparation and Handling**

Experiments with female C3H/HeN mice, weighing 20-30 g, were conducted according to a protocol approved by the University of Florida Institutional Animal Care and Use Committee. NMR measurements and surgeries were completed under general anesthesia. Anesthesia was

induced by inhalation of 2% isoflurane in oxygen and maintained for the duration of the surgery or NMR measurement by ventilating a mixture of 1% isoflurane in oxygen via a nose cone. Under deep anesthesia, the sterile construct was implanted into the peritoneal cavity via a small (2 cm) midline celiotomy. The animal was placed prone on the surface coil/cradle apparatus for NMR measurements afterwards. The construct was either surrounded by an IC, to create the inductively-coupled coil system when placed on the coil/cradle apparatus, or a coil-free construct studied with an SC to compare an inductively-coupled implantable coil system to an SC. The animal respiration and skin temperature was monitored using a monitoring and gating system (Small Animal Instruments, Inc., Stony Brook, NY). Its respiration was maintained between 20 and 30 breaths/min and its skin temperature between 24 and 26 °C. Upon completion of NMR measurements, animals were euthanized and the coil-construct assembly or coil-free construct were retrieved.

### **3.3.7 NMR Measurements**

NMR measurements were performed on an 11.1 T 40 cm clear horizontal bore Magnex magnet equipped with a Bruker Avance console and on a 4.7 T 33 cm horizontal bore Oxford Magnet equipped with a Bruker Biospin console (Bruker Instruments, Billerica, MA). Data acquisition and processing were done using Bruker Paravision software. The SNR was determined for each coil system with custom image analysis software written in IDL (ITT Visual Information Solutions, Boulder, CO). For coil system comparisons with phantoms,  $^1\text{H}$  images were acquired using a spin-echo (SE) pulse sequence with a repetition time (TR) of 1000 ms, an echo time (TE) of 10 ms, 1-mm slice thickness, 1 average,  $4 \times 4 \text{ cm}^2$  field-of-view (FOV) and a  $256 \times 256$  matrix. Coating signal was suppressed when required using a spectrally selective saturation pulse centered on the coating signal. For *in vivo* coil system comparisons,  $^1\text{H}$  images

were acquired using a SE pulse sequence with the parameters given above, except that the TR was lengthened to account for the animal breathing and reducing its artifacts. To reduce breathing artifact for the *in vivo* studies, other parameters were varied as well, such as number of averages and number of averaged experiments. Conventional respiratory gating was also tested.

To compare results obtained at 11.1 T and 4.7 T, differences in relaxation times of the phantom water were taken into account. De Graaf et al. have shown that the longitudinal relaxation time ( $T_1$ ) of water and metabolites increases whereas their transverse relaxation time ( $T_2$ ) decreases with magnetic field strength (152). Therefore, a long TR and short TE were used at both magnetic fields to minimize the signal dependence of these parameters. NMR images were acquired using an SE pulse sequence with the following parameters: TR of 15,000 ms, TE of 10 ms, 1-mm slice, 2 averages, 4x4 cm<sup>2</sup> FOV and a 64x64 matrix on both systems.

### **3.3.8 SNR Measurement and Statistical Analysis**

Five different coil-systems/configurations were tested in the magnet: 1) SC; 2) coupled-coil system with an implantable solenoid in the co-rotating (+) mode; 3) coupled-coil system with an implantable solenoid in the counter-rotating (-) mode; 4) coupled-coil system with an implantable loop-gap resonator in the co-rotating (+) mode; and 5) coupled-coil system with an implantable loop-gap resonator in the counter-rotating (-) mode. The SNR of these different coil-systems/configurations was evaluated from the NMR images by choosing a signal region-of-interest (ROI) at the IC position and a noise ROI outside of the sample. Saved signal and noise 770-pixel ROIs were used for each SNR determination. The Henkelman method (153) was utilized to calculate the SNR. Images in three orthogonal directions (transversal, sagittal, coronal) were acquired for each system/configuration. The number, n, of independently-made coil systems tested to assess the reproducibility of the system construction is indicated for every experiment by (n). At least two set of images were acquired for each coil system to assess the

reproducibility of signal detection and the sensitivity of the systems. The SNR determined for each similar system/configuration in the three orthogonal direction was then averaged and normalized to the SNR of SC at 4.7 T (normalized to 1). This normalization was appropriate because the SC at 4.7 T had the same size and shape as the SC at 11.1 T. All the results are indicated as a mean  $\pm$  standard deviation (relative standard deviations are indicated in parentheses in percentage). The propagation of error was included in the normalization statistics. A statistical analysis was performed using a two-sample unequal-variance t-test. The results of this analysis were considered statistically significant when p-values were less than 0.05.

### 3.4 Results

#### 3.4.1 RF Coil System

The loop-gap resonator and solenoid IC (Figure 3-5) as well as the SC (Figure 3-6) were successfully built and tested on the bench and in the magnet. However, the loosely-coupled coil system performed poorly on the bench because the coupled-coil system could not be tuned or matched to  $50 \Omega$  once the IC was coupled to the SC under variable conditions of coil loading (16). Furthermore, the establishment of critical coupling was never achieved in this case since the size and position of the two system coils are fixed by the experiment settings. Due to those limitations, this configuration was not included in this study.



Figure 3-5. Photographs of implantable coils developed as part of an inductively-coupled implantable coil system. A) Loop-gap resonator and B) Two-turn solenoid. (Photo by N.A. Volland).



Figure 3-6. Photograph of the surface coil developed as part of an inductively-coupled implantable coil system. This surface coil design was also used as a single surface coil at both 470 and 200 MHz. (Photo by N.A. Volland).

The characteristics of the different coils and overcoupled systems tested are summarized in Table 3-1. The implantable loop-gap resonator has an average Q of  $203.90 \pm 6.20$  ( $\pm 3.04\%$ ) when resonating at  $491.81 \pm 3.38$  ( $\pm 0.69\%$ ) MHz, an average Q of  $151.8 \pm 11.6$  ( $\pm 7.64\%$ ) when resonating at  $451.4 \pm 2.4$  ( $\pm 0.53\%$ ) MHz, the implantable solenoid an average Q of  $180.0 \pm 19.0$  ( $\pm 10.6\%$ ) when resonating at  $497.2 \pm 5.21$  ( $\pm 1.05\%$ ) MHz, and the implantable solenoid an average Q of  $158.5 \pm 20.3$  ( $\pm 12.81\%$ ) when resonating at  $450.2 \pm 1.62$  ( $\pm 0.36\%$ ) MHz. The surface coil has a Q of  $72.2 \pm 4.95$  ( $\pm 6.86\%$ ) when resonating at 493.2 MHz, a Q of 87.4 when resonating at 450.8 MHz, an average Q of  $87.0 \pm 5.67$  ( $\pm 6.52\%$ ) when resonating at 470 MHz, and an average Q of  $69.7 \pm 1.98$  ( $\pm 2.84\%$ ) when resonating at 200 MHz. When resonating at 470.75 MHz, the inductively-coupled implantable coil system including the LG implantable coil has a Q of  $96.21 \pm 3.70$  ( $\pm 3.85\%$ ) in the (+) mode, a Q of  $89.35 \pm 4.17$  ( $\pm 4.66\%$ ) in the (-) mode, whereas the inductively-coupled implantable coil system including the solenoid implantable coil has an average Q of  $92.80 \pm 2.65$  ( $\pm 2.85\%$ ) in the (+) mode and an average Q of  $71.18 \pm 6.65$  ( $\pm 9.35\%$ ) in the (-) mode.

Table 3-1. Implantable coil (IC), surface coil (SC), and inductively-coupled implantable coil system characteristics. Resonant frequency (f) and quality factor (Q) for: SC at 4.7 T (SC 4.7T) and at 11.1 T (SC), IC solenoid (IC\_Sol-) and loop-gap (IC\_LG-), SC (SC-), and coupled-coil systems (Sol- and LG-) in the (-) mode, and IC solenoid (IC\_Sol+) and loop-gap (IC\_LG+), SC (SC+), and coupled-coil systems (Sol+ and LG+) in the (+) mode.

Coil #	# of coils tested*	f (MHz)	Q
IC_LG+	7	491.81 ± 3.38 (± 0.69%)	203.90 ± 6.20 (± 3.04%)
IC_LG-	4	451.4 ± 2.4 (± 0.53%)	151.8 ± 11.6 (± 7.64%)
IC_Sol+	5	497.2 ± 5.21 (± 1.05%)	180.0 ± 19.0 (± 10.6%)
IC_Sol-	4	450.2 ± 1.62 (± 0.36%)	158.5 ± 20.3 (± 12.81%)
SC+	2	493.2	72.2 ± 4.95 (± 6.86%)
SC-	1	450.8	89.3 ± 2.69 (± 3.01%)
SC	4	470.75	87.0 ± 5.67 (± 6.52%)
SC 4.7T	1	200.0	69.7 ± 1.98 (± 2.84%)
LG+	5	470.75	96.21 ± 3.70 (± 3.85%)
LG-	4	470.75	92.80 ± 2.65 (± 2.85%)
Sol+	5	470.75	71.18 ± 6.65 (± 9.35%)
Sol-	4	470.75	89.35 ± 4.17 (± 4.66%)

\* All coils taken individually and all systems were tested under unloaded conditions. Even when there was only one coil built, it was tested more than once.

Figure 3-7 shows the resonant frequencies and the B<sub>1</sub> magnetic field produced by a SC alone, an overcoupled system in the (+) mode, and an overcoupled system in the (-) mode. All the RF coils were optimized to resonate at 470.75 MHz. The magnetic field was calculated along the axis of symmetry of the coils, with the SC position set at 0 and the IC centered at 1 cm (macroconstruct location). The position of the simulation and images are aligned in the horizontal direction for ease of comparison. The (+) mode (Figure 3-7I & 3-7J) corresponds to

the lower resonant frequency of the system (Figure 3-7C) where the currents in the two coils rotate in the same direction and their magnetic fields are additive. The (-) mode (Figure 3-7G & 3-7H) corresponds to the higher frequency of the system (Figure 3-7B) where the currents in the two coils rotate in opposite direction and their magnetic fields are subtractive resulting in a null between the two coils (14,143).

The peak voltage developed across the capacitor of the implantable coil varied from less than 2 V up to 24 V when the implantable coil was coupled with the surface coil and the RF pulse power was scaled within a large range of settings (over 20 dB) beyond the experimental range to obtain the proper excitation for a SE sequence. This voltage range is much lower than the one developed across the surface coil as the coupling factor between the two coils was estimated at 0.083 (142). Furthermore, knowing that the power requirement for an inductively-coupled coil system is much less than the power requirement for a single surface coil (10 dB on average), the power deposited in the mouse was revealed to be much lower than the power deposited by a surface coil used alone and no further power measurements were performed (154).

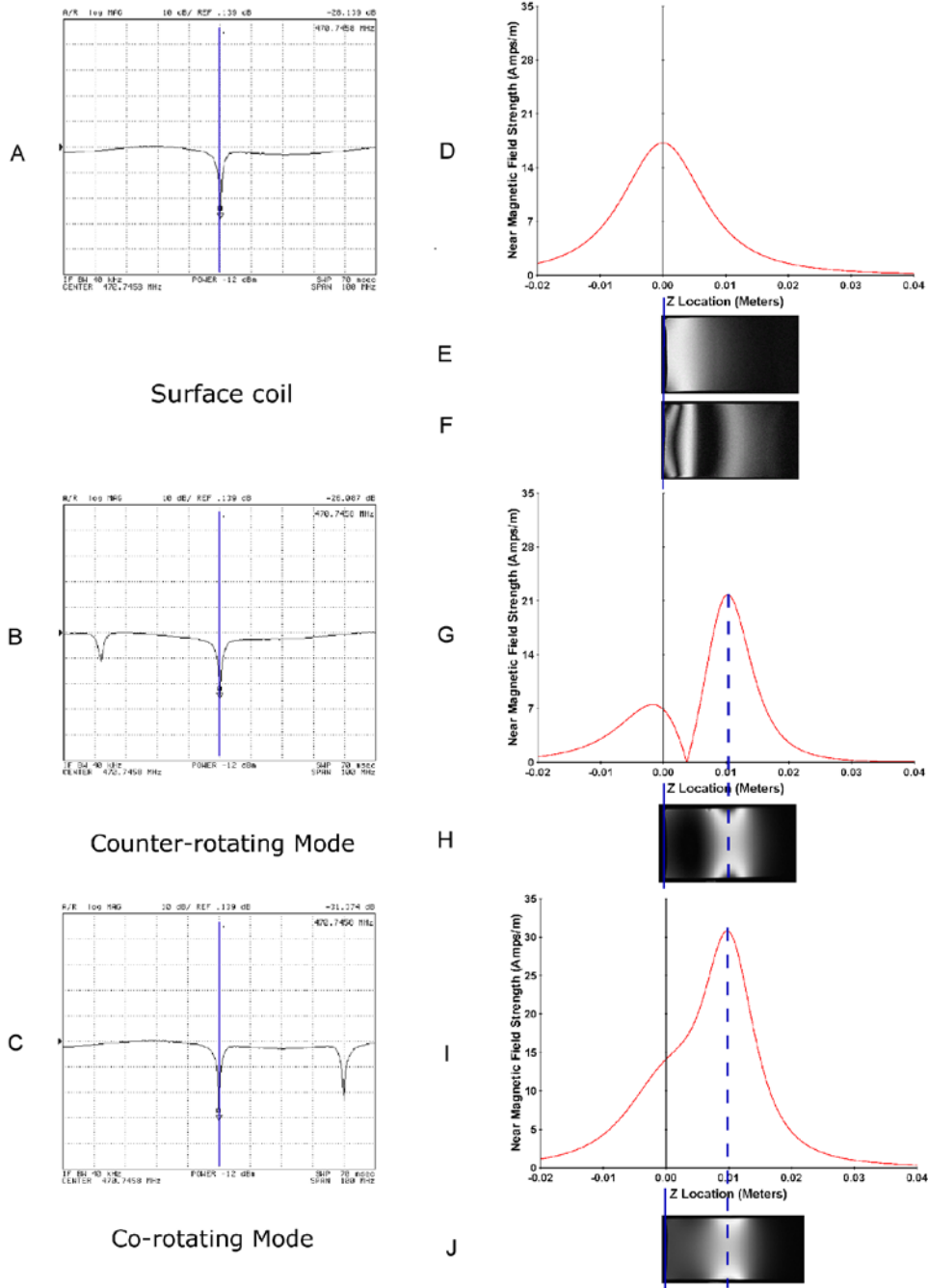


Figure 3-7. RF coil frequency traces, simulated  $B_1$  magnetic field magnitude, and their respective corresponding spin-echo images along the axis of symmetry of the coils. These graphs are for a surface coil (A, D, E, & F); an inductively-coupled coil system in the (-) mode (B, G, & H) and in the (+) mode (C, I, & J) at 11.1T. In D through I, the SC position was set at 0 and represented by a solid line, while the IC is located at 1 cm and represented by a dashed line. Water sample images shown when the NMR excitation is optimized for maximum signal near the SC in E and when the excitation is optimized for maximum signal at the location of the tissue construct (1 cm away from the SC) in F.

### 3.4.2 Implantable Coil Coating

#### 3.4.2.1 Polystyrene

Every PS layer added an average shift of the resonant frequency of the coil of -2.33 (0.48%) MHz (Table 3-2). The Q did not vary significantly when more layers were added. However, both the resonant frequency and the Q of the coil varied largely when the PS-coated coils were put in a phantom and left in there over time (up to 15 hours). The resonant frequency shifted on average by -150 MHz (or 32.4%) when embedded, and by another -100 MHz (22.1%) after 15 hours. The Q dropped 4-fold after the coil was embedded in the phantom, and could not be measured anymore after 15 hours.

Table 3-2. Implantable coil characteristics when coated with PS. f: resonant frequency and # of PS layer: number of PS layers coating solenoid implantable coils.

Coil #	# of PS layer	f (MHz)
Solenoid IC (n = 2)	0	489.25 ± 3.89 (± 0.79%)
	1	486.50 ± 6.36 (± 1.31%)
	3	484.00 ± 2.83 (± 0.58%)
	4	479.25 ± 4.60 (± 0.96%)
	5	477.25 ± 3.89 (± 0.81%)
	6	474.75 ± 1.06 (± 0.22%)
	7	475.25 ± 2.47 (± 0.52%)

#### 3.4.2.2 Polytetrafluoroethylene

The thickness of each layer of PTFE never exceeded 2-3  $\mu\text{m}$  with the 6% PTFE solution when performing the dip coating. It also took approximately five hours of continuous labor to add 3 layers onto one coil. In addition, bubbles were present in large number. When the PTFE block-drying was attempted to get a thicker coating in a short amount of time, a skin formed at

the top of the solution. This skin blocked the evaporation of the solvent trapped underneath it and had to be broken apart midway through the drying process to allow the PTFE to continue gelling. The beaker was then left overnight in the hood to allow the solution gel completely. A number of bubbles were present in the 4mm-thick layer. However, a coil was placed on top of this first layer along with more PTFE solution. By the end of the second layer procedure, the coil had moved from in between the two PTFE layers to the lower edge of the first layer at the bottom of the beaker. This occurrence made the coating incomplete as the coil was never fully covered by PTFE.

### 3.4.2.3 Polymethylmethacrylate and polydimethylsiloxane

**Coating materials selection:** The coating of the implantable coil with PMMA and PDMS were successfully achieved because of their easy and fast preparation and handling of these two materials (Figure 3-8). Both coatings could easily be made bubble-free. The PDMS curing in an oven was avoided due to the increased risk of air bubble entrapment. A small hollow punch was used to create the construct cavity at the center of the coil (1-cm diameter) and a larger one was used to give the outer shape to the coated coil including the capacitor (2-cm diameter).

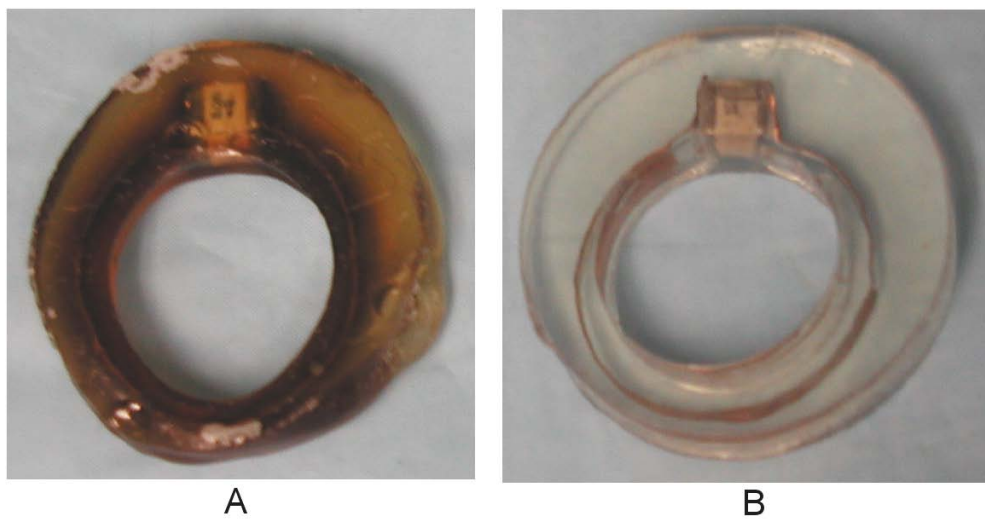


Figure 3-8. Photograph of the successfully coated implantable coils. A) With PMMA; and B) with PDMS. (Photo by N.A. Volland).

A 1-mm coating layer was used to coat the coils afterwards to determine the changes in the coil characteristics due to the coating and make the final coating material selection. A resonant frequency shift of  $-8.13 \pm 1.09$  ( $\pm 13.35\%$ ) MHz was detected for the PDMS-coated coils compared to the non-coated loop-gap resonator ( $n = 6$ ). This shift was in the same order of magnitude ( $-11.3$  MHz,  $n = 1$ ) for the PMMA-coated coil tested. The quality factor of these coils was only slightly different ( $214.50 \pm 20.95$  ( $\pm 9.77\%$ ) for PDMS-coated coils ( $n = 6$ ) and  $169.7$  for PMMA-coated coils ( $n = 1$ )) from their non-coated counterparts ( $< 10\%$ ). However, the Q of the inductively-coupled implantable coil system with the PDMS-coated implantable coil was more than twice the Q of the inductively-coupled implantable coil system with the PMMA-coated implantable coil ( $104.82 \pm 3.22$  ( $\pm 3.07\%$ ) ( $n = 4$ ) vs.  $49.5$  ( $n = 1$ )) a couple of days only after the implantable coils were coated. Signs of oxidation were observed at that time on the copper part of the coil (green color) with the PMMA coating. Nonetheless, both the PMMA- and PDMS-coated implantable coils were tested in the magnet, as their resonant frequency shift did not create any problems to tune the inductively-coupled coil system (surface and implantable coils coupled together) at  $470.75$  MHz and match to  $50 \Omega$ . The SNR determined from the images of the water sample acquired using the PDMS-coated coils was  $29.0\%$  ( $\pm 5.63\%$ ) better than the SNR determined with the PMMA-coated coil. These results made PDMS the coating materials of choice for the implantable coil in all the future studies of this project. Further considerations of these results are detailed in Section 3.5.

**Coating thickness determination:** The effects of coating on the coil were further characterized next and the optimal coating thickness was determined. Figure 3-9 illustrates changes in coil characteristics as the thickness of the PDMS around the coil is varied ( $n = 2$  for each coating thickness). The coating caused the coil resonant frequency to shift down (Figure 3-

9A, black triangles). However, the Q of a PDMS-coated coil is similar to that of a non-coated coil, (Figure 3-9B, black triangles). When a PDMS-coated coil is loaded (e.g., in a gel phantom), an additional negative frequency shift occurs (Figure 3-9A, grey diamonds) and the Q decreases (Figure 3-9B, grey diamonds).

The frequency shift is caused by the addition of capacitance to the coil circuit. Even though Q was determined at a different frequency, the changes in Q can be attributed to the addition of resistance from the coating and the sample. If the coating thickness altered the frequency slightly, with a maximum shift approaching -10 MHz (Figure 3-9A, black squares), upon immersion, the frequency shift decreased as the coating thickness increased, with only a 3% drop in the coil containing an 8-mm PDMS coating (Figure 3-9A, open diamonds). Moreover, having a thicker coat reduced the capacitive coupling of the coil to the sample and reduced the effect of sample loading on the coil Q. Further considerations of these results for the final selection of the coating thickness and the practical limitation of construct fabrication are detailed in Section 3.5. However, a 1-mm coating thickness was chosen as the optimal coating thickness for the purpose of the work presented here.

**Coated implantable coil characterization:** With the thickness of coating set, PDMS-coated implantable coils could be generated and fully characterized prior to *in vitro* and *in vivo* testing. The large hollow punch used to define the outer edge of the coating coil had a 2-cm diameter. The PDMS left in the center of the coated coil was removed with a 1-cm-diameter hollow punch. As previously reported in Section on Coating materials selection, the 1-mm PDMS layer created a  $-8.67 \pm 1.12$  ( $\pm 12.97\%$ ) MHz ( $n = 4$ ) frequency shift in the coil resonant frequency. In addition, loading further changes the coil characteristics.

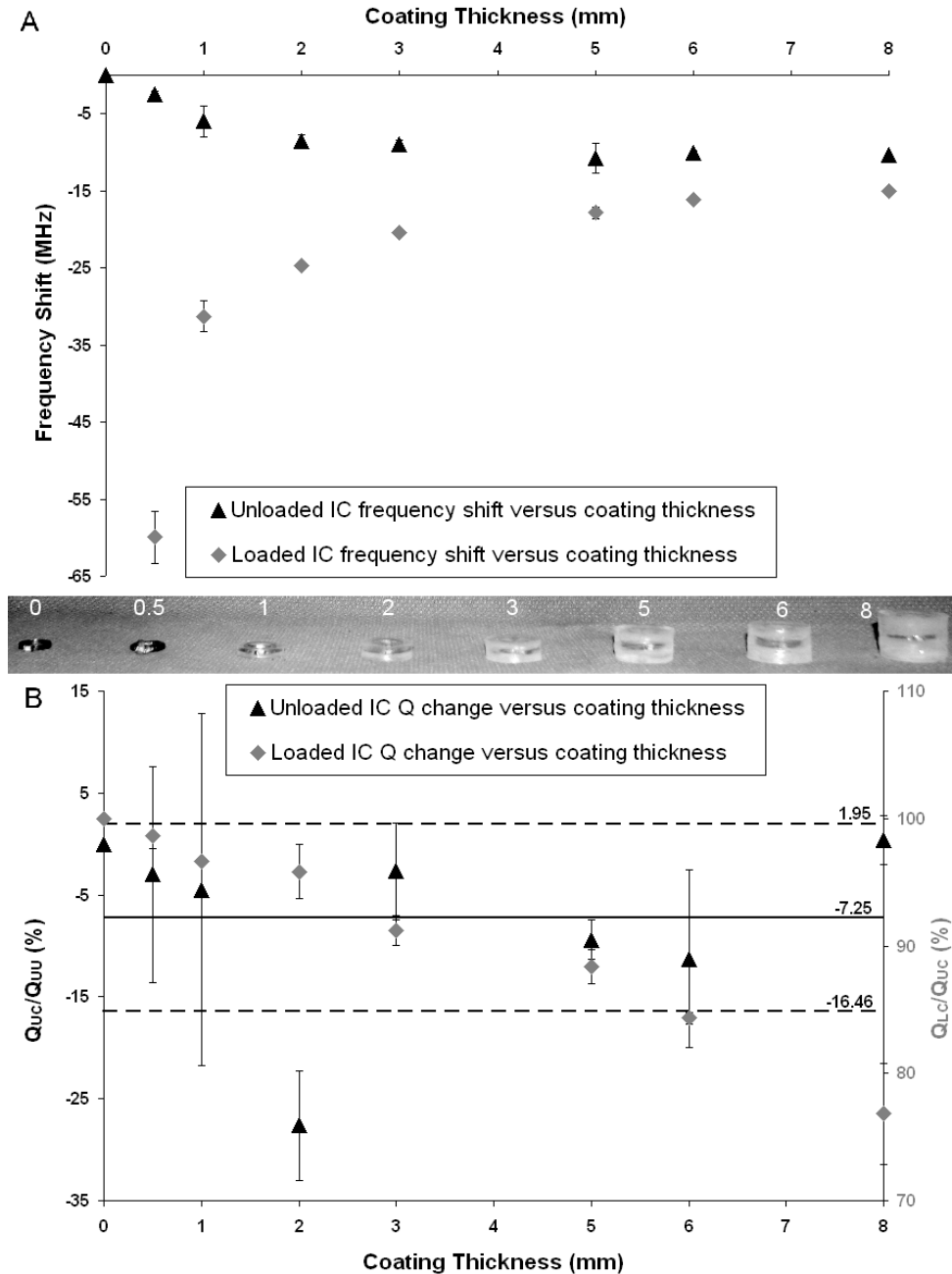


Figure 3-9. Effects of PDMS coating thickness on the implantable coil characteristics. A) Frequency shift of an unloaded IC ( $\blacktriangle$ ) and a loaded IC ( $\blacklozenge$ ) versus coating thickness; and B) % change of an unloaded IC Q ( $\blacktriangle$ , vertical scale on the right) and a loaded IC Q ( $\blacklozenge$ , vertical scale on the left) versus coating thickness. The right-side vertical scale compares the ratio of unloaded coated coil Q ( $Q_{UC}$ ) to unloaded, uncoated coil Q ( $Q_{UU}$ ) and the left-side vertical scale compares the ratio of coated, loaded coil quality factor ( $Q_{LC}$ ) to coated, unloaded coil quality factor ( $Q_{UC}$ ). A photograph of the different coated IC tested is shown between graphs A and B.

When the PDMS-coated implantable coils were embedded in the mouse abdomen-like phantom, an additional resonant frequency shift from the PDMS coating of  $-25.70 \pm 1.79$  ( $\pm 6.95\%$ ) MHz ( $n = 4$ ) was observed. These two successive shifts made it impossible to tune the coupled-coil system to the desired frequency of 470.75 MHz and were taken into account to build the implantable loop-gap resonator coils which were used for *in vitro* and *in vivo* studies. Hence, the implantable coils to be used loaded were constructed with a resonant frequency approximately 34 MHz higher than their predecessors ( $530.23 \pm 3.71$  ( $\pm 0.70\%$ ) MHz,  $n = 4$ ). This made the inductively-coupled coil systems resonate at the desired frequency of 470.75 MHz after coating and loading into the gel phantom or *in vivo* and ready to be tested in the magnet. The implantable coils resonated at  $497.64 \pm 3.58$  ( $\pm 0.72\%$ ) MHz when embedded  $0.42 \pm 0.02$  ( $\pm 5.31\%$ ) cm deep in the phantoms and at  $492.93 \pm 3.44$  ( $\pm 0.70\%$ ) MHz when embedded  $0.74 \pm 0.06$  ( $8.46\%$ ) cm deep in the phantoms ( $n = 4$ ). The quality factor of the loaded implantable coils was affected by the loading and decreased by a factor of 13 ( $18.51 \pm 3.99$  ( $\pm 21.57\%$ )) when embedded 0.42 cm in the phantom and by a factor of 16 ( $15.41 \pm 0.79$  ( $\pm 5.12\%$ )) when embedded 0.70 cm in the phantom implanted in the peritoneal cavity of a mouse. The Q of the inductively-coupled implantable coil system was dropped down to  $9.39 \pm 0.32$  ( $\pm 3.45\%$ ) MHz when the PDMS-coated implantable coil was embedded 0.70 cm deep in the gel phantom and to  $10.96 \pm 0.33$  ( $\pm 3.02\%$ ) MHz when the PDMS-coated implantable coil was embedded 0.42 cm deep in the gel phantom.

### **3.4.3 Coil-Construct Assembly**

The three constructs were successfully generated and placed in the middle of a PDMS-coated implantable coil as presented on Figure 3-10. These implantable coil-construct assemblies were all kept intact when soaked into HBSS for over 2 weeks.

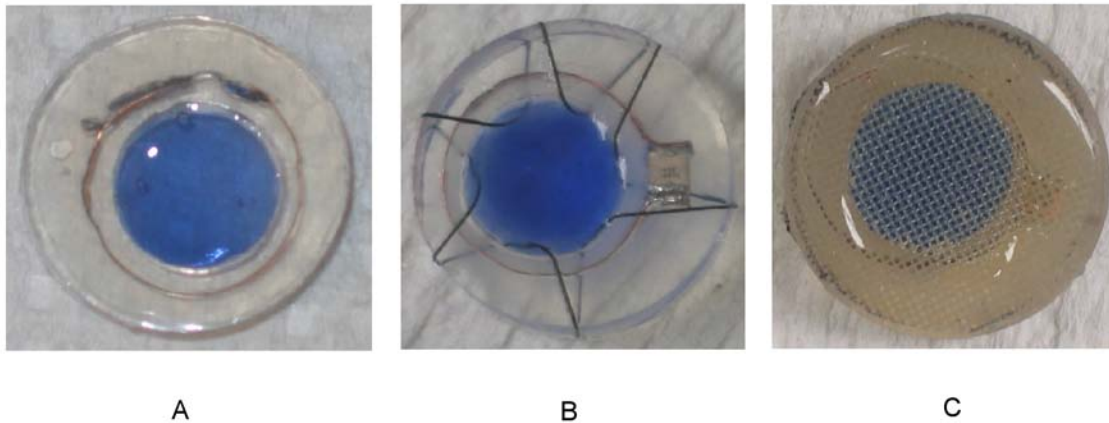


Figure 3-10. Photograph of the implantable coil-construct assemblies considered in this study. A) Agarose gel construct; B) alginate foam construct; and C) alginate beads hold in the middle of the coated coil by two meshes. Every construct has been dyed with trypan blue to help their localization. (Photo by N.A. Volland).

However, the agarose construct did not hold very firmly at the center of the coated coil and was also brittle. This could create a problem when the construct was implanted *in vivo* as it may easily separate from the implantable coil simply with the regular movement of the host and was not considered any further for the purpose of this study. The alginate foam construct was later found to have pores too large to properly host cells within the construct as it is shown in Chapter 6 and was not implemented further either in this study. Consequently, the alginate beads hold together by a mesh glued on a coated coil was the construct selected for the purpose of this study. Cells could be kept alive within the construct (Chapter 6) in the middle of the coil to allow their direct and non-invasive monitoring with NMR methods.

### 3.4.4 Phantom Studies

Figure 11 illustrates differences in SNR gain for different configurations and types of coils studied under unloaded conditions. The RF coils compared in this study include: 1) an SC at both 4.7 T and 11.1 T ( $n = 1$  for each field); 2) the two resonance modes of an overcoupled system with an SC and a solenoid IC at 11.1 T ( $n = 5$  for the (+) mode and  $n = 4$  for the (-) mode); and 3) the two resonance modes of an overcoupled SC and a loop-gap IC at 11.1 T ( $n = 7$

for the (+) mode and n = 4 for the (-) mode). The implantable loop-gap resonator in the (+) mode was coated with a 1-mm PDMS layer and tested when inductively-coupled with a SC (n = 4).

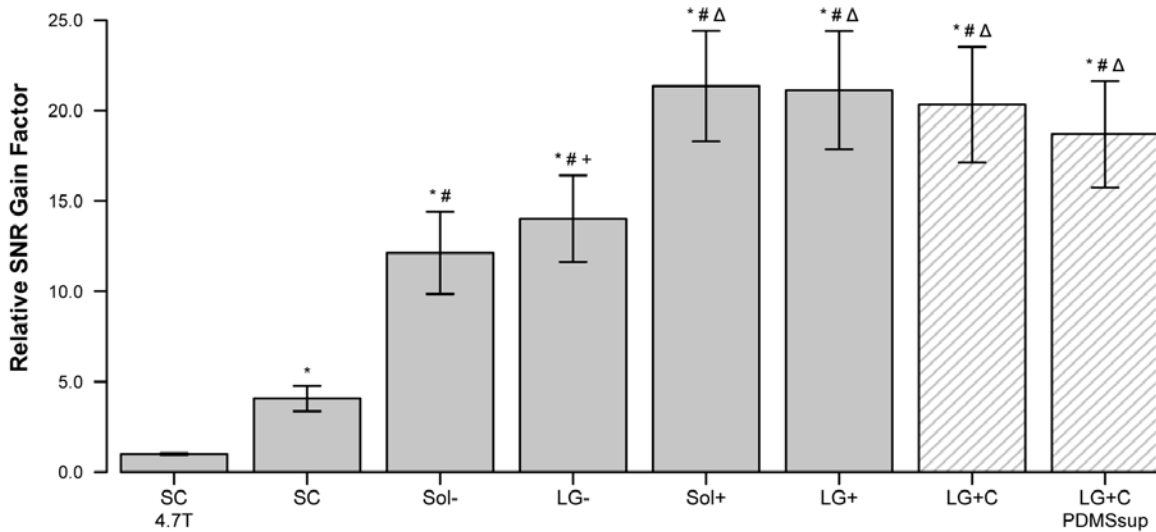


Figure 3-11. SNR comparison between different RF coils tested under unloaded conditions using a water sample. The coils tested were: an SC at 4.7 T (SC 4.7T) and at 11.1 T (SC), coupled-coil systems with a solenoid IC, or a loop-gap IC in the (-) mode (Sol- & LG-) and in the (+) mode (Sol+ & LG+), or a PDMS-coated loop-gap in the (+) mode (LG+ C) placed 1 cm away from the SC. PDMSsup indicates that a PDMS suppression schema was tested for LG+ C. \* denotes the statistical difference between the coil SNR at 11.1T and the SC SNR at 4.7 T; # the difference between the coupled coil system SNR and the SC SNR at 11.1T; Δ the difference between the coupled-coil system SNR in the (+) and (-) mode; and + between the SNR of LG- and Sol-.

The SNR of SC (SC) was better at the higher magnetic field strength of 11.1 T (Figure 3-11), approximately 4 times higher, than at 4.7 T (SC 4.7T) [ $4.07 \pm 0.70$  ( $\pm 17.2\%$ ),  $p \ll 0.001$ ]. At 11.1 T all coupled-coil systems performed better than the SC. The SNR of the coupled-coil system in the (-) mode was approximately 3 times greater than the SC (SC 11T) [ $12.1 \pm 2.27$  ( $\pm 18.8\%$ ),  $p \ll 0.001$ ] when the IC was a solenoid (Sol -) and 3.4 times greater [ $14.0 \pm 2.40$  ( $\pm 17.1\%$ ),  $p \ll 0.001$ ] when the IC was a loop-gap (LG-). The (+) mode of these coupled-coil systems surpassed the performances of the (-) mode. The coupled-coil system with a solenoid IC

(Sol+) was approximately 5.3 times greater than the SC (SC 11T) [ $21.4 \pm 3.06$  ( $\pm 14.5\%$ ),  $p \ll 0.001$ ] and the system with the loop gap resonator IC (LG+) nearly 5.2 times greater [ $21.1 \pm 3.27$  ( $\pm 15.5\%$ ),  $p \ll 0.001$ ]. Therefore, the (+) mode coupled-coil systems outperformed the (-) mode coupled-coil systems when either a solenoid ( $p \ll 0.001$ ) or a loop gap ( $p \ll 0.001$ ) were used as IC. The coupled coil system with a loop-gap resonator IC performed better than the system with a solenoid IC in the (-) mode ( $p \ll 0.001$ ), but was not statistically better in the (+) mode ( $p > 0.05$ ). The coupled-coil system in the (+) mode with a PDMS coated loop gap resonator IC also showed an SNR improvement of approximately 5 times that of the SC (LG+ C) [ $20.3 \pm 3.20$  ( $\pm 15.8\%$ ),  $p \ll 0.001$ ]. Furthermore, PDMS suppression used with the implantable coated coil, did not significantly affect the inductively-coupled coil system SNR (LG+ C PDMSsup) [ $18.7 \pm 2.94$  ( $\pm 15.7\%$ ),  $p \ll 0.001$ ].

Figure 3-7 illustrates SNR differences between the (+) and (-) modes. The ratio of  $B_1$  between the (+) and (-) modes for similar coils approaches 1.5, as shown by comparing the ratio of SNR for the inductively-coupled coil system in the (+) to (-) mode first, with the loop-gap IC [ $1.51 \pm 0.35$  ( $\pm 23.1\%$ )] and second, with the solenoid IC [ $1.76 \pm 0.42$  ( $\pm 26.6\%$ )]. The magnetic field distribution of a SC is also represented for comparison (Figure 3-7D & 3-7E). The non-uniformity of the image in Figure 3-7F is due to the overtipping of spins necessary to obtain the proper excitation at the implanted construct location. These simulations indicate that the  $B_1$  field magnitude is highest at the IC location in the (+) configuration (Figure 3-7I & 3-7J). The ratio between the simulated  $B_1$  field magnitude at the construct location of a SC and an inductively-coupled coil system in the (+) mode is 4.5 (Figure 3-7D & 3-7I). This ratio agrees reasonably well with the SNR ratio of  $\sim 5.2$  between the measured SNR at the construct location for a SC and a coupled-coil system in the (+) mode for the water and gel phantoms (Figure 3-11 & 3-12).

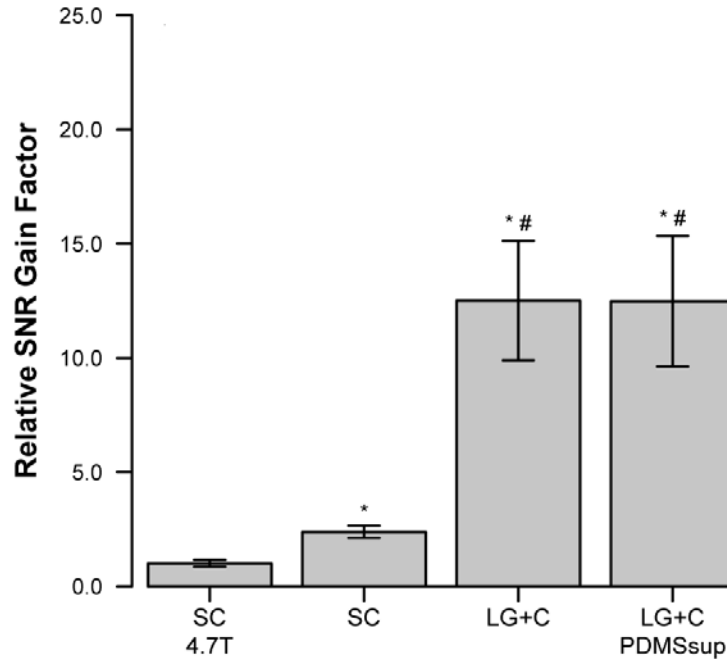


Figure 3-12. SNR comparison between different RF coils tested under loaded conditions in a gel phantom. An SC at 4.7 T (SC 4.7T) and at 11.1 T (SC), and a coupled-coil system with a PDMS-coated loop-gap IC in the (+) mode placed 1 cm away from the surface (LG+ C) were tested. PDMSsup indicates that a PDMS suppression schema was tested the PDMS-coated IC. \* denotes the statistical difference between the SNR of the RF coils at 11.1T and the SC at 4.7 T); and # the difference between the coupled-coil system SNR and the SC SNR at 11.1T.

Because the coupled coil system in the (+) mode gives the highest SNR under unloaded conditions (Figure 3-11) when either the solenoid or loop-gap IC was used, the effect of loading on the measured SNR for a coupled-coil system were investigated in the (+) mode only. The loop-gap IC design was selected for ease of construction. Figure 3-12 depicts the SNR gain obtained at the construct location (approximately 1 cm away from the SC) when coupled-coil systems comprising PDMS-coated loop-gap IC (implantable-coil-construct assembly) and SC were tested under loaded conditions (n = 4). With an SC, the SNR increase factor at 11.1 T compared to 4.7 T is significant [ $2.38 \pm 0.27$  ( $\pm 11.4\%$ ),  $p << 0.001$ ]. At 11.1 T the coupled-coil system shows an SNR increase of more than 5.25 times that of the SC [ $12.5 \pm 2.61$  ( $\pm 20.9\%$ ),  $p << 0.001$ ] when the implantable coil-construct assembly was placed approximately 1 cm away

from the SC [ $0.74 \pm 0.06$  ( $\pm 8.46\%$ ) cm]. The PDMS suppression did not significantly alter the results [ $12.5 \pm 2.85$  ( $\pm 22.9\%$ ),  $p < 0.001$ ].

Figure 3-13 displays the SNR gain obtained when the distance between the implantable coil-construct assembly and the SC approximated 0.5 cm ( $0.42 \pm 0.05$  ( $\pm 10.6\%$ ) cm in a gel phantom and  $0.62 \text{ cm} \pm 0.08$  ( $\pm 18.8\%$ ) *in vivo*). The sensitivity improvement reduces to a factor of  $\sim 1.7$  with the reduced distance between the two coils of the system [ $4.03 \pm 0.90$  ( $\pm 22.3\%$ ),  $p < 0.001$  in a gel phantom and  $4.34 \pm 1.51$  ( $\pm 34.8\%$ ),  $p < 0.001$  *in vivo*]. The PDMS suppression did not significantly alter the results [ $4.02 \pm 0.88$  ( $\pm 22.4\%$ ),  $p < 0.001$  in a gel phantom and  $4.86 \pm 1.60$  ( $\pm 32.9\%$ ),  $p < 0.001$  *in vivo*] at this separating distance either.

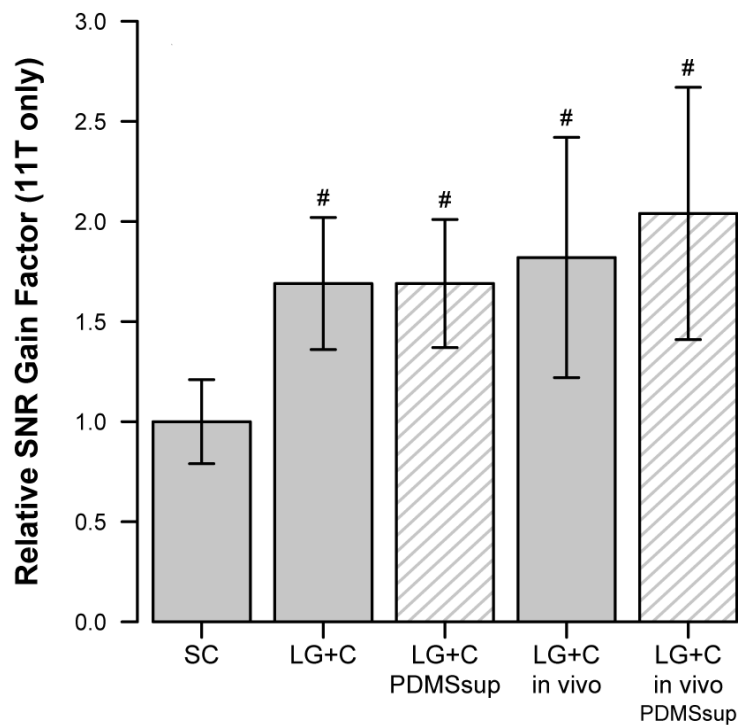


Figure 3-13. SNR comparison between different RF coils tested under loaded conditions using a gel phantom or *in vivo* conditions at 11.1T. Were tested: an SC (SC) and coupled-coil systems with a PDMS-coated loop-gap IC in the (+) mode placed 0.5 cm away from the surface in the phantom (LG+ C) or implanted *in vivo* (LG+ C *in vivo*). PDMSsup indicates that a PDMS suppression schema was tested. # denotes the statistical difference between the SNR of the inductively-coupled coil systems and the SC.

### 3.4.5 *In vivo* Studies in Mice

Bioartificial pancreatic constructs containing PDMS-coated loop-gap coils were successfully implanted into mice peritoneal cavities ( $n = 3$ ). The implantable coils were found to resonate at  $501.59 \pm 2.63$  ( $\pm 0.53\%$ ) MHz when in the peritoneal cavity of mice.  $Q$  was found to have decreased by a factor 11.5 ( $20.08 \pm 3.73$  ( $\pm 18.58\%$ )) when implanted in the peritoneal cavity of mice compared to the coil  $Q$  before implantation. The inductively-coupled implantable coil system  $Q$  was now  $35.25 \pm 10.25$  ( $\pm 29.08\%$ ) MHz when the implantable coil was in the mouse peritoneal cavity. Constructs without the implantable coil but with the same characteristics than the constructs including a coil have also been implanted successfully ( $n = 3$ ). The surface coil  $Q$  was  $61.78 \pm 5.78$  ( $\pm 9.35\%$ ) MHz when the implantable coil was in the mouse peritoneal cavity.

*In vivo* images (Figure 3-14) were acquired within 1 hour following implantation using conventional respiratory gating and an effective TR of 2500ms. These images provided a clear visualization of the construct. If increasing the number of averages and the number of averaged experiments reduced the animal breathing artifact on the images, these two improvements increased the acquisition time and were consequently not used in this study. However, better respiratory gating without an significant increase in acquisition time could be investigated in the future: self-gating (155-157) or an image reconstruction using a motion artifact correction post-processing imaging gating (158).

The inductively-coupled coil system shows better localization of the construct than the SC ( $n = 3$ ), because it is more spatially selective. The average distance from the implanted construct to the mouse skin was  $0.42$  cm [ $\pm 0.08$  ( $\pm 18.8\%$ )] making separation between the IC and the SC about  $0.6$  cm, when accounting for the mouse holder. The inductively-coupled coil system

shows an SNR increase of approximately 2 times over an SC at 11.1 T [ $4.34 \pm 1.51$  ( $\pm 34.8\%$ ),  $p \ll 0.001$ , without PDMS suppression;  $4.86 \pm 1.60$  ( $\pm 32.9\%$ ),  $p \ll 0.001$ , with PDMS suppression] (Figure 3-13). With this sensitivity improvement, *in vivo* images of the construct allowed distinction of individual alginate beads, 400-to-700- $\mu\text{m}$ -diameter, entrapped within its cavity (Figure 3-14B) with an in-plane resolution of 78.125  $\mu\text{m}$ , demonstrating the potential of this inductively-coupled implantable coil system to directly and non-invasively monitor a bioartificial pancreas *in vivo*.

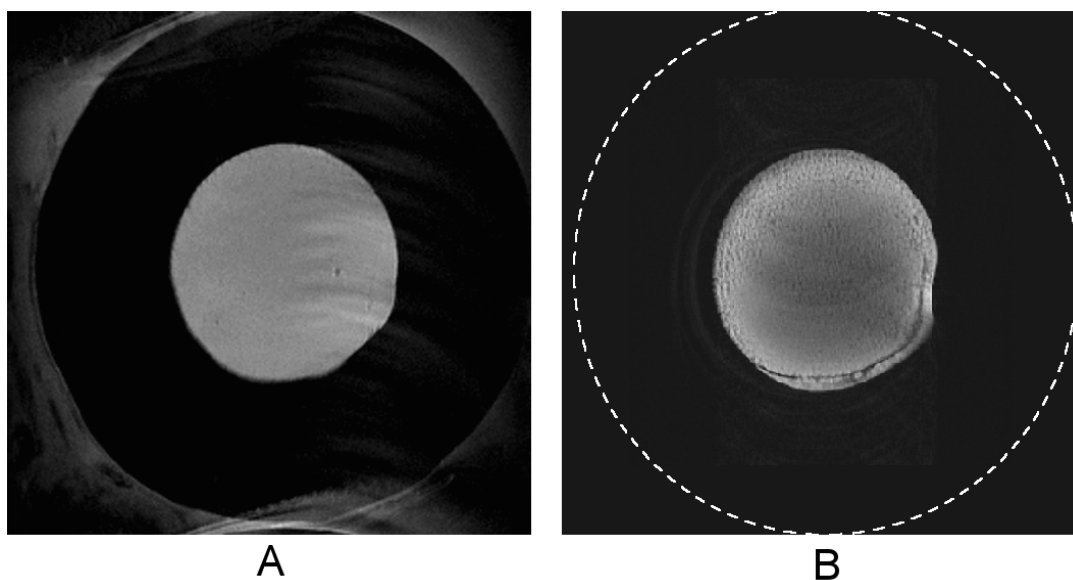


Figure 3-14. Cross-sectional images of two bioartificial constructs implanted *in vivo*. A) Plain construct imaged using an SC; and B) an implantable coil-construct assembly (with the same characteristic as the plain construct) imaged using the coupled-coil system. The white circle delineates the construct outer edge, visible in A, but not in B. An SE pulse sequence was used to acquire these images: TR = 2500 ms, TE = 10 ms, 1-mm slice thickness, 1 average, FOV 2 x 2  $\text{cm}^2$  and matrix size 256 x 256. Respiratory gating was also applied.

### 3.5 Discussion

NMR is a powerful technique for acquiring images and spectroscopic data, but its inherent insensitivity limits application of this technique when studying implanted bioartificial constructs. To overcome this limitation, the use of an inductively-coupled, implanted coil system for NMR

measurements was explored. This system has substantive advantages over an SC, and a working *in vivo* implantable coil system that can be implanted with the bioartificial construct was developed. For the study of tissue-engineered constructs, this inductively-coupled, implantable coil system has the following advantages: 1) measured NMR signal is more homogeneous throughout the construct; 2) the coil system is more spatially selective without the use of selective pulse sequences because the IC surrounds the construct; and 3) if implantation depth is variable, the inductively-coupled coil system allows tighter control over RF coil tuning and matching, and the  $B_1$  field distribution is more uniform. Additionally, when applied *in vivo* with respiratory gating, this system is less sensitive to breathing artifacts: the implantable coil system resonant frequency shift is small with motion, whereas with an SC the loading and sensitivity at the construct location changes more with motion.

The available SNR in the NMR measurement is a primary concern when obtaining useful information from an implanted construct. Increasing the static magnetic field strength improves sensitivity. Under unloaded conditions, the SNR is proportional to  $(B_1/B_2)^{7/4}$ , where  $B_1$  and  $B_2$  are the magnetic field strengths being compared ( $B_1 > B_2$ ) (139) and primarily due to the higher sensitivity obtained at higher field (97). This predicted enhancement in SNR of 4.5 times between 4.7 T and 11.1 T is similar to the measured SNR improvement of  $4.07 \pm 0.18$  ( $\pm 4.34\%$ ) when SC were tested. Under loaded conditions (like tissue over a surface coil and surrounding an implanted coil), the loading reduces the SNR gain to a linear increase with magnetic field strength (7). For field strengths considered here, the predicted SNR improvement is 2.36-fold, agreeing well with the measured value of  $2.38 \pm 0.27$  ( $\pm 11.4\%$ ).

The inductively-coupled, implanted coil system also demonstrates an SNR improvement over a single SC at 11.1 T from a minimum of about 1.7 to over 5, depending on the implantable

coil location. The inductively-coupled coil systems in (+) mode with both the solenoid and loop-gap resonator IC yield better SNR as shown on Figure 3-11A. These systems were chosen for NMR measurements. Although the inductively-coupled coil systems in the (+) mode with the solenoid IC gave slightly better SNR than the inductively-coupled system with the loop-gap IC, the difference is not statistically significant. The solenoid IC require small series capacitances for both (+) and (-) modes, due to the high inductance of the solenoid design, making the system harder to build and compensate for coating and loading effects. Since the loop-gap coil has lower inductance, which requires larger series capacitance, it is easier to build and coat than the solenoid. Therefore, these important considerations (lower inductance and ease of construction) make the loop-gap resonator IC the best overall choice to build bioartificial constructs.

With regards to coating, the frequency shift and the decrease in quality factor of the implantable over time observed with PS coating was explained by the PS layer tendency to absorb water over time (136) and thus modifying the coating properties. This evolutionary behavior was not acceptable for the purpose of this study. PS was consequently disregarded. PTFE was set aside as it was hard to handle, even though it has good dielectric properties. Furthermore, PTFE is a thermoplastic polymer, not a thermosetting polymer (crosslinked polymer fixed once and for all). This means that if it is reheated above its glass temperature, it will melt again. This was the explanation for the coil falling to the bottom of the beaker repeatedly. The bottom layer of PTFE melted making the coil fall to the bottom of the beaker. The two PTFE layers then became one. Injection and/or compression molding, and chemical vapor deposition (CVD) procedures could have been considered. However, more attention will have to be given to these techniques as they have high temperature (250-400 °C) and/or high pressure (4-7 MPa or 500-1,000 psi) requirements. PMMA coating was abandoned since images

acquired using the implantable coils with this coating displayed a lower SNR compared to the ones acquired using implantable coil with PDMS coating. The coil oxidation that appeared within days of the coil coating may have been the reason for the SNR deterioration. It was also slightly harder to handle than PDMS. For this study, only PDMS met all the criteria to easily and efficiently coat the implantable coils and was used for the *in vitro* and *in vitro* studies.

The PDMS coil coating induces mainly capacitance losses, shifting the resonant frequency, while coil loading mainly introduces resistive losses, decreasing the Q of the system (see Figure 3-9). Taking into account these consequences, these results suggest that an 8-mm coating would minimize changes to both the Q and frequency shift of the IC. However, the resultant implantable coil-construct assembly is unrealistically large for monitoring the construct *in vivo*. The size of the mouse peritoneal cavity limits the coating thickness to no more than 1 mm. Furthermore, the insertion of the coil around the construct requires the coil to be close to the construct to maximize sensitivity (filling factor). Therefore, a PDMS coating thickness of 1-mm is the best compromise to maximize coil function while allowing sufficient space for a viable construct (i.e., sufficient biological component of a bioartificial organ). The inductively-coupled coil system with the coated loop-gap IC was successfully developed, tested in a mouse abdomen-like gel phantom, and implanted in a mouse, and observed in the (+) mode. Although the SNR decreases under loaded conditions compared to the unloaded conditions, there is sufficient SNR to obtain better images than with a SC.

The coated loop-gap system was successfully developed and tested in a phantom (loaded conditions similar to *in vivo* conditions), as well as implanted in a mouse and observed in the (+) mode. Although the SNR decreases under loaded conditions (mouse abdomen-like phantom or

actual mouse) compared to the unloaded conditions, there is sufficient SNR to obtain better images than with a surface coil.

For *in vivo* imaging, only respiratory gating and increased TR close to the breathing rate of the animal were kept to image the bioartificial pancreas as the best compromise between acquisition time and SNR. The 400-to-700- $\mu\text{m}$ -diameter beads within the construct were visualized *in vivo* (Figure 3-14) with an in-plane resolution of 73.13  $\mu\text{m}$ , demonstrating the potential of this inductively-coupled implanted coil system to directly and non-invasively monitor a bioartificial pancreas *in vivo*.

With fixed coil sizes, the advantage of an inductively-coupled implanted coil over an SC will increase as the depth of the implanted coil increases, such as in larger animal models (e.g. humans), since the SC sensitivity drops rapidly with distance (Figure 3-7D & I). If a larger SC can obtain a greater depth of sensitivity for NMR measurements, the noise sensitivity would increase with the SC sensitive volume. Therefore, the inductively-coupled implanted coil presents an optimum configuration for NMR detection from implanted tissue constructs, though not restricted to use with implanted tissue-engineered constructs.

### **3.6 Summary**

Implantable inductively-coupled loop-gap coils assembled within bioartificial constructs have been constructed, implanted into mice, and their performance analyzed. NMR images from these assemblies were easily obtained at 11.1 T, demonstrating the capability of this inductively-coupled implanted coil system. The sensitivity improvement of this implantable coil system over SC at 11.1 T is approximately 2-fold. This gain was multiplied by the improvement of 2.4-fold obtained from the magnetic field strength increase from 4.7T to 11.1T. The sensitivity improvement available with the use of inductively-coupled, implantable coil system allows significant gains in information obtained from an implanted construct, providing images with

higher contrast to noise, spectroscopy with greater SNR (e.g.,  $^1\text{H}$  observation of choline for cell-containing constructs), and allowing detection of other key, but less-sensitive nuclei (e.g.,  $^{31}\text{P}$ ,  $^{19}\text{F}$ ) critical in the efforts to quantify implanted bioartificial organ function. It is important to emphasize that the approach outlined here can be applied to other situations, and is not restricted to use with implanted tissue-engineered constructs, although its inherent strength make it a desirable choice when obtaining information from implantable constructs.

With the technology of implanted coil established, this research focused then on perfecting NMR acquisition parameters (e.g. eliminating artifacts, due to hardware and physiology issues); developing a receive-only inductively-coupled implantable coil system that will further enhance the ability to perform  $^1\text{H}$  NMR localized spectroscopy, and studying ‘cellularized’ constructs through NMR imaging and spectroscopy.

CHAPTER 4  
DEVELOPMENT OF A RECEIVE-ONLY INDUCTIVELY-COUPLED RF COIL SYSTEM  
TO ENHANCE  $^1\text{H}$  NMR LOCALIZED SPECTROSCOPY TO MONITOR AN  
IMPLANTABLE BIOARTIFICIAL CONSTRUCT

### 4.1 Introduction

The monitoring of bioartificial pancreas (BAP) viability is of primary importance as it directly reflects its well being and functioning. Choline is a vital amine molecule present in every living cell, whose NMR signal can be detected when performing  $^1\text{H}$  MR spectroscopy (MRS) and has been linked to the number of viable cells within the area of detection. To allow optimal MRS, a uniform NMR excitation and a highly sensitive NMR response signal detection is recommended. In order to achieve this optimum, a receive-only inductively-coupled, implanted coil system was developed in this study. Its use was demonstrated at high field (11.1 T) in combination with a transmit-only birdcage volume coil. Its specific requirements for monitoring a bioartificial construct *in vitro* were also investigated. The results establish that even though no overall gain in signal-to-noise was obtained with this receive-only inductively-coupled implanted coil system over that which can be obtained with a transmit-receive inductively-coupled implanted coil system, this coil system provides a greater signal uniformity and a means to analyze the function of implanted bioartificial organs quantitatively using choline NMR detection.

### 4.2 Background

The monitoring of the viability of cells within a tissue-engineered construct, such as a bioartificial pancreas (BAP), is of primary importance as it directly reflects the well being and functioning of the construct. NMR has been shown to be well-suited for monitoring a bioartificial pancreatic construct non-invasively and temporally, *in vitro* and *in vivo*, because of its penetration depth, resolution, contrast, and ability to probe both metabolism and anatomy (2-

4). While NMR imaging mainly provides anatomical information, Stabler *et al.* developed an NMR-based method to non-invasively assess the viability of cells within a bioartificial pancreatic construct using  $^1\text{H}$  MR spectroscopy (MRS) (5,6) and detecting the NMR choline signal.

Choline is a vital amine molecule, which is present in every living cell. It participates in cell-signaling, serves as an acetylcholine precursor, and adds structural integrity to cell membranes. The choline NMR signal, also referred to as total choline (TCho) signal, includes the signal from the following aqueous compounds found intracellularly: phosphocholine (PCho, a precursor of membrane phospholipids), glycerophosphocholine (GPCho, a product of the degradation of membrane phospholipids) and free choline (Cho) (159). Their contribution to the total choline signal has been determined at 64% for PCho, 33% for GPCho, and 3% for Cho (88). The signal can be detected when performing  $^1\text{H}$  MR spectroscopy (MRS). Even though the choline molecule has several resonance peaks on a  $^1\text{H}$  spectrum as shown on Figure 2-3B, its strongest one can be found at 3.2 ppm due to the molecule's three equivalent methyl groups. Variations in the signal intensity of the TCho signal at 3.2 ppm have been shown to represent the increase of membrane phospholipid biosynthesis and serve as an active marker for cellular proliferation in tumors (86,87). By localizing the spectroscopy to within the BAP, TCho intensity changes have been shown to be linked to oxygen concentration (88) and proportional to cell viability variation (5,6). These later studies clearly demonstrate that acquisition of metabolic information from cells imbedded within tissue-engineered constructs implanted intraperitoneally in mice abdomen is possible by MRS. Unfortunately, the sensitivity of the method used was limited by the strength of the magnetic field and the radiofrequency (RF) coils used to excite and detect the signal (a 4.7 T NMR instrument and a surface coil). The threshold of NMR signal

detection due to these experimental conditions were approximately one million cells per construct under *in vitro* (ideal) conditions and two million cells under *in vivo* conditions. Consequently, the constructs were generated with a large number of cells and could still only be monitored for a maximum of two weeks due to the lack of sensitivity of the monitoring method.

Recently, the use of higher magnetic field strength along with inductively-coupled implantable coil systems was shown to greatly improve the sensitivity of this method (Chapter 3 and (160)). This sensitivity improvement would allow the detection and study of lower density of cells within constructs *in vitro* and *in vivo* over a longer period of time. Furthermore, the selectivity of inductively-coupled implantable coil system demonstrated to be superior to the surface coil alone (Chapter 3). This gives an advantage to inductively-coupled implantable coil system when performing localized spectroscopy with a high sensitivity as it decreases the signal contamination from outside of the construct. However, this system does not produce a homogeneous RF magnetic field over a large enough volume to use volume selective pulse sequences to their full extent (81). In order to optimize the power of selective pulse sequences, a uniform excitation magnetic field pattern within the sample is preferable. Large surface coils or volume coils can achieve such an excitation pattern, though decreasing the signal detection sensitivity. Combining a volume coil and an inductively-coupled implantable coil system closer to the area of interest allows production of a uniform excitation and detection of the NMR signal with a higher sensitivity. However, the two systems have to be decoupled from each other to prevent their interaction and allow the proper functioning of this two RF-coil setup. The volume coil was actively decoupled by an external bias current source (104,106) since the NMR signal from the sample would not be high enough to generate the power required to make the transmit-only coil decoupling circuit function properly. Unlike the volume coil, the inductively-coupled

coil system (implantable and surface coils included) was passively decoupled (105). The use of a passive decoupling avoided the requirement for external diode bias connection to the implantable coil running through the skin.

This report investigates the use of receive-only inductively-coupled RF coil systems at a high field (11.1 T) to monitor implanted tissue-engineered constructs with NMR and perform  $^1\text{H}$  localized spectroscopy to detect choline signal. It also compares NMR sensitivities for monitoring an implanted bioartificial pancreatic construct using either an inductively-coupled implanted coil system for both excitation and detection or the combination of a birdcage volume coil for excitation and a receive-only inductively-coupled implanted coil system for detection. This report also discusses technical aspects important toward generating receive-only inductively-coupled coil systems for  $^1\text{H}$  detection using passive decoupling, and issues to consider when applying these coils in conjunction with implanted bioartificial constructs for localized spectroscopy.

### **4.3 Materials and Methods**

#### **4.3.1 RF Coil System Development**

All the inductively-coupled implantable coil systems used in this study were constructed, tested, and compared for NMR imaging and spectroscopy at 11.1 T. Because of the results obtained in Chapter 3, these coupled-coil systems consisted of an internal (implantable) loop-gap resonator coil inductively-coupled to a surface coil. They were also used when overcoupled in their co-rotating mode (see Section 3.3.3 for more details on inductive coupling and overcoupling). The two different inductively-coupled systems developed were: 1) one system functioning as both transmitter and receiver; and 2) one system functioning as receiver only for  $^1\text{H}$  NMR (470.75 MHz at 11.1 T). This second system was coupled with a transmit-only home-built bird-cage volume coil providing the NMR excitation. The volume coil was actively

decoupled from the inductively-coupled implantable coil system when this latter system was detecting the sample signal, whereas the inductively-coupled coil system was passively decoupled from the volume coil when the volume coil was exciting the sample. The first inductively-coupled system was the system used in the previous study presented in Chapter 3 as well as the implantable coil- construct assembly (160).

To render the second inductively-coupled implantable coil system receive-only, the addition of a passive decoupling circuit was required on both the surface and implantable coils (104,105). This circuit was composed of anti-parallel diodes ( $D_{1s}$  and  $D_{2s}$  for the surface coil and  $D_{1i}$  and  $D_{2i}$  for the implantable coil on Figure 4-1) and a small solenoid inductor ( $L_{Ds}$  for the surface coil and  $L_{Di}$  for the implantable coil on Figure 4-1) in parallel to one of the tuning capacitors on the resonant circuit (American Technical Ceramics, Hartford, CT;  $C_{Ts}$  for the surface coil and  $C_{Ti}$  for the implantable coil on Figure 4-1).

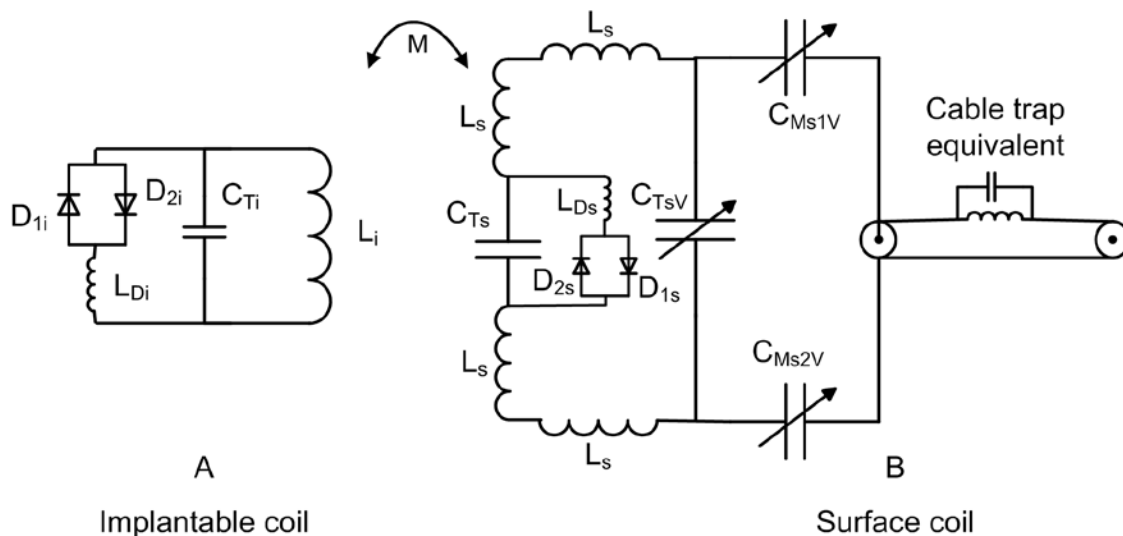


Figure 4-1. Circuit diagram for a receive-only inductively-coupled implantable coil system for  $^1\text{H}$  detection. A) Implantable coil; and B) surface coil. Inductors (L), capacitors (C), and diodes (D) are shown with subscripts denoting implantable (i) or surface (s) coil. Capacitors are also designated as tuning ( $C_T$ ) or matching ( $C_M$ ) as well as inductor as main circuit inductor (L) and decoupling inductor ( $L_D$ ). M indicates the mutual inductance or inductive coupling and V variable. A cable trap equivalent, including an inductor and a capacitor, is also shown in the diagram.

The diode had an active (ON) and an inactive (OFF) state that could be modeled with equivalent circuits as follows: 1) when the diode was in the OFF position allowing the coil to function as a detector, the diode was equivalent to a capacitor in parallel with a high value resistance (leakage resistance), no current was flowing in the decoupling circuit, the receive-only coil functioned as if the decoupling circuit was not there; and 2) when the diode was turned ON, the receiving coil was prevented from functioning. The diode was then equivalent to a small series resistance and effectively switched the decoupling circuit inductor in parallel with the capacitor, creating a high impedance in the coil circuit. This impeded the current flow in the coil circuit making the receive-only system invisible to the transmit-only coil. In the magnet, this circuit was activated by the RF excitation signal from the transmit-only volume coil and did not require the use of a pulsed DC control signal source (as does an active decoupling circuit).

To achieve this decoupling at the coil resonant frequency, the impedance of the decoupling circuit has to be equal to the impedance of the capacitor in parallel. This means that the decoupling inductor's impedance equals the tuning capacitor impedance (105) when the diode equivalent series resistance can be considered small enough. The decoupling circuit solenoid was made of 25 AWG (American Wire Gauge) copper wires hand wound around a 16 AWG copper wire. Its value was verified using the RF impedance test adapter HP 1620A spring clip fixture of the network analyzer (8752C Hewlett Packard, Santa Rosa, CA) before being placed perpendicular to the main coil loop to limit the interaction between each other.

Different inductively-coupled implantable coil system layouts were built and tested to optimize the design. These layouts differed from each other mainly by the type of diodes used and their characteristics (mainly their parallel capacitance, equivalent series and parallel resistance, and transition time values) and the number of capacitors the coils comprised. The

diodes used were: 1) Schottky fast recovery small signal anti-parallel diodes (M/A COM MA45471, Tyco Electronics, Berwyn, PA); and 2) PIN diode (DH80052-40N, Chelton Telecom & Microwave, Grigny, France). The number of tuning capacitor was varied from one to four in the implantable coil circuit, and from two to four in the surface coil circuit.

#### **4.3.2 Coating Techniques**

The material used to coat the receive-only implantable coil was the same as the one used for the transmit-receive implantable coil: polydimethylsiloxane (PDMS, Medical Grade Silicone Elastomer, Factor II, Lakeside, AZ). The technique applied to coat the coil has been described in details in Section 3.3.2.4 (160). However, adaptations had to be made to this coating procedure to accommodate the receive-only coil extra components. Instead of generating a 1-mm PDMS layer first, a 0.5-mm one was generated to compensate for the slightly wider than 2-mm diode. A 4-mm layer was then added on top to cast the coils and make sure the coating was properly sealed all around the coils. Over 24 hours the PDMS would flow in the gap between the coil and the first PDMS layer. The outer edge of the coated coil was shaped using a 2.6-cm-diameter hollow punch instead of the 2-cm-diameter one used in the study presented in Chapter 3, since the decoupling circuit made the coil outer edge larger. Furthermore, the coating of the hand-wound decoupling-circuit solenoids was tested prior to the coating of the entire coil as they could be easily deformed under pressure resulting in drastic changes in their characteristics (inductance in this case).

#### **4.3.3 RF Coil Testing**

In order to have the receive-only inductively-coupled coil system resonating at 470.75 MHz, the implantable and surface coil were individually tuned and matched at the same higher frequency (490.1 MHz) as the transmit-receive system after the decoupling circuit was added in

their circuit. The capacitors  $C_{M1V}$ ,  $C_{M2V}$ , and  $C_{TsV}$  (Figure 4-1) of the surface coil were adjusted to achieve the match of the whole system to  $50 \Omega$  at 470.75 MHz.

The receive-only coils were constructed and optimized on the bench with a network analyzer (Hewlett Packard 8752C, Santa Rosa, CA) before being tested in the magnet. The quality factor (Q) of each coil taken individually and of the whole system was recorded after construction with and without load and every time the system was tested in the magnet as described in details in Section 3.3.3. The effects of the decoupling circuit were also tested here by determining changes in the resonant frequency and Q for all the coils and systems (139) after its insertion in the coil main circuit.

The difference in power transmitted to an external field probe located 1 cm away from all the coils when their decoupling circuit was ON and OFF was also determined. A 20 dB difference was at least required for the proper functioning of the decoupling circuit. This means that over 90% of the signal from the coil was attenuated when the decoupling circuit was ON compared to when it was OFF. The effects of the 1-mm coatings on the coils were also tested the same way both in air and in a gel phantom. The results obtained in Chapter 3 (Section 3.4) for the transmit-receive coupled-coil system were used as a reference here.

#### **4.3.4 Samples**

Receive-only coil systems (both coated and uncoated) were first tested using a distilled water sample placed in a 10 mm-diameter thin-wall glass tube (Wilma Labglass, Buena, NJ) on the bench and in the magnet to assess their sensitivity. This water phantom was considered to represent the unloaded condition because of its small size compared to the SC and the non-conductive nature of the sample. The implantable coils (IC) were placed around this sample no more than a 1 cm away from the surface coil. To test their performances under loaded conditions

(similar to *in vivo* conditions) next, the implantable coated coils were placed in a phantom comprised of a viscous 6.7% (w/w) polysaccharide gel (TX-151; Oil Center Research, International LLC, Lafayette, LA), with the average dielectric characteristics of a mouse abdomen (146-148,161) as described in details in Section 3.3.4. Inductive coupling was accomplished by placing the phantom (with implantable coil) on top of the surface coil. Different types of phantoms were also created for localized spectroscopy testing. First, solutions of different concentration of choline were prepared (100 mM, 10 mM, and 1mM), placed in 10 mm-diameter thin-wall glass tubes (Wilmad Labglass, Buena, NJ), and used to perform <sup>1</sup>H spectroscopy and localized spectroscopy. Then, a 1 mM solution of choline was placed in a sealed 5-mm thin-wall glass tube at the center of a 10 mm-diameter thin-wall glass tube filled with glycerin to assess the performance of the localized spectroscopy method when using the two inductively-coupled implantable coil systems under investigation in this study under unloaded condition. Then, a 1 mM solution of choline was also placed in the middle of an ‘altered’ coil-construct assembly to test the method using the same systems under loaded conditions (see Section 4.3.5). *In vitro* (live cells in a construct) localized spectroscopy was attempted last.

#### **4.3.5 Cell Culture**

Murine insulinoma  $\beta$ TC-tet cells (48) were obtained from Shimon Efrat’s laboratory (Albert Einstein College of Medicine, Bronx, NY). They were cultured in T-flasks in monolayers and fed every 2-to-3 days with high glucose Dulbecco’s Modified Eagle’s Medium (DMEM, Invitrogen Corp., Carlsbad, CA), supplemented with 10% fetal bovine serum (FBS, Lonza, Williamsport, PA), 1% penicillin-streptomycin (Cellgro, Manassas, VA), and 1% L-glutamine (Cellgro, Manassas, VA) until they reached confluence. The cells were then collected from the flasks for construct fabrication using 0.01% Trypsin (Sigma, St. Louis, MO).

### 4.3.6 Construct Development

A 16-mm diameter biocompatible polyetheretherketone (PEEK) 300- $\mu$ m mesh (Small Parts, Inc., Miami Lakes, FL) was added on the top and bottom of the ring formed by the PDMS-coated coil to create the construct cavity (Figure 4-2) in both implanted coil types (receive-only and transmit-receive). For *in vitro* studies only, 2mm-diameter stainless steel spheres were attached with the mesh to one side of the PDMS ring to create a stand and help with the homogeneous diffusion of nutrients and oxygen through the construct. Three spheres were necessary for the implantable coil-construct assembly including the transmit-receive implantable coil. Four spheres were added to the assembly including the receive-only implantable coil to increase its stability as it was larger.

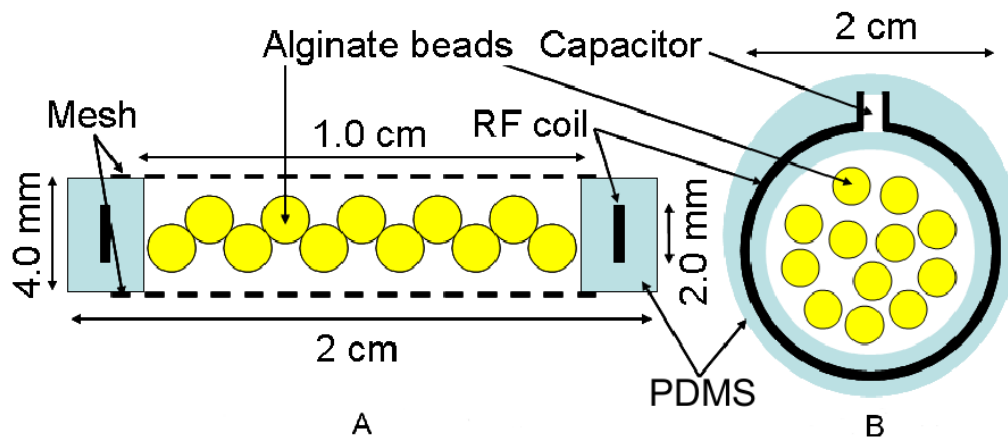


Figure 4-2. Implantable coil - bioartificial pancreas macroconstruct assembly schematic and dimensions for the transmit-receive implantable coil. A) Transverse view and B) coronal view of the assembly.

Some of these coil-construct assemblies were altered to receive choline solution instead of cell-containing beads by replacing the 2 meshes of the construct by 2 pieces of transparencies the choline to keep within the construct.

The empty coil-construct assemblies made to receive cell-containing beads (the ones with the meshes only) were then acid washed and rinsed to remove proteins left over during

manufacturing. They were afterwards autoclaved to become sterile and able to receive the alginate beads containing a known concentration of  $\beta$ TC-tet cells. The alginate beads were generated as described by Simpson et al. (151). A known number of freshly trypsinized cells was mixed with a 2% (w/v) sodium alginate solution using alginate with 62% / 38% mannuronic/guluronic content (Novomatrix, Trondheim, Norway) to set an initially cell density in the alginate solution of  $3.5 \times 10^7$  cells/ml of alginate. Aliquots of freshly made beads (~0.3 ml each) were transferred into the constructs using a syringe and a 16 G needle directly after manufacturing. The filled constructs were then placed in a 5-cm diameter deep Petri dish containing sterile phosphate buffer saline (PBS, Invitrogen, Carlsbad, CA) for the duration of the NMR imaging sessions to reduce the TCho NMR signal contamination by glucose NMR signal (see 4.3.7. for more details on glucose and choline NMR signal interferences). The PBS was containing antibiotics (100 U/ml penicillin and 100 ng/ml streptomycin) and 20 mM of the buffering agent HEPES (Mediatech, Inc., Manassas, VA) to keep the pH of the culture stable outside of the incubator. PBS was replaced by culture media as soon as the imaging session was done.

#### **4.3.7 NMR Measurements**

NMR measurements were performed on an 11.1 T 40 cm clear horizontal bore Magnex magnet equipped with a Bruker Avance console (Bruker Instruments, Billerica, MA). When the receive-only inductively-coupled coil systems were tested, an in-house custom built transmit-only birdcage volume coil provided the sample excitation (Figure 4-3).

Imaging and spectroscopy data acquisition and image processing were done using Bruker Paravision software. The spectroscopy data processing was done via a Bruker XWin-NMR software. The SNR was determined for each coil system using either a custom image-analysis

software written in IDL (ITT Visual Information Solutions, Boulder, CO) for images or the XWin-NMR software for spectra.

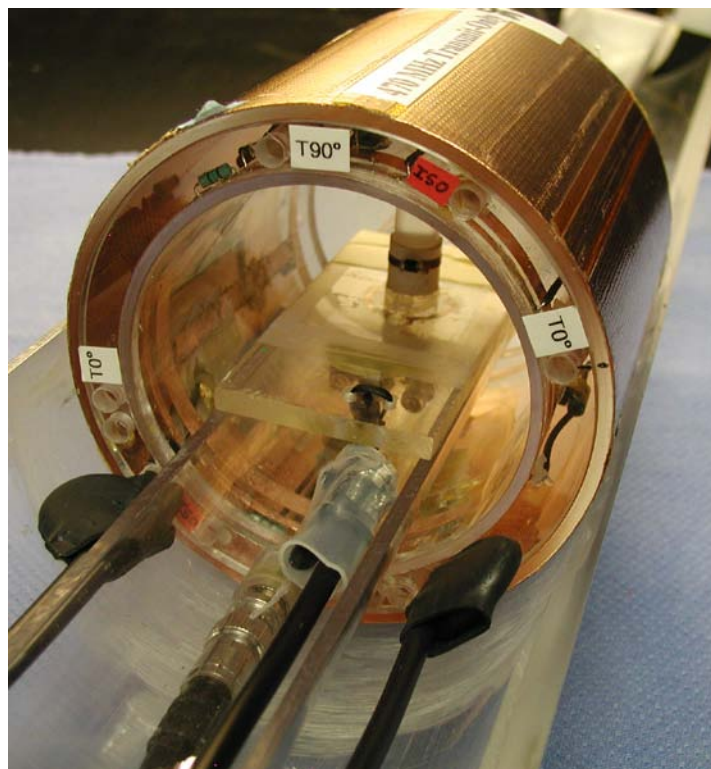


Figure 4-3. Photograph of the RF coil setup to acquire NMR images. This setup included a receive-only inductively-coupled coil system and a transmit-only birdcage volume coil. (Photo by N.A. Volland).

For coupled-coil system comparisons with phantoms (water and gel),  $^1\text{H}$  images were acquired using a spin-echo (SE) pulse sequence with a repetition time (TR) of 1000 ms, an echo time (TE) of 10 ms, 1-mm slice thickness, 1 average,  $6 \times 6 \text{ cm}^2$  field-of-view (FOV) and a  $256 \times 256$  matrix. PDMS signal was suppressed when required using a spectrally selective saturation pulse centered on the PDMS signal (5 ppm away from the water signal).

For the coupled-coil system comparisons for localized spectroscopy, both localized images and  $^1\text{H}$  spectra were acquired on a  $3 \times 3 \times 3 \text{ mm}^3$  voxel using a point resolved spectroscopy (PRESS) sequence (see Section 2.3.2.1). Different pulses were tested for excitation and refocusing to optimize the sequences used for localized imaging and spectroscopy and obtain

uniform signal intensity across the voxel: sinc3, sinc5, sinc7H, Mao and Mao\_4. All of these pulses were based on sinc functions. Their difference was the number of side lobes the sinc function included and the function that multiplied the sinc function to reduce the truncation effects on the pulse. Sinc3 and Sinc5 pulses were the product of a sinc function with 3 or 5 side lobes respectively and a Gaussian function with a 25% truncation level. They were both available in the localized imaging PRESS sequence. Sinc7H pulses were the product of a sinc function with 7 side lobes and a Hamming window (162), and available in the localized spectroscopy PRESS sequence. The Mao\_4 (imaging PRESS sequence) and Mao (spectroscopy PRESS sequence) pulses used an optimized sinc4 function for spin refocusing (163). The voxel imaging acquisition parameters were a sinc5 excitation and a Mao\_4 refocusing pulses, a TE of 10 ms, a TR of 1 s, and 1 average. The localized spectrum acquisition parameters were a sinc7H excitation and a Mao refocusing pulses, a TE of 10 ms, a TR of 2 s and 1 average. Adiabatic pulses were applied when localized spectroscopy was performed with the transmit-receive inductively-coupled implantable coil systems to alleviate the excitation magnetic field inhomogeneity (164).

<sup>1</sup>H spectra focusing on the TCho detection were also acquired to assess the sensitivity of the method on identifying this signal peak at 3.2 ppm to later determine the cell viability within the construct. To allow the detection of the Tcho signal, a chemical shift selective (CHESS) water suppression schema was used to suppress the water signal (84). It included 3 presaturation sinc3 pulses, one in each spatial direction. Up to 128 averages were used to detect the TCho signal. An outer-volume-suppression (OVS) scheme was also used when needed to suppress signal coming from outside the voxel and contaminating the NMR signal from the voxel (165). In the OVS schema used here, 3 repeats of a series of 6 presaturation sech pulses were performed

on slices outside the voxel and parallel to its surface. Furthermore, care was taken to avoid contamination of the TCho signal resonance at 3.2 ppm by the glucose signal with a resonance at 3.22 ppm. Rinsing and incubating the cell-containing constructs in PBS prior to and during all the NMR measurements was implemented in this matter.

#### **4.3.8 SNR Measurements and Statistical Analysis**

To assess the performances of the different coil systems/configurations tested in the magnet, their SNR was evaluated from the NMR images by choosing a signal region-of-interest (ROI) at the IC position and a noise ROI outside of the sample as described in details in Section 3.3.8. To assess the performances of the localized spectroscopy method, the SNR was evaluated from the NMR spectra by determining the ratio between the intensity of the TCho signal peak and the average noise intensity from the spectra baseline. The number,  $n$ , of independently-made coil systems tested to assess the reproducibility of the system construction is indicated for every experiment by  $(n)$ . At least two set of NMR data were acquired for each coil system to assess the reproducibility of signal detection and the sensitivity of the systems when possible. The averaged SNR determined for each similar system/configuration was then normalized to the SNR obtained with the TRX system which was used as the reference and normalized to 1. This normalization was appropriate because the TRX and RX system had the same size and shape. All the results are indicated as a mean  $\pm$  standard deviation (relative standard deviations are indicated in parentheses in percentage). A statistical analysis was performed using a two-sample unequal-variance t-test. The results of this analysis were considered statistically significant when p-values were less than 0.05.

## 4.4 Results

### 4.4.1 RF Coil System

Five different receive-only implantable coils, using three different layouts and two different diode types, were tested. The three basic layout, shown in Figure 4-4, consisted of 1) loop-gap resonator with one tuning capacitor and Schottky anti-parallel diodes; 2) loop-gap resonator with two tuning capacitors and either Schottky anti-parallel diodes or two PIN diodes placed in anti-parallel configuration, and 3) loop-gap resonator with four tuning capacitors and either Schottky anti-parallel diodes or two PIN diodes placed in anti-parallel configuration.

The coil characteristics were tested before and after the introduction of the decoupling circuit to quantify the changes due to the insertion. After the decoupling circuit addition, the coil resonant frequency was shifted and its Q decreased compared to the characteristics of the coil before the insertion. These changes were attributed to the diode characteristics. The equivalent series resistance of the Schottky anti-parallel diodes ( $n = 6$ ) was evaluated above  $1 \Omega$ , their parallel resistance approximately  $3 \text{ k}\Omega$ , and their parallel capacitance, at  $4.26 \pm 0.19 \text{ pF}$  ( $\pm 4.54\%$ ), whereas the coil capacitance varied between 4 and 5 pF when the implantable coil had only one tuning capacitor (Figure 4-4A). When the decoupling circuit was introduced in parallel to the tuning capacitor of the transmit-receive implantable coil (IC\_RX\_1M; Figure 4-4A), its resonant frequency of the coil shifted by over  $-125 \text{ MHz}$ . Furthermore, the diode parallel resistance was low enough to lower the Q of the coil over threefold compared to the transmit-receive implantable coil. Because of the drastic changes the decoupling circuit introduced in the implantable coil circuit, this layout was quickly abandoned and other designs had to be investigated.

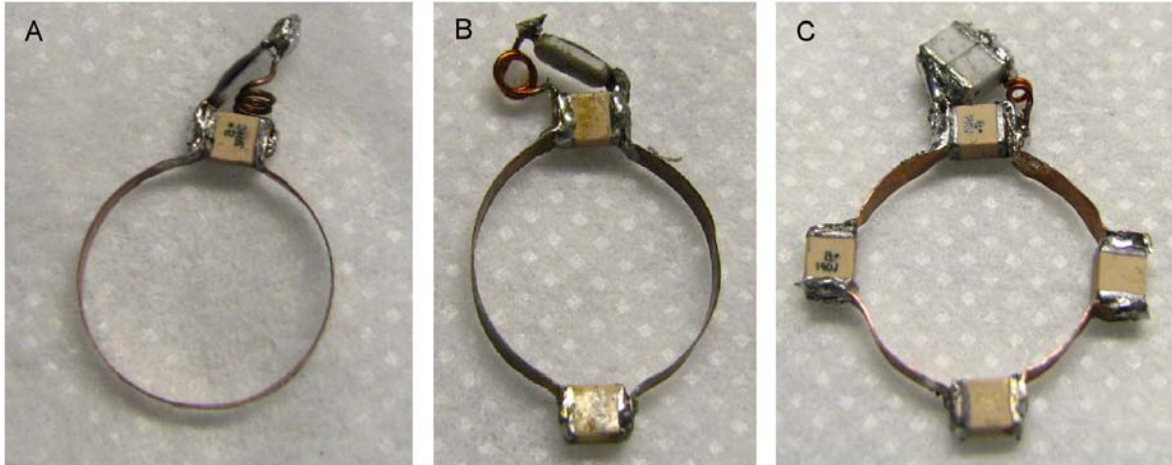


Figure 4-4. Photographs of the different receive-only implantable coil layouts built and tested. A) Loop-gap resonator with one tuning capacitor and a decoupling circuit including a hand wound inductor and Schottky anti-parallel diodes; B) loop-gap resonator with two tuning capacitors and a decoupling circuit including a hand wound inductor and Schottky anti-parallel diodes; C) loop-gap resonator with four tuning capacitors and a decoupling circuit including a hand wound inductor and two PIN diodes. (Photo by N.A. Volland).

The first improvement attempted was to double the number of tuning capacitors in the coil to increase their intrinsic value (IC\_RX\_2M, Figure 4-4B) and decrease the diode capacitance influence on the coil characteristics. When the receive-only implantable coil comprised two capacitors instead of one, the frequency shift became only -49 MHz, and the Q decreased by only a factor of 2. The number of tuning capacitors in the coil was further increased to 4, the maximum number the coil could practically comprise. Different limiter and PIN diodes with lower junction capacitance were also investigated. The PIN diodes ( $n = 4$ ) were selected for their non-magnetic properties, their parallel capacitance at  $1.55 \pm 0.07$  pF ( $\pm 4.56\%$ ), their equivalent series resistance below  $1 \Omega$ , and their parallel resistance approximate  $25 \text{ k}\Omega$ . Three more configurations were then characterized: 1) a receive-only implantable coil with 4 capacitors and Schottky anti-parallel diodes (IC\_RX\_4M); 3) a receive-only implantable coil with 2

capacitors and 2 PIN diodes (IC\_RX\_2C); and 3) a receive-only implantable coil system with 4 capacitors and 2 PIN diodes (IC\_RX\_4C, Figure 4-4C).

The receive-only implantable coil with 4 capacitors saw its resonant frequency shifted by -22 MHz, when the decoupling circuit comprising the Schottky anti-parallel diodes was added onto it. Its Q was also lowered by 1.5 compared to same coil without the decoupling circuit. The receive-only implantable coil with 2 capacitors saw its resonant frequency shifted by -25.5 MHz, when the decoupling circuit comprising 2 PIN diodes was added onto it. Its Q was also lowered by 1.9 compared to same coil without the decoupling circuit. The receive-only implantable coil with 4 capacitors saw its resonant frequency shifted by -6 MHz, when the decoupling circuit comprising 2 PIN diodes was added onto it. Its Q was also lowered by 1.13 compared to same coil without the decoupling circuit. These results are summarized in Table 4-1. Even though the Q were determined at different frequencies, the results still indicate an increase in resistive losses as the differences in Q between coils were always larger than their frequency shifts.

Table 4-1. Implantable coil characteristic changes after the addition of a decoupling circuit onto the coil.  $\Delta f$  represents the coil resonant frequency shift and  $\Delta Q$  the Q ratio between the implantable coil without the decoupling circuit and the same coil after the addition of the decoupling circuit. # of caps indicates the number of capacitors in the coil and # of coils tested the total number of coil tested.

Coil #	# of coils tested	# of caps	Diode type	$\Delta f$ (MHz)	$\Delta Q$
IC_RX_1M	2	1	Schottky	$-127.18 \pm 7.18$ ( $\pm 5.64$ %)	$5.46 \pm 3.61$ ( $\pm 66.11$ %)
IC_RX_2M	4	2	Schottky	$-49.14 \pm 4.38$ ( $\pm 8.92$ %)	$1.95 \pm 0.13$ ( $\pm 6.69$ %)
IC_RX_4M	2	2	Schottky	$-25.48 \pm 0.74$ ( $\pm 2.91$ %)	$1.48 \pm 0.22$ ( $\pm 14.88$ %)
IC_RX_2C	2	4	PIN	$-22.20 \pm 1.27$ ( $\pm 5.73$ %)	$1.90 \pm 0.08$ ( $\pm 4.27$ %)
IC_RX_4C	2	4	PIN	$-6.89 \pm 4.11$ ( $\pm 59.67$ %)	$1.13 \pm 0.07$ ( $\pm 6.41$ %)

When the transmit-receive surface coil received the decoupling circuit in parallel of its fixed tuning capacitor, the same behavior as that observed on the implantable coil happened. The capacitance of the diodes was large enough compared to the coil capacitors to fundamentally influence the coil resonant frequency (over -100 MHz shift), and lower its Q (approximately by 5). Consequently, the receive-only surface coil was also quickly designed with 2 fixed tuning capacitors instead of one (Figure 4-5A). The frequency shift of the resonant frequency of the coil was then below -30 MHz, and its Q decreased by approximately a factor 1.8. When the receive-only surface coil was designed with 3 fixed tuning capacitors and 2 PIN diodes (Figure 4-5B) to match the best implantable coil design, the resonant frequency shifted was only -3 MHz, and its Q was only lowered by a factor 1.15 compared to the same coil without the decoupling circuit.

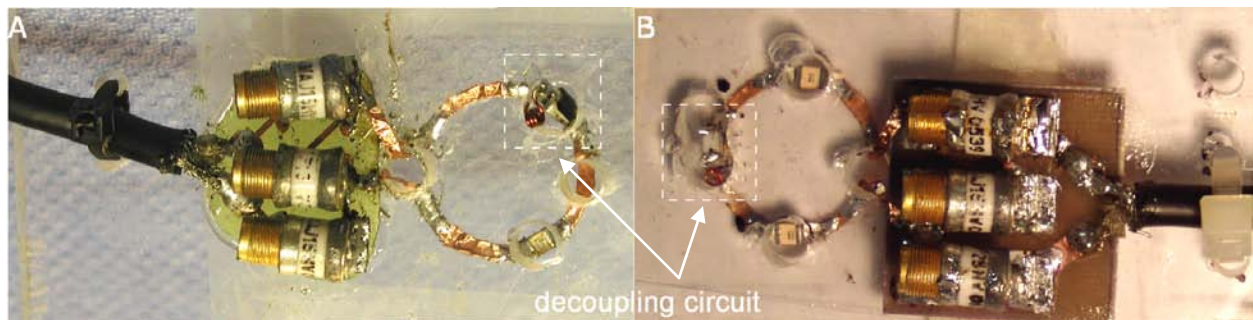


Figure 4-5. Photographs of the receive-only surface coils tested. A) Two fixed tuning capacitors and a decoupling circuit including a hand wound inductor and Schottky anti-parallel diodes; and B) 3 fixed tuning capacitors and a decoupling circuit including a hand wound inductor and two PIN diodes. (Photo by N.A. Volland).

As the receive-only inductively-coupled systems with the lowest number of capacitors (one fixed tuning capacitor on each coil) had poor characteristics, they were not considered for magnet testing. Two of the four remaining receive-only inductively-coupled systems constructed were selected to be tested in the magnet. The first system selected was the system with 2 fixed tuning capacitors, and Schottky anti-parallel diodes on each coil. This system had the lowest

characteristics of the four remaining receive-only systems and was chosen to show how the least favorable coil system characteristics influence the NMR method sensitivity. The second system was the system with 4 fixed tuning capacitors and 2 PIN anti-parallel diodes on the implantable coil, and 3 fixed tuning capacitors and 2 PIN anti-parallel diodes on the surface coil. This system had the most favorable characteristics of every system built. The coupled-coil system with the Schottky diode (n = 3) has a Q of  $35.13 \pm 4.22$  ( $\pm 12.01\%$ ), whereas the coupled-coil system with the PIN diodes (n = 1) has a Q of 37.4, when both systems resonate at 470.75 MHz using a 1-cm diameter tube water sample. These results are summarized in Table 4-2.

Table 4-2. Receive-only inductively-coupled implantable coil system characteristics. Resonant frequency (f) and quality factor (Q) for the coupled-coil system including the IC with 2 capacitors and a Schottky diode (RX\_M) and the system including the IC with 4 capacitors and 2 PIN diode (RX\_C).

Coil #	# of coils tested	f (MHz)	Q
RX_M	3	470.75	$35.13 \pm 4.22$ ( $\pm 12.01\%$ )
RX_C	1	470.75	37.4

However, a technical problem occurred that prevented the testing of the inductively-coupled coil system comprising PIN diodes in the magnet. The RF power supply available to run through the surface coil of the receive-only inductively-coupled implantable coil system and turn the diodes ON at the time of the experiment was not powerful enough. This rendered the tuning of the transmit-only volume coil prior to magnet testing and the magnet testing of the receive-only inductively-coupled coil system with the PIN diodes compromised. A DC power supply could have been considered as it was to test the coils on the bench. However, it would require the addition of connections onto both coils of the systems. This was not applicable to the implantable coil, as it would not be accessible when used coated *in vitro* and *in vivo*. It would have been possible for the surface coil. However, leaving the system settings undisturbed while

connecting and disconnecting the DC supply was another concern since even small displacement can greatly affect the loading and tuning of the systems. The tuning and matching of the systems directly in the magnet may have to be investigated in the future along with the use of other diodes with similar favorable characteristics, but a lower activation power requirement to allow the use of these systems in the magnet and improve their characteristics.

The adequate decoupling performances were also assessed by verifying that there was at least a 20dB difference between the power the coils could transmit to the external probe when the decoupling circuit was ON compared to when it was OFF. The implantable coils ( $n = 5$ ) showed a difference of  $24.03 \pm 0.39$  ( $\pm 1.64\%$ ) dB, while the surface coil showed a difference of 21.8 ( $n = 1$ ). Only the coils including the Schottky diodes were tested for reasons given in the previous paragraph.

#### **4.4.2 Implantable Coil Coating**

The hand-wound decoupling-circuit solenoids were found not to be influenced by the PDMS coating. Their deformation during this process was found to be minimal and their characteristics did not change at all. Only one type of implantable coils was coated (the one with 2 fixed capacitors and Schottky diodes) as it was the only functional type. The coating of these receive-only implantable coils was easily adapted from the transmit-receive implantable coil coating technique and successfully achieved (Figure 4-6). The coating thickness on the receive-only implantable coil ended up at 1.25 mm instead of the 1-mm thickness of the transmit-receive implantable coil. This was necessary to achieve a perfectly sealed coating all around the coil including every component.

The frequency shift observed for the transmit-receive implantable coils was also observed for the receive-only coil along with a change in Q. A resonant frequency shift of  $-5.83 \pm 1.62$  ( $\pm$

27.80%) MHz was detected for the coated implantable coils compared to the non-coated similar coil (n = 4). The quality factor of these coils was not significantly different from the uncoated coils (within 5% of the non-coated Q). As this resonant frequency shift did not create any problems to tune the inductively-coupled coil system (surface and implantable coils coupled together) at 470.75 MHz, these implantable coils were tested in the magnet.



Figure 4-6. Photograph of a receive-only PDMS-coated implantable coil. (Photo by N.A. Volland).

As loading further changes the coil characteristics, the PDMS-coated coil were embedded in the mouse abdomen-like phantom. This loading caused an additional resonant frequency shift from the PDMS coating one of  $-16.43 \pm 1.50$  ( $\pm 9.10\%$ ) MHz, making it impossible to tune the whole system to the desired frequency of 470.75 MHz (n = 3; one coil had an open coating and was remove for the study). This shift in addition to the ‘coating’ and the decoupling frequency shift were taken into account to build the implantable loop-gap resonator coils which were used for phantom and *in vitro* studies. However, one more consideration needed to be taken in account here. As the capacitor values were decreased to increase the resonant frequency of the implantable coil prior to its coating, the resonant frequency shift due to the decoupling circuit

addition became larger and larger. The implantable coils to be used loaded were then created with a resonant frequency over 30 MHz higher than their predecessors ( $590.42 \pm 5.54$  ( $\pm 0.94\%$ ) MHz) to compensate for this extra shift. The implantable coils resonated at  $499.08 \pm 3.42$  ( $\pm 0.69\%$ ) MHz when coated and embedded  $0.74 \pm 0.08$  ( $\pm 11.08\%$ ) cm deep in the phantoms ( $n = 4$ ). The quality factor of the loaded implantable coils was affected by the loading and decreased by almost a factor 4 ( $15.43 \pm 2.42$  ( $\pm 15.68\%$ )) when embedded 0.74 cm in the phantom. Because the diode had such an influence of the tuning and matching of the system, the inductively-coupled coil systems could not resonate at the desired frequency of 470.75 MHz after adding the decoupling circuit, coating the implantable coil, and loading it into the gel phantom. The surface coil had to be altered to allow the system to resonate at 470.75 MHz. One fixed tuning capacitance of the surface coil had to be lowered to make the inductively-coupled coil systems resonate at the desired frequency of 470.75 MHz. The Q of the inductively-coupled implantable coil system was dropped down to  $9.68 \pm 0.78$  ( $\pm 8.07\%$ ) when the PDMS-coated implantable coil was embedded 0.74 cm deep in the gel phantom.

Once the receive-only inductively-coupled implantable coil systems were fully characterized, their characteristics could be compared to the transmit-receive inductively-coupled implantable coil system ones (Table 4-3). If the quality factor of the two sets of implantable and surface coils and the inductively-coupled systems differ significantly when unloaded, the difference fades away when they are loaded.

Prior to any *in vitro* studies, the receive-only coated implantable coils had to be acid wash and autoclave. These cleaning and sterilization procedure did not alter the coils, which were then ready to receive cell-containing alginate beads.

Table 4-3. Comparison of coil characteristics between transmit-receive and receive-only coils and coupled-coil systems. Resonant frequency (f) and quality factor (Q) for both the transmit-receive and receive-only implantable coil (IC), surface coil (SC), and inductively-coupled implantable coil system (system).

n	Transmit-receive system		Coil and system type	Receive-only system		n
	f (MHz)	Q		f (MHz)	Q	
7	491.81 ± 3.38 (±0.69%)	203.9 ± 6.20 (±3.04%)	IC	495.88 ± 3.45 (±0.70%)	81.03 ± 12.19 15.04%	4
4	494.36 ± 2.34 (± 0.47%)	214.5 ± 20.95 (±9.77%)	IC_C*	490.12 ± 3.55 (±0.72%)	83.49 ± 18.40 (±22.04%)	3
2	493.5	72.2 ± 4.95 (±6.86%)	SC	493.5	40.35 ± 2.05 (±5.08%)	1
4	492.93 ± 3.44 (±0.70%)	15.41 ± 0.79 (±5.12%)	IC_L#	499.08 ± 3.42 (±0.69%)	15.43 ± 2.42 (±15.68%)	4
2	493.5	15.20 ± 0.42 (±2.79%)	SC_L#	493.5	12.05 ± 0.35 (±2.93%)	1
7	470.75	96.21 ± 3.70 (±3.85%)	System	470.75	35.13 ± 4.22 (±12.01%)	4
4	470.75	104.82 ± 3.22 (±3.07%)	System_C*	470.75	30.74 ± 3.31 (±10.76%)	3
4	470.75	9.39 ± 0.32 (±3.75%)	System_L#	470.75	9.68 ± 0.78 (±8.07%)	4

\* C indicates that the implantable coils were coated when tested individually and inductively-coupled with the surface coil

# L indicates that the implantable coil was coated and embedded in a gel phantom when tested individually and inductively-coupled with the surface coil.

#### 4.4.3 Phantom Studies

Two different coil-systems/layouts were tested and compared in this study: 1) inductively-coupled coil system (or TRX system) for both excitation and detection; 2) a receive-only inductively-coupled coil system (RX system) with 2 fixed tuning capacitors and Schottky anti-parallel diodes on each coil and a birdcage volume coil for excitation. Figure 4-7 illustrates differences in SNR for these two different types of coils when studied under unloaded conditions (water sample) at 11.1 T. These systems were also tested with their implantable loop-gap resonators coated with a PDMS layer. Their SNR results were compared to each other using the SNR obtained with the TRX system. The SNR determined from the images of the water sample (equivalent to unloaded conditions) acquired with the receive-only inductively-coupled

implantable coil systems was never more than 25% below the one when the images were acquired with the inductively-coupled implantable coil system. The RX system shows a 23% SNR decrease compared to that of the TRX system [ $0.77 \pm 0.18$  ( $\pm 23.52\%$ ),  $p \ll 0.001$ ] when the IC was placed approximately 1 cm away from the SC [ $0.87 \pm 0.08$  ( $\pm 9.66\%$ ) cm]. However, the PDMS coating of the implantable coil makes the SNR of the RX system higher than the SNR of the TRX system with a PDMS coated implantable coil by approximately 10% [ $0.97 \pm 0.22$  ( $\pm 22.51\%$ ),  $p \ll 0.001$ ]. The PDMS suppression scheme used to acquire the images did not significantly alter these previous result [ $0.94 \pm 0.20$  ( $\pm 21.82\%$ )].

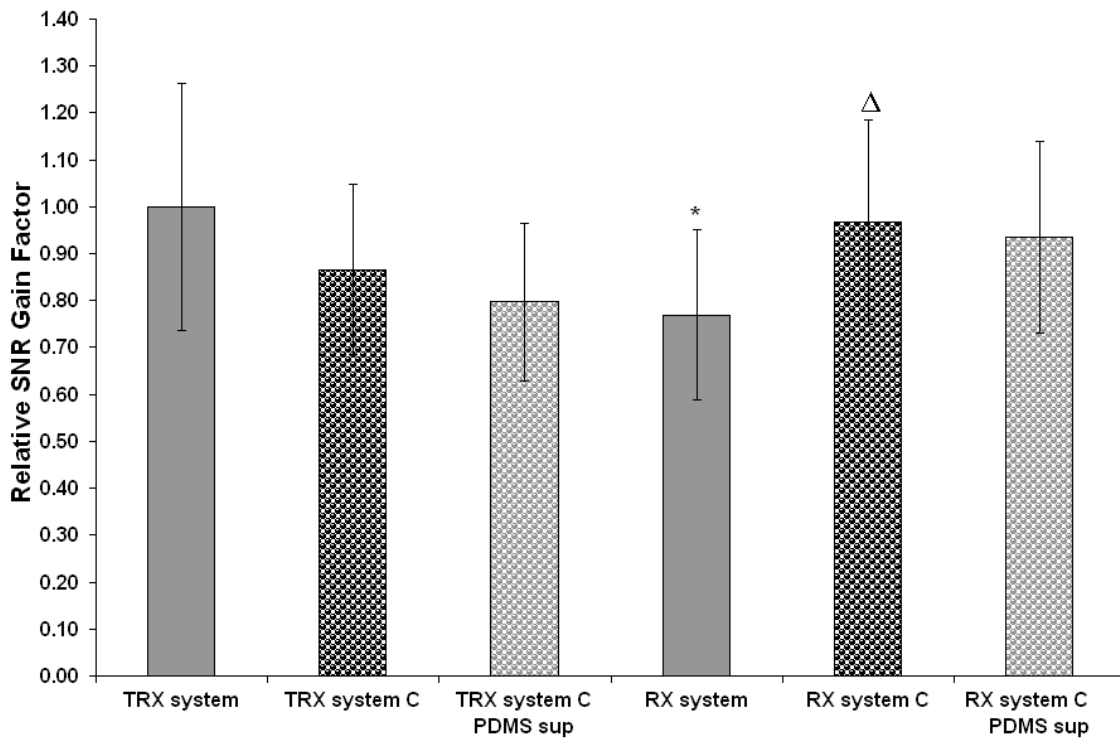


Figure 4-7. SNR comparison between transmit-receive and receive-only inductively-coupled implantable coil systems under unloaded conditions using a water sample. TRX system represents the transmit-receive coupled-coil system and RX system the receive-only coupled-coil system where the IC was placed 1 cm away from the SC. C indicates that the IC was PDMS-coated. PDMSsup indicates that PDMS suppression was used during the NMR data acquisition. \* denotes the statistically difference between the SNR of the transmit-receive coupled-coil and the receive-only systems;  $\Delta$  the difference between the SNR of the receive-only coupled-coil system with an IC, coated or not.

The effect of loading on the measured SNR for both coil systems was also investigated. Figure 4-8 depicts the SNR obtained at the IC (macroconstruct) location under loaded coil system conditions (0.74 cm) using either the RX system or the TRX system with both a PDMS-coated loop-gap IC, with and without PDMS suppression scheme. These measurements were also compared to the SNR obtained with a loaded TRX system. The RX system did actually perform better than the TRX system under loading condition. It consistently displayed a SNR 13% higher than the TRX IC system [ $1.13 \pm 0.19$  ( $\pm 16.71\%$ ),  $p \ll 0.001$ ]. Using a PDMS suppression scheme when acquiring the NMR images with coated coils did not significantly affect this SNR [ $1.10 \pm 0.19$  ( $\pm 16.96\%$ )].

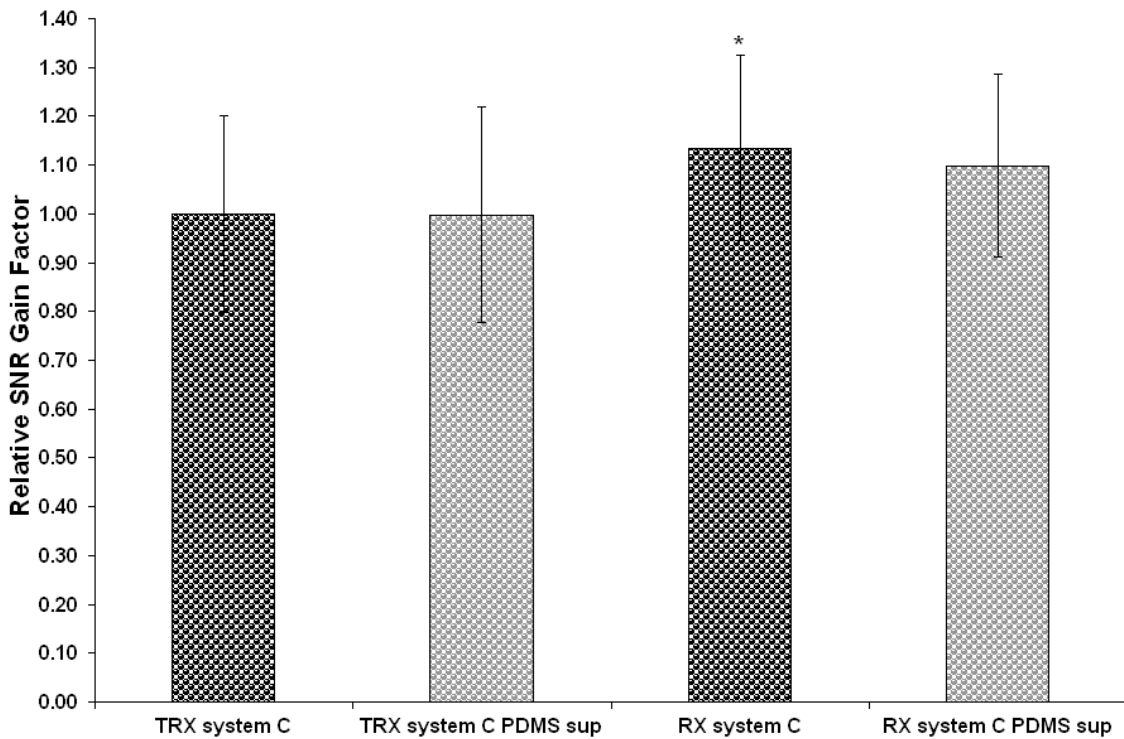


Figure 4-8. SNR comparison between transmit-receive and receive-only inductively-coupled implantable coil systems under loaded conditions using a gel phantom. TRX system represents the transmit-receive coupled-coil system and RX system the receive-only coupled-coil system where the IC was placed 1 cm away from the SC. C indicates that the IC was PDMS-coated. PDMSsup indicates that PDMS suppression was used during the NMR data acquisition. \* denotes the statistically difference between the SNR of the transmit-receive coupled-coil and the receive-only systems.

Furthermore, the magnetic field distribution generated by volume coil made the RX system much more suitable for localized spectroscopy as it is more uniform than the magnetic field distribution generated by the TRX system. Figure 4-9 shows the response profile obtained with the transmit-receive (TRX) and the receive-only inductively-coupled (RX) systems. The profile differences are clearly displayed. The response profile obtained when using the RX system was much more homogeneous across the construct (within the implantable coil) in any direction compared to the response profile from the TRX system.

#### 4.4.4 NMR Spectroscopy Studies

$^1\text{H}$  spectra were acquired without using any volume selective methods on all the solutions with different concentrations (100 mM, 10 mM, and 1 mM). The 3.2 ppm choline resonance was easily identified on the 100 mM solution spectra since it was even observable when no water suppression scheme was used. However, water suppression was necessary to observe the choline resonance at 3.2 ppm for the less concentrated solutions.

Since physiological concentration of choline is closer to 1 mM,  $^1\text{H}$  localized spectroscopy was then performed on a 1 mM choline/glycerin sample (unloaded conditions) using a PRESS pulse sequence on a  $3 \times 3 \times 3 \text{ mm}^3$  cubic voxel entirely confined within the construct. Either coupled-coil systems, transmit-receive and receive-only, were used. Images of the voxel of interest were acquired first to demonstrate the feasibility of the volume selection and the localization of signal within the construct (Figure 4-10). Volume selection was achieved with both RF systems since only signal from within the choline sample can be detected on Figure 4-10B and Figure 4-10E.

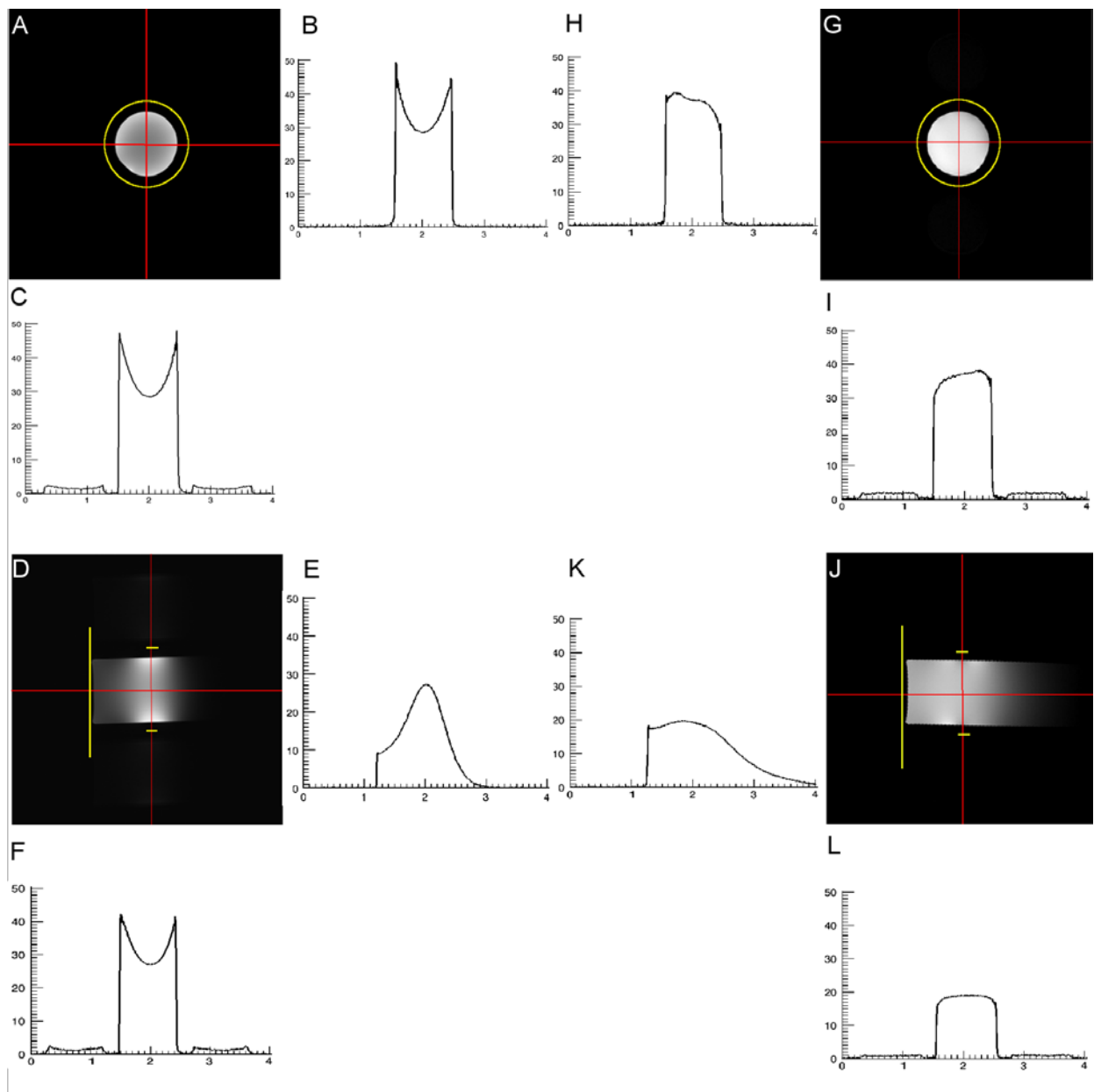


Figure 4-9. Signal profiles obtained from NMR images acquired with TRX and RX inductively-coupled systems. A TRX system was used to acquire image A and D, while a RX system was used to acquire image G and J. Coronal images of a water sample are presented in A and G, while transversal images are presented in D and J. Signal profiles from the readout direction of images A, D, G, and G are presented in B, E, H, and K respectively. Signal profiles from the phase encode direction of images A, D, G, and G are presented in C, F, I, and L. The yellow circles and lines represent the coils of the different systems used to acquire the images. The circle in A and G represent the IC, as well as the two short horizontal lines in D and J. The long vertical line in D and J shows the position of the SC below the sample.

Optimization of the method was explored to obtain the cubic voxel originally selected with the desired size and a more uniform signal intensity across this voxel. The Sinc5 pulses for excitation and the Mao\_4 pulses for refocusing were found to be the most appropriate pulses available to use in the PRESS imaging sequence. Signal could be detected from outside the voxel. While an OVS scheme could have helped suppress these undesired signals, the OVS was not available when the volume selective imaging sequence was used to locate the voxel of interest.

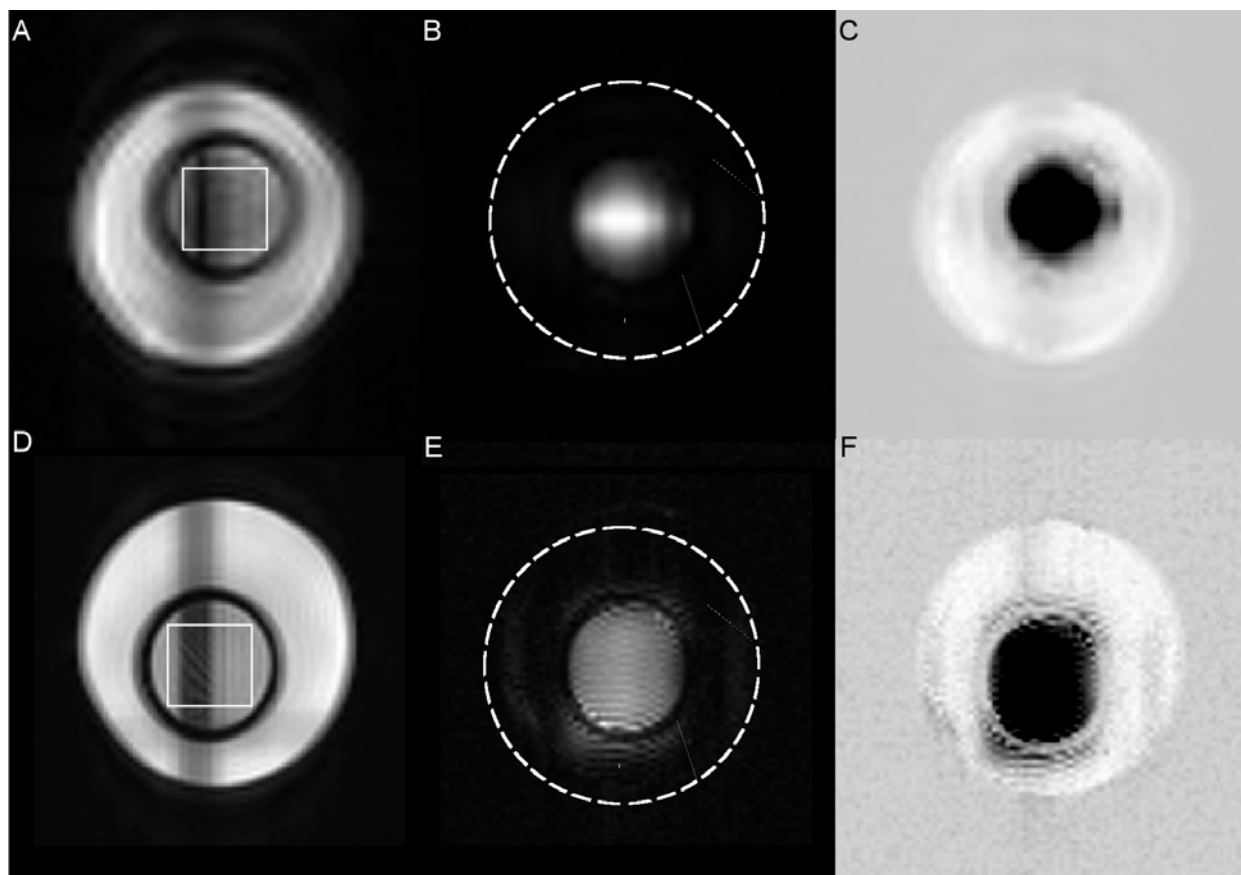


Figure 4-10. Volume selective imaging acquisition in preparation for  $^1\text{H}$  localized spectroscopy. A transmit-receive inductively-coupled implantable coil system was used in A through C. A receive-only inductively-coupled implantable coil system was used in D through F. A & D represent scout coronal image of a glycerin vial including 1-mM choline sample at its center. B & E represent the voxel volume selective image. C & F represent the subtraction of images B & E from images A & D respectively. The white square on A & D represents the voxel selected. The white dashed circle in B & E represents the outer edge of the glycerin vial.

$^1\text{H}$  spectra were acquired next and choline signal was detectable from the 1mM choline solution with a SNR of 12.5 after the water signal was suppressed from the spectrum (Figure 4-11C). OVS schema was used to decrease the glycerin signal detected from outside the voxel, although the signal could not be completely removed. Better shimming procedure and pulses selection should alleviate this issue later on (see Section 4.5). Choline was also detected from a 1 mM choline solution within an altered coil-construct assembly soaked in PBS (loaded condition, Figure 4-11E) with a SNR of 16.41.

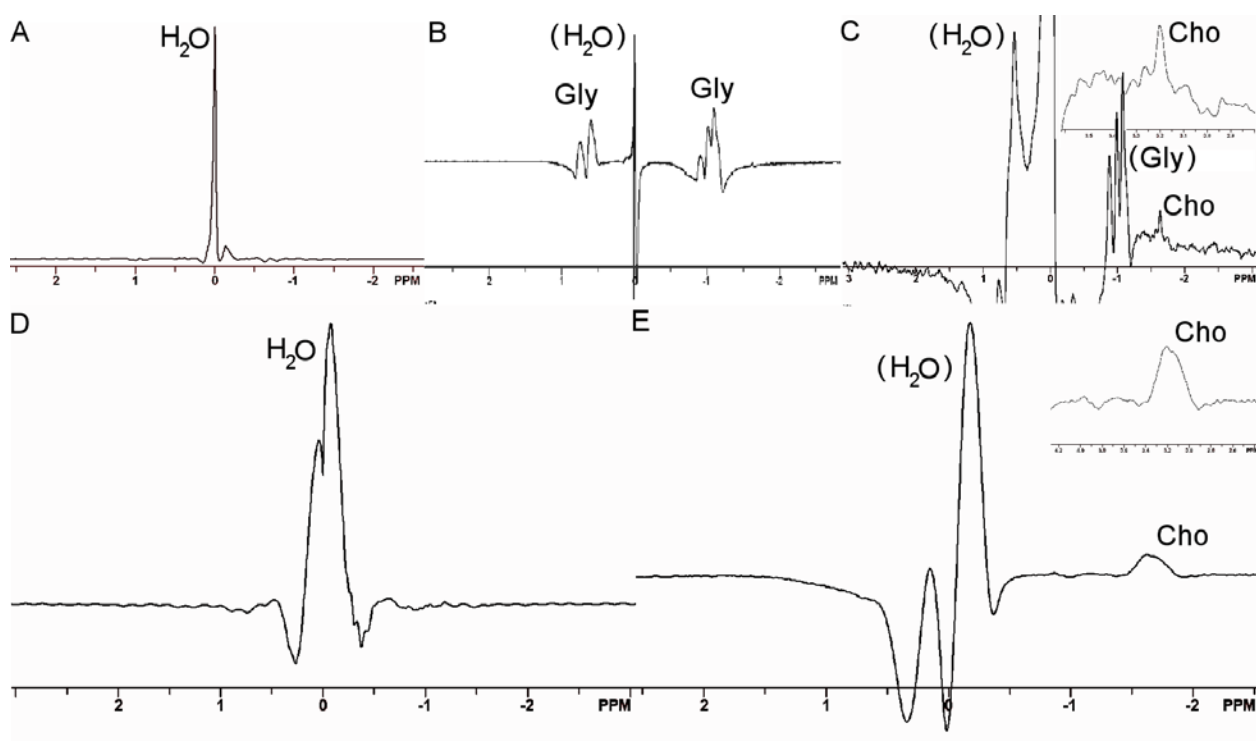


Figure 4-11.  $^1\text{H}$  localized spectroscopy data acquired using a transmit-receive inductively-coupled implantable coil system. A 1mM choline [Cho] sample surrounded by a glycerin [Gly] solution in a 1 cm NMR tube was used in A through C and in an IC-construct assembly soaked in PBS in D and E. A & D represent spectra acquired without water suppression or outer volume suppression. B & E represent spectra acquired with water suppression [(H<sub>2</sub>O)] but without outer volume suppression [Gly]. C represents a spectrum acquired with both water suppression [(H<sub>2</sub>O)] and outer volume suppression [(Gly)]. The data were acquired using a PRESS sequence with a 1ms sinc7H excitation pulse and a 1ms Mao refocusing pulse, TE = 10 ms, TR = 2 s and 128 average. Adiabatic pulses were used.

No line broadening was applied during the processing of these data. Even though the volume selective method was not fully optimized, these spectra show the potential of the use of inductively-coupled coil systems with NMR methods and the feasibility of the NMR spectroscopy methods. No spectrum was acquired using the receive-only inductively-coupled implantable coil system on the choline-glycerin sample or the choline sample loaded in the phantom gel.

Cells were successfully encapsulated in alginate beads and inserted in the implantable coil-construct cavity of both types of coil.  $^1\text{H}$  localized spectroscopy was attempted with the transmit-receive implantable coupled-coil system. The parameters used with the 1mM choline solution were utilized in this experiment as well. Choline was never detected. However, the viability of the cells was questionable. The number of cells in the sample may have been too low and will need to be increased in future experiments, at least initially to optimize the method and determine its limit of sensitivity.

#### **4.5 Discussion**

NMR spectroscopy (MRS) is a powerful technique to obtain metabolically and physiologically relevant compound information from a sample. Detecting the total choline signal from within the bioartificial pancreatic substitute using localized spectroscopy would allow a direct assessment of the cell viability in the construct (5,6). However, the proper localization of the spectroscopic data is often crucial for the accurate determination of the studied compound characteristics at a microscopic level (choline concentration) and for its link to an important macroscopic state (cell viability). To facilitate MRS data acquisition within a bioartificial construct and enhance the method volume selectivity, the use of a receive-only inductively-coupled implantable coil system for MRS was explored. This coupled-coil system has substantive advantages over a transmit-receive inductively-coupled implantable coil system

for the study of tissue-engineered constructs because of the more uniform NMR excitation produce by a volume coil: 1) the measured NMR signal is more homogeneous throughout the construct (Figure 4-9), 2) the volume selectivity of the MRS techniques is enhanced and easier to implement, and 3) the power requirements are not so demanding since the use of adiabatic pulses is not required.

A homogenous excitation in MRS is key to obtaining accurate information from an implanted construct. The receive-only inductively-coupled implantable coil system showed a more homogeneous response NMR signal than the transmit-receive inductively-coupled implantable coil system indicating a better  $B_1$  excitation field distribution. Initially, the sensitivity (SNR) of the two systems gave advantage to the transmit-receive inductively-coupled system under unloaded condition (Figure 4-7). This could be explained by the drop in Q of the receive-only system compared the transmit-receive system by a factor of 2.75 (from  $96.21 \pm 3.70$  ( $\pm 3.85\%$ ) to  $35.13 \pm 4.22$  ( $\pm 12.01\%$ )). The addition of more components in the receive-only circuit of both coils, particularly the low Q diode, is the reason of the lower Q of the receive-only coupled-coil system. However, the SNR only dropped by a factor 1.30 ( $\pm 0.31$  ( $\pm 23.52\%$ )), which may be attributed to the higher average NMR signal when a receive-only coil system is used compared to when a transmit-receive coil system is used because of the higher homogeneity of the signal throughout the sample. To alleviate the frequency shift and the Q and SNR decrease, diodes with smaller parallel capacitances, higher Q, and low power activation requirement could be used. The diodes found commercially thus far with such favorable characteristics were magnetic, such as the SM1330 limiter diodes (Skyworks, Woburn, MA). However, under loaded conditions the SNR difference between the two systems is minimal, down to 13% and inverted, the receive-only system performed better than the transmit-receive

system (Figure 4-8). This can be explained by the fact that the loading effects are large on both coil systems especially at the high frequency they performed at (470.75 MHz), that their Q are very similar, and that the average signal obtained using the receive-only system is higher than that obtained with the transmit-receive system. In addition to the higher detected signal homogeneity when the receive-only inductively-coupled implantable coil system was used, these results are encouraging and showed the potential of the use of such receive-only coupled coil systems to monitor a bioartificial pancreas non-invasively using NMR imaging and spectroscopy methods.

Noise was added into the image when the receive-only inductively-coupled coil system was used. This noise was signal detectable from the sample outside of the construct due to the volume excitation even outside of the construct. This was never seen when a transmit-receive inductively-coupled implantable coil system was used (more obvious in the coronal plan, construct cross-section) as the NMR excitation was mainly localized inside the construct. However, this was not an issue and as this noise was located far from the region of interest within the construct. The fact that the receive-only inductively-coupled implantable coil system with the PDMS-coated implantable coil tested under unloaded condition gives an SNR higher than its uncoated counterpart and the transmit-receive inductively-coupled implantable coil system with a PDMS-coated implantable coil has no founded explanation. It is not even consistent with the Q difference between all these systems as this difference is largely unfavorable to the receive-only inductively-coupled implantable coil system with the PDMS-coated implantable coil.

The PDMS coating procedure for the implantable coil was easy even with the additional components included in the coil to coat. The coating acted similarly on the receive-only coil as it

did on the transmit-receive implantable coil. The coating thickness was increased to 1.25 mm to optimize the coating of all the component of the receive-only implantable coil without compromising the construct space and the system detection sensitivity when loaded. The outer space taken by the coil increased due to the additional components (use of a larger hollow punch). The frequency shift introduced by this coating along with the one introduced by the decoupling circuit was taken into account when building these coils. The implantable coil was made to resonate as closely as possible to 590 MHz to allow the receive-only inductively-coupled system to tune and match at 470.75 MHz when the implantable coil was coated with PDMS and embedded with the gel phantom or used *in vitro*. If the resonant frequency shift and Q change of the receive-only implantable coil when coated and loaded were not as pronounced as when a transmit-receive implantable coil was coated and loaded, it was changing with the coil capacitor's values. The frequency shift due to the decoupling circuit addition, the coating, and subsequently the loading, was getting larger and larger as the capacitor's values were decreasing to increase the coil initial resonant frequency to try to compensate for the shifts due to the coating and loading. Similarly, the Q also decreased further and further with the decoupling circuit addition, the coating, and the loading, as the capacitor's values were decreased to make the coil resonate at a higher and higher frequency to compensate for all the shifts. Consequently, the larger capacitor values used for the receive-only implantable coil construction compared to the ones used for transmit-receive one may make the effects of coating and loading on the coil less influential. Nonetheless, the decoupling circuit addition created a lot more discrepancy (larger deviation of the results) in the coating and loading results than that found for a transmit-receive coil. Also, at least one receive-only implantable coil stopped working properly after every set of tests showing how fragile these coils have become due to their larger size and

increased number of components. Even a careful handling could not insure coil integrity for an extended period of time. The larger the coil surface is, the more likely the coil is subject to deform and its functioning to be impaired. This could be a problem with possible deformation of the implantable coil-construct assembly at the time of surgical implantation and also over time when floating in the peritoneal cavity of a recipient. This issue will have to be investigated more in depth when *in vivo* experience will be preformed. However, this observation brought the issue of the implantable-coil construct assembly size limitation for the animal model (mouse) used in this study with the use of a slightly larger implantable coil of. Even with the most careful construction, the smallest receive-only implantable coil with the characteristics presented here cannot fit in a mouse peritoneal cavity anymore. Moving to a bigger animal model such as rat is one possibility. Using miniaturized integrated circuits is another possibility. If not explored here, there are certainly to be investigated in the future to make the coils more stable, their construction more consistent, and their use possible *in vivo*.

Localized spectroscopy was also performed using both inductively-coupled coil systems to assess the superior ability of the receive-only inductively-coupled coil system in performing localized spectroscopy. Choline signal was detected from a 1 mM solution under unloaded and loaded conditions when a transmit-receive inductively-coupled implantable coil system was used, while the technique was not optimized. This demonstrates the potential of performing localized spectroscopy with inductively-coupled implantable coil system. With the improvement of the shimming procedure and a better selection of the pulses used, *in vitro* and *in vivo* studies will be possible. Often only the linear shims were used to make the static magnetic field as homogenous as possible within the voxel. If signal line width of 5 to 15 Hz could be obtained under unloaded conditions, it was never achievable under loaded conditions. Manual shim and

fast automatic shimming technique by mapping along projection (FASTMAP, (166)) were explored occasionally. However, a FASTMAP calibration for the excitation and detection system and the voxel size required in the study may help in obtaining more optimal results in the future. Better water suppression and OVS could also benefit from a better shimming over the voxel of interest. Improving the RF pulse profiles to obtain a better voxel shape and signal uniformity across the voxel would be the second step toward a better localized spectroscopy. The RF\_profile sequences included in the Paravision software were mainly made for volume coil excitation and detection as the profile can only be obtained in the direction of the static magnetic field and not in any other direction as needed for the systems investigated in this study. One type of PRESS sequences (the one designated as ParaVision Method or PVM) had some profiling capability to be explored once the shim procedure is optimized. Moreover, with increasing magnetic field, longitudinal relaxation times ( $T_1$ ) tend to increase and transversal relaxation times ( $T_2$ ) tend to decrease (152). No previous work was found to lead to a  $T_2$  range for total choline at 11.1T. However, a stimulated echo acquisition mode (STEAM, see Section 2.3.2.1) pulse sequence may be used to acquire these data if total choline  $T_2$  is found to be relatively short (83). These are suggestions to consider in the future to enable the optimum detection of the total choline NMR signal at high field (11.1T and up) to monitor the functioning of a bioartificial pancreatic construct with cell viability.

Furthermore, the buffering agent HEPES used to maintain a physiologic pH for the cells in PBS outside of the incubator (when  $CO_2$  is in limited quantity) when NMR experiments were conducted *in vitro* was found to have a resonance close enough to the 3.2 ppm of the choline and could have potentially masked it. It was subsequently removed of the PBS solution already used instead of culture media to eliminate the glucose interference with the choline resonance at 3.2

ppm. Furthermore, the fact also the no choline signal could be detected from the *in vitro* sample with cells brought the issue of the viability of the cells in pure PBS for an extended period of time. The period of time during which the cells can be kept alive in PBS at room temperature will have to be attested before new experiments are conducted.

#### 4.6 Summary

Receive-only implantable inductively-coupled loop-gap coils assembled within bioartificial pancreas macroconstructs have been constructed and their performance analyzed on the bench, in phantoms, and *in vitro*. NMR images from coil-construct assemblies were obtained under unloaded and loaded conditions in gel phantoms at 11.1 T, demonstrating the capability of a receive-only inductively-coupled implanted coil system to perform NMR imaging and spectroscopy to monitor a bioartificial pancreas non-invasively. The SNR gain that the receive-only inductively-coupled implantable coil system has over a transmit-receive system at 11.1 T was similar under loaded conditions (*in vitro* and *in vivo* environment equivalent). However, the increased excitation homogeneity and selectivity available with the use of this receive-only inductively-coupled implantable coil system allows further gains in information obtained from an implanted construct.

Spectra were acquired using a transmit-receive inductively-coupled coil system and the Cho signal could be observed from the construct location, even though the localized spectroscopy method was not fully optimized. These results show the potential of performing localized spectroscopy with high sensitivity using inductively-coupled implantable coil systems to detect the TCho signal from live cells and link this information to cell viability within the construct. This gives a fundamental basis toward the detection of early marker of pancreatic construct failure *in vivo*.

With the feasibility assessment of receive-only inductively-coupled implantable coil systems, the focus of this research was next directed toward the feasibility assessment of another type of complex inductively-coupled implantable coil system: multi-frequency systems. These multiple-frequency coupled-coil systems are of primary interest as they would allow the detection of less-sensitive, yet important, nuclei, such as  $^{31}\text{P}$  and  $^{19}\text{F}$ , and generate direct correlation of the results from the different nuclei detection to fully characterize a bioartificial construct.

CHAPTER 5  
TOWARD THE DEVELOPMENT OF A MULTIPLE-FREQUENCY INDUCTIVELY-  
COUPLED RF COIL SYSTEM FOR SIMULTANEOUS  $^1\text{H}$ ,  $^{19}\text{F}$ , AND  $^{31}\text{P}$  DETECTION FOR  
IMAGING AND SPECTROSCOPIC ANALYSIS OF AN IMPLANTABLE BIOARTIFICIAL  
CONSTRUCT AT 11.1T

### 5.1 Introduction

Monitoring the viability and the bioenergetics status of cells as well as the oxygen concentration within a bioartificial pancreas, is of primary importance to directly reflect the well being and functioning of the construct. NMR imaging (MRI) and spectroscopy (MRS) have shown to be well-suited techniques for such a non-invasive and temporal monitoring of such a device *in vitro* and *in vivo*. However, to achieve a complete monitoring, these NMR techniques depend on the detection of specific nuclei including, but not limited to, hydrogen ( $^1\text{H}$ ), phosphorus ( $^{31}\text{P}$ ), and fluorine ( $^{19}\text{F}$ ). In this study, the detection of physiological levels of these nuclei was investigated while using high sensitivity single-frequency inductively-coupled implantable RF coil systems at high field (11.1T). Moreover, the feasibility of multiple-frequency inductively-coupled implantable coil systems, (a  $^1\text{H}$ - $^{31}\text{P}$  & a  $^1\text{H}$ - $^{19}\text{F}$  one), was examined as only one implantable coil can be implanted with the construct at a time. Standards were established using single-frequency inductively-coupled implantable coil systems and the feasibility of double frequency inductively-coupled implantable coil systems was assessed.

### 5.2 Background

The well being and functioning of a bioartificial pancreas can be directly assessed by the monitoring of the viability and the bioenergetics status of its cells as well as the oxygen concentration within the tissue-engineered construct. In order to perform such a complete monitoring of a bioartificial pancreas using NMR methods, the nuclei of interest include, but are not limited to, hydrogen ( $^1\text{H}$ ) (5,6), phosphorus ( $^{31}\text{P}$ ) (47,91,95), and fluorine ( $^{19}\text{F}$ ) (94-96). To detect these different nuclei different NMR methods can be developed. However, due to the low

NMR sensitivity of some of these nuclei, the methods must have an optimal detection sensitivity to be able to monitor physiological level of these nuclei. If the method developed by Stabler *et al.* showed promises in detecting  $^1\text{H}$  choline signal and linking it to the cell viability within the construct (5,6), this method sensitivity threshold prevented its use with low densities of cell within bioartificial construct and the detection of other less sensitive nuclei, such as  $^{31}\text{P}$ . Recently, the use of higher magnetic field strength along with inductively-coupled implantable coil systems was shown to improve the sensitivity of the NMR methods by a factor of 4 (160). This would allow the detection and study of lower density of cells within constructs *in vitro* and *in vivo* as well as less sensitive nuclei (compared to  $^1\text{H}$ ), such as  $^{19}\text{F}$  and  $^{31}\text{P}$ . However, only one coil can be implanted per construct. Furthermore, the construct is neither retrievable from the middle of the coil (without being impaired) nor interchangeable. This shows the need for a combined coil system tuned to multiple frequencies that would gather information from more than one nucleus at once and allow an easy correlation of the results obtained for the different nucleus signal simultaneous detection.

For *in vivo* studies, these multiple-frequency coils are generally birdcage volume coils (112) or surface coils (113,114), essentially double-tuned  $^1\text{H}$  and  $^{31}\text{P}$ , due to the importance of the biological compounds observed at these frequencies (112,113,115,116). These RF coils are mainly based on tank, or “trap”, circuits (107) and transformer-coupled circuits (108). Tank circuits are introduced into the circuits to add poles in the complex reactance equation and create additional resonant frequencies. Transformer-coupled (or inductive overcoupling) method uses inductive coupling to introduce additional resonance in the circuits. The efficiency of these two methods is relatively similar (113). However, transformer-coupled coils do not seem appropriate for the purpose of this study since inductive overcoupling is already used to enhance the

sensitivity of the NMR methods under investigation (see Section 3.3.3 for inductively-coupled implantable coil system) focusing on only one of the resonant frequencies of the system (the co-rotating mode). Furthermore, the distance between the implantable and surface coils is fixed by the design of the experiment studied and the anatomy of the implantable-coil recipient, such that the degree of coupling may be too small for the successful operation of the transformer-coupled double-frequency coil system.

Thus, this report investigates and discusses the feasibility, the technical aspects, and the use of multiple-frequency ( $^1\text{H}$ - $^{31}\text{P}$  and  $^1\text{H}$ - $^{19}\text{F}$ ) inductively-coupled RF coil systems using tank circuits at a high field (11.1 T) to monitor implanted tissue-engineered constructs with NMR. It also specifies the maximum performances these types of systems will achieve for  $^{19}\text{F}$  and  $^{31}\text{P}$  detection by testing single-frequency inductively-coupled implantable coil system (one  $^{19}\text{F}$  and one  $^{31}\text{P}$  system) detecting: 1) the  $\gamma$ -P signal of adenosine triphosphate (ATP), which can be linked to the cell bioenergetics within the bioartificial pancreas (BAP), and 2) the  $^{19}\text{F}$  signal of added perfluorocarbons, which can be linked to the oxygen tension within a construct.  $^1\text{H}$  spectroscopy and the choline signal link to the cell density within a BAP was investigated in Chapter 4.

## **5.3 Materials and Methods**

### **5.3.1 RF Coil System Development**

Single-frequency and multiple-frequency inductively-coupled implantable coil systems were constructed, tested, and compared at 11.1 T. Following the results obtained in Chapter 3, the five coupled-coil systems developed in this study consisted of an implantable loop-gap resonator coil inductively-coupled to a surface coil for NMR imaging and spectroscopy. All systems function as both transmitter and receiver at every frequency. The  $^1\text{H}$  and  $^{19}\text{F}$  single frequency inductively-coupled implantable coil systems were similar to each other and similar to

the system described in Section 3.3.1 (160). The implantable coil-bioartificial pancreatic macroconstruct assembly was similar to the one described in Section 3.3.5.3. Only the fixed capacitors' values were different to reflect the difference in resonant frequency of  $^1\text{H}$  and  $^{19}\text{F}$ . The single-frequency inductively-coupled implantable coil system had to be slightly modified to obtain a practical  $^{31}\text{P}$  single-frequency coupled-coil system. Since  $^{31}\text{P}$  has such a low NMR sensitivity (6% sensitivity compared to  $^1\text{H}$ ), sample positioning at the center of the magnet and shimming procedure are usually done by detecting a more sensitive nuclei, such as  $^1\text{H}$ . Consequently, this  $^{31}\text{P}$  system had a double frequency ( $^1\text{H}$ - $^{31}\text{P}$ ) surface coil (Figure 5-1A) and an implantable coil (similar to the one presented on Figure 3-2A) only tuned to  $^{31}\text{P}$  frequency. The surface coil was not optimized to  $^1\text{H}$  resonant frequency (not matched to  $50\ \Omega$ ) as it was only used for positioning and shim purposes.

To render the two last coupled-coil systems double-frequency, the addition of tank circuits on both the implantable and surface coils of the single-frequency system was required (107) in order to introduce extra resonance to the circuit (Figure 5-1). A tank circuit consists of a parallel capacitor and inductor added in series with a tuning capacitor of a resonant circuit. The tank circuit is a resonant circuit in itself. It is inductive at the lower circuit resonant frequency since the resonant frequency of the tank circuit is higher than the main circuit lower resonant frequency. At the higher circuit resonant frequency, the tank circuit becomes more capacitive as the resonant frequency of the tank circuit is lower than the main circuit resonant frequency. This allows the tuning of both resonant frequencies individually (118).

To generate the inductively-coupled double-frequency  $^1\text{H}$ - $^{31}\text{P}$  implantable coil system, a standard tank circuit was added onto the implantable and surface coil (190.5 MHz and 470.75 MHz were the respective resonant frequency of  $^1\text{H}$  and  $^{31}\text{P}$  at 11.1 T). The double-frequency

implantable coil was developed based on the design of the loop-gap single-frequency implantable coil. Its inductor was made of a 2-mm-wide 202- $\mu\text{m}$ -thick copper foil and had a 1.2-cm diameter ( $L_i$  on Figure 5-1A). Its capacitive part included two fixed tuning capacitors ( $C_{Tui}$ ,  $C_{Tai}$  on Figure 5-1A), which divided the loop into two parts to spread the voltage more evenly throughout the circuit and allow the addition of an inductor in parallel to one of the capacitors to form a tank circuit. The double-frequency surface coil inductor was also constructed based on the characteristics of the surface coil of the single-frequency system. It was a single 2-cm-diameter circular loop of 2-mm wide 35- $\mu\text{m}$ -thick copper tape ( $L_s$  on Figure 5-1) held flat on a 5mm thick Plexiglas platform. The capacitive portion of the surface coil includes two variable matching capacitors (Voltronics Corporation, Denville, NJ, 1-15 pF,  $C_{Ms1V}$  and  $C_{Ms2V}$  on Figure 5-1B), one fixed tuning capacitor (American Technical Ceramics, Hartford, CT,  $C_{Tus}$  on Figure 5-1B), one variable tuning capacitor (1-15 pF,  $C_{TusV}$  on Figure 5-1), and one variable tank capacitor (1-15 pF,  $C_{TasV}$  on Figure 5-1B). The fixed tuning capacitor placed on the inductive loop divides this loop into two parts to distribute the voltage more evenly throughout the circuit. The addition of an inductor in parallel to the variable tank capacitor formed the tank circuit. The tank circuit and three variable capacitors were soldered onto a circuit board to provide variable tuning and matching of the system to 50  $\Omega$  at both frequencies. A coaxial cable (RG 58 C/U) connected the coil to either the  $^1\text{H}$  source and preamplifier or the  $^{31}\text{P}$  ones. Two cable traps were added to the shield of the coaxial cable to block shield currents that contribute to parasitic losses when working at both these high frequency (140). The  $^{31}\text{P}$  cable trap was placed at the circuit board end of the coaxial cable and the  $^1\text{H}$  a  $\frac{1}{4}$  wavelength away from the circuit board end. As phosphorus is the least sensitive nucleus to be studied here,

the design of the system was assembled in a way that phosphorus was optimized over the other nuclei.

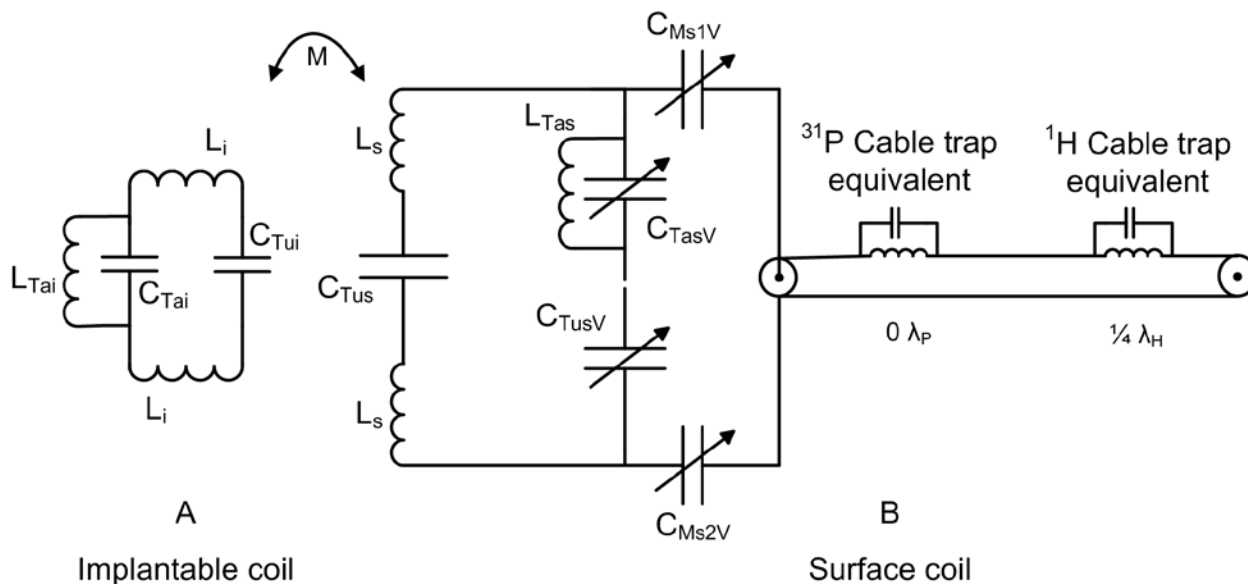


Figure 5-1. Circuit diagram for an inductively-coupled double-frequency ( $^1\text{H}$ - $^{31}\text{P}$ ) implantable coil system. A) An implantable coil; and B) a surface coil. Inductors (L) and capacitors (C) are shown with subscripts denoting implantable (i) or surface (s) coils. Capacitors are also designated as tuning ( $C_{Tu}$ ), tank ( $C_{Ta}$ ), or matching ( $C_M$ ). M indicates the mutual inductance or inductive coupling and V variable. A cable trap equivalent, including an inductor and a capacitor, is also shown in the diagram.

The  $^{19}\text{F}$ - $^1\text{H}$  double-frequency inductively-coupled coil system was implemented slightly differently than the  $^{31}\text{P}$ - $^1\text{H}$  system since  $^{19}\text{F}$  and  $^1\text{H}$  resonated too close to each other to make the system work with a tank circuit only. The fact that  $^{19}\text{F}$  and  $^1\text{H}$  have resonant frequencies close to each other (442.86 MHz and 470.75 MHz respectively at 11.1 T) required circuit modifications to avoid large resistive losses at both frequencies. This can be explained by the large current that will be circulating in the tank circuit because the tank circuit resonant frequency will be close to both resonant frequencies. To allow one circuit to resonate properly at multiple frequencies when frequencies were close to one another, such as the case of  $^{19}\text{F}$  and  $^1\text{H}$ , capacitive coupling (120,167) was used between the tank circuit and the main circuit. To generate the inductively-coupled double-frequency  $^1\text{H}$ - $^{19}\text{F}$  implantable coil system, a tank circuit was capacitively

coupled to both the implantable and surface coil. The implantable coil of this double-frequency system was developed based on the design of the loop-gap single-frequency implantable coil. Its inductor was a 1.2-cm diameter 2-mm-wide 202- $\mu\text{m}$ -thick copper foil ( $L_i$  on Figure 5-2). A fixed tuning capacitor was soldered between the ends of this resonator loop ( $C_{Tui}$  on Figure 5-2A). A tank circuit including a capacitor ( $C_{Tai}$  on Figure 5-2A) and an inductor ( $L_{Tai}$  on Figure 5-2A) was added in parallel to this tuning capacitor along with a coupling capacitor ( $C_{Ki}$  on Figure 5-2A). The surface coil inductor of this double-frequency system was also constructed based on the characteristics of the single-frequency surface coil. It was a single 2-cm-diameter circular loop of 2-mm wide 35- $\mu\text{m}$ -thick copper tape ( $L_s$  on Figure 5-2) held flat on a 5mm thick Plexiglas platform. The capacitive portion of the surface coil includes two variable matching capacitors (Voltronics Corporation, Denville, NJ, 1-15 pf,  $C_{Ms1V}$  and  $C_{Ms2V}$ ), one fixed tuning capacitor (American Technical Ceramics, Hartford, CT,  $C_{Tus}$  on Figure 5-2B), one variable tuning capacitor ( $C_{TusV}$  on Figure 5-2B, 1-15 pf) in parallel to a tank circuit including a variable capacitor ( $C_{TasV}$  on Figure 5-2B) and an inductor ( $L_{Tas}$  on Figure 5-2B) along with a variable coupling capacitor ( $C_{Ks}$  on Figure 5-2B). The fixed tuning capacitor was placed on the inductive loop and divided it into two parts to spread the voltage more evenly throughout the circuit. The tank circuit, the tuning and the two matching variable capacitors were soldered onto a circuit board to provide variable tuning and matching of the system to 50  $\Omega$  at both frequencies. A coaxial cable (RG 58 C/U) connected the coil to either the  $^1\text{H}$  source and preamplifier or the  $^{19}\text{F}$  ones. Two cable traps were added to the shield of the coaxial cable to block shield currents that contribute to parasitic coupling when working at both these high frequency (140). The  $^{19}\text{F}$  cable trap was placed at the circuit board end of the coaxial cable and the  $^1\text{H}$  a  $\frac{1}{4}$  wavelength away

from the  $^{19}\text{F}$  one. As Fluorine is a less sensitive nucleus than  $^1\text{H}$ , the design of the system was assembled without trying to optimize one nucleus over the other one.

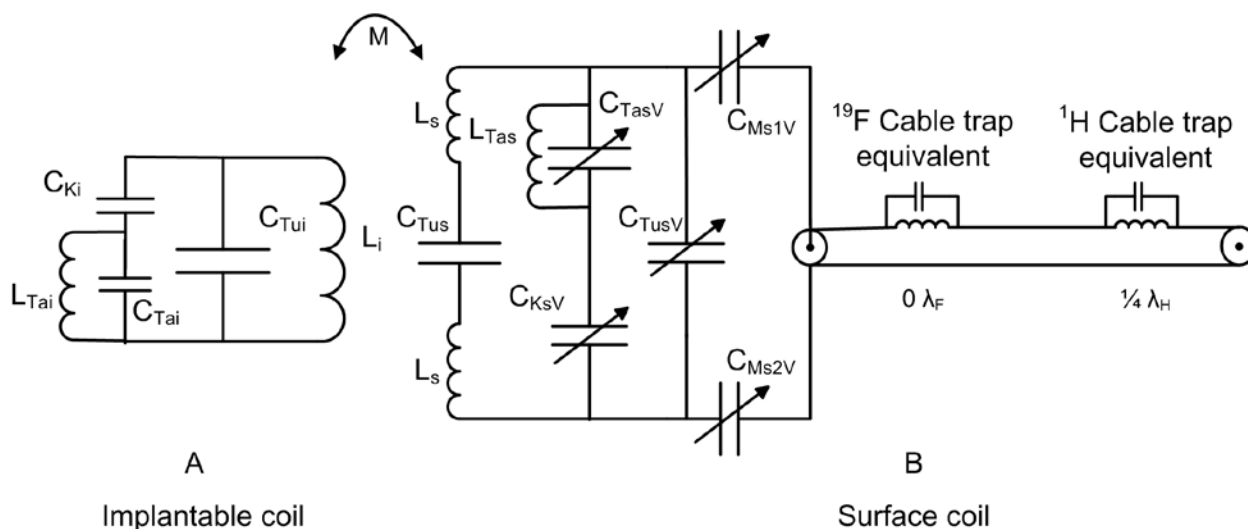


Figure 5-2. Circuit diagram for an inductively-coupled double-frequency ( $^1\text{H}$ - $^{19}\text{F}$ ) implantable coil system. A) An implantable coil; and B) a surface coil. Inductors (L) and capacitors (C) are shown with subscripts denoting implantable (i) or surface (s) coil. Capacitors are also designated as tuning ( $C_{Tu}$ ), tank ( $C_{Ta}$ ), or matching ( $C_M$ ). M indicates the mutual inductance or inductive coupling and V variable. A cable trap equivalent, including an inductor and a capacitor, is also shown in the diagram.

Even though the multiple-frequency coupled-coil system requires more components than the single frequency system, the size of the implanted coil needed to be kept small to be usable *in vivo*. This size restriction also applied to the surface coil as tank circuits are resonating loops themselves and can introduce undesired loss in the main circuit if made too large. The inductors of the tank circuits ( $L_{Tas}$  and  $L_{Tai}$  on Figure 5-1 and 5-2) were small solenoids, made of 25 AWG (American Wire Gauge) copper wires, hand wound around a 16 AWG copper wire making their self-resonance much higher than the tank and the main circuit resonance. Their values were verified using the RF impedance test adapter HP 1620A spring clip fixture of the network analyzer (8752C Hewlett Packard, Santa Rosa, CA). These inductors were placed perpendicular to the main coil loop of the implantable coil to limit the interaction between each other ( $L_{Tai}$  on

Figure 5-1A and 5-2A) and over the tank capacitor ( $L_{Tas}$  and  $C_{TasV}$  on Figure 5-1B and 5-2B) on the surface coil circuit board. This limited signal degradation due to the addition of extra undesired frequencies in the system because of inductively coupling between the tank inductor and the main circuit inductor. Furthermore, to allow further flexibility in the frequencies tuning and the matching to  $50 \Omega$  of both double frequency coil systems, the capacitor of the tank circuit ( $C_{TasV}$  on Figure 5-1) and the coupling capacitor of the surface coils ( $C_{KsV}$  on Figure 5-1) were also variable.

### **5.3.2 Coating Techniques**

The material used for the coating of the implantable coils used in this study was the same one as the one used for the transmit-receive and receive-only implantable coil presented in Chapter 3 and 4: polydimethylsiloxane (PDMS, Medical Grade Silicone Elastomer, Factor II, Lakeside, AZ). The technique applied has been described in details in Section 3.3.2.4 (160). However, adaptations were made to this coating procedure to accommodate the double-frequency coil extra components. The coating of the hand-wound tank-circuit solenoids was tested prior to the coating of the entire coil as described in Section 4.3.2 as they could be easily deformed under pressure resulting in drastic changes in their characteristics (inductance in this case).

### **5.3.3 RF Coil Testing**

When surface and implantable coils are in proper orientation and close proximity, they inductively couple (143) as described in Section 3.3.3. In order to have the  $^{19}\text{F}$  single-frequency coil system resonating at 442.86 MHz, the implantable and surface coil had to be individually tuned and matched to a higher frequency (464.8 MHz) in the (+) mode, and to a lower frequency (421.6 MHz) in the (-) mode. In order to have the  $^{31}\text{P}$  single-frequency coil system resonating at

190 MHz, the implantable and surface coil had to be individually tuned and matched to a higher frequency (199.6 MHz) in the (+) mode, and to a lower frequency (181.9 MHz) in the (-) mode.

The inductive coupling of the surface and implantable coils of the two double-frequency inductively-coupled implantable coil systems induced a total of 4 resonant frequencies since every coil already had 2 resonant frequencies each. This means that the systems had 2 current modes for each resonant frequency. In order to have the double-frequency  $^{31}\text{P}$ - $^1\text{H}$  inductively-coupled coil system resonating at both 190.5 MHz and 470.75 MHz, the implantable and surface coil had to be individually tuned and matched to a higher frequency for both frequency (195.8 and 475.5 MHz) in the (+) mode, whereas the implantable and surface coil had to be individually tuned and matched to a lower frequency for both frequency (185.4 and 465.8 MHz) in the (-) mode. In order to have the double-frequency  $^{19}\text{F}$ - $^1\text{H}$  inductively-coupled implantable coil system resonating at both 442.86 and 470.75 MHz, the implantable and surface coil had to be individually tuned and matched to a higher frequency (449.3 and 481.8 MHz) in the (+) mode, whereas the implantable and surface coil had to be individually tuned and matched to a lower frequency for both frequency (436.4 and 459.7 MHz) in the (-) mode.

The five different inductively-coupled systems developed were: 1) one single-frequency system for  $^1\text{H}$  detection (470 MHz) (referred as to  $^1\text{H}$  system); 2) one single-frequency system for  $^{19}\text{F}$  detection (442.86 MHz); 3) one single-frequency system for  $^{31}\text{P}$  detection (190.5 MHz); 4) one double-frequency system for both  $^1\text{H}$  and  $^{31}\text{P}$  detection; and 5) one double-frequency system for both  $^1\text{H}$  and  $^{19}\text{F}$  detection. For all these systems, all variable capacitors  $C_{M1V}$ ,  $C_{M2V}$ ,  $C_{TusV}$ ,  $C_{TasV}$ , and  $C_{KsV}$  (Figure 5-1 and 5-2) in the surface coils were adjusted to achieve a match to 50  $\Omega$  at each resonant frequency. These different systems were first simulated with antenna analysis software (Graphical Numerical Electromagnetics Code, Nittany, Inc. Riverton, UT).

These systems were then optimized on the bench with a network analyzer (Hewlett Packard 8752C, Santa Rosa, CA) before testing in the magnet. The quality factor (Q) of each coil taken individually and of the whole system was recorded after construction with and without load and every time the system was tested in the magnet. The measurements were performed as described in details in Section 3.3.3.

A coupling factor was also determined for every coupled-coil system to characterize its inductive coupling. Usually, this coupling factor ( $k$ ) represents the amount of magnetic flux transmitted from one coil (the surface coil in the case of transmission in this study for example) to the other (the implantable coil here) and is often described as:

$$k = \frac{M}{\sqrt{L_{IC} \cdot L_{SC}}}; \quad (5-1)$$

where  $k$  is the coupling factor,  $M$  the mutual inductance of the inductively-coupled implantable coil system,  $L_{IC}$  the total inductance of the implantable coil of the system, and  $L_{SC}$  the total inductance of the surface coil of the system (118,142). However, the determination of the coupled-coil system mutual inductance is not easy or exact (168). Here, the coupling factor was determined for every coupled-coil system by calculating the ratio of the frequency split existing between the co- and counter rotating mode of each system over their center frequency (or frequency at which the two coils of the inductively-coupled system resonated at individually) as the frequency split does depend on the coupling between the two coil of a system.

#### 5.3.4 Samples

All the samples were placed in 10 mm-diameter thin-wall glass tubes (Wilmad Labglass, Buena, NJ) to test the coil systems under unloaded conditions on the bench and in the magnet. The implantable coils were placed around this sample no more than a 1 cm away from the surface coil. Water was used for  $^1\text{H}$  detection, perfluorocarbon (PFC) samples for  $^{19}\text{F}$  detection,

and phosphoric acid sample for  $^{31}\text{P}$  detection. If high concentration sample were initially used to test the functionality of the systems, more realistic samples were generated afterwards to define the sensitivity and limit of detection of the different coupled-coil systems for *in vivo* use under loaded conditions.

#### 5.3.4.1 Perfluorocarbons

The PFC introduced in the samples of this study for  $^{19}\text{F}$  detection was perfluoro-[15]-crown-5 ether (PFCE, Exflur Research Corp., Round Rock, TX). It was selected for its single sharp  $^{19}\text{F}$ -resonance signal from its 20 equivalent fluorine nuclei. It was prepared following a protocol adapted from Joseph *et al.* (169). Egg yolk lecithin (95 mg, Sigma-Aldrich Corp., St. Louis, MO) was added to 600 mL of Tyrode's salt solution kept at 0°C (pH 7.4, Sigma-Aldrich Corp., St. Louis, MO) as a surfactant. While kept in an ice bath, this mixture was sonicated twice at 300 W for 15 s with a 1 min interval between sonications (Branson Ultrasonics, Danbury, CT) to create an aqueous phase of lecithin. A volume of 400  $\mu\text{L}$  of PFCE was then added to the mixture. Sonication was repeated seven more times under the conditions described above to disperse the PFCE in the mixture. This emulsion contained PFCE spheroids between 200 and 300 nm in diameter (Figure 5-3A).

The emulsion was filtered through a 0.4  $\mu\text{m}$  membrane filter to make it sterile without destroying the preparation. It was shown not to affect the cells or their surrounding up to 10% (v/v) (170). Different amounts of emulsion (0.4%, 1%, 2.5%, 5%, and 10%) were then incorporated to an alginate solution.

Cell-free PFC-alginate beads were then generated as described by Simpson *et al.* (Figure 5-3B and (151)). The alginate solution was a 2% (w/v) sodium alginate solution generated from alginate powder (Novomatrix, Trondheim, Norway) and a solution of 0.85% sodium chloride.

Aliquots of freshly made beads (~0.3 ml each) were transferred into the coil-construct assembly with an implantable coil resonating at the desired frequency for  $^{19}\text{F}$  detection using a syringe and 16 G needle (Figure 5-4).

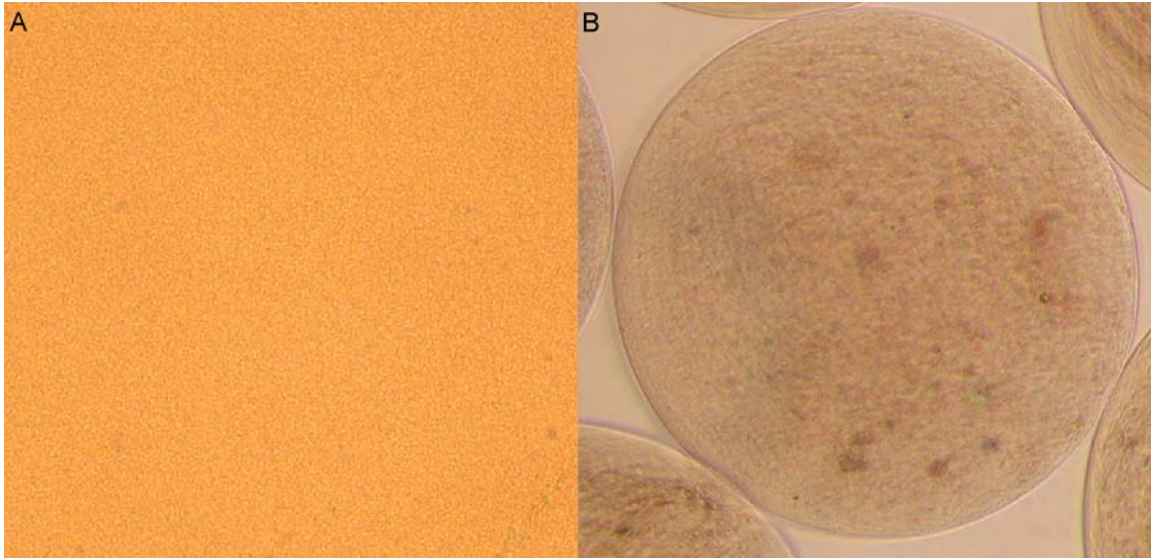


Figure 5-3. Photograph of PFCE emulsion. A) In solution; and B) in beads. (Photo by N.A. Volland).

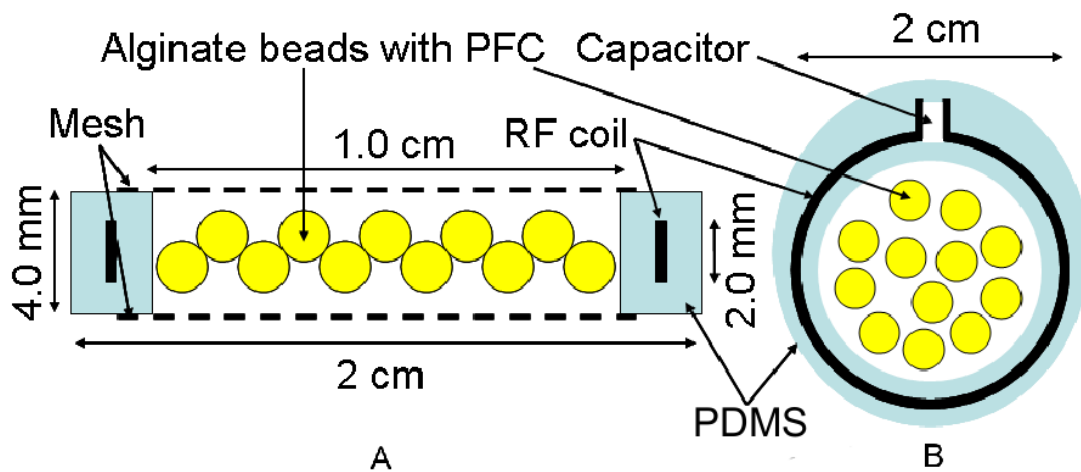


Figure 5-4. Implantable coil - bioartificial pancreas macroconstruct assembly schematic and dimensions. A) Transverse view and B) coronal view of the assembly. The alginate beads are contained in the cylindrical cavity created by the PDMS-coated circular MR implantable coil and 300- $\mu\text{m}$  mesh screen.

#### 5.3.4.2 Phosphorus samples

*In vivo* physiological concentrations of phosphorus containing metabolites do not exceed 10 mM. Consequently, to assess the sensitivity of  $^{31}\text{P}$  detection, a sample of saline solution containing different concentration down to 500  $\mu\text{M}$  of sodium phosphate ( $\text{Na}_2\text{HPO}_4^{-2}$ ) and adenosinetriphosphate (ATP) were created, before cell-containing beads were tested *in vitro*.

To make the cell-containing beads for *in vitro* testing, murine insulinoma  $\beta\text{TC-tet}$  cells (48) were cultured and collected as described in Section 4.3.5. Cell-containing alginate beads (with a initial density of  $3.5 \times 10^7$  cells/ml of alginate) were then generated and inserted in a coil-construct assembly with an implantable coil resonating at the desired frequency for  $^{31}\text{P}$  detection as described in Section 5.3.4.1 (Figure 5-4). The cell-containing assembly was placed in a 3-cm-diameter flat-bottom Plexiglas tube closed with a vented cap. The cells were fed every 2-3 days and kept alive for the duration of the study.

#### 5.3.5 NMR Measurements

NMR measurements were performed on an 11.1 Tesla (T) 40 cm clear horizontal bore Magnex magnet equipped with a Bruker Avance console. Data acquisition was done using Bruker Paravision software as well as the imaging data processing. The spectroscopy data processing was done via a Bruker Xwin-NMR software. The signal-to-noise ratio (SNR) for each measurement was then determined for each coil system with a custom image analysis software written in IDL (ITT Visual Information Solutions, Boulder, CO) when images could be acquired or the Xwin-NMR software when spectrum were acquired.

When characterizing the single-frequency coil systems for  $^{19}\text{F}$  detection,  $^{19}\text{F}$  images were acquired using a spin-echo (SE) pulse sequence with sinc3 pulses, a repetition time (TR) of 1000 ms, an echo time (TE) of 10 ms, 1-mm slice thickness, 1 average,  $4 \times 4 \text{cm}^2$  field-of-view (FOV) and a  $256 \times 256$  matrix on pure PFCE sample. When characterizing the single-frequency coil

systems for  $^{31}\text{P}$  detection,  $^{31}\text{P}$  images were acquired using a spin-echo (SE) pulse sequence with sinc3 pulses, a repetition time (TR) of 1000 ms, an echo time (TE) of 10 ms, 1-mm slice thickness, 1 average,  $4 \times 4 \text{ cm}^2$  field-of-view (FOV) and a  $64 \times 64$  matrix on a phosphoric acid sample. PDMS signal suppression was not necessary for  $^{19}\text{F}$  and  $^{31}\text{P}$  detection since PDMS does not contain these nuclei.

For the limit of detection studies, images were acquired ( $^{19}\text{F}$  images) when possible using a spin-echo (SE) pulse sequence with sinc3 pulses, a repetition time (TR) of 1000 ms, an echo time (TE) of 10 ms and  $2 \times 2 \text{ cm}^2$  field-of-view (FOV). The slice thickness (1-3 mm), the number of signal averages (up to 10), and the matrix size (from  $256 \times 256$  down to  $32 \times 32$ ) were varied to obtain images with acceptable SNR ( $> 2$ ). Spectra were also acquired using one-pulse sequence with a hard pulse and a repetition time (TR) of 1000 ms. The number of averages was varied up to 256 to obtain spectra with acceptable SNR ( $> 2$ ) within 10 minutes. The longitudinal relaxation times ( $T_1$ ) of PFCE were then determined from either  $^{19}\text{F}$  image or spectrum acquisition. To allow this determination, a saturation recovery spin echo imaging pulse sequence was used with sinc3 pulses with an echo time (TE) of 10 ms, and variable repetition time (TR) of 5000, 2500, 2000, 1500, 1000, 750, 500, 200 ms to acquire the imaging data, when 2.5% PFCE emulsion or more was used (171,172). Otherwise, a non-selective inversion recovery spectrum pulse sequence with hard pulses and the inversion time (TI) of 5000, 2500, 2000, 1500, 1000, 750, 500, 200 ms was used to acquire the spectral data (171,172). The slice thickness (1-3 mm), the number of signal averages (up to 3), and the matrix size (from  $128 \times 128$  down to  $32 \times 32$ ) were varied for the imaging series to be acquired within 30 minutes. Only the number of averages was varied up to 256 for the spectra to be acquired within 30 minutes as well. Spectra of ATP were acquired using one-hard-pulse sequence with a hard pulse, a repetition time (TR) of 2000 ms.

The number of averages (up to 1024) was varied to obtain spectra with acceptable SNR ( $> 2$ ) within 30 minutes.

### 5.3.6 SNR Measurements and Statistical Analysis

The results of the characterizations presented in this study were compared to each other and to the results obtained in the characterization of inductively-coupled implantable coil systems dedicated to  $^1\text{H}$  detection. These results gave a reference for the multiple-frequency systems that have been developed in parallel of the single-frequency coil systems. The comparison would assess the losses of sensitivity associated with multiple-frequency inductively-coupled implantable coil systems.

Five different inductively-coupled systems were tested: 1) one single-frequency system for  $^1\text{H}$  detection (470.75 MHz); 2) one single-frequency system for  $^{19}\text{F}$  detection (442.86 MHz); 3) one single-frequency system for  $^{31}\text{P}$  detection (190.5 MHz); 4) one double-frequency system for both  $^1\text{H}$  and  $^{31}\text{P}$  detection; and 5) one double-frequency system for both  $^1\text{H}$  and  $^{19}\text{F}$  detection. The SNR of the different coil-systems were evaluated from the NMR images, when possible, by choosing a signal region-of-interest (ROI) at the IC position and a noise ROI outside of the sample as described in Section 3.3.8 for inductively-coupled implantable coil system for  $^1\text{H}$  detection. To assess the performances of spectroscopy methods, the SNR was evaluated from the NMR spectra as described in Section 4.3.8 for receive-only inductively-coupled implantable coil system for  $^1\text{H}$  detection. Multiple images or spectra were acquired for each coil system to assess the reproducibility of signal detection and the sensitivity of the systems. All the results are indicated as a mean  $\pm$  standard deviation (relative standard deviations are indicated in parentheses in percentage).

## 5.4 Results

### 5.4.1 RF Coil System

The simulations of the single-frequency inductively-coupled implantable coil systems for  $^{19}\text{F}$  and  $^{31}\text{P}$  detection were similar to the ones of the coupled-coil system presented in Section 3.4.1. Figure 5-5 displays the simulated voltage standing wave ratio (VSWR) plots of the double-frequency  $^1\text{H}$ - $^{31}\text{P}$  inductively-coupled implantable coil system. The four resonant frequencies, 2 modes per resonant frequency, can be clearly seen.

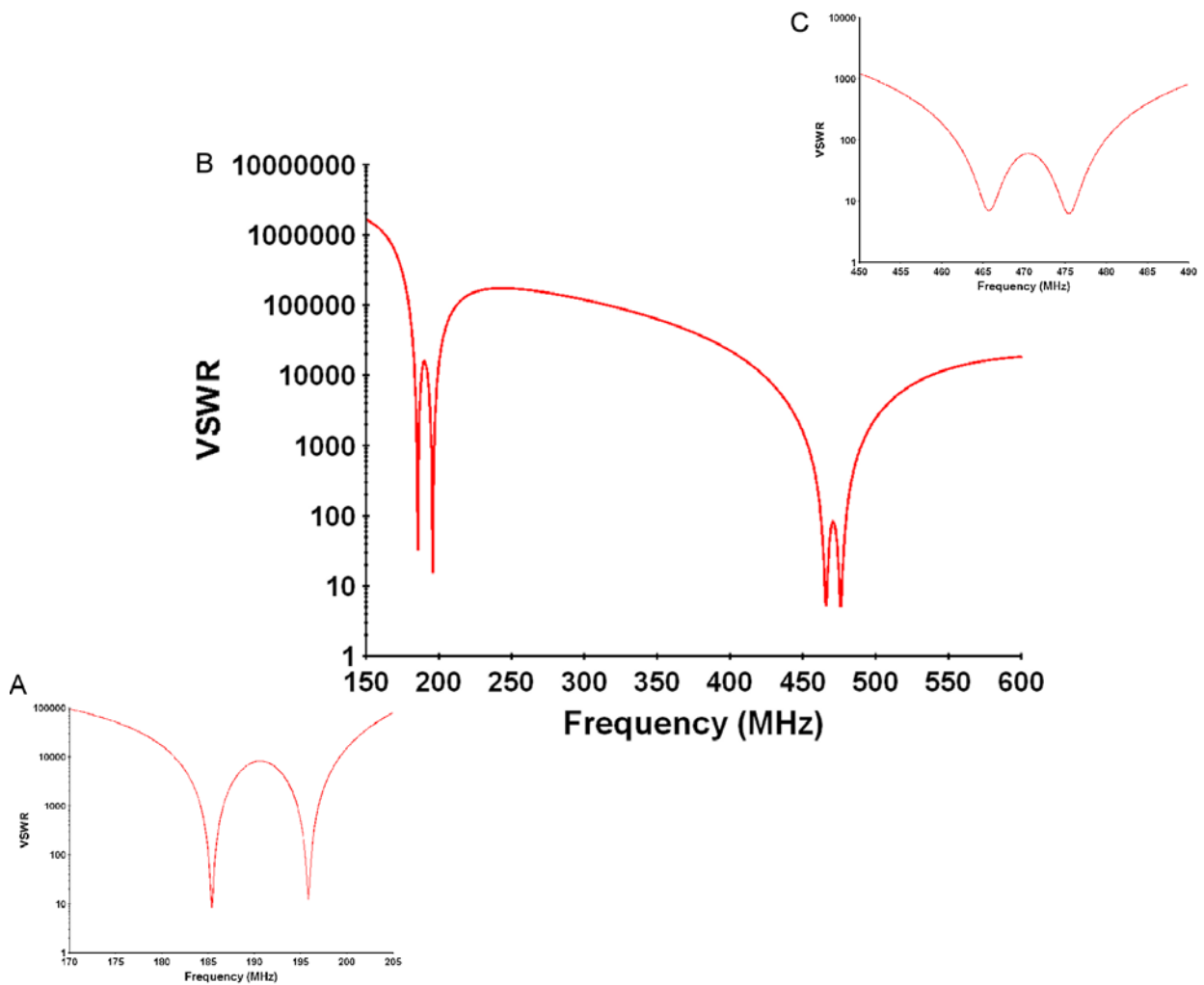


Figure 5-5. Voltage Standing Wave Ratio (VSWR) of the double frequency  $^1\text{H}$ - $^{31}\text{P}$  inductively-coupled coil system at both frequencies. A) Zoom in around 190.5 MHz ( $^{31}\text{P}$  resonant frequency at 11.1 T), B) entire frequency sweep; and C) zoom in around 470.75 MHz ( $^1\text{H}$  resonant frequency at 11.1 T).

The near magnetic field at these resonant frequencies was also simulated (Figure 5-6). The co- and counter-rotating modes are present at both frequencies. The double-frequency  $^1\text{H}$ - $^{31}\text{P}$  circuit matching to  $50\ \Omega$  (VSWR=1) was never achieved for all the resonant frequencies of the coupled-coil system at once. Consequently, the magnetic fields simulated at any resonant frequency of the system were lower than the ones generated by single-frequency inductively-coupled systems and only had qualitative value for the different modes generated by the overcoupling at the two resonant frequencies. Furthermore, the double-frequency  $^1\text{H}$ - $^{31}\text{P}$  circuit matching for the  $^{31}\text{P}$  resonances was worse than for the  $^1\text{H}$  ones, which lead to weaker magnetic fields at  $^{31}\text{P}$  resonances than at  $^1\text{H}$  resonances.

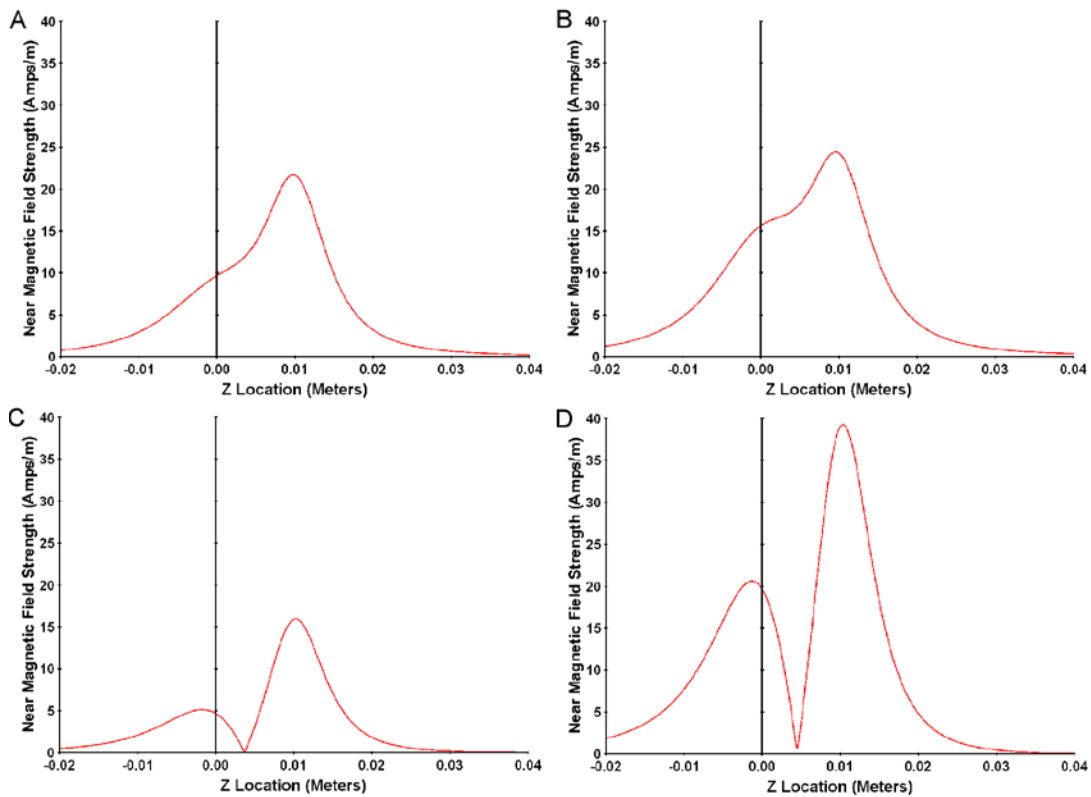


Figure 5-6. Near magnetic field distribution along the axis of symmetry of the double-frequency  $^1\text{H}$ - $^{31}\text{P}$  inductively-coupled coil system at 190.5 MHz and 470.75 MHz. A) Distribution at 185.45 MHz in the (+) mode, B) distribution at 465.75 MHz in the (+) mode, C) distribution at 195.8 MHz in the (-) mode, and D) distribution at 475.45 MHz in the (-) mode. The position of the surface coil was set at 0 and the implantable coil one at 1 cm.

Figure 5-7 displays the simulated VSWR plots of the double-frequency  $^1\text{H}$ - $^{19}\text{F}$  inductively-coupled coil system. The four resonant frequencies and 2 modes per resonant frequency can be clearly seen as well. However, this VSWR graph looks different from the  $^1\text{H}$ - $^{31}\text{P}$  system one. The frequency split at both  $^1\text{H}$  and  $^{19}\text{F}$  frequencies is not symmetric around 442.86 and 470.75 MHz compared to any other inductively-coupled coil system built, single or double-frequency. The asymmetry seems more pronounced at the lower frequency ( $^{19}\text{F}$ ) than at the higher one ( $^1\text{H}$ ). At the higher frequency, the split only looked shifted by 4 MHz, whereas at the lower frequency, the counter-rotating (-) mode frequency seemed to have shifted away from the original lower 442.86 MHz frequency compared to the co-rotating (+) mode frequency. The counter-rotating mode of the lower frequency and the co-rotating mode of the higher frequency seem to interact with each other.

This double-frequency  $^1\text{H}$ - $^{19}\text{F}$  circuit matching to  $50\ \Omega$  (VSWR=1) was not achieved for any of resonant frequencies of the system either. Consequently, the simulated magnetic fields (Figure 5-8) at any resonant frequency of the system only had qualitative values for the different modes generated by the overcoupling of the system at the two resonant frequencies. The co- and counter-rotating modes at both frequencies are present in this system. However, the observation made on the VSWR graph can be seen here too. The counter-rotating mode of the lower frequency (442.86 MHz, Figure 5-8C) is largely affected by the co-rotating mode of the higher frequency (470.75 MHz, Figure 5-8D) as its magnetic field magnitude is 10 times lower than the other ones.

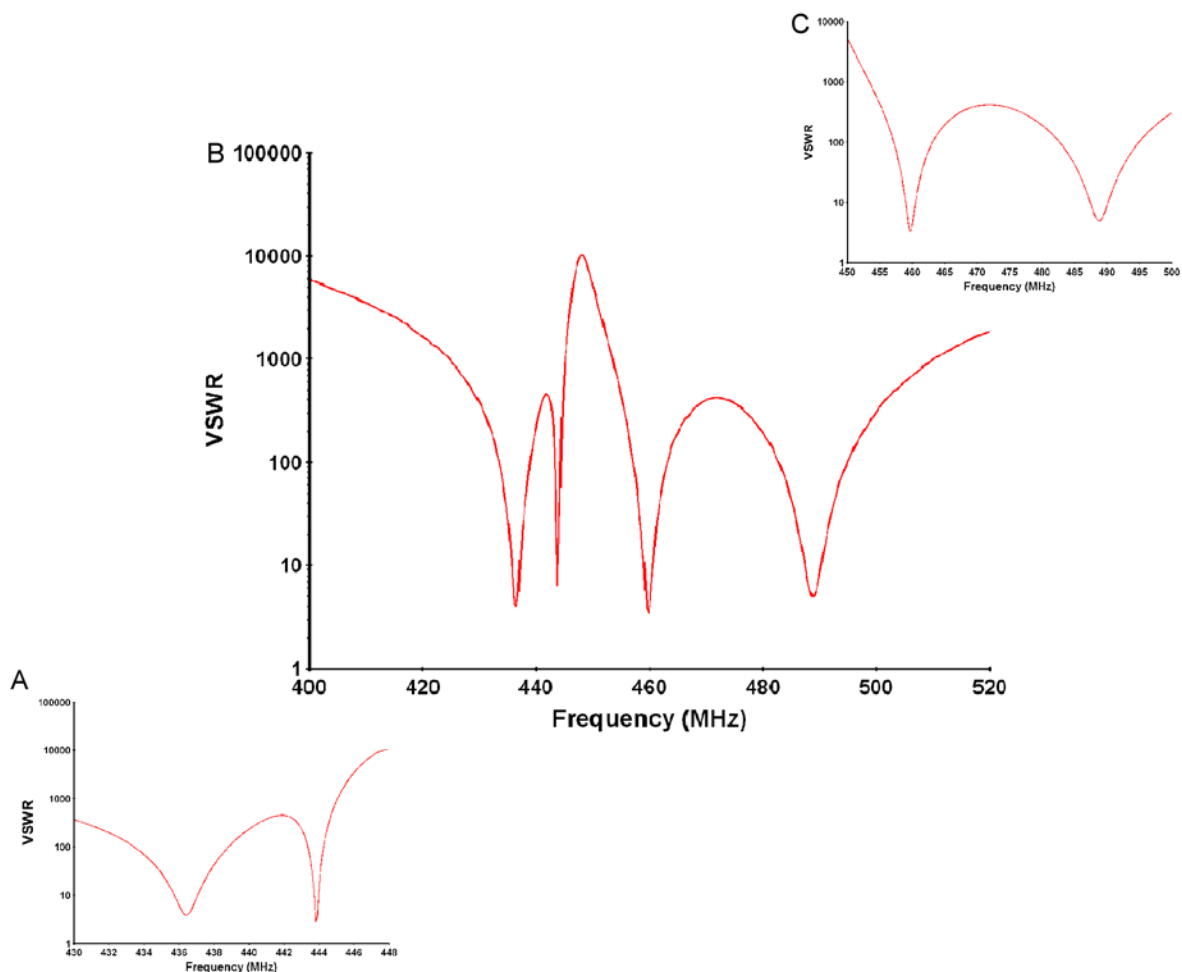


Figure 5-7. Voltage Standing Wave Ratio (VSWR) of the double frequency  $^1\text{H}$ - $^{19}\text{F}$  inductively-coupled coil system at both frequencies. A) Zoom in around 442.86 MHz ( $^{19}\text{F}$  resonant frequency at 11.1 T), B) entire frequency sweep; and C) zoom in around 470.75 MHz ( $^1\text{H}$  resonant frequency at 11.1 T).

Single-frequency inductively-coupled coil systems for  $^{31}\text{P}$  and  $^{19}\text{F}$  detection have been successfully developed. The implantable coil (Figure 5-9) and the surface coil (Figure 5-10) of a double-frequency  $^1\text{H}$ - $^{31}\text{P}$  inductively-coupled prototype system were also designed and built. These systems were all built in their (+) mode only, because previous inductively-coupled implantable coil systems have shown a higher sensitivity in this mode than their counterpart (see Section 3.3.4).

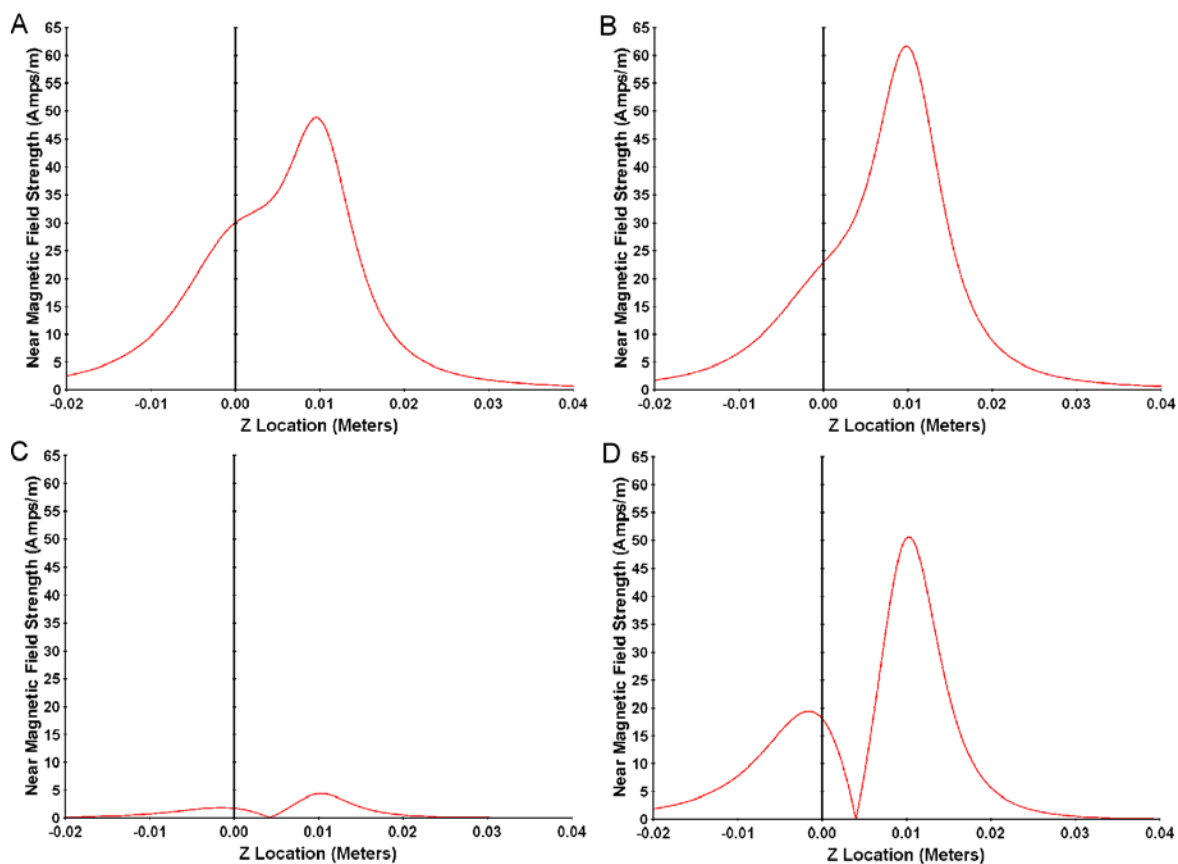


Figure 5-8. Near magnetic field distribution along the axis of symmetry of the double frequency  $^1\text{H}$ - $^{19}\text{F}$  inductively-coupled coil system at 442.86 MHz and 470.75 MHz. A) Distribution at 436.4 MHz in the (+) mode, B) distribution at 459.7 MHz in the (+) mode, C) distribution at 443.75 MHz in the (-) mode, and D) distribution at 488.8 MHz in the (-) mode. The position of the surface coil was set at 0 and the implantable coil one at 1 cm.

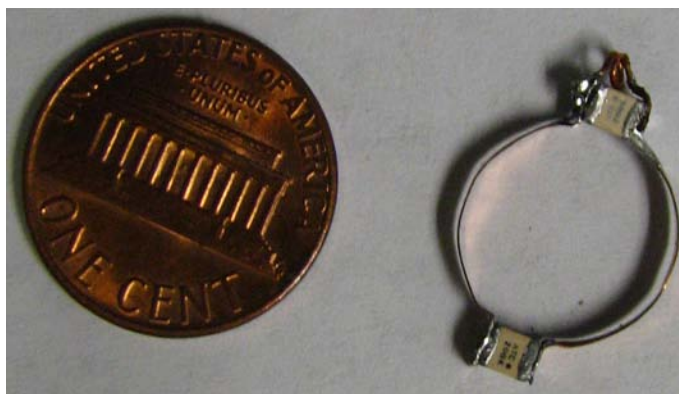


Figure 5-9. Photograph of the double-frequency  $^1\text{H}$ - $^{31}\text{P}$  implantable coil. (Photo by N.A. Volland).

Even though the double-frequency inductively-coupled coil system could be matched to  $50\ \Omega$  on the bench using the two variables matching capacitors originally placed in the circuit, it was only for one frequency at a time. It was found that the matching at  $^{31}\text{P}$  frequency required high matching capacitors values, while the matching at  $^1\text{H}$  frequency required smaller capacitor values. To compensate for this matching issue, a matching network was quickly implemented on the double-frequency surface coil (107). A tank circuit was used as a matching network (Figure 5-10). The initial matching capacitors were replaced by capacitors with smaller capacitance values (Voltronics Corporation, Denville, NJ, 0.5-8 pF) to allow the matching network to match the system to  $50\ \Omega$  at the higher frequency since the tank capacitor dominated the matching of the high frequency. The inductors were small solenoids, made of 28 AWG copper wires, hand wound around a 16 AWG copper wire, and placed over the small matching capacitors to allow the matching network to match the system to  $50\ \Omega$  at the lower frequency since the tank inductor dominated the matching of the system.

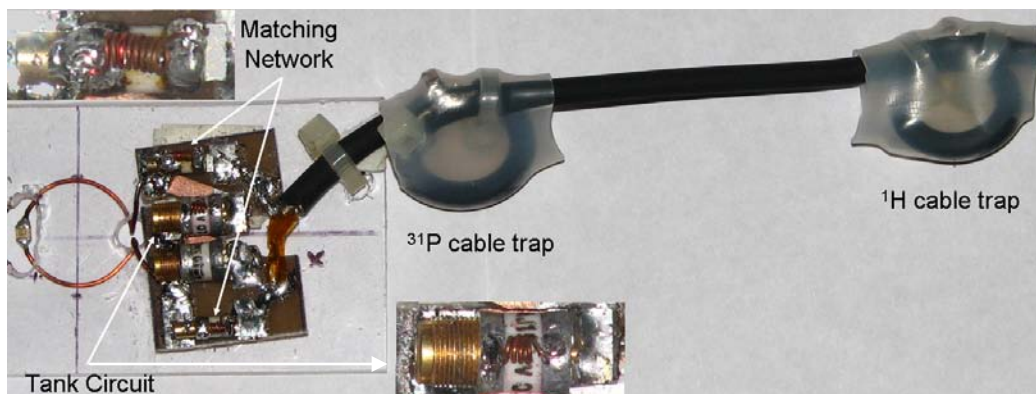


Figure 5-10. Photograph of the double-frequency  $^1\text{H}$ - $^{31}\text{P}$  surface coil. (Photo by N.A. Volland).

No  $^1\text{H}$ - $^{19}\text{F}$  inductively-coupled implantable coil system was built. The fact that the (-) mode of the lower frequency and the (+) mode of the higher frequency coupled to each other because of their closeness and their shift away from each other made it harder to actually tune the system at the desired high frequency. Furthermore, the coupling capacitors ( $C_{\text{Tui}}$  and  $C_{\text{Ksv}}$  on

Figure 5-2) were very small ( $< 1\text{pF}$ ), which anticipated problems for the implantable coil to be properly tuned when coated and loaded. In order to build and test a  $^1\text{H}$ - $^{19}\text{F}$  system, a better design will have to be investigated in the future.

Bench testing was performed and resonant frequency and Q factor of the different coils built and tested are summarized in Table 5-1. The inductively-coupled systems for  $^{31}\text{P}$  detection (single and double frequencies) had to be quickly adapted to account for a skin depth of  $4.75\ \mu\text{m}$  in the circuit at  $190.5\ \text{MHz}$ . To decrease the resistive loss in the circuit as much as possible, the wire thickness needed to be more than 5 times the skin depth. This involved the replacement of the  $35\text{-}\mu\text{m}$ -thick copper tape of the surface coils by a round 20 AWG wire ( $0.812\ \text{mm}$  diameter). The Q of the surface coils of these coupled-coil systems improved by at least 20% after this change and they are the only ones listed on Table 5-1 for these systems.

The surface coil of the single-frequency inductively-coupled implantable coil systems has a Q of  $72.2 \pm 4.95$  ( $\pm 6.86\%$ ) when resonating at  $493.2\ \text{MHz}$  for  $^1\text{H}$  detection ( $n = 4$ ), a Q of  $63.3$  when resonating at  $464.27\ \text{MHz}$  for  $^{19}\text{F}$  detection ( $n = 1$ ), and a Q of  $54.6$  when resonating at  $199.6\ \text{MHz}$  for  $^{31}\text{P}$  detection ( $n = 1$ ). The surface coil of the double-frequency inductively-coupled implantable coil system has a Q of  $50.81$  when resonating at  $475.1\ \text{MHz}$  for  $^1\text{H}$  detection ( $n = 1$ ) and a Q of  $34.30$  when resonating at  $195.5\ \text{MHz}$  for  $^{31}\text{P}$  detection ( $n = 1$ ). The implantable loop-gap resonator has an average Q of  $203.90 \pm 6.20$  ( $\pm 3.04\%$ ) when resonating at  $491.81 \pm 3.38$  ( $\pm 0.69\%$ )  $\text{MHz}$  for  $^1\text{H}$  detection ( $n = 7$ ), an average Q of  $171.86 \pm 13.78$  ( $\pm 8.01\%$ ) when resonating at  $467.22 \pm 2.49$  ( $\pm 0.53\%$ )  $\text{MHz}$  for  $^{19}\text{F}$  detection ( $n = 3$ ), and an average Q of  $122.9 \pm 5.18$  ( $\pm 4.22\%$ ) when resonating at  $202.6 \pm 0.14$  ( $\pm 0.53\%$ )  $\text{MHz}$  for  $^{31}\text{P}$  detection ( $n = 3$ ). The implantable loop gap resonator of the double-frequency inductively-coupled implantable coil system has an average Q of  $20.26 \pm 4.34$  ( $\pm 21.44\%$ ) when resonating

at  $491.27 \pm 1.75$  ( $\pm 0.36\%$ ) MHz for  $^1\text{H}$  detection, and an average Q of  $47.93 \pm 13.40$  ( $\pm 27.95\%$ ) when resonating at  $202.35 \pm 2.05$  ( $\pm 1.01\%$ ) MHz for  $^{31}\text{P}$  detection ( $n = 2$ ). The single-frequency inductively-coupled implantable coil system has an average Q of  $96.21 \pm 3.70$  ( $\pm 3.85\%$ ) when resonating at 470.75 MHz for  $^1\text{H}$  detection ( $n = 7$ ), an average Q of  $85.56 \pm 3.00$  ( $\pm 3.51\%$ ) when resonating at 442.86 MHz for  $^{19}\text{F}$  detection ( $n = 3$ ), and an average Q of  $73.23 \pm 4.60$  ( $\pm 6.28\%$ ) when resonating at 190.5 MHz for  $^{31}\text{P}$  detection ( $n = 3$ ). The double-frequency inductively-coupled implantable coil system has an average Q of  $31.05 \pm 0.49$  ( $\pm 1.59\%$ ) when resonating at 470.75 MHz for  $^1\text{H}$  detection and an average Q of  $36.25 \pm 0.35$  ( $\pm 0.95\%$ ) when resonating at 190.5 MHz for  $^{31}\text{P}$  detection ( $n = 2$ ).

The single-frequency inductively-coupled coil systems have an average coupling factor (k) of  $0.082 \pm 0.0035$  ( $\pm 4.22\%$ ) determined from the frequency split around the desired resonant frequency obtained on the simulated voltage standing wave ratio (VSWR) graph from the systems for the detection of  $^1\text{H}$ ,  $^{19}\text{F}$ , and  $^{31}\text{P}$ . On the bench this average k became  $0.086 \pm 0.007$  ( $\pm 7.63\%$ ). The double-frequency  $^1\text{H}$ - $^{31}\text{P}$  inductively-coupled coil system, however, has a different coupling factor (k) for both frequencies when determined from the frequency split around the desired resonant frequency obtained on the simulated voltage standing wave ratio (VSWR) graph: 0.055 at 190.5 MHz ( $^{31}\text{P}$ ) and 0.021 at 470.75 MHz ( $^1\text{H}$ ). On the bench this average k became  $0.074 \pm 0.0023$  ( $\pm 3.19\%$ ) and  $0.049 \pm 0.0001$  ( $\pm 0.28\%$ ) respectively. The double-frequency  $^1\text{H}$ - $^{19}\text{F}$  inductively-coupled coil system also has a different coupling factor (k) for both frequencies when determined from the frequency split around the desired resonant frequency obtained on the simulated voltage standing wave ratio (VSWR) graph: 0.017 at 442.8 MHz ( $^{19}\text{F}$ ) and 0.062 at 470.75 MHz ( $^1\text{H}$ ). This last factor is biased by the coupling occurring between the (-) mode of the lower frequency and the (+) mode of the higher frequency.

Table 5-1. Implantable coil, surface coil, and inductively-coupled implantable coil system characteristics. Resonant frequency (f) and quality factor (Q) for: SC, IC, and coupled-coil systems for  $^1\text{H}$  detection (SCH; ICH; SH),  $^{19}\text{F}$  detection (SCF; ICF; SF),  $^{31}\text{P}$  detection (SCP; ICP; SP), and  $^1\text{H}$ - $^{31}\text{P}$  simultaneous detection (SCHP; ICHP; SHP).

Coil #*	# of coils tested	f (MHz)	Q
SCH	4	493.2	72.2 ± 4.95 (± 6.86%)
SCF	1	464.27	65.25 ± 2.76 (± 4.23%)
SCP	1	199.6	54.6
-----			
SCHP_H	1	475.1	50.81
SCHP_P <sup>+</sup>	1	195.5	34.30
-----			
ICH	7	491.81 ± 3.38 (± 0.69%)	203.90 ± 6.20 (± 3.04%)
ICF	3	468.39 ± 1.55 (± 0.33%)	182.54 ± 3.55 (± 1.95%)
ICP	3	202.60 ± 0.14 (± 0.07%)	122.90 ± 5.18 (± 4.22%)
-----			
ICHP_H	2	491.27 ± 1.75 (± 0.36%)	20.26 ± 4.34 (± 21.44%)
ICHP_P	2	202.35 ± 2.05 (± 1.01%)	47.93 ± 13.40 (± 27.95%)
-----			
SH	7	470.75	96.21 ± 3.70 (± 3.85%)
SF	3	442.86	80.4 ± 3.11 (± 3.87%)
SP	3	190.5	73.23 ± 4.60 (± 6.28%)
-----			
SHP_H	2	470.75	31.05 ± 0.49 (± 1.59%)
SHP_P <sup>+</sup>	2	190.5	36.25 ± 0.35 (± 0.97%)

\*The SC and IC were tested individually unloaded. The inductively-coupled implantable coil systems were tested using the 1-cm diameter tube water sample.

<sup>+</sup> The double frequency  $^1\text{H}$ - $^{31}\text{P}$  surface coil and inductively-coupled coil system could not be matched to 50  $\Omega$  (or 20dB). Consequently, the Q indicated above was determined when the coils had a match around 10 dB and not comparable to the other coils characteristics (144).

The double-frequency inductively-coupled implantable coil system did not pass the test since the system could not be match to 50  $\Omega$  for both frequencies at once when using the

matching network. The matching network will have to be optimized before this system can be tested further. Using variable inductors instead of hand-wound inductors would be the first improvement to be investigated.

#### 5.4.2 Implantable Coil Coating

The single-frequency  $^{19}\text{F}$  and  $^{31}\text{P}$  implantable coils were coated with PDMS for *in vitro* testing as the double-frequency systems did not pass the bench test. Similar to the  $^1\text{H}$  implantable coil coating, a 1-mm PDMS layer and a 2-step process were used as described in Section 3.3.2.4. The frequency shift observed for the single frequency  $^1\text{H}$  implantable coils was also observed for the  $^{19}\text{F}$  coils. A resonant frequency shift of  $-6.46 \pm 0.82$  ( $\pm 12.75\%$ ) was detected for the coated implantable coils compared to the non-coated similar coil ( $n = 5$ ). Three coils were found with a defective coating and were removed from the experiments. The quality factor of these coated coils was better than the one of the uncoated coils (22% higher on average) as the frequency of the coated coil shifted down compared to the uncoated coil and its bandwidth decrease slightly. As mentioned in Section 3.5, this indicates that the coating introduces more capacitance in the circuit than resistance. As loading further changes the coil characteristics, these  $^{19}\text{F}$  coated implantable coils were embedded in the mouse abdomen-like phantom. The loading caused an additional resonant frequency shift from the PDMS coating one of  $-28.19 \pm 2.48$  ( $\pm 8.78\%$ ) MHz. This shift in addition to the ‘coating’ shift was taken into account to build the  $^{19}\text{F}$  implantable loop-gap resonator coils which were used for *in vitro* and *in vivo* studies. The quality factor of these loaded coated coils decreased by a factor 9.5 compared to the coated coil Q determined in air ( $17.85 \pm 1.92$  ( $\pm 10.77\%$ )). The implantable coils to be used loaded were created with a resonant frequency at least 35 MHz higher than their predecessors ( $506.12 \pm 5.20$  ( $\pm 1.03\%$ );  $n = 7$ ). This made the inductively-coupled  $^{19}\text{F}$  coil systems resonate at the

desired frequency of 442.86 MHz after coating and loading with media culture and ready to be tested in the magnet for *in vitro* studies.

The frequency shift caused by the coating and observed for the single-frequency  $^{31}\text{P}$  implantable coils was very small [ $-1.71 \pm 1.28$  ( $\pm 74.94\%$ )] compared to the two other higher frequency implantable coils ( $n = 6$ ). The quality factor of these coated coils was slightly lower than the one of the uncoated coils (9% lower on average). As loading further changes the coil characteristics, these  $^{31}\text{P}$  coated implantable coils were embedded in the mouse abdomen-like phantom. This loading caused an additional resonant frequency shift from the PDMS coating one of  $-2.58 \pm 0.3$  ( $\pm 11.76\%$ ) MHz. This shift was small again. The quality factor of these loaded coated coils decreased by a factor 2.75 compared to the coated coil Q determined in air [ $42.85 \pm 3.01$  ( $\pm 7.03\%$ )]. Combining the coating and loading effects, the implantable total frequency shift was below -5 MHz. This allowed the coils to be used for *in vitro* and *in vivo* studies without even altering them and made the inductively-coupled  $^{31}\text{P}$  implantable coil systems resonate at the desired frequency of 190.5 MHz after coating and loading and ready to be tested in the magnet for *in vitro* studies.

### 5.4.3 Sample Studies

The coupled-coil systems used in the magnet study included: 1) one single-frequency coupled-coil system for  $^{19}\text{F}$  detection (442.86 MHz); 2) one single-frequency coupled-coil system for  $^{31}\text{P}$  detection (190.5 MHz). The single-frequency coupled-coil system for  $^1\text{H}$  detection (470.75 MHz) developed in Chapter 3 was used as a reference. Images were successfully acquired using all systems on their respective high concentration samples under unloaded conditions.  $^{19}\text{F}$  images and spectra were also achieved from the beads with PFCE emulsion, and  $^{31}\text{P}$  spectra from cells in alginate beads were attempted. The multiple-frequency

$^1\text{H}$ - $^{31}\text{P}$  inductively-coupled implantable coil system was not tested in the magnet as the matching of the system to  $50\ \Omega$  was not achieved in the bench.

#### **5.4.3.1 Perfluorocarbon detection**

For the different concentrations of PFCE emulsion (0.4%, 1%, 2.5%, 5%, and 10% (v/v) /mL of alginate) used, images and spectra were acquired from the cell-free bead samples. 10% PFCE emulsion was given the most signal for both images and spectra. However, 2.5% PFCE emulsion was thought more appropriate to use for imaging as it is a relatively low PFCE content and it still allow an SNR of  $5.15 \pm 0.29$  ( $\pm 5.56\%$ ) within 4 minutes (Figure 5-11). This result would potentially allow  $T_1$  mapping imaging throughout the construct in the future. It is worthwhile noting that non-spatially selective sequences were used to acquire these  $^{19}\text{F}$  images and spectra and no signal coming from outside the construct was detected (Figure 5-11).

$^{19}\text{F}$  spectra were also acquired with acceptable SNR ( $> 2$ ) with all concentration of PFCE within a maximum of 8 minutes. When using the 0.4% PFCE emulsion, the spectra were acquired in 4.25 minutes with the SNR over 100 when using 256 averages. The longitudinal relaxation time ( $T_1$ ) of PFCE could not be determined from a series of images acquired with 2.5% PFCE emulsion within 30 minutes, the SNR may have been too low to allow the program to properly determine the value, since the results obtained for  $T_1$  were unrealistic. However, PFCE  $T_1$  was estimated at  $940 (\pm 8.7 \times 10^{-3})$  ms from spectrum data of a 0.4% PFCE emulsion entrapped in beads within 30 minutes (Figure 5-12).

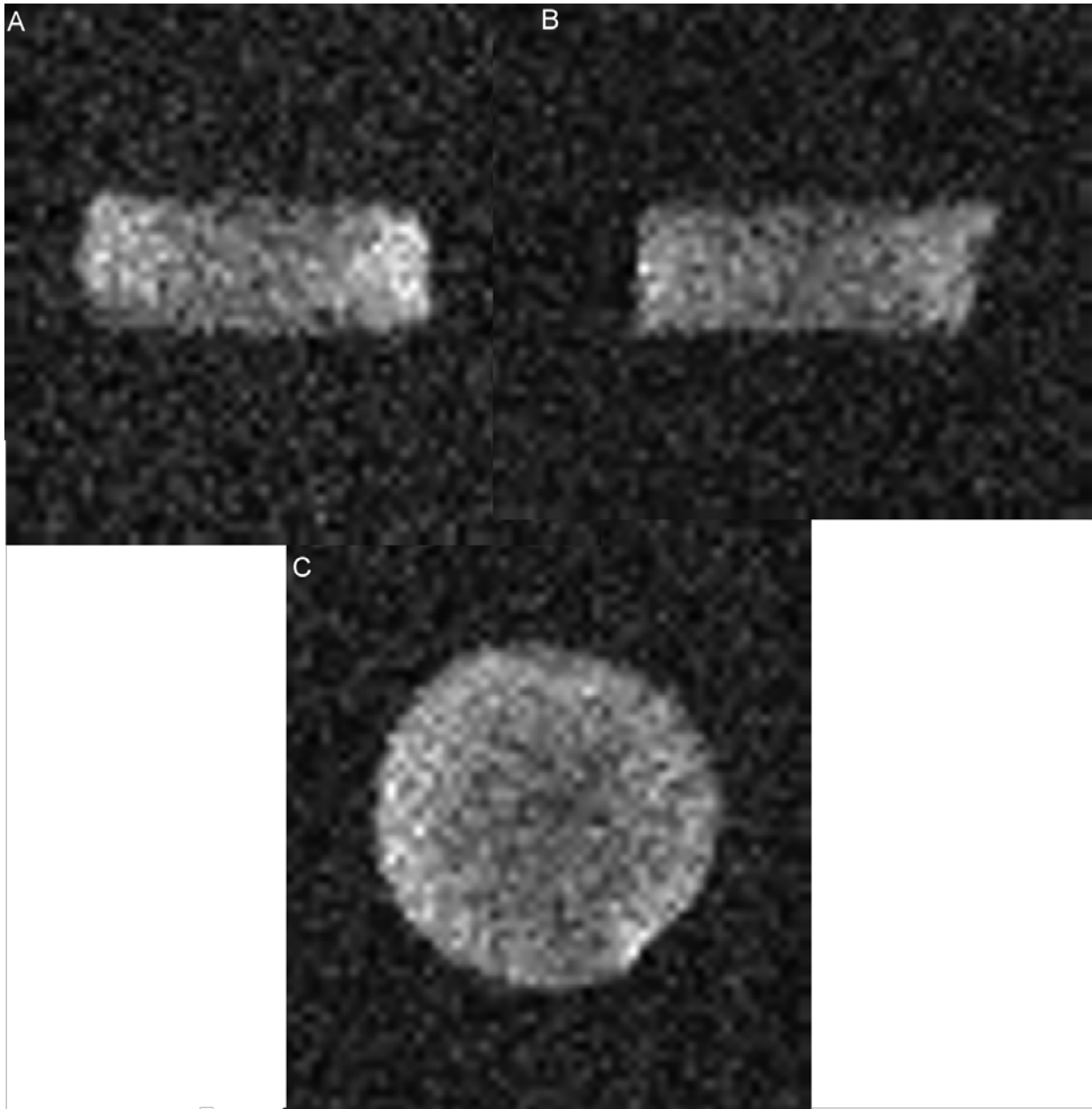


Figure 5-11.  $^{19}\text{F}$  images of a pancreatic construct surrounded by an implantable coil and containing BaA beads with 2.5% PFCE. A) Transversal view; B) sagittal view; and C) coronal view. An SE pulse sequence was used to acquire these images: TR = 1000 ms, TE = 10 ms, 2-mm slice thickness, 3 averages, FOV  $2 \times 2 \text{ cm}^2$  and matrix size  $64 \times 64$ .

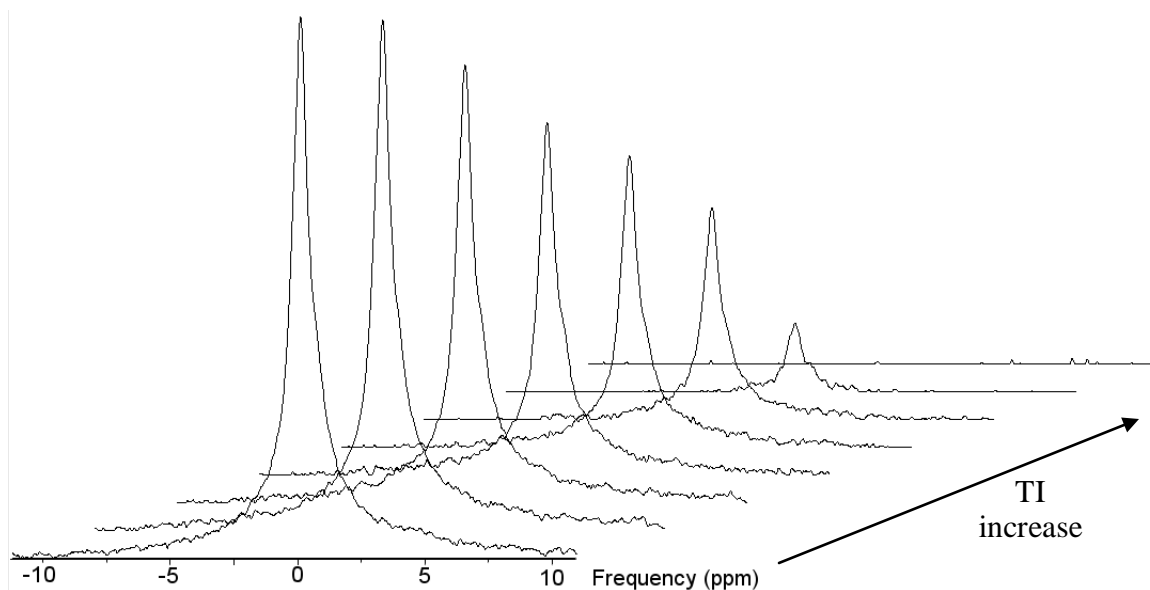


Figure 5-12.  $^{19}\text{F}$  spectrum series from BaA beads containing 0.4% PFCE within a pancreatic construct surrounded by an implantable coil. A series of inversion recovery pulse sequences were used to acquire these spectra in 30 mins (TR = 5013 ms, TI= 5000, 2500, 1500, 1000, 750, 500, 250, 10 ms, 256 averages) using an inductively-coupled implantable coil system for  $^{19}\text{F}$  detection under loaded conditions.

#### 5.4.3.2 Phosphorus detection

Spectra were successfully acquired from the solution samples with different concentrations of  $\text{Na}_2\text{HPO}_4^{-2}$  and ATP (100mM, 10mM, 5mM, 1mM, and 0.5 mM). Figure 5-13 displays a  $^{31}\text{P}$  spectrum obtained from a 0.5 mM of sodium phosphate and ATP solution. The spectrum was acquired in 35 minutes using a one-hard-pulse pulse sequence with TR = 2s and 1024 averages and an inductively-coupled implantable coil system for  $^{31}\text{P}$  detection under unloaded conditions. The SNR displayed on this spectrum was determined at 3.2, which is encouraging even though under unloaded conditions because physiological ATP level should be between 1 and 10 mM.

Spectra acquired from  $\beta\text{TC-tet}$  cells encapsulated in BaA beads did not display more than the signal from the inorganic phosphate (Pi) contained in the culture media. This proved that the inductively-coupled implantable coil system for  $^{31}\text{P}$  detection worked. However, the viability of the entrapped cells was questionable. The culture media was used during the magnet testing as

none of its compounds was known to interfere with ATP detection. However, it was later found that the pH of the media changed rather rapidly when in a low CO<sub>2</sub> concentration environment and this could have killed the cells. Cell density may have also been an issue in this early study on ATP detection. The number of cells in the sample may have also been too low to be detected.

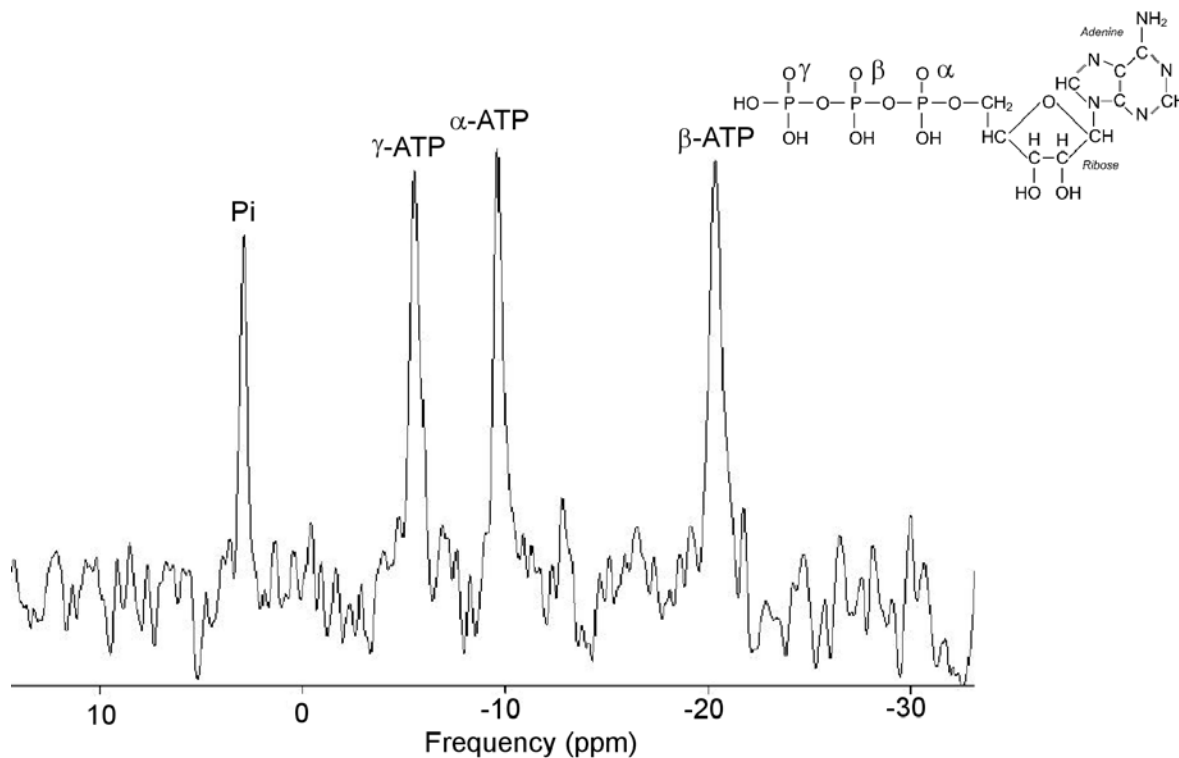


Figure 5-13. <sup>31</sup>P spectrum of a saline solution containing 500 μM of ATP and PO<sub>4</sub><sup>-2</sup>. The spectrum, displaying the peaks of the three different phosphate groups of ATP and inorganic phosphate (P<sub>i</sub>), was acquired using an inductively-coupled implantable coil system at 11.1 T within 35 minutes with an SNR of 3.2.

## 5.5 Discussion

Monitoring the viability and the bioenergetics status of cells as well as the oxygen concentration within a tissue-engineered construct, such as a bioartificial pancreas, using NMR techniques is a powerful tool to directly reflect the well being and functioning of the construct. In order to achieve such a complete monitoring, the use of different single-frequency inductively-coupled, implantable coil systems for <sup>1</sup>H, <sup>19</sup>F, and <sup>31</sup>P detection to perform NMR

measurements was explored. The development of double-frequency inductively-coupled implantable coil systems for simultaneous detection of  $^1\text{H}$  and  $^{19}\text{F}$ , and  $^1\text{H}$  and  $^{31}\text{P}$  detection was investigated in parallel to the construction of single-frequency coupled-coil systems. The single-frequency systems would serve as standards to assess the efficacy of the double-frequency systems. The double-frequency coupled-coil systems have the following advantages over single frequency systems for the study of tissue-engineered constructs: 1) simultaneous NMR measurements from  $^1\text{H}$ ,  $^{19}\text{F}$ , and  $^{31}\text{P}$  nuclei; and 2) direct correlation of the NMR results obtained from the detection of the different nuclei under investigation.

The well-being and appropriate functioning of a bioartificial construct in its environment and the time line prediction of its potential failure are key in monitoring such an implanted device. Obtaining NMR measurements for different nuclei helps reach these goals. The use of single-frequency inductively-coupled coil systems has shown a high sensitivity for  $^1\text{H}$  detection (Chapter 3). The use of these systems for  $^{19}\text{F}$  and  $^{31}\text{P}$  detection here also showed to be of high sensitivity in phantoms. A concentration of 2.5% PFCE emulsion was detected *in vitro* with both  $^{19}\text{F}$  MRI and MRS, with an SNR above 5 for imaging and above 100 for spectroscopy. Lower than physiological levels of ATP were also detected with a SNR over 3 under unloaded conditions. If these levels of detection of fluorine and phosphorus ( $^{19}\text{F}$  and  $^{31}\text{P}$ ) are encouraging, the use of multiple-frequency inductively-coupled implantable coil systems is more desirable than the use of single-frequency inductively-coupled system as only one coil can be implanted within a construct *in vivo* and the correlation of the results would be made easier.

However, their construction requires several considerations as a large number of parameters intervene when the coils have two resonant frequencies each. The main parameter was the ratio of the tank circuit inductance to the coil/sample inductance (main circuit

inductance). To engender fewer resistive losses in the main circuit at the lower frequency (less sensitive nucleus) compared to the higher frequency (107), this ratio was kept at 5 in the case of the  $^{31}\text{P}$ - $^1\text{H}$  inductively-coupled implantable coil system since the lower frequency was much less sensitive than the higher one. This also kept the circuit sensitivity at lower frequency close to 90%. However, overall resistive losses at each frequency for a multiple-frequency tank system are always higher than the losses at the same frequency for a single-frequency system (118).

In the development of  $^{19}\text{F}$ - $^1\text{H}$  inductively-coupled implantable coil system; the tank inductance to main circuit inductance ratio was kept close to 1 since the frequencies had almost the same high sensitivity (167) and the resistive losses were going to be comparable (about 20% for both). Even though the multiple-frequency inductively-coupled implantable coil systems were not tested in the magnet, their higher electrical losses than the single frequency system may have been observable through their  $Q$  and coupling factor ( $k$ ) determined at the system different frequencies. The coupling factor is defined as a geometry factor (Equation 5-1) which was easily verified with the different single-frequency inductively-coupled coil systems developed at different frequencies in this study. However, it does not appear to be the same for multiple-frequency inductively-coupled coil systems as  $k$  of both frequencies of the system is smaller than  $k$  of the single-frequency inductively-coupled coil system when the geometry of all the systems is identical. Furthermore, the higher frequency had a smaller coupling factor than its lower frequency counterpart. It is possible that the simple relationship between the mutual inductance and the coupling factor of the system does not hold for double-frequency inductively-coupled coil system because the system inductances and mutual inductance has a complex dependence on more than one inductor and different at both frequencies. It is also worthwhile noted that the  $Q$

of the double-frequency inductively-coupled implantable coil system is lower than that of its single-frequency counterparts at both frequencies.

The construction of multiple-frequency implantable coils was rendered difficult because of the fixed capacitor used. Even though the tuning capacitor mainly affects the tuning of the lower frequency and the tank capacitor the tuning of the higher frequency, the discrete capacitor values available prevented tuning to the exact frequency required. Multiple capacitors configured in parallel could have facilitated obtaining the right combination, but size restriction will have to be considered before doing this. Furthermore, matching the circuit to  $50 \Omega$  for both frequencies simultaneously was rendered difficult by the use of fixed inductors. Variable inductors may be preferable to allow fine tuning with different loading and need to be considered for further work on the multiple-frequency inductively-coupled coil system.

The study of the coating and loading effects on single-frequency implantable coils showed that coating and loading have larger effects at higher frequencies than at lower ones. Even though working at higher field means better sensitivity, this could be an advantage for multiple-frequency inductively-coupled systems as  $^{31}\text{P}$  (less sensitive nuclei) will not be affected as drastically as  $^{19}\text{F}$  or  $^1\text{H}$  at 11.1 T.

In the sample studies, the SNR and acquisition time of  $^{19}\text{F}$  images obtained using a 2.5% PFCE emulsion entrapped in beads confined in the construct indicated the possibility of generating  $T_1$  mapping images within 30 mins. Such a measurement would carry information on the oxygenation throughout the constructs *in vivo* at different time point during a study period. However, when attempted, the images acquired in the imaging series to determine  $T_1$  had a too low SNR to allow an accurate determination of  $T_1$ . No image series could be acquired in a reasonable amount of time when using a 0.4% PFCE emulsion. Nonetheless, a series of spectra

was acquired from a construct containing beads with 0.4% PFCE emulsion *in vitro* and  $T_1$  of PFCE was determined accurately (940 ms). This value represents the average longitudinal relaxation time of PFCE throughout the construct under normoxic conditions. It is in agreement with the estimation done by Gross *et al.* at a similar magnetic field strength (11.7T) with a similar sample (0.4% PFCE). Furthermore, the  $^{19}\text{F}$  detection sensitivity was kept constant over at least 2 weeks (95). This demonstrates the possibility to conduct studies on the evolution of the oxygen level within the pancreatic constructs over time *in vitro* and *in vivo* using a single or double-frequency inductively-coupled coil system and MRS, localized or not. Either the concentration of PFCE in the beads or the sensitivity of the method will have to be increased, or localized spectroscopy will have to be implemented to be able to perform  $T_1$  mapping and study the oxygenation in different regions of the construct over time.

The SNR displayed on the ATP spectrum (3.2) acquired from a 0.5 mM ATP solution shows adequate sensitivity ( $\text{SNR} > 2$ ) to perform studies on cell bioenergetics *in vitro* and *in vivo* over time using a single-frequency implantable coil system. However, no ATP signal could be detected from cells entrapped in beads confined in a coil-construct assembly. The cells viability was questionable during the NMR experiments and will have to be checked more closely in the future, since ATP washed out relatively rapidly after cell death. The cell density within the construct may also be of concern and will need to be increased in future experiments, at least initially to optimize the method and determine the limit of sensitivity of the method. Other groups have successfully performed  $^{31}\text{P}$  MRS at the same field strength (11.1 T) using the same pulse sequence and parameters in combination with a surface coil of similar size (173), but less sensitive than an inductively-coupled implantable coil system (Chapter 3). Coupled-coil system design adaptation will have to be made prior to a double-frequency inductively-coupled

implantable coil system development since its design will only preserve 90% of  $^{31}\text{P}$  detection sensitivity from a single frequency system (118).

## 5.6 Summary

Inductively-coupled implantable coil system for  $^1\text{H}$ ,  $^{19}\text{F}$ ,  $^{31}\text{P}$ , simultaneous  $^1\text{H}$  and  $^{31}\text{P}$ , and simultaneous  $^1\text{H}$  and  $^{19}\text{F}$  detection have been developed and their performance analyzed.  $^1\text{H}$ ,  $^{19}\text{F}$ ,  $^{31}\text{P}$ , and  $^1\text{H}$ - $^{31}\text{P}$  systems were successfully built and characterized on the bench. NMR images and spectra were also obtained at 11.1 T with the three single-frequency coupled-coil systems demonstrating the capability of inductively-coupled implantable coil systems to monitor bioartificial pancreas constructs using different nuclei detection at high field.

$^{19}\text{F}$  NMR imaging was successfully performed on a 2.5% PFCE emulsion sample when a single-frequency inductively-coupled coil system for  $^{19}\text{F}$  detection was used. These images also showed that no localization was necessary when performing  $^{19}\text{F}$  spectroscopy since fluorine was confined to the bioartificial construct.  $^{19}\text{F}$  spectra were also easily acquired with even lower PFCE emulsion concentration (0.4%) under loaded conditions allowing the determination of PFCE  $T_1$ . This attests the feasibility of monitoring the evolution of the oxygen level within the construct via spectrum series acquisitions. Similarly, ATP was found to be detectable at cellular concentration via NMR spectroscopy using a single-frequency inductively-coupled implantable coil system for  $^{31}\text{P}$  detection. These results suggest the performance standards for the development of multiple-frequency inductively-coupled implantable coil systems.

The feasibility of double-frequency inductively-coupled implantable coil systems for the detection of  $^1\text{H}$ ,  $^{31}\text{P}$ , and  $^{19}\text{F}$  were also explored, as these systems would allow the simultaneous detection of key nuclei of different sensitivity, yet critical, to quantify implanted bioartificial organ function. The development of such systems thus far shows that they are feasible using tank circuit theory, even though these systems are complex and requires lots of considerations.

They also showed their potential over single-frequency coupled-coil systems, as they can detect more than one nucleus at a time and allow direct correlation of the results from these multiple detections. The pursuance of their development is encouraged by the possibility of developing a triple frequency inductively-coupled implantable coil system in the future.

Efforts can now focus on further developments of the double-frequency inductively-coupled implantable coil systems to allow the detection of more potential early marker of pancreatic construct failure before hyperglycemia could be detected. However, having a functioning construct is also a major consideration for future studies on the non-invasive monitoring and complete characterization of a bioartificial construct. Consequently, generating cell-containing bioartificial construct and keeping the insulin-producing cells alive within a bioartificial construct (including an implantable coil) *in vitro* and *in vivo* was studied next.

CHAPTER 6  
CHARACTERIZATION OF A BIOARTIFICIAL PANCREAS AS PART OF AN  
IMPLANTABLE COIL-CONSTRUCT ASSEMBLY

**6.1 Introduction**

Bioartificial pancreatic substitutes, generated by either microencapsulation or macroencapsulation, have already shown potential as alternative to current treatments of type 1 diabetes. Non-invasive, high-sensitivity monitoring techniques, like NMR imaging and spectroscopy using inductively-coupled implantable coil systems, are well-suited and preferable to directly monitor these pancreatic constructs, their performances, and life span in a given environment. However, the inclusion of the implantable RF coil within the bioartificial construct places some restrictions on the construct design. In this study, two flat-disk macroconstructs were studied: (1) one made with alginate foam, and (2) one made with alginate beads. Their design and materials, their construction, and inclusion in the middle of an implantable RF coil were investigated. Their effects on the entrapped  $\beta$ TC-tet cells viability and function and their ability to reverse a streptozotocin-induced diabetic state in mice were evaluated. The data show that a coil-construct assembly allowed insulin-producing cells to function and stay viable for extended period of time. The implantable coil – bioartificial construct assembly implantation in a mouse peritoneal cavity also demonstrates the return of normoglycemia in diabetic mice while allowing for enhanced non-invasive monitoring of implanted constructs using NMR methods. Assembly pre-treatment and coating are also discussed to decrease construct fibrotic overgrowth.

**6.2 Background**

Tissue-engineered pancreatic constructs emerged over twenty-five years ago. Bioartificial pancreatic substitutes, also called bioartificial pancreas (BAP), have already shown potential as an alternative to current treatments of type 1 diabetes. These constructs are comprised of individual insulin-producing cells or islet-like clusters of insulin-producing cells within a

biocompatible, semipermeable membrane. The membrane provides mechanical protection and partial immunoisolation. Optimally, it should be permeable to low molecular weight nutrients and metabolites, but impermeable to higher molecular weight molecules, such as immunoglobulin and albumin. Current techniques to generate these constructs are microencapsulation (29,34) and macroencapsulation (5,6). Microencapsulation creates microspheres or beads with diameter from a fraction of a millimeter to a couple of millimeters (33). Their small size makes the capsules implantable almost anywhere in the body with a simple needle, the peritoneal cavity being the main and easiest implantation site (33,35,36). Alginate has often been used as the semipermeable membrane for microencapsulation (33,37,55). Its structural integrity, ease of handling, and diffusion properties allow the entrapped cells to live and function as normally as possible. One drawback of these microconstructs is their dispersion throughout the body making *in vivo* close monitoring and retrieval of this type of construct nearly impossible. Macroencapsulation generates large semipermeable capsules in which a large number of cells can be suspended (38-41). The macroconstruct semipermeable matrix can be made with different polymers (38,41) or nuclepore membranes can be mounted on a silicone ring (39). They can take the shape of a tube or a planar sheet. Their size renders them confined to their site of implantation and easy to locate, monitor directly, and retrieve. Furthermore, the use of higher magnetic field strength along with inductively-coupled implantable coil systems showed a great improvement in the sensitivity of NMR imaging and spectroscopy to non-invasively monitor a bioartificial pancreas (see Chapter 3). However, the inclusion of the implantable RF coil within the BAP places some restrictions on the construct design. Per coil design, a flat-disk BAP represents the optimal design for this approach.

This chapter investigates two type of flat-disk bioartificial construct design amenable for inclusion in the implantable RF coil: (1) one implantable coil-alginate foam assembly, and (2) one implantable coil-alginate bead assembly. The preliminary *in vitro* and *in vivo* studies presented in this chapter outline the design, construction, and characterization of a BAP and its inclusion in the middle of an implantable RF coil. It reports the impact of the materials used to build the construct on the entrapped insulin-secreting cells (viability essentially) and on the coil (stability), and discusses technical aspects important in developing a construct with appropriate structural integrity and adequate cell function while being monitored directly via NMR.

### **6.3 Materials and Methods**

#### **6.3.1 Cell Culture**

Murine insulinoma  $\beta$ TC-tet cells (48) were obtained from Shimon Efrat's laboratory (Albert Einstein College of Medicine, Bronx, NY). They were cultured in T-flasks in monolayers and fed every 2-to-3 days with high glucose Dulbecco's Modified Eagle's Medium (DMEM, Invitrogen Corp., Carlsbad, CA), supplemented with 10% fetal bovine serum (FBS, Lonza, Williamsport, PA), 1% penicillin-streptomycin (Cellgro, Manassas, VA) , and 1% L-glutamine (Cellgro, Manassas, VA) until they reached confluence. Cultures were maintained at 37°C under humidified and gas-regulated (5% CO<sub>2</sub> / 95% air) conditions in an incubator. The cells were collected from the flasks for construct fabrication using 0.01% Trypsin (Sigma, St. Louis, MO). Cell passages from 31-55 were used for these studies.

#### **6.3.2 Implantable Coil-Pancreatic Construct Assembly**

Two types of pancreatic constructs were generated from the ring formed by the PDMS-coated coil presented in Section 3.4.3: 1) including alginate sponge or foam disks (149,150); and 2) including alginate beads (33,37,55). The diameter of the construct did not exceed 1 cm in

order to fit within the middle of the coated implantable coil and its thickness did not exceed 500  $\mu\text{m}$  to minimize the diffusion limitations.

### 6.3.2.1 Implantable coil-alginate foam assembly

Alginate foam was purchased (Novomatrix, Trondheim, Norway). Three types of foam were considered: 25%, 50%, and 75% calcium-cation saturated. Circular, 1-cm diameter pieces were punched out of this foam and placed in the middle of the PDMS-coated coil (Figure 6-1). The ability of the different foams to swell or shrink was tested first by soaking them in PBS. The piece of foam with the minimal deformation capability in solution was selected as this can largely influence the viability of the cells and stability of the construct during the course of an *in vitro* and *in vivo* study. This piece of foam was then fixed in the middle of a PDMS-coated coil with non-absorbable surgical sutures prior to *in vitro* testing.



Figure 6-1. Photograph of an implantable coil - alginate foam construct assembly prior to being soaked in PBS. (Photo by N.A. Volland).

### 6.3.2.2 Implantable coil-alginate beads assembly

To keep the small-diameter beads together in the middle of the implantable coil, a biocompatible polyetheretherketone (PEEK) 300- $\mu\text{m}$  mesh (Small Parts, Inc., Miami Lakes, FL) was added on the top and bottom of the ring formed by the PDMS-coated coil (Figure 6-2). The cavity created, similar to the construct developed by Hirotsu *et al.* (39,56), was 4mm high and 10mm in diameter, or a volume of 0.31  $\text{mm}^3$  (0.31  $\mu\text{l}$ ). The meshes were fixed on the ring with a

very fine layer of PDMS. A small portion of one of the meshes was left unattached to allow the bead insertion after their creation via a 16G needle. For *in vitro* studies only, three 2-mm diameter stainless steel spheres were attached with the mesh to one side of the meshed PDMS ring to create a stand and help with the homogeneous diffusion of nutrients and oxygen through the construct.

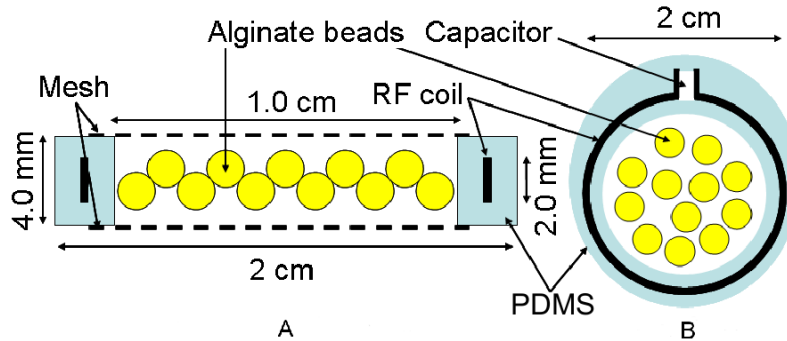


Figure 6-2. Implantable coil-bioartificial pancreatic construct assembly diagram and dimensions. A) Transverse view and B) coronal view of the assembly. The alginate beads are contained in the cylindrical cavity created by the PDMS-coated implantable coil and a 300- $\mu$ m mesh screen.

All the implantable coil-construct assemblies were first acid washed and soaked in a 0.1 M solution of hydrochloric acid for 30 minutes to break down the proteins left on the coil during manufacturing, then soaked with a 75% ethanol solution for one hour to neutralize the broken down proteins. These assemblies were then rinsed with distilled water to wash out the proteins and autoclaved for sterilization prior to *in vitro* or *in vivo* use.

### 6.3.3 Cell Entrapment

#### 6.3.3.1 Alginate foam

The coil-construct assemblies were first soaked into culture media for 2 hours to get the foam wet prior to *in vitro* studies. PBS was used as a wetting agent prior to *in vivo* studies. Freshly trypsinized cells ( $3.5 \times 10^7$  cells/ml alginate) were then seeded at the top and/or bottom of the foam via a micropipette.

### 6.3.3.2 Alginate beads

A low viscosity (325 mPa) high (62%) mannuronic / low (38%) guluronic (LVM) alginate (NovaMatrix, Oslo, Norway) was used to generate the beads (174). The alginate solutions were prepared by dissolving LVM alginate powder into physiological saline (0.85% NaCl) at a 2% w/v concentration overnight. Both cell-free and cell-containing beads were prepared. Freshly trypsinized cells were mixed with the 2% alginate solution right before making the cell-containing beads. Beads were generated by running the alginate solution (with or without cells) through a syringe at a constant flow rate and dropping it in a cationic cross-linking solution with an electrostatic bead generator (Nisco, Zurich, Switzerland) to set the bead diameter. The bead diameter was kept between 400 and 600  $\mu\text{m}$  as physiology indicates that confluent cells should be within 200-250  $\mu\text{m}$  of an oxygen and nutrient access for sufficient oxygenation and adequate nutrient supply essential to their well-being. The number of cells in the solution at the time of encapsulation was set at  $3.5 \times 10^7$  cells/ml of alginate. Calcium cations from a 100 mM  $\text{CaCl}_2$  solution and barium cations from a 55 mM  $\text{BaCl}_2$  solution were indifferently used as crosslinkers.

Calcium-crosslinked alginate beads were then coated with poly-L-lysine (PLL; Sigma, St. Louis, MO) using protocols developed by Lim and Sun (34) and implemented regularly by our laboratory (151,175) to increase the bead stability and give them an acceptable porosity. These beads were then dipped in a 0.2% w/v alginate solution (using the same alginate composition as the core alginate) to decrease the potential immune response to PLL and form the alginate/poly-L-lysine/alginate (APA) beads. As barium is a stronger ionic crosslinker, no further processing was needed to produce barium-crosslinked alginate (BaA) beads (176). The beads were only washed up to 3 times in  $\text{BaCl}_2$  solution of decreasing concentration to increase the saturation of alginate with  $\text{Ba}^{2+}$  and enhance the of the alginate network.

Both types of beads were rinsed three times in culture media after manufacturing to make sure all potential harmful compounds used in the process were removed from the solution. Different aliquots (up to 0.3 mL) of freshly made beads (APA or BaA) were transferred in the middle of the meshed PDMS-coated coil ring constructs directly after manufacturing.

#### **6.3.4 Culture Propagation**

For *in vitro* studies, three similar cell-containing implantable coil - construct assemblies were placed into one high-walled 60 mm Petri dish, fed with complete DMEM every 2-3 days and placed on a platform rocker (Stovall Life Sciences, Greensboro, NC) in the incubator. The sensitivity of temporal glucose changes was increased by this practice. The error in cell number estimation was also decreased.

To reduce immune response to implanted coil-construct assemblies, construct made for *in vivo* work were never rinsed with culture media at any time during the preparation, but with sterile phosphate buffer saline (PBS, Invitrogen, Carlsbad, CA), supplemented with 20 mM glucose, antibiotics (100 U/ml penicillin, 100 ng/ml streptomycin, and 100 nM dexamethasone), and buffering agent (20 mM HEPES). The constructs were kept in this solution until implantation in a mouse peritoneal cavity. Implantation occurred less than 2 hours after the construct preparation ended.

#### **6.3.5 Glucose Consumption**

Cell glucose consumption rates (GCR) were determined for every *in vitro* study at different point in time to determine cell growth. Samples of the culture media were collected from each assembly-containing Petri dish immediately after every feeding ( $T_0$ ) and 24 hours later ( $T_1$ ) during the *in vitro* studies. Sample glucose levels were measured on a Vitros DT60II bioanalyzer (Ortho-Clinical Diagnostics, Rochester, NY). Glucose consumption rates (GCR)

were then determined by calculating the difference between the sample glucose level at  $T_0$  and  $T_1$ . The results were normalized to  $10^5$  cells at the time of encapsulation.

### **6.3.6 Histology**

Histology samples of alginate beads were taken at the start and conclusion of the studies both *in vitro* and *in vivo*. They were fixed in 3% glutaraldehyde for at least 10 mins upon retrieval. They were then rinsed in successive ethanol washes (25%, 50%, 75% EtOH) over the next 3 hours, embedded in paraffin, sliced, and stained with hematoxylin/eosin (H/E). Beads retrieved from *in vitro* studies were first rinsed in their respective cationic solution ( $\text{CaCl}_2$  or  $\text{BaCl}_2$ ) before being fixed to increase the strength of the alginate bead network before histology processing. Digital photomicrographs were taken using a 10x objective (Nikon, Japan).

### **6.3.7 Streptozotocin Injection and Blood Glucose Monitoring**

Diabetes was induced in normal female C3H/HeN mice through a series of streptozotocin (STZ; SIGMA, St. Louis, MO) injections of 100 mg/kg intraperitoneally (IP) over 5 days. The blood glucose levels in the mice were checked daily taking blood samples from the tail vein. The glucose levels were measured using a OneTouch Ultra2 (LifeScan, Milpitas, CA) blood glucose monitoring system. The mice were considered diabetic once their blood glucose levels exceeded 300 mg/dL of blood for three consecutive days.

### **6.3.8 Animal Preparation and Handling**

Experiments with adult female C3H/HeN mice, weighing 20-30 g, were conducted according to a protocol approved by the University of Florida Institutional Animal Care and Use Committee. NMR measurements and surgeries were completed under general anesthesia. Anesthesia was induced by inhalation of 2% isoflurane in oxygen and maintained for the duration of the surgery. Subcutaneous buprenorphine injections were given prior to surgery and 24 h later at doses of 0.05 mg/kg. Under deep anesthesia, the sterile construct was implanted

into the peritoneal cavity via a small (2 cm) midline celiotomy. It was placed into the peritoneal cavity and washed with saline containing 1% penicillin-streptomycin prior to closing. Two types of constructs surrounded by an implantable coil were studied: a cell-free implantable coil-construct assembly and a cell-containing implantable coil-construct assembly. Cell-containing coil-construct assemblies were implanted in diabetic mice, whereas cell-free coil-construct assemblies were implanted in non-diabetic mice. In addition, cell-containing free floating beads were injected into the peritoneal cavity of diabetic mice via a syringe with a 16G needle under anesthesia for comparison studies. For diabetic mice, blood glucose measurements were taken daily to monitor the effectiveness of the constructs. Once blood glucose levels exceeded 600 mg/dL, or the mice appeared distressed and weak, they were euthanized and the construct was retrieved for histological analysis. For non-diabetic mice, magnetic resonance imaging (NMR) was performed from time to time.

### **6.3.9 Results and Statistical Analysis**

All GCR measurements and measurements performed on mice are indicated as the means  $\pm$  standard deviation of multiple measurements derived from at least two independently encapsulated cultures. If a meaningful average could not be determined, the individual results are presented and commented.

## **6.4 Results**

### **6.4.1 Implantable Coil-Construct Assembly Development**

#### **6.4.1.1 Implantable coil- alginate foam assembly**

$\beta$ TC-tet cells were successfully seeded in the alginate foam in the middle of the coated coil. The cells were growing in the foam and the constructs were kept alive for 56 days *in vitro*. However, the cells grew slower than in a flask. They also kept falling out of the foam very rapidly. The alginate foam was later found to have high guluronic content which has already

shown cell growth limitation (175). Furthermore, the pores of alginate foams, even the 75%  $\text{Ca}^{2+}$  saturated ones (the least swelling foam type), were found to be too large to properly host cells within the construct. Regular autoclave sterilization methods did not seem the most appropriate for the alginate foam either. These concerns compromised the use of alginate foam design in the scope of this study. If reducing alginate foam pore size could have been achieved by adding extra alginate gel layers around the foam, this implantable coil-construct assembly was not considered further in this study due to time constraints.

#### 6.4.1.2 Implantable coil-alginate bead assembly

$\beta\text{TC-tet}$  cells were successfully encapsulated in alginate beads, either APA beads (Figure 6-3A) or BaA beads (Figure 6-3B). The beads were between 400 and 600  $\mu\text{m}$  in diameter and successfully inserted in the constructs immediately after generation. The constructs were then tested *in vitro* or *in vivo* in diabetic and non-diabetic mice.

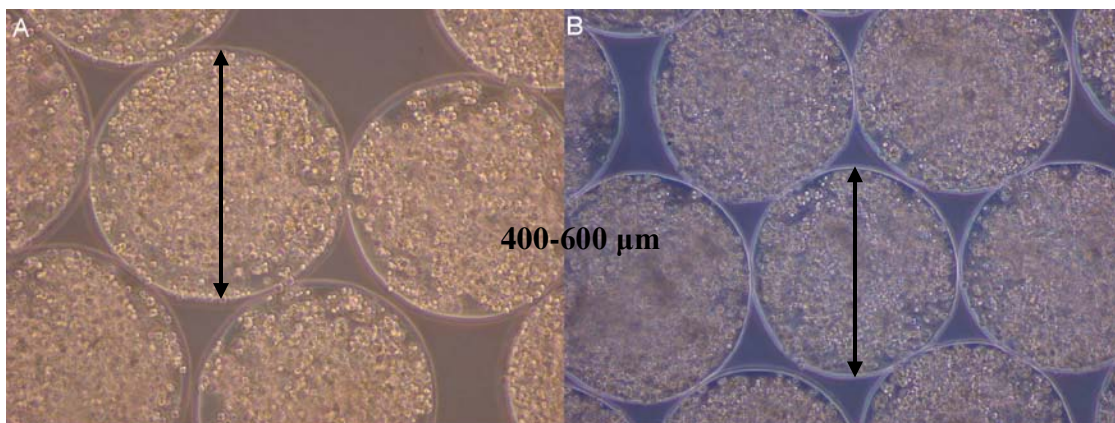


Figure 6-3. Photograph of  $\beta\text{TC-tet}$  cells encapsulated in alginate beads prior to insertion in a construct. A) APA beads; B) BaA beads. (Photo by N.A. Volland).

#### 6.4.2 *In vitro* Study

If originally the entire construct cavity was filled with beads ( $\sim 0.3$  mL), it was quickly observed that the cells did not survive very well in such an environment. Implantable coil-construct assemblies were placed in flasks containing free floating beads to determine if the

construct materials were an issue. No difference in bead-entrapped cell viability was observed between these two sets of free-floating beads leading to state that the construct materials had no effects on the cells. The restricted movement of the beads due to their promiscuity when confined in the construct cavity compared to free floating beads was another possible issue.

To increase the well-being of the encapsulated cells in beads, the volume of beads inserted in the construct was limited to 200  $\mu$ l for every study. This volume allows the beads to move more freely within the construct cavity and the total number of cells presented in the construct cavity is still high enough to potentially reverse diabetes in later studies.

Figure 6-4A illustrates the temporal changes in the glucose consumption rate (GCR) of  $\beta$ TC-tet cells encapsulated in 2% (w/v) LVM alginate gelled either with 100 mM  $\text{CaCl}_2$  (APA beads) or 55 mM  $\text{BaCl}_2$  (BaA beads) and confined in constructs compared to beads free floating in flasks (Figure 6-4B). Solid black square points (■) correspond to data obtained from BaA bead culture in constructs (n = 6 constructs in 2 Petri dishes) whereas solid grey circle points (●) correspond to data obtained from APA bead culture in constructs (n = 6 constructs in 2 Petri dishes). On Figure 4B, the solid black square points (■) and solid grey circle points (●) correspond to data obtained from beads cultured in flasks, APA beads and BaA beads respectively, used for comparison between restrained beads in constructs and free floating beads. The data show that both sets of cultures (APA and BaA beads) in constructs displayed an overall increase in glucose consumption comparable to the free-floating bead trend for both cultures as well. This increase in glucose consumption relates to an increase in cell proliferation as depicted by beads histology cross-sections (Figure 6-5 and 6-6).

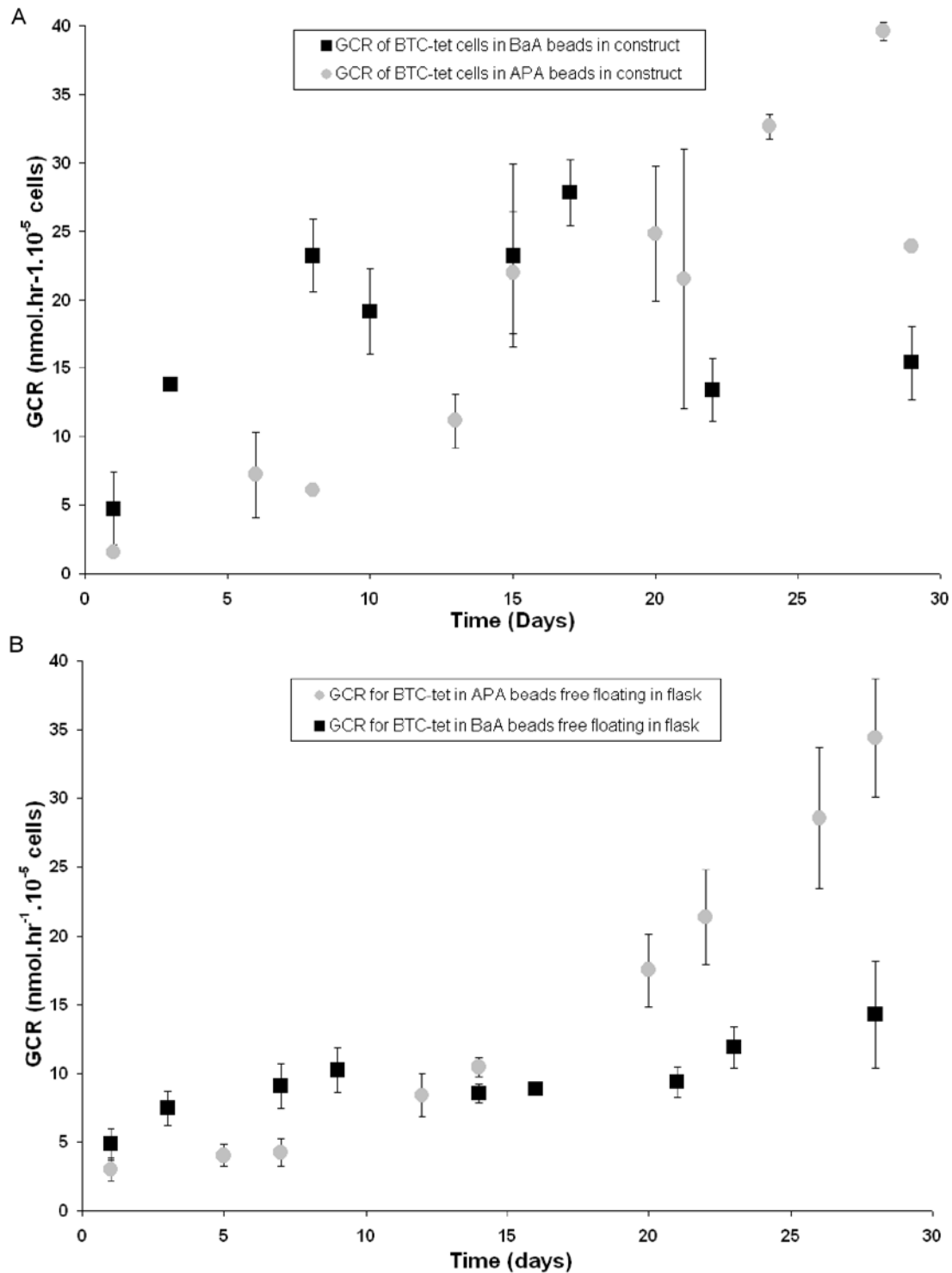


Figure 6-4. Temporal changes in the glucose consumption rate (GCR) of  $\beta$ TC-tet cells encapsulated in APA and BaA beads. A) When the beads were confined in coil-construct assemblies; and B) when the beads were floating free in flasks. Solid square points (■) correspond to the BaA beads and solid circle points (●) correspond to the APA beads.

If three phases of glucose consumption can be observed on Figure 6-4 for both types of beads (APA and BaA) in both environments (restrained or not), differences can be seen as well. In both environments, the cells in APA beads did not consume as much glucose early on as the cells in BaA beads. This pattern shows the influence of the manufacturing stress on the cell growth (longer generation procedure for APA beads). However, this trend reverses around Day 14 indicating the alginate network strength influence over time. It is also worthwhile mentioning that the alginate network strength may also influence the larger disparity in cell GCR for cells entrapped in APA beads only. Furthermore, cells in restrained beads in constructs seem to suffer more severe changes than the cells in non-restrained beads. They consume more glucose immediately after insertion in the constructs compared to cells in free floating beads. Their consumption stabilizes later on before significantly dropping and increasing again. This pattern shows the influence of the construct confinement on the bead-entrapped cell growth. Nonetheless, this study shows that cells entrapped in alginate beads (APA and BaA) confined in construct can survive over a month *in vitro*.

The analysis of the histological cross-sections also shows that the  $\beta$ TC-tet cells grew in clusters throughout the bead for both types of beads (APA and BaA) in both environments (restrained in construct or not). However, these clusters are more but smaller in BaA beads (Figure 6-5) than they are in the APA beads (Figure 6-6) in both environments. A similar observation was made earlier between APA beads made with alginates of different compositions (high mannuronic content vs. high guluronic content) (174,175). Furthermore, the clusters were slightly fewer and smaller for both types of beads when the beads were confined within a construct compared to when they were free floating in flask.

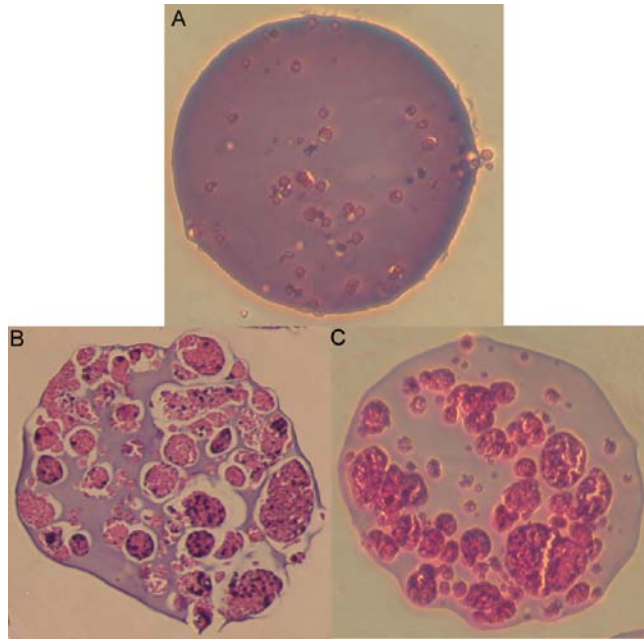


Figure 6-5. Hematoxylin/eosin stained cross-sections from BaA beads prepared by encapsulating  $\beta$ TC-tet cells in 2% (w/v) LVM alginate gelled with 55 mM  $\text{BaCl}_2$ . A) At Day 0, B) at Day 36 after retrieval from the construct; and C) at Day 30 after retrieval from the flask. (Photo by N.A. Volland).

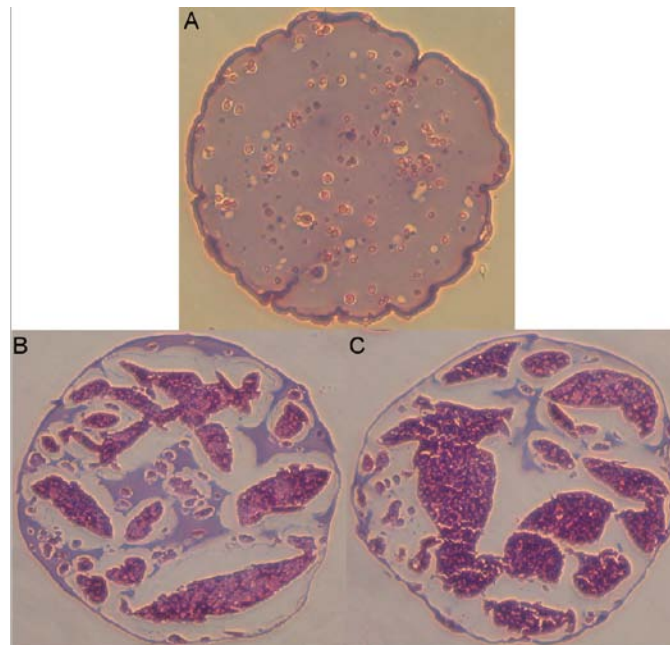


Figure 6-6. Hematoxylin/eosin stained cross-sections from APA beads prepared by encapsulating  $\beta$ TC-tet cells in 2% (w/v) LVM alginate gelled with 100 mM  $\text{CaCl}_2$ . A) At Day 0, B) at Day 30 after retrieval from the construct; and C) at Day 30 after retrieval from the flask. (Photo by N.A. Volland).

These histological observations corroborate well with the differences in glucose consumption displayed between the two beads types in both environments (restrained in construct or free floating). This indicates that BaA bead and construct environment both hindered the cell growth. Although only one bead histology cross-section photograph is presented here for each type of beads per environment. It is also worthwhile mentioning that the APA bead histology cross-sections did display a larger discrepancy among themselves than the BaA made cross-sections as larger discrepancies were since in the GCR graphs.

### **6.4.3 *In vivo* Study**

Two *in vivo* studies were performed: 1) the implantation of cell-free implantable-coil-construct assemblies and cell-free coil-free constructs in non diabetic mice to study the effect of the assemblies on the animal and vice versa, and 2) the implantation of cell-containing implantable-coil-construct assemblies in diabetic mice to assess the efficacy of the construct and determine possible issues and/or improvements.

Cell-free implantable coil-construct assemblies and cell-free coil-free constructs were kept in mice peritoneal cavities up to 123 days without apparent external problem for the animals (n = 14) with an average of 40 days. None of the implantable coils ever failed (n = 7). NMR images were taken at any given day on any mouse without a problem. Every assembly implanted for 4 days or less was perfectly clean upon retrieval. However, every construct assemblies but two (n = 9) which stayed implanted for more than 4 days had a thin (200  $\mu\text{m}$ ) fibrotic layer (Figure 6-7A) around them even when antibiotics, such as penicillin and streptomycin, and the steroid dexamethasone were used to reduce the immune response. 58% of these assemblies had the construct cavity filled up with more fibrous connective tissue (Figure 6-7B). This second fibrous tissue layer only seems to develop around the alginate beads and never attack them directly since the beads have always been appeared intact on histology cross-sections (Figure 6-7B).

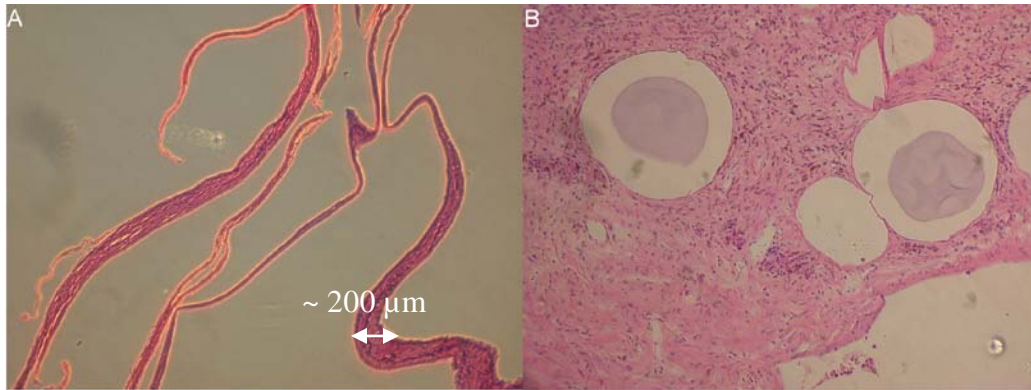


Figure 6-7. Hematoxylin/eosin stained cross-sections of the tissues found inside and around the construct after its retrieval from a mouse peritoneal cavity. A) Fibrotic tissue layer piece found around the construct at the time of retrieval; and B) Connective tissue present inside the construct cavity at the time of retrieval and surrounding the cell-free alginate beads inserted in the cavity before implantation. (Photo by N.A. Volland).

If the fibrous connective tissue layer inside the assembly cavity was often seen on the MR images (Figure 6-8), the thin fibrotic layer around the construct was never observable. It was collected at the time of construct retrieval. It was never attached onto the PDMS part of the construct, but onto the mesh.

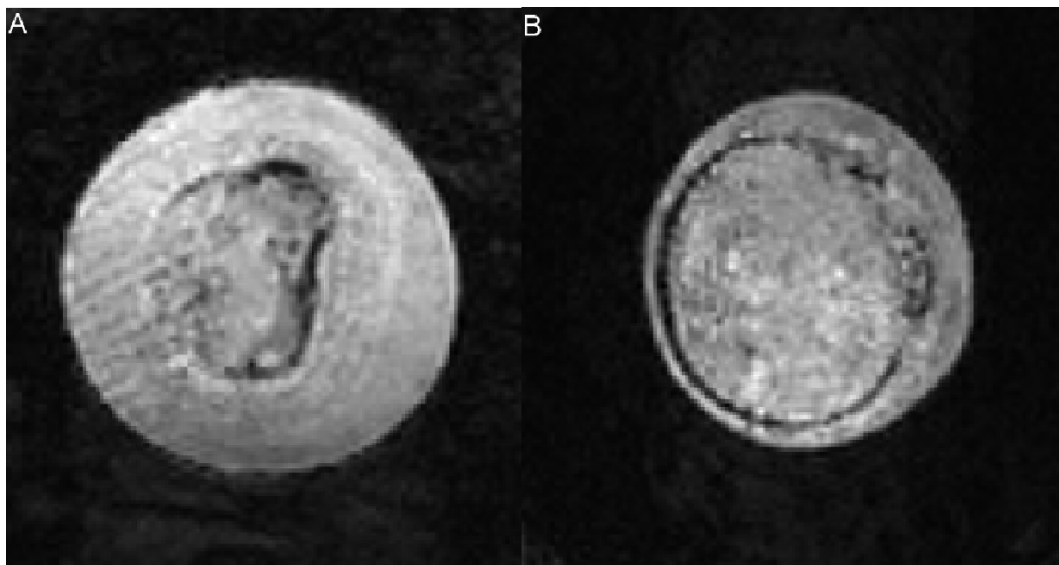


Figure 6-8. MR images of pancreatic substitutes implanted in the peritoneal cavity of two different mice. The images show the presence of connective tissue within the construct cavity after: A) 39 days of implantation; and B) 98 days of implantation.

Changes in construct irrigation could be perceived on the MR images as a result of this fibrotic encapsulation of the whole construct since the beads appeared more distinctively within the cavity over time as the construct water content decreased (Figure 6-9).

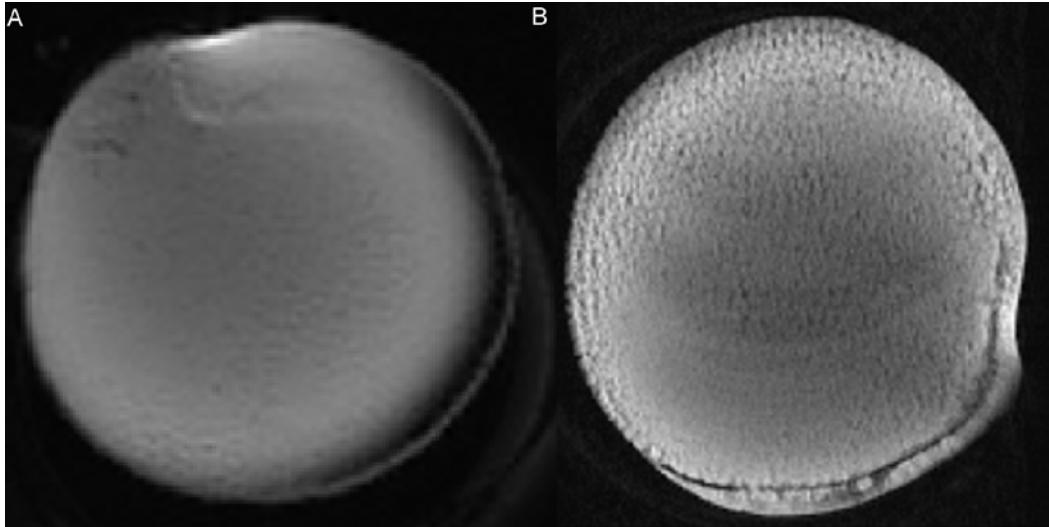


Figure 6-9. MR images of cell-free beads within the construct cavity over time. A) At day 10; and B) at day 42.

Upon these results, mice were implanted with either a piece of PEEK mesh only or a ring of PDMS over one week. If the PDMS rings were retrieved perfectly clean, the PEEK mesh was well covered (Figure 6-10B).

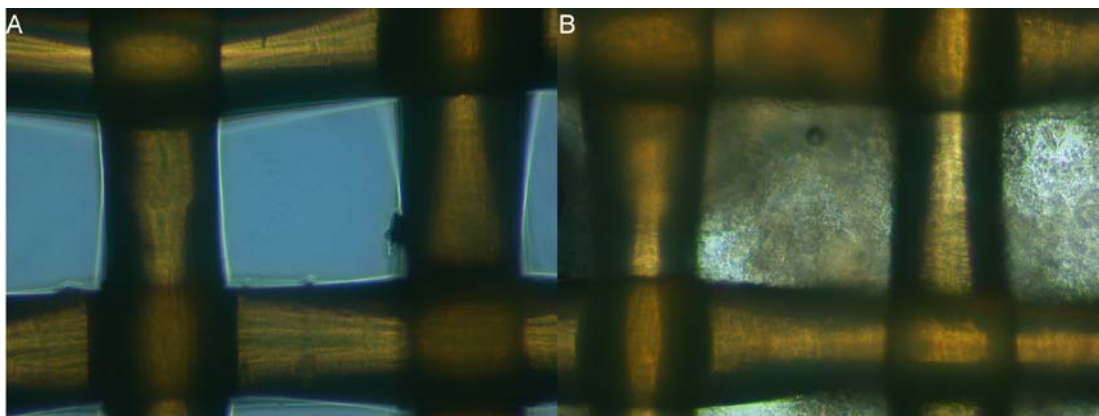


Figure 6-10. Photographs of a piece of PEEK mesh. A) prior to; and B) after implantation in a mouse peritoneal cavity for a week. (Photo by N.A. Volland).

Two diabetic mice were also implanted with coil-construct assemblies containing a volume of 200  $\mu$ l of  $\beta$ TC-tet cells entrapped in alginate beads gelled with 55 mM BaCl<sub>2</sub> (n = 2). Two other diabetic mice were injected with 150  $\mu$ l of BaA beads for comparison purposes. The mice became diabetic within 10 to 15 days of the last STZ injection and were all successfully implanted (Day 14) or injected (Day 18).

Figure 6-11A illustrates the temporal changes in the blood glucose levels of diabetic mice implanted with constructs containing BaA beads. Solid grey square points (■) and solid black circle points (●) correspond to data obtained from the mice which received the coil-construct assembly containing BaA beads. In figure 6-11B, Solid grey square points (■) and solid black circle points (●) correspond to data obtained from the mice which received the free floating BaA bead injection. These last mice were used for comparison between the mice receiving the restrained beads in constructs and the ones receiving the free floating one. Blood glucose levels of normal mice (naïve controls, solid light grey rhombus points (◆) on Figure 6-11) and untreated diabetic mice (negative controls) were also checked to give a reference to how well the constructs and beads were performing. No averaging was done in this experiment to generalize the findings obtained since the number of animals tested was very small (up to 2 animals per set) and the results would have been biased by the large disparity from one animal to another. However, encouraging observations can be made.

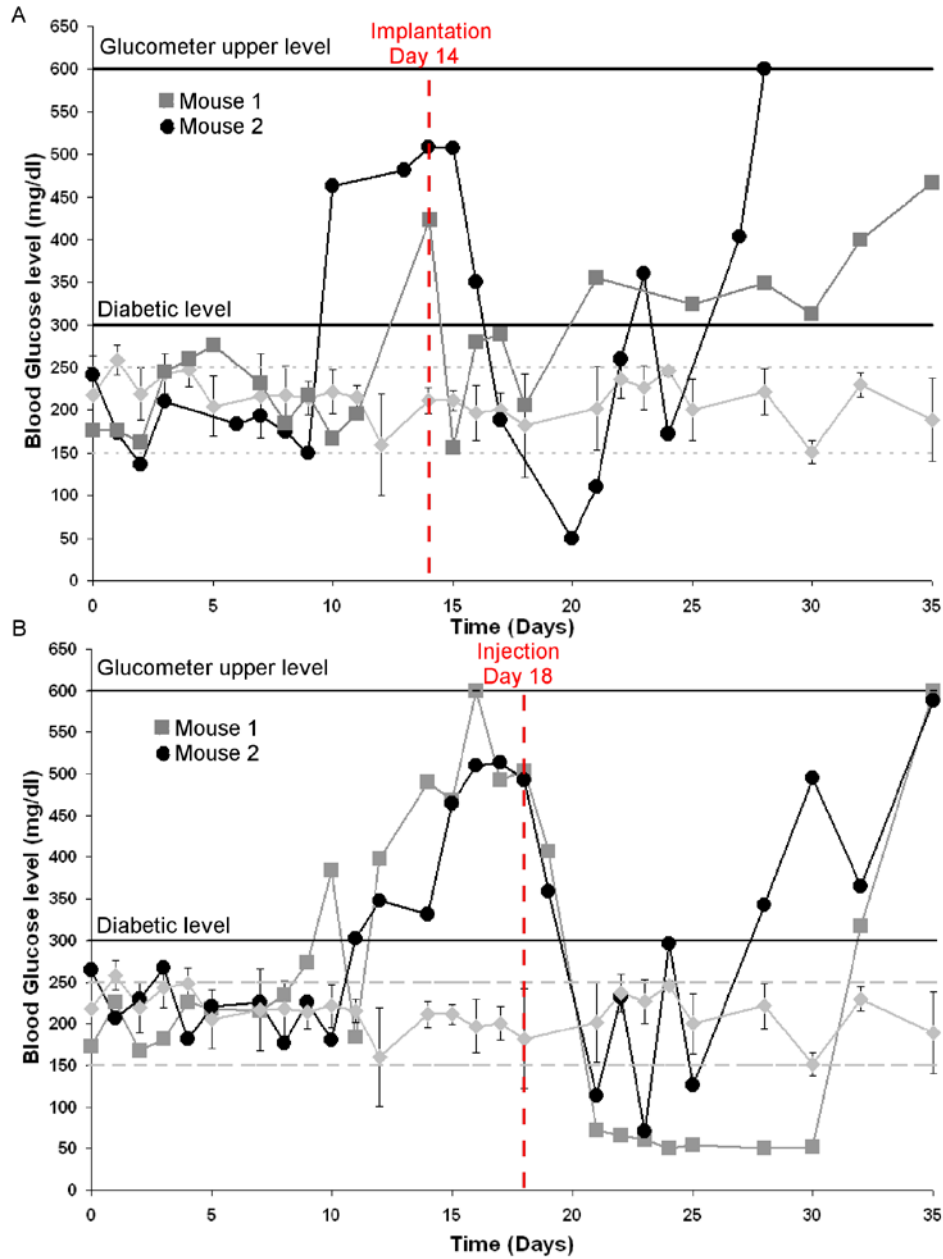


Figure 6-11. Temporal changes in diabetic mice blood glucose levels after implantation of  $\beta$ TC-tet cells encapsulated in BaA beads. A) As part of a coil-construct assembly; and B) free floating in the peritoneal cavity. Solid squares (■) and solid circles (●) correspond to two different mice which received the beads either confined in construct (A) or through injection (B). Solid rhombus points (◆) correspond to the naïve control mice. The dashed grey lines placed at 150 and 250 mg/ml set the average blood glucose level range for control mice. The solid black line placed at 300 mg/ml set the blood glucose level above which mice are considered diabetic after their blood glucose is detected 3 days above this level. The solid black line placed at 600 mg/ml set the blood glucose level above which mice have to be sacrificed after their blood glucose is detected 3 days above this level.

The data show that the two mice which received the constructs return to normoglycemia within 24 or 48 hours of implantation indicated that the constructs are playing their role of pancreatic substitutes in producing insulin to compensate the lack of this hormone due to diabetes. Despite the fact that free floating beads restored normoglycemia for a longer period (up to 10 days) than coil-construct assembly beads, normoglycemia was restored for between 6 and 12 days in diabetic mice which received the constructs. The mice were considered diabetic again 13 days after implantation. It is worthwhile noting that it took more than 10 days for the blood glucose to reach the pre-implantation levels again. If the constructs were retrievable for histology studies, none of free floating beads could ever be retrieved for comparison. This shows the advantage of a pancreatic construct assembly to help toward the development of a practical bioartificial pancreas in the treatment of diabetes. Figure 6-12 displays a histological cross-section photograph of a piece of tissue including a cell-containing bead obtained from inside the construct cavity of one of the mice implanted with a coil-construct assembly. The construct was retrieved on Day 35 of the study or 21 days after implantation.

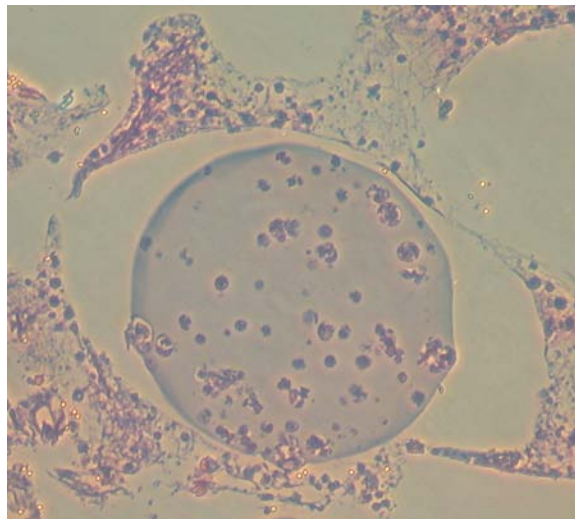


Figure 6-12. Hematoxylin/eosin stained cross-section from implantable coil-construct assembly cavity tissue after 21 days of implantation in a mouse peritoneal cavity. The cavity included beads prepared by encapsulating  $\beta$ TC-tet cells in 2% (w/v) LVM alginate, gelled with 55 mM  $\text{BaCl}_2$ . (Photo by N.A. Volland).

Cells can be spotted inside the bead present on the cross-section photograph (Figure 6-12). However, their number seems closer to the initial number of cells ( $3.5 \times 10^7$  cells/ml of alginate, Figure 6-5A) than to the number of cells at the end of the *in vitro* study (Figure 6-5B). Fibrous connective tissue can also be seen in the cavity outside of the beads attesting of an immune response toward the construct.

## 6.5 Discussion

Alginate beads have previously been shown to restore normoglycemia in mice (35,177,178) over a period of 5 days. However, their dispersion throughout the host's body limits obtaining valuable information on structure, metabolic activity, or function of cells entrapped in the beads and optimizing such a construct. To overcome this limitation, the use of a macroconstruct was investigated and characterized *in vitro* and *in vivo*. Macroconstructs have the following advantages over microconstructs, such as beads: 1) they can be held in place in the host peritoneal cavity, and 2) they can be surrounded by an RF coil (implantable coil-construct assembly), so that its monitoring can be done performing NMR imaging and spectroscopy.

Data in this study shows that an implantable coil-construct assembly including alginate beads can allow insulin-producing cells to stay viable for an extended period of time *in vitro*. The growth of the bead-entrapped cells restrained in a construct may not have been as steady as when the beads were not restrained. However, these results shows that cells can be entrapped in beads restrained in construct and their number increased to compensate for their performance limitation due to their environment restrictions. This allows the bioartificial pancreas to be non-invasively monitored *in situ*. If APA beads have been generated routinely in our laboratory (151,175), BaA bead generation was implemented in an effort to accelerate the bead-making process with less washes not to leave the cells in a harsher environment than normal for an extended period of time. Figure 6-4 attested of the slower cell growth early on in APA beads

due to the length of their generation process and its potential to be more harmful than the BaA bead generation process. As the ionic binding between alginate chain and barium cations is stronger than the binding between alginate chain and calcium cations (59), no PLL coating and additional washes were necessary to shape the BaA beads and give them the desired porosity. The histology cross-sections attested of the stronger network provided by the BaA beads than the network provided by the APA beads as the cell clusters are smaller in BaA beads than in APA beads. From the previous studies between APA beads made with alginates of different compositions (high mannuronic content vs. high guluronic content) (174,175), the softer alginate network was often favored. However, the BaA beads may be more appropriate to use in a construct *in vivo*. The fact that no PLL is used to make BaA beads may help decrease the host immune response and ease protein assay tests upon retrieval, such as the Lowry protein assay to determine cell numbers and growth with accuracy. Furthermore, with a tighter network, beads are holding together better and longer, allowing the construct to last longer and generate more reproducible and consistent results. Our laboratory is currently investigating the optimal strength of alginate bead network for cell growth when cells are entrapped in beads confined in a construct. Generating beads using different concentration of barium cations is being testing for this matter.

It is worthwhile noting that no tetracycline was used in the *in vitro* studies to regulate the growth of the  $\beta$ TC-tet cells and that the study was stopped at 30 days before the beads broke apart due to the large number of cells in them. Adding tetracycline in the culture media will prevent cell growth and allow the studies to go on for a longer time more appropriate for future *in vivo* studies (151).

The implantable coil-construct assembly implantation in a mouse peritoneal cavity demonstrates the capacity of cells entrapped in alginate beads confined in construct to detect glucose and release insulin to control the host blood glucose levels, while allowing for enhanced non-invasive monitoring of the construct using NMR methods. The fact that every implantable coil implanted never failed over the course of the *in vivo* studies shows how steady and reliable these coils are. These results also showed that the cells were not impaired by coils and that the return to normoglycemia in diabetic mice was possible upon coil-construct assembly implantation. The cells were shown to produce enough insulin to keep the mice blood glucose levels below the diabetic range for no more than 5 consecutive days. Upon retrieval, most of the construct cavities were filled with extracellular tissue and surrounded by a fibrotic layer typical of a host immune response. Assembly pre-treatments decreased this host immune response, but did not eliminate it completely. Nonetheless, it is worthwhile noting that 10 days were necessary to see the mice blood glucose levels back to their preimplantation levels. This study will need to be repeated over a larger number of animals to obtain better statistics as the differences between animals can be wide. Furthermore, STZ solutions were found to be very instable and hard to properly implement all the time to render the mice diabetic in a reasonable number of days (5-10 days). The type of mice used in this study was also found to be mildly responsive to STZ. IP Alloxan injections are currently under investigation in our laboratory to increase the efficiency in rendering mice diabetic.

Further studies of the host immune response on the pancreatic construct found that the PEEK mesh triggered a large reaction of the host and its rapid coverage by host fibrotic cell layer (within less than 10 days) even though biocompatible, protein-free, and sterile. This reaction could explain the filling of the construct cavity with connective tissue, the fibrotic layer

appearance outside the construct, and the rapid decrease of construct performances over time. If the connective tissue in the construct cavity may not have killed the cells directly as it does not appear densely cellularized, its cells certainly compete with the insulin-producing cells for nutrient and oxygen. On the contrary, the fibrotic layer outside the construct does appear very dense and could be responsible for the cell oxygen deprivation and lack of fluid irrigation. All of these assumptions are possible schemas of rapid construct failure which NMR methods have already been able to partially identify. The mesh composition, roughness and topography have been mentioned as possible reasons for triggering a response from the host immune system. Studies in our laboratory currently investigate the coating of the mesh with pure alginate to alleviate the issues and allow the construct to perform optimally for an extended period of time. The use of a different type of mesh may also help decreasing the immune response and will need to be investigated in the future.

## 6.6 Summary

The implantable coil-construct assemblies were successfully developed and their performances analyzed. The increased cell viability when using microencapsulation and the cell confinement when using macroencapsulation was combined to: 1) allow the generation of a bioartificial pancreas with higher diffusion capability; and 2) keep the cells together in one location to monitor them closely and easily *in vivo* using NMR techniques and implantable coils. The cells entrapped in alginate beads confined inside the construct cavity were maintained alive for over a month *in vitro*. This could be extended in the future with the use of tetracycline to regulate cell growth. Additionally, these assemblies show their potential to restore normoglycemia in diabetic mice. Some of the immune response issues which prevented the construct to function properly more than 5 consecutive days have already been isolated. The PEEK mesh used to create the construct cavity to hold the beads in place was shown to trigger a

large immune response within 10 days after implantation. Construct pretreatment in parallel to the use of antibiotic were found to slightly decrease the fibrotic overgrowth around the construct. However, the close NMR non-invasive monitoring possible because of the implantable RF coil around the construct showed how the MR images could allow the identification of such a host reaction prior to the return of hyperglycemia. It is worthwhile noting that the coil function was never impaired by this host immune response.

Since any immune response will impaired the construct function within days after implantation, this issue needs to be addressed before the bioartificial pancreas performances can be fully assessed. Consequently, future investigations should focus on modifying the construct to decrease, and even eliminate, the host immune response to maintain the cells alive longer and allow the construct to restore normoglycemia in diabetic mice over an extended period of time.

## CHAPTER 7 CONCLUSIONS AND FUTURE WORK

### 7.1 Conclusions and Contributions

A sensitive and non-invasive monitoring is of critical importance for a complete and accurate characterization of tissue-engineered constructs *in vitro* and *in vivo* and the early detection of construct failure markers. The primary contribution of this work is the sensitivity improvement of an existing non-invasive NMR monitoring method by developing inductively-coupled implantable coil system for use at high field. This is the first time that the use of inductively-coupled coil systems was implemented at a magnetic field as high as 11.1T. While the sensitivity improvement was essential, the ease of coil system construction and the implantable coil coating procedure were all taken into account to decide the most advantageous design overall. Simulations, phantom, and *in vivo* studies helped to characterize the coil systems and provided valuable information regarding the changes in coil resonant frequency, quality factor, and inductive coupling, under different loading conditions. Different designs (loop-gap resonators and solenoids) and configurations (co- and counter-rotating modes) were evaluated. The use of inductively-coupled implantable coil system in the co-rotating mode allowed the highest sensitivity improvement of the NMR monitoring method for  $^1\text{H}$  detection. The loop-gap resonator was selected as the system implantable coil because of easy construction and reproducibility. The coating of the implantable coil was a significant part of the system development and the effects of coating on the implantable coil and the whole system were determined for different materials. PDMS was selected to be the most appropriate coating material and allow the use of the coupled-coil system *in vitro* and *in vivo* with the least sensitivity sacrifices. The design of the best possible inductively-coupled implantable coil system for the model tissue-engineered construct and NMR applications specific to this research

was achieved. The developed coupled-coil system with a PDMS-coated loop-gap resonator allowed a sensitivity improvement of a non-invasive NMR monitoring technique at 11.1 T for  $^1\text{H}$  detection *in vivo* over 4 times when compared to the same technique using a surface coil at 4.7 T.

The second phase of the research upgraded the inductively-coupled implantable coil system to receive-only and multiple-frequency coupled-coil systems. Receive-only systems were successfully built using passive decoupling circuit. Design and coating adaptations from the inductively-coupled system construction for  $^1\text{H}$  detection were effectively implemented validating that more complex coupled-coil systems are feasible. NMR images and spectra were also obtained using receive-only coupled-coil systems at 11.1 T demonstrating the capability of these systems to detect NMR signal with a high sensitivity. The excitation homogeneity and increased selectivity available using the receive-only inductively-coupled implantable coil system allowed the acquisition of spectroscopic data with greater SNR and better localization. The development of multiple-frequency coupled-coil system for  $^1\text{H}$  and  $^{31}\text{P}$  and  $^1\text{H}$  and  $^{19}\text{F}$  simultaneous detection were also investigated to assess their feasibility. Single-frequency systems for  $^{19}\text{F}$  and  $^{31}\text{P}$  detection were constructed and indicated the possibility of detecting several different relevant nuclei in the monitoring of a bioartificial pancreas. The single-frequency inductively-coupled implantable coil systems also gave the reference characteristics for the multiple-frequency inductively-coupled implantable coil systems. The use of tank circuits and capacitive overcoupling showed the feasibility of multiple-frequency coupled-coil systems. Matching issues, resistive losses, and unexpected frequency coupling within the double frequency systems indicated how complex these systems can become and that the development requires extensive considerations prior to magnet testing. However, the technology of inductively-coupled implantable coil systems, even the complex ones, has been established and

allowed the monitoring of a bioartificial pancreas and the detection of early markers of construct failure using NMR methods with a high sensitivity.

The final phase of this dissertation tested the pancreatic construct characteristic when inserted in the middle of the implantable coil. This was the first time an implantable coil surrounded a pancreatic construct for the direct monitoring of its function. The design of a hybrid micro/macroconstruct using a ring of polydimethylsiloxane (PDMS) encasing alginate beads and an implantable coil proved that entrapped cells can be kept alive *in vitro* for over a month and can restore normoglycemia in diabetic mice for 5 consecutive days. These results showed that cells can survive, grow, and function properly when confined within a pancreatic construct including an implantable RF coil. The results also demonstrated the ability of the inductively-coupled implantable coil system to directly monitor a viable bioartificial construct *in vivo* with high sensitive using NMR methods. Pre-treating the construct prior to implantation was found to be of primary importance to limit construct fibrotic overgrowth and preserve the longevity of the construct *in vivo* as much as possible.

The data presented in this dissertation outlines the quantitative criteria for the capability and limitations, such as coil design and coating materials, of using inductively-coupled implantable coil systems with an NMR method for monitoring a bioartificial pancreas non-invasively. The use of inductively-coupled implantable coil system, under the specific conditions used in this study, was found to improve the sensitivity of a non-invasive NMR monitoring technique for  $^1\text{H}$  detection by a factor of 2 compared to the same technique when using a surface coil (SC) at 11.1 T. This was added to the sensitivity improvement of 2.4 when going to a higher magnetic field than the previous studies (from 4.7 to 11.1 T). In addition, these inductively-coupled implanted coil systems will have larger advantages over an SC as the depth

of the implanted coil increases, such as in larger animal models (e.g. humans), since the SC sensitivity drops rapidly with distance. While the implantable coil design discussed here appear to limit the scope of the NMR non-invasive monitoring to bioartificial pancreatic construct, it is worthwhile mentioning that the coil developments outlined in this thesis can also be applied to monitor other systems, tissue and/or organs, bioartificial or not, with NMR methods. In these cases, the coil geometry may have to be adapted to better fit the studied structure shape and size. Moreover, this increase in sensitivity has driven the development of more complex systems, such as receive-only and multiple-frequency inductively-coupled implantable coil systems. The receive-only coupled-coil systems were investigated to allow a better localization within the construct to perform spectroscopy and the multiple-frequency coupled-coil systems to detect important nuclei other than  $^1\text{H}$ . Their development has shown the potential for higher sensitivity localized spectroscopy and the creation of a unique implantable coil system for the simultaneous assessment of different physiologically relevant parameters within a single tissue-engineered construct.

## **7.2 Future Work**

The data presented in this thesis were primarily relegated to developing inductively-coupled implantable coil system to improve the sensitivity of an NMR non invasive monitoring method. In order to increase the sensitivity even further different designs, different coating materials, and different diodes need to be tested. Using a coating material with better dielectric properties than PDMS would further limit the electrical losses encountered during the coating and loading of the coil. PTFE, with its excellent dielectric properties, was tested without success, but reconsidering this material with more adequate coating process may work and help better isolate the implantable coil from its surrounding. However, caution will have to be taken when  $^{19}\text{F}$  detection is performed. Signal suppression schema may have to be applied if PTFE

signal is detectable by NMR. If this signal interferes with the PFC signal of interest in this study, other materials, which are non-detectable by NMR, should be considered or even developed, such as parylene C (132) or polyurethane (12).

Even though the receive-only inductively-coupled coil system was successfully tested in the magnet, the use of diodes with more favorable characteristics would minimally alter the coils and inductively-coupled system characteristics, ease the system construction, and potentially increase the sensitivity of NMR method sensitivity when the receive-only system is used. The non-magnetic passively activated Schottky diode used in this study had a series resistance superior to  $1 \Omega$ , a parallel capacitance superior to  $3 \text{ pF}$ , and a parallel resistance averaging  $5 \text{ k}\Omega$ . These characteristics largely influence both the surface and implantable coils because the diode parallel capacitance is of the order of magnitude of the circuit capacitance during NMR signal reception when the diode is reverse biased, or OFF. A diode with a smaller parallel capacitance ( $\leq 1 \text{ pF}$ ) will significantly decrease its influence on the circuit when OFF. Furthermore, when the diode is OFF and acting as a capacitance, it has a specified parallel resistance indicative of the component quality factor. The larger this resistance, the least influence the decoupling circuit will have on the main circuit when the diode is OFF. Moreover, during NMR excitation, the diode is forward biased, or ON, and equivalent to a series resistance. The smaller this resistance ( $< 1 \Omega$ ), the better decoupled the coils will be since the current will mostly flow in the decoupling circuit and not the main circuit. PIN diodes can achieve series resistance inferior to  $1 \Omega$ , parallel capacitance inferior  $1 \text{ pF}$ , and parallel resistance superior to  $25 \text{ k}\Omega$  to minimally influence the system they are inserted in, but require external DC power to achieve such characteristics. The passive activation required in these experiments does not allow the use of actively driven PIN diodes. The development of non-magnetic diodes with lower series

resistance and parallel capacitance when passively driven may be worthwhile, if not found commercially.

The interference of breathing artifacts on the acquisition of NMR data is another aspect of this research that would benefit from future studies (179). Although the use of respiratory gating in this thesis was able to effectively reduce the artifacts to the noise level, this technique could not be accurately implemented when the mice were breathing irregularly, which could happen frequently when the mice are diabetic and weak, and/or under low SNR conditions (low magnetic field strength and clinical setting). Different strategies can be implemented to eliminate these breathing artifacts. If self-gating is widely used in cardiac MR imaging (155-157), a user-defined gating technique looking more promising as the acquisition time of standard MR images is longer (158). However, an image reconstruction using a motion artifact correction post-processing could enhance the image quality even further. Different techniques have already been developed for abdominal imaging in clinical settings and may be implemented in the frame of this research to reduce breathing artifact when imaging the construct implanted in a mouse peritoneal cavity (180,181).

Another aspect for future studies would be the improvement of the multiple-frequency inductively-coupled implantable coil system. Future work in this area should focus on two aspects: (1) tuning a multiple-frequency inductively-coupled implantable coil system at two frequencies ( $^1\text{H}$ - $^{31}\text{P}$  &  $^1\text{H}$ - $^{19}\text{F}$ ) and match it to  $50 \Omega$ , and (2) tuning a multiple-frequency inductively-coupled implantable coil system at three frequencies ( $^1\text{H}$ - $^{31}\text{P}$ - $^{19}\text{F}$ ) and match to  $50 \Omega$  as well. Either of these approaches would result in the system ability to allow direct cross-correlation studies between the different cell metabolic activities and functions. Obtaining a better matching networking for the  $^1\text{H}$ - $^{31}\text{P}$  system using adequate variable inductors can be

investigated. Different system designs have to be studied to obtain a working  $^1\text{H}$ - $^{19}\text{F}$  system without  $^1\text{H}$  and  $^{19}\text{F}$  frequencies interacting with each other to test these systems in the magnet. However, because adding resonances into a coil circuit generate more and more resistive losses at any given resonant frequency of the system, an alternative multiple-frequency inductively-coupled implantable coil system using a ‘single resonance’ approach is under development in our laboratory (182). A microcontroller embedded within a microchip and integrated to the coils can switch an array of capacitors to make the coil resonate at the desired frequency when remotely activated. The arrays have been shown to allow the tuning of the coils at any frequency making the system multiple-frequency with a single frequency system behavior.

The techniques demonstrated in this dissertation were intended to be used in total-choline signal measurement for construct cell viability determination, ATP signal measurement for construct bioenergetics status determination, and PFCE  $T_1$  relaxation time measurement to assess the oxygenation of the construct over time. Nonetheless, all those measurements need to be carefully calibrated for the use of inductively-coupled implantable coil system before studying a construct over time. Total-choline and ATP measurements are relatively easy to calibrate as they only require using sample of different concentration of the desired compound (known cell density) to be studied. However, PFCE  $T_1$  measurement calibration will require the construction of a perfusion system where the system oxygenation is known and can be carefully regulated. All these measurements would provide a large step forward in the eventual realization of practical, clinically relevant constructs. Furthermore, total-choline signal has yet to be acquired *in vitro* at 11.1T before the calibration and longitudinal studies of the construct can be done. The shim procedure can be improved by manually shimming of the second-order shims or optimizing the FASTMAP for the voxel size required in the study. Pulse sequences can also be optimized or

changed to a stimulated echo acquisition mode (STEAM) pulse sequence to take into account the possibility of a relatively short  $T_2$  (83). Reproducing the previous study at 4.7 T may also be a good starting point before going to higher field and more complex coil systems.

No extensive construct viability and performance *in vivo* studies were performed in the scope of this research as the host immune response was impairing the construct function within days after implantation. However, this immune response problem triggered preliminary studies as it was a major issue to be addressed before going any further with any construct viability and performances studies. Besides pretreating the construct prior to implantation and using antibiotics, coating the coil-construct assembly with a more bioinert material, such as ultra pure alginate, is currently under investigation in our laboratory. The use of a different mesh material has also been brought up and will be considered upon the alginate ‘overcoating’ results to decrease, and even eliminate, the host immune response, maintain the cells alive longer and allow the construct to restore normoglycemia in diabetic mice over an extended period of time.

## LIST OF REFERENCES

1. Silva AI, de Matos AN, Brons IG, Mateus M. An overview on the development of a bio-artificial pancreas as a treatment of insulin-dependent diabetes mellitus. *Medicinal Research Reviews* 2006;26(2):181-222.
2. Constantinidis I, Long RCJ, Weber C, Safley S, Sambanis A. Noninvasive monitoring of a bioartificial pancreas in vitro and in vivo. *Annals of the New York Academy of Sciences* 2001;944:83-95.
3. Constantinidis I, Sambanis A. Noninvasive monitoring of tissue-engineered constructs by nuclear magnetic resonance methodologies. *Tissue Engineering* 1998;4(1):9-17.
4. Constantinidis I, Stabler CL, Long RCJ, Sambanis A. Noninvasive monitoring of a retrievable bioartificial pancreas in vivo. *Annals of the New York Academy of Sciences* 2002;961:298-301.
5. Stabler CL, Long RCJ, Constantinidis I, Sambanis A. Noninvasive measurement of viable cell number in tissue engineered constructs in vitro using  $^1\text{H}$  NMR spectroscopy. *Tissue Engineering* 2005;11(3-4):404-414.
6. Stabler CL, Long RCJ, Constantinidis I, Sambanis A. In vivo noninvasive monitoring of viable cell number in tissue engineered constructs using  $^1\text{H}$  NMR spectroscopy. *Cell Transplantation* 2005;14(2-3):139-149.
7. Hoult DI, Lauterbur PC. The sensitivity of the zeugmatographic experiment involving human samples. *Journal of Magnetic Resonance* 1979;34:425-433.
8. Haase A, Odoj F, von Kienlin M, Warnking J, Fidler F, Weisser A, Nikita M, Rommel E, Lanz T, Kalusche B, Griswold M. NMR probeheads for in vivo applications. *Concepts in Magnetic Resonance* 2000;12:361-388.
9. Koretsky AP, Wang S, Murphy-Boesch J, Klein MP, James TL, Weiner MW.  $^{31}\text{P}$  NMR spectroscopy of rat organs, *in situ*, using chronically implanted radiofrequency coils. *Proceedings of the National Academy of Sciences USA: Biochemistry* 1983;80:7491-7495.
10. Murphy-Boesch J, Koretsky AP. An in vivo NMR probe circuit for improved sensitivity. *Journal of Magnetic Resonance* 1983;54:526-532.
11. Hollett MD, Cofer GP, Johnson GA. In situ magnetic resonance microscopy. *Investigative Radiology* 1987;22:965-968.
12. Schnall MD, Barlow C, Subramanian VH, Leigh JSJ. Wireless implanted magnetic resonance probes for in vivo NMR. *Journal of Magnetic Resonance* 1986;68:161-167.

13. Zhang X, Zhu XH, Tian R, Zhang Y, Merkle H, Chen W. Measurement of arterial input function of  $^{17}\text{O}$  water tracer in rat carotid artery by using a region-defined (REDE) implanted vascular RF coil. *MAGMA* 2003;16(2):77-85.
14. Silver X, Ni WX, Mercer EV, Beck BL, Bossart EL, Inglis B, Mareci TH. In vivo  $^1\text{H}$  magnetic resonance imaging and spectroscopy of the rat spinal cord using an inductively-coupled chronically implanted RF coil. *Magnetic Resonance in Medicine* 2001;46:1216-1222.
15. Bilgen M. Simple, low-cost multipurpose RF coil for MR microscopy at 9.4T. *Magnetic Resonance in Medicine* 2004;52:937-940.
16. Bilgen M. Inductively-overcoupled coil design for high resolution magnetic resonance imaging. *Biomedical Engineering online* 2006;5(3).
17. Bilgen M, Al-Hafez B, He Y-Y, Brooks WM. Magnetic resonance angiography of rat spinal cord at 9.4T: a feasibility study. *Magnetic Resonance In Medicine* 2005;53:1459-1461.
18. Bilgen M, Elshafiey I, Narayana PA. In vivo magnetic resonance microscopy of rat spinal cord at 7 T using implantable RF coils. *Magnetic Resonance in Medicine* 2001;46(6):1250-1253.
19. Fenyas DA, Narayana PA. In vivo echo-planar imaging of rat spinal cord. *Magnetic Resonance Imaging* 1998;16(10):1249-1255.
20. Narayana PA, Fenyas D, Zacharopoulos N. In vivo relaxation times of gray matter and white matter in spinal cord. *Magnetic Resonance Imaging* 1999;17(4):623-626.
21. Wirth EDI, Mareci TH, Beck BL, Fitzsimmons JR, Reier PJ. A comparison of an inductively coupled implanted coil with optimized surface coils for *in vivo* NMR imaging of the spinal cord. *Magnetic Resonance in Medicine* 1993;30:626-633.
22. National Diabetes Information Clearinghouse. National Diabetes Statistics, 2007. National Institute of Diabetes and Digestive and Kidney Diseases. Ed: National Institute of Health; 2007.
23. Yoon J-W, Jun H-S. Autoimmune destruction of pancreatic  $\beta$ -cells. *American Journal of Therapeutics* 2005;12:580-591.
24. National Diabetes Information Clearinghouse. Diabetes Type I. National Institute for Diabetes and Digestive and Kidney Diseases ed. Washington, D.C.: National Institute of Health; 2008.
25. Robertson RP. Pancreatic and islet transplantation for diabetes-cures or curiosities. *New England Journal of Medicine* 1992;327:1861-1868.

26. Sutherland DER. Pancreas and islet cell transplantation: now and then. *Transplantation Proceedings* 1996;28:2131-2133.
27. Shapiro AM, Lakey JRT, Ryan E, Korbitt G, Toth E, Warnock GL, Kneteman NM, Rajotte RV. Islet transplantation in seven patients with type I diabetes mellitus using a glucocorticoid-free immunosuppressive regimen. *New England Journal of Medicine* 2000;343:230-238.
28. Shapiro AM, Lakey JR, Ryan EA, Korbitt GS, Toth E, Warnock GL, Kneteman NM, Rajotte RV. Islet transplantation in seven patients with type 1 diabetes mellitus using a glucocorticoid-free immunosuppressive regimen. *New England Journal of Medicine* 2000;343(4):230-238.
29. Sun AM, Parisius W, Macmorine H, Sefton MV, Stone R. An artificial pancreas containing cultured islets of Langerhans. *Artificial Organs* 1980;4:275-278.
30. Sullivan SJ, Maki T, Borland KM, Mahoney MD, Solomon BA, Muller TE, Monaco AP, Chick WL. Biohybrid artificial pancreas: long-term implantation studies in diabetic, pancreatectomized dogs. *Science* 1991;252(5006):718-721.
31. Lembert N, Peterson P, Wesche J, Zschocke P, Enderle A, Doser M, Plank H, Becker HD, Ammon HPT. In vitro test of new materials for the development of a bioartificial pancreas. *Annals of the New York Academy of Sciences* 2001;944(1):271-276.
32. Sun AM, Parisius W, Healy GM, Vacek I, Macmorine H. The use in diabetic rats and monkeys, of artificial capillary units containing cultured islets of Langerhans (artificial endocrine pancreas). *Diabetes* 1977;26:1136-1139.
33. Sun AM, O'Shea GM. Microencapsulation of living cells: a long-term delivery system. *Journal of Controlled Release* 1985;2:137-141.
34. Lim F, Sun AM. Microencapsulated islets as bioartificial endocrine pancreas. *Science* 1980;210:908-910.
35. Soon-Shiong P, Feldman E, Nelson R, Komtebedde J, Smidsrød O, Skjåk-Bræk G, Espevik T, Heintz R, Lee M. Successful reversal of spontaneous diabetes in dogs by intraperitoneal microencapsulated islets. *Transplantation* 1992;54:769-774.
36. Sakai S, Ono T, Ijima H, Kawakami K. In vitro and in vivo evaluation of alginate/sol-gel synthesized aminopropyl-silicate/alginate membrane for bioartificial pancreas. *Biomaterials* 2002;23:4177-4183.
37. Benson JP, Papas KK, Constantinidis I, Sambanis A. Towards the development of a bioartificial pancreas: effects of poly-L-lysine on alginate beads with  $\beta$ TC3 cells. *Cell Transplantation* 1997;6:395-402.
38. Lanza RP, Sullivan SJ, Chick WL. Islet transplantation with immunoisolation. *Diabetes* 1992;41:1503-1510.

39. Hirotani S, Ohgawara H, Agishi T, Akaike T, Miyazaki S. A bio-artificial endocrine pancreas for the treatment of diabetes. *Transplantation Proceedings* 1998;30:485-489.
40. Ohgawara H, Miyazaki J, Karibe S, Tashiro F, Akaike T, Hashimoto Y. Embedded-culture of pancreatic  $\beta$ -cells derived from transgenic mouse insulinoma as a potential source for xenotransplantation using a diffusion chamber. *Cell Transplantation* 1995;4:307-313.
41. Qi M, Gu Y, Sakata N, Kim D, Shirouzu Y, Yamamoto C, Hiura A, Sumi S, Inoue K. PVA hydrogel sheet macroencapsulation for the bioartificial pancreas. *Biomaterials* 2004;25:5885-5892.
42. Halban PA, Wollheim CB. Intracellular degradation of insulin stores by pancreatic islets in vitro. An alternative pathway for homeostasis of pancreatic insulin content. *Journal of Biological Chemistry* 1980;255 (13):6003-6006.
43. Efrat S, Linde S, Kofod H, Spector D, Delannoy M, Grant S, Hanahan D, Baekkeskov S. Beta-cell lines derived from transgenic mice expressing a hybrid insulin gene-oncogene. *Proceedings of the National Academy of Sciences USA: Cell Biology* 1988;85:9037-9041.
44. Miyazaki J-I, Araki K, Yamato E, Ikegami H, Asano T, Shibasaki Y, Oka Y, Yamamura K-I. Establishment of a pancreatic  $\beta$  cell line that retains glucose-inducible insulin secretion: special reference to expression of glucose transporter isoforms. *Endocrinology* 1990;127(1):126-132.
45. Dionne KE, Colton CK, Yarmush ML. Effect of hypoxia in insulin secretion by isolated rat and canine islets of Langerhans. *Diabetes* 1993;42(1):12-21.
46. Dionne KE, Colton CK, Yarmush ML. Effect of oxygen on isolated pancreatic tissue. *ASAIO transactions* 1989;35(3):739-741.
47. Papas KK, Long RCJ, Constantinidis I, Sambanis A. Effects of oxygen on the metabolic and secretory activities of bTC3 monolayers. *Biochimica Biophysica Acta* 1996;1291:163-166.
48. Efrat S, Fusco-DeMane D, Lemberg H, Emran OA, Wang X. Conditional transformation of a pancreatic  $\beta$ -cell line derived from transgenic mice expressing a tetracycline-regulated oncogene. *Proceedings of the National Academy of Sciences USA: Biochemistry* 1995;92:3576-3580.
49. Thule PM, Liu J, Phillips LS. Glucose regulated production of human insulin in rat hepatocytes. *Gene Therapy* 2000;7:205-214.
50. Tang S-C, Sambanis A. Development of genetically engineered human intestinal cells for regulated insulin secretion using rAAV-mediated gene transfer. *Biochemical and Biophysical Research Communications* 2003;303:645-652.

51. Cheung AT, Dayanandan B, Lewis JT, Korbitt GS, Rajotte RV, Bryer-Ash M, Boylan MO, Wolfe MM, Kieffer TJ. Glucose-dependant insulin release from genetically engineered K cells. *Science* 2000;290:1959-1962.
52. Lumelsky N, Blondel O, Laeng P, Velasco I, Ravin R, Mckay R. Differentiation of embryonic stem cells to insulin-secreting structures similar to pancreatic islets. *Science* 2001;292:1389-1394.
53. Peck AB, Cornelius JG, Schatz D, Ramiya VK. Generation of islets of Langerhans from adult pancreatic stem cells. *Journal of Hepatobiliary and Pancreatic Surgery* 2002;9:704-709.
54. Bonner-Weir S, Sharma A. Pancreatic stem cells. *Journal of Pathology* 2002;197:519-526.
55. Kuo CK, Ma PX. Ionically crosslinked alginate hydrogels as scaffolds for tissue engineering: part 1. Structure, gelation rate, and mechanical properties. *Biomaterials* 2001;22:511-521.
56. Hirotani S, Eda R, Kawabata T, Fuchinoue S, Teraoka S, Agishi T, Ohgawara H. Bioartificial endocrine pancreas (Bio-AEP) for treatment of diabetes: effect of implantation of Bio-AEP on the pancreas. *Cell Transplantation* 1999;8:399-404.
57. Lahooti S, Sefton MV. Agarose enhances the viability of intraperitoneally implanted microencapsulated L929 fibroblasts. *Cell Transplantation* 2000;9:785-796.
58. Martinsen A, Skjåk-Bræk G, Smidsrød O. Alginate as immobilization material: I. Correlation between chemical and physical properties of alginate gel beads. *Biotechnology and Bioengineering* 1989;33(1):79 - 89.
59. Mørch YA, Donati I, Strand BL, Skjåk-Bræk G. Effect of Ca<sup>2+</sup>, Ba<sup>2+</sup>, and Sr<sup>2+</sup> on Alginate microbeads. *Biomacromolecules* 2006;7:1471-1480.
60. Martinsen A, Storrø I, Skjåk-Bræk G. Alginate as immobilization material: III. Diffusional properties. *Biotechnology and Bioengineering* 1992;39(2):186-194.
61. Smidsrød O, Skjåk-Bræk G. Alginate as immobilization matrix for cells. *Trends in Biotechnology* 1990;8:71-78
62. Augst AD, Kong HJ, Mooney DJ. Alginate hydrogels as biomaterials. *Macromolecular Biosciences* 2006;6:623-633.
63. Normand V, Lootens DL, Amici E, Plucknett KP, Aymard P. New insight into agarose gel mechanical properties. *Biomacromolecules* 2000;1:730-738.
64. Fatin-Rouge N, Milon A, Buffle J. Diffusion and partitioning of solutes in agarose hydrogels: the relative influence of electrostatic and specific interactions. *Journal of Physical Chemistry* 2003;107:12126-12137.

65. Young T-H, Chuang W-Y, Hsieh M-Y, Chen L-W, Hsu J-P. Assessment and modeling of poly(vinyl alcohol) bioartificial pancreas *in vivo*. *Biomaterials* 2002;23:3495-3501.
66. Isayeva IS, Kasibhatla BT, Rosenthal KS, Kennedy JP. Characterization and performance of membranes designed for macroencapsulation/implantation of pancreatic islet cells. *Biomaterials* 2003;24:3483-3491.
67. Sakai S, Ono T, Ijima H, Kawakami K. Newly-developed aminopropyl-silicate immunoisolation membrane for a microcapsule-shaped bioartificial pancreas. *Annals of the New York Academy of Sciences* 2001;944(1):277-283.
68. Massoud TF, Gambhir SS. Molecular imaging in living subjects: seeing fundamental biological processes in a new light. *Genes & Developments* 2003;17:545-580.
69. Lu X, Dang H, Middleton B, Campbell-Thompson M, Atkinson MA, Gambhir SS, Tian J, Kaufman DL. Long-term monitoring of transplanted islets using positron emission tomography. *Molecular Therapy* 2006;14(6):851-856.
70. deLonlay P, Simon-Carre A, Ribeiro M-J, Boddaert N, Giurgea I, Laborde K, Bellane-Chantelot C, Verkarre V, Polak M, Rahier J, Syrota A, Seidenwurm D, Nihoul-Fekete C, Robert J-J, Brunelle F, Jaubert F. Congenital hyperinsulinism: pancreatic [<sup>18</sup>F]fluoro-L-dihydroxyphenylalanine (DOPA) positron emission tomography and immunohistochemistry study of DOPA decarboxylase and insulin secretion. *The Journal of Clinical Endocrinology & Metabolism* 2006;91(3):933-940.
71. Yang Y, Dubois A, Qin X-P, Li J, Haj AE, Wang RK. Investigation of optical coherence tomography as an imaging modality in tissue engineering. *Physics in Medicine and Biology* 2006;51:1649-1659.
72. Gambhir SS. Molecular imaging of cancer with positron emission tomography. *Nature Reviews* 2002;2:683-693.
73. Fowler MJ, Virostko J, Chen Z, Poffenberger G, Radhika A, Brissova M, Shiota M, Nicholson WE, Y. S, Hirshberg B, Harlan DM, D. JE, Powers AC. Assessment of pancreatic islet mass after islet transplantation using *in vivo* bioluminescence imaging. *Transplantation* 2005;79(7):768-776.
74. Chan WC-W, Maxwell DJ, Gao X, Bailey RB, Han M, Nie S. Luminescent quantum dots for multiplexed biological detection and imaging. *Current opinion in biotechnology* 2002;13:40-46.
75. Biju V, Itoh T, Anas A, Sujith A, Ishikawa M. Semiconductor quantum dots and metal nanoparticles: syntheses, optical properties, and biological applications. *Analytical and Bioanalytical Chemistry* 2008;391(7):2469-2495.
76. Tan W, Sendemir-Urkmez A, Fahrner LJ, Jamison R, Leckband D, Boppart SA. Structural and functional optical imaging of three-dimensional engineered tissue development. *Tissue Engineering* 2004;10(11-12):1747-1756.

77. MacDonald JM, Grillo M, Schmidlin O, Tajiri DT, James TL. NMR spectroscopy and MRI investigation of a potential bioartificial liver. *NMR in Biomedicine* 1998;11:55-66.
78. Schoeniger J, Aiken N, Hsu E, Blackband S. Relaxation time and diffusion NMR microscopy of single neurons. *Journal of Magnetic Resonance Series B* 1994;103:261-273.
79. Johnson KMR, Leavitt GD, Kayser HWM. Total-body MR imaging in as little as 18 seconds. *Radiology* 1997;202:262-267.
80. Armstrong P, Keevil SF. Magnetic resonance imaging--1: Basic principles of image production. *British Medical Journal* 1991;303(6793):35-40.
81. Keevil SF. Spatial localization in nuclear magnetic resonance spectroscopy. *Physics in Medicine and Biology* 2006;51:R579-R636.
82. Kimmich R, Hoepfel D. Volume-selective multipulse spin-echo spectroscopy. *Journal of Magnetic Resonance* 1987;72(2):379-384.
83. Moonen CTW, von Kienlin M, van Zijl PCM, Cohen J, Gillen J, Daly P, Wolf G. Comparison of single-shot localization methods (STEAM and PRESS) for *in vivo* proton NMR spectroscopy. *NMR in Biomedicine* 1989;2(5/6):201-208.
84. Haase A, Frahm J, Hanicke W, Matthaei D.  $^1\text{H}$  NMR chemical shift selective (CHESS) imaging. *Physics in Medicine and Biology* 1985;30(4):341-344.
85. Hurd RE, Freeman DM. Metabolite specific proton magnetic resonance imaging. *Proceedings of the National Academy of Sciences USA: Biochemistry* 1989;86:4402-4406.
86. Bolan PJ, Meisamy S, Baker EH, Lin J, Emory T, Nelson M, Everson LI, Yee D, Garwood M. In vivo quantification of choline compounds in the breast with  $^1\text{H}$  MR spectroscopy. *Magnetic Resonance in Medicine* 2003;50(6):1134-1143.
87. Negendank W. Studies of human tumors by MRS: a review. *NMR in Biomedicine* 1992;5:303-324.
88. Long RCJ, Papas KK, Sambanis A, Constantinidis I. In vitro monitoring of total choline levels in a bioartificial pancreas:  $^1\text{H}$  NMR spectroscopic studies of the effects of oxygen level. *Journal of Magnetic Resonance* 2000;146(1):49-57.
89. Hoult DI, Busby SJW, Gadian DG, Radda GK, Richards RE, Seeley PJ. Observation of tissue metabolites using  $^{31}\text{P}$  nuclear magnetic resonance. *Nature* 1974;252:285-287.
90. Moon RB, Richards JH. Determination of intracellular pH by  $^{31}\text{P}$  magnetic resonance. *Journal of Biological Chemistry* 1973;248:7276-7278.

91. Papas KK, R. C. Long J, Constantinidis I, Sambanis A. Role of ATP and P<sub>i</sub> in the mechanism of insulin secretion in the mouse insulinoma  $\beta$ TC3 cell line. *Biochemistry Journal* 1997;326:807-814.
92. Papas KK, Long RCJ, Constantinidis I, Sambanis A. Effects of short-term hypoxia on a transformed cell-based bioartificial pancreatic construct. *Cell Transplantation* 2000;9:415-422.
93. Taylor J, Deutsch C. <sup>19</sup>F-nuclear magnetic resonance: measurements of [O<sub>2</sub>] and pH in biological systems. *Biophysical Journal* 1988;53:227-233.
94. McGovern KA, Schoeniger JS, Wehrle JP, Ng CE, Glickson JD. Gel-entrapment of perfluorocarbons: a fluorine-19 NMR spectroscopic method for monitoring oxygen concentration in cell perfusion system. *Magnetic Resonance in Medicine* 1993;29:196-203.
95. Gross JD, Long RCJ, Constantinidis I, Sambanis A. Monitoring of dissolved oxygen and cellular bioenergetics within a pancreatic substitute. *Biotechnology and Bioengineering* 2007;98(1):261-270.
96. Nöth U, Gröhn P, Jork A, Zimmermann U, Haase A, Lutz J. <sup>19</sup>F-MRI in vivo determination of the partial oxygen pressure in perfluorocarbon-loaded alginate capsules implanted into the peritoneal cavity and different tissues. *Magnetic Resonance In Medicine* 1999;42:1039-1047.
97. Bloembergen N, Purcell EM, Pound RV. Relaxation effects in magnetic resonance absorption. *Physical Reviews* 1948;73(7):679-712.
98. Hyde JS, Jesmanowicz A, Grist TM, Fencisz W, Kneeland JB. Quadrature detection surface coil. *Magnetic Resonance in Medicine* 1987;4:179-184.
99. Roemer PB, Edelstein WA, Hayes CE, Souza SP, Mueller OM. The NMR phased array. *Magnetic Resonance in Medicine* 1990;16:192-225.
100. Arnder L, Shattuck MD, Black RD. Signal-to-noise ratio comparison between surface coils and implanted coils. *Magnetic Resonance In Medicine* 1996;35:727-733.
101. Hoult DI, Tomanek B. Use of mutually inductive coupling in probe design. *Concepts in Magnetic Resonance (Magnetic Resonance Engineering)* 2002;15(4):262-285.
102. Hardy WN, Whitehead LA. Split-ring resonator for use in magnetic resonance from 200-2000 MHz. *Review of Scientific Instruments* 1981;52(2):213-216.
103. Vullo T, Zipagan RT, Pascone R, Whalen JP, Cahill PT. Experimental design and fabrication of birdcage resonators for magnetic resonance imaging. *Magnetic Resonance in Medicine* 1992;24(2):243-252.

104. Edelstein WA, Hardy CJ, Mueller OM. Electronic decoupling of surface-coil receivers for NMR imaging and spectroscopy. *Journal of Magnetic Resonance* 1986;67:156-161.
105. Hyde JS, Rilling RJ, Jesmanowicz A. Passive decoupling of surface coils by pole insertion. *Journal of Magnetic Resonance* 1990;89:485-495.
106. Boskamp EB. Improved surface coil imaging in MR: Decoupling of the excitation and receiver coils. *Radiology* 1985;157(2):449-452.
107. Schnall MD, V. HS, J. S. Leigh J, B. C. A new double-tuned probe for concurrent  $^1\text{H}$  and  $^{31}\text{P}$  NMR. *Journal of Magnetic Resonance* 1985;65:122-129.
108. Fitzsimmons JR, Brooker HR, Beck BL. A transformer-coupled double-resonant probe for NMR imaging and spectroscopy. *Magnetic Resonance in Medicine* 1987;5:471-477.
109. Li Y, Logan TM, Edison AS, Webb A. Design of small volume HX and triple-resonance probes for improved limits of detection in protein NMR experiments. *Journal of Magnetic Resonance* 2003;164:128-135.
110. Sinha N, Grant CV, Rotondi KS, Feduik-Rotondi L, Gierasch LM, Opella SJ. Peptides and the development of double- and triple-resonance solid state NMR of aligned samples. *Journal of Peptide Research* 2005;65:605-620.
111. Martin RW, Paulson EK, Zilm KW. Design of a triple resonance magic angle sample spinning probe for high field solid state nuclear magnetic resonance. *Review of Scientific Instruments* 2003;74(6):3045-3061.
112. Tomanek B, Volotovskyy V, Gruwel MLH, McKenzie E, King SB. Double-frequency birdcage volume coils for 4.7T and 7T. *Concepts in Magnetic Resonance Part B* 2005;26B(1):16-22.
113. Fitzsimmons JR, Brooker HR, Beck BL. A comparison of double-tuned surface coil. *Magnetic Resonance in Medicine* 1989;10:302-309.
114. Leroy-Willig A, Bittoun J, Kan S, Gonord P. A simplified double-tuned  $^{31}\text{P}$ - $^1\text{H}$  circuit for NMR *in vivo* spectroscopic experiments. *Review of Scientific Instruments* 1990;61(2):799-801.
115. Schnall MD, Subramanian VH, Leigh JSJ, Gyulai L, McLaughlin A, Cance B. A technique for simultaneous  $^1\text{H}$  and  $^{31}\text{P}$  NMR at 2.2T *in vivo*. *Journal of Magnetic Resonance* 1985;63:401-405.
116. Chang L-H, Chew WM, Weinstein PR, James TL. A balanced-matched double-tuned probe for *in vivo*  $^1\text{H}$  and  $^{31}\text{P}$  NMR. *Journal of Magnetic Resonance* 1987;72:168-172.
117. Kan S, Gonord P. Single-input double-tuned mutually coupled surface coil circuits: an analysis. *Review of Scientific Instruments* 1991;62(10):2427-2429.

118. Schnall MD. Probes tuned to multiple frequencies for in-vivo NMR. In: Rudin M, de Beer R, Cady EB, Garwood M, Link J, Moonen CTW, Morris PG, Müller S, van Ormondt D, Schnall MD, K. U, van Zijl PCM, editors. In-vivo Magnetic Resonance Spectroscopy 1: Probeheads and radio frequency pulses, Spectrum Analysis. Volume 26, NMR Basic Principles and Progress. Berlin, Heidelberg: Springer-Verlag; 1992. p 33-63.
119. Gonen O, Murphy-Boesch J, Li CW, Padavic-Shaller K, Negendank WG, Brown TR. Simultaneous 3D NMR spectroscopy of proton-decoupled fluorine and phosphorus in human liver during 5-fluorouracil chemotherapy. *Magnetic Resonance in Medicine* 1997;37(2):164-169.
120. Eleff SM, Schnall MD, Ligetti L, Osbakken M, Subramanian VH, Chance B, Leigh JSJ. Concurrent measurements of cerebral blood flow, sodium, lactate, and high-energy phosphate metabolism using  $^{19}\text{F}$ ,  $^{23}\text{Na}$ ,  $^1\text{H}$ , and  $^{31}\text{P}$  nuclear magnetic resonance spectroscopy. *Magnetic Resonance Imaging* 1988;7:412-424.
121. McNichols RJ, Wright SM, Wasser JS, Coté GL. An inductively coupled, doubly tuned resonator for *in vivo* nuclear magnetic resonance spectroscopy. *Review of Scientific Instruments* 1999;70(8):3454-3456.
122. Schmidt HC, Gooding CA, James TL, Gonzalez-Mendez R, James JL. Comparison of *in vivo*  $^{31}\text{P}$ -NMR spectra of the brain, liver, and kidney of adult and infant animals. *Pediatric Radiology* 1986;16:144-149.
123. Schmidt HC, Gooding CA, James TL. *In vivo*  $^{31}\text{P}$ -MR spectroscopy of the liver in the infant rabbit to study the effect of hypoxia on the phosphorus metabolites and intracellular pH. *Investigative Radiology* 1986;21:156-161.
124. Farmer THR, Johnson GA, Cofer GP, Maronpot RR, Dixon D, Hedlund LW. Implanted coil MR microscopy of renal pathology. *Magnetic Resonance In Medicine* 1989;10:310-323.
125. Ford JC, Shlansky-Goldberg RD, Golden M. MR microscopy of the arterial wall in an experimental model of atherosclerosis: preliminary results. *Journal of Vascular and Interventional Radiology* 1997;8(1):93-99.
126. Summers RM, Hedlund LW, Cofer GP, Gottman MB, Manibo JF, Johnson GA. MR microscopy of the rat carotid artery after balloon injury by using and implanted imaging coil. *Magnetic Resonance In Medicine* 1995;33:785-789.
127. Arnder L, Zhou X, G.P.Cofer, Hedlund LW, Johnson GA. Magnetic resonance microscopy of the rat carotid artery at 300 megahertz. *Investigative Radiology* 1994;29(9):822-826.
128. Malloy CR, Cunningham CC, Radda GK. The metabolic state of the rat liver *in vivo* measured by  $^{31}\text{P}$ -NMR spectroscopy. *Biochimica et Biophysica Acta* 1986;885:1-11.

129. MacDonald JM, Schmidlin O, James TL. In vivo monitoring of hepatic glutathione in anesthetized rats by  $^{13}\text{C}$  NMR. *Magnetic Resonance In Medicine* 2002;48:430-439.
130. Quistorff B, Engkagul A, Chance B.  $^{31}\text{P}$  NMR in the study of liver metabolism in vivo. *Pharmacology Biochemistry & Behavior* 1983;18(Suppl. 1):241-244.
131. Shine NR, Xuan JA, Koretsky AP, Weiner MW. Determination of renal molar concentrations of phosphorus-containing metabolites *in vivo* using  $^{31}\text{P}$  NMR. *Magnetic Resonance In Medicine* 1987;4:244-251.
132. Kivelitz D, Wagner S, Schnorr J, Wetzler R, Busch M, Melzer A, Taupitz M, Hamm B. A vascular stent as an active component for locally enhanced magnetic resonance imaging. *Investigative Radiology* 2003;38(3):147-152.
133. Morikawa S, Inubushi T, Kito K, Amano S. Long-term observation of *in vivo*  $^{31}\text{P}$  NMR spectra in carbon tetrachloride-intoxicated rabbit liver using implanted wireless surface coil. *NMR Biomedicine* 1995;8(1):3-8.
134. Frazer RQ, Byron RT, Osborne PB, West KP. PMMA: an essential material in medicine and dentistry. *Journal of Long-Term Effects of Medical Implants* 2005;15(6):629-639.
135. Licari JJ, Hughes LA. Chemistry and Properties of Coatings - Polyesters-Polyvinyls-Polystyrenes-Acrylics-Diallylphthalates-Polyamides-Phenolics-Polysulfides. In: Licari JJ, Hughes LA, editors. *Handbook of Polymer Coatings for Electronics - Chemistry, Technology and Applications (2nd Edition)*: William Andrew Publishing/Noyes; 1990. p 85-102.
136. Reichlin J, Bormashenko E, Sheshnev A, Pogreb R, Shulzinger E, Katzir A. Investigation of water penetration in polystyrene by use of polymer-coated AgClBr fibers and development of new sensor intended for the FEWS spectroscopy of organic compounds in water. *Proceedings of SPIE* 2000 4129:305-313.
137. Mata A, Fleischman AJ, Roy S. Characterization of polydimethylsiloxane (PDMS) properties for biomedical micro/nanosystems. *Biomedical Microdevices* 2005;7(4):281-293.
138. Kannan RY, Salacinski HJ, Butler PE, Hamilton G, Seifalian AM. Current status of prosthetic bypass grafts: a review. *Journal of Biomedical Material Research Part B: Applied Biomaterials* 2005;74(1):570-581.
139. Hoult DI, Richards RE. The signal-to-noise ratio of the nuclear magnetic resonance experiment. *Journal of Magnetic Resonance* 1976;24:71-85.
140. Peterson DM, Beck BL, Duensing GR, Fitzsimmons JR. Common mode signal rejection methods for MRI: reduction of cable shield currents for high static magnetic field systems. *Concepts in Magnetic Resonance Part B (Magnetic Resonance Engineering)* 2003;19B(1):1-8.

141. Regan F, MacCraith BD, Walsh JE, O'Dwyer K, Vos JG, Meaney M. Novel Teflon-coated optical fibres for TCE determination using FTIR spectroscopy. *Vibrational Spectroscopy* 1997;14(2):239-246.
142. Terman FE. *Radio engineers' handbook*. New York and London: McGraw-Hill Book Company, Inc.; 1943.
143. Froncisz W, Jesmanowicz A, Kneeland JB, Hyde JS. Counter rotating current local coils for high-resolution magnetic resonance imaging. *Magnetic Resonance in Medicine* 1986;3:590-603.
144. Jacobs G, Assefa A, Willig-Onwuachi J. Q measurement and simulation for RF coils. 2008; Toronto, Ontario, Canada. Mira Digital Publishing. p 1082.
145. Chen C-N, Sank VJ, Cohen SM, Hoult DI. The field dependence of NMR imaging: I. Laboratory assessment of signal-to-noise ratio and power deposition. *Magnetic Resonance In Medicine* 1985;3:722-729.
146. Gabriel C, Gabriel S, Corthout E. The dielectric properties of biological tissues: I. Literature survey. *Physics in Medicine and Biology* 1996;41:2231-2249.
147. Gabriel C, Lau RW, Gabriel S. The dielectric properties of biological tissues: II. Measurements in the frequency range 10 Hz to 20 GHz. *Physics in Medicine and Biology* 1996;41:2251-2269.
148. Gabriel C, Lau RW, Gabriel S. The dielectric properties of biological tissues: III. Parametric models for the dielectric spectrum of tissues. *Physics in Medicine and Biology* 1996;41:2271-2293.
149. Shapiro L, Cohen S. Novel alginate sponges for cell culture and transplantation. *Biomaterials* 1997;18:583-590.
150. Glicklis R, Shapiro L, Agbaria R, Merchuk JC. Hepatocyte behavior within three-dimensional porous alginate scaffolds. *Biotechnology and Bioengineering* 2000;67(3):344-353.
151. Simpson NE, Khokhlova N, Oca-Cossio JA, McFarlane SS, Simpson CP, Constantinidis I. Effects of growth regulation on conditionally-transformed alginate insulin secreting cell lines *in vitro*. *Biomaterials* 2005;26:4633-4641.
152. de Graaf RA, Brown PB, McIntyre S, Nixon TW, Behar KL, Rothman DL. High magnetic field water and metabolite proton T<sub>1</sub> and T<sub>2</sub> relaxation in rat brain *in vivo*. *Magnetic Resonance In Medicine* 2006;56:386-394.
153. Henkelman RM. Measurement of signal intensities in the presence of noise in MR images. *Medical Physics* 1985;12(2):232-233.

154. Keltner JR, Carlson JW, Roos MS, Wong ST, Wong TL, Budinger TF. Electromagnetic fields of surface coil *in vivo* NMR at high frequencies. *Magnetic Resonance In Medicine* 1991;22(2):467-480.
155. Nijm GM, Sahakian AV, Swiryn S, Carr JC, Sheehan JJ, Larson AC. Comparison of self-gated cine MRI retrospective cardiac synchronization algorithms. *Journal of Magnetic Resonance Imaging* 2008;28:767-772.
156. Hiba B, Richard N, Janier M, Croisille P. Cardiac and respiratory double self-gated cine MRI in the mouse at 7T. *Magnetic Resonance in Medicine* 2006;55:506-513.
157. Larson AC, White RD, Laub G, McVeight ER, Li D, Simonetti OP. Self-gated cardiac cine MRI. *Magnetic Resonance in Medicine* 2004;51:93-102.
158. Cassidy PJ, Schneider JE, Grieve SM, Lygate C, Neubauer S, Clarke K. Assessment of motion gating strategies for mouse magnetic resonance at high magnetic fields. *Journal of Magnetic Resonance Imaging* 2004;19:229-237.
159. Griffin JL, Mann CJ, Scott J, Shoulders CC, Nicholson JK. Choline containing metabolites during cell transfection: an insight into magnetic resonance spectroscopy detectable changes. *FEBS Letter* 2001;509:263-266.
160. Volland NA, Mareci TH, Simpson NE. Development of an inductively-coupled MR coil system for imaging and spectroscopic analysis of an implantable bioartificial construct at 11.1T. *Magnetic Resonance In Medicine* 2009:(submitted).
161. Beck BL, Jenkins KA, Rocca JR, Fitzsimmons JR. Tissue-equivalent phantoms for high frequencies. *Concepts in Magnetic Resonance Part B (Magnetic Resonance Engineering)* 2004;20B(1):30-33.
162. Harris FJ. On the use of Windows for Harmonic Analysis with the Discrete Fourier Transform. *Proceedings of the IEEE* 1978;66(1):51-83.
163. Mao J, Mareci TH, Andrew ER. Experimental Study of Optimal Selective 180° Radiofrequency Pulses. *Journal of Magnetic Resonance* 1988;79(1):1-10.
164. Tanuus A, Garwood M. Adiabatic pulses. *NMR in Biomedicine* 1997;10:423-434.
165. Chew WM, Chang L-H, Flamig DP, James TL. The SWIFT method for *in vivo* localized excitation (SMILE). *Journal of Magnetic Resonance* 1987;75:523-528.
166. Gruetter R. Automatic localized *in vivo* adjustment of all-first and second-order shim coils. *Magnetic Resonance In Medicine* 1993;29:804-811.
167. Schnall MD, Subramanian VH, Leigh JS. The application of overcoupled tank circuits to NMR probe design. *Journal of Magnetic Resonance* 1986;67:129-134.
168. Grover FW. Inductance calculations: Dover Publications; 1946. 286 p.

169. Joseph PM, Fishman JE, Mukherji B, Sloviter HA. In vivo  $^{19}\text{F}$  NMR imaging of the cardiovascular system. *Journal of Computer Assisted Tomography* 1985;9(6):1012-1019.
170. Gross JD. Non-invasive monitoring of oxygen concentrations and metabolic functions in pancreatic substitutes. Atlanta, GA: Georgia Institute of Technology; 2007. 189 p.
171. Haake EM, Brown RW, Thompson MR, Venkatesan R. Introductory signal acquisition methods: Free induction decay, spin echoes, inversion recovery and spectroscopy. *Magnetic resonance imaging. Volume 1*. New York: John Wiley & Sons, Inc.; 1999. p 111-137.
172. Bernstein MA, King KF, Zhou XJ. Basic Pulse sequences. *Handbook of MRI pulse sequences. Volume 1*. Boston: Elsevier Inc.; 2004. p 579-647.
173. Shah P. Magnetic resonance characterization of skeletal muscle adaptations after incomplete spinal cord injury. Gainesville, FL: University of Florida; 2008. 245 p.
174. Stabler CL, Wilks K, Sambanis A, Constantinidis I. The effects of alginate composition on encapsulated  $\beta\text{TC3}$  cells. *Biomaterials* 2001;22:1301-1310.
175. Simpson NE, Stabler CL, Simpson CP, Sambanis A, Constantinidis I. The role of the  $\text{CaCl}_2$ -guluronic acid interaction on alginate encapsulated  $\beta\text{TC3}$  cells. *Biomaterials* 2004;25:2603-2610.
176. Zekorn T, Horcher A, Siebers U, Schnettler R, Klöck G, B. H, Zimmermann U, Bretzel RG, Federlin K. Barium-cross-linked alginate beads: a simple, one-step method for successful immunoisolated transplantation of islets of Langerhans. *Acta Diabetologica* 1992;29(2):99-106.
177. Petruzzo P, Cappai P, Ruiu G, Brotzu G. Cell Microencapsulation: A new method. *Transplantation Proceedings* 1994;26:3507-3508.
178. Black SP, Constantinidis I, Cui H, Tucker-Burden C, Weber CJ, Safley SA. Immune responses to an encapsulated allogenic islet  $\beta$ -cell line in diabetic NOD mice. *Biochemical and Biophysical Research Communications* 2006;340:236-243.
179. Axel L, Summers RM, Kressel HY, Charles C. Respiratory effects in two-dimensional Fourier transform MR imaging. *Radiology* 1986;160:795-801.
180. Batchelor PG, Atkinson D, Irarrazaval P, Hill DLG, Hajnal J, Larkman D. Matrix description of general motion correction applied to multishot images. *Magnetic Resonance in Medicine* 2005;54:1273-1280.
181. Odille F, Vuissoz P-A, Marie P-Y, Felblinger J. Generalized reconstruction by inversion of coupled systems (GRICS) applied to free-breathing MRI. *Magnetic Resonance in Medicine* 2008;60:146-157.

182. Beck BL, Letzen BS, Bashirullah R, Mareci TH. Wireless control of an implantable coil system for MRI/S. In: 16th Scientific Meeting and Exhibition of the International Society for Magnetic Resonance in Medicine Proceedings, editor; 2008; Toronto, Ontario, Canada. p 1111.

## BIOGRAPHICAL SKETCH

Nelly Aline Volland was born in Bourgoin-Jallieu, France, in 1979. She was successively raised in Bourgoin-Jallieu, Montceau, Faverges, Mercury, and Luxeuil-les-Bains, due to her parents' numerous relocations. She quickly decided to concentrate on sciences since physics and mathematics were her favorite subjects. She received her scientific baccalauréat with honors from Lycée Jean Moulin in Albertville, France, where she graduated high school in June 1997. She then joined the pre-engineering school Cycle Préparatoire Polytechnique in Nancy (CPP, France) to gain the scientific skills necessary to enter the Ecole Nationale Supérieure de Physique de Grenoble (ENSPG, France), where she was accepted in September 1999. She chose to focus on physical instrumentation during the second year of engineering school to get closer to the area of specialization she was truly interested in, Biomedical Engineering. During her third and last year of engineering school, she enrolled at the University of Florida where she finally specialized in the biomedical engineering with a concentration in biomedical imaging and signal processing. This opportunity allowed her to be awarded a dual degree, one French and one American. She received her Diplôme d'Ingénieur (master equivalent) in physics from the Institut National Polytechnique de Grenoble (INPG, France) in September 2002 and was awarded a Master of Science in biomedical engineering from the University of Florida in December 2003. To further specialize in the field of biomedical engineering she enrolled in the Ph.D program at the University of Florida in August 2003. Her primary focus has been on biomedical imaging instrumentation. She hopes to continue developing and improving imaging methods to see smaller and smaller biological entities and contribute to the understanding of diseases and the development of their treatment.